Structure-property relationships in stimulus-responsive cadmium- and zinc-based metal-organic framework materials

by

Isabella Elizabeth Claassens

Dissertation presented for the degree of Doctor of Philosophy in the Faculty of Science at Stellenbosch University

Supervisor: Prof. Delia A. Haynes

Co-supervisor: Prof. Leonard J. Barbour

Department of Chemistry and Polymer Science

Faculty of Science

University of Stellenbosch

March 2020

Declaration

By submitting this proposal, I declare that the entirety of the work contained therein is my own, original work, that I am the sole author thereof (save to the extent explicitly otherwise stated), that reproduction and publication thereof by Stellenbosch University will not infringe any third party rights and that I have not previously in its entirety or in part submitted it for obtaining any qualification. This dissertation includes 2 original papers published in peer-reviewed journals and 1 unpublished publication. The development and writing of the papers (published and unpublished) were the principal responsibility of myself and, for each of the cases where this is not the case, a declaration is included in the dissertation indicating the nature and extent of the contributions of co-authors.

March 2020

Acknowledgements

First and foremost I would like to thank my supervisors, Profs. Delia Haynes and Len Barbour. You have been an inspiration. Without your guidance and mentorship, this document would not have been possible. You have instilled in me a great enthusiasm and admiration for the fascinating field of solid-state research. Thank you for the opportunity to work in a world-class laboratory where I had the freedom to explore my own research interests while learning many valuable and specialised skills. I am truly appreciative of the numerous opportunities you have provided me with.

I would also like to thank the Supramolecular Research Group members and support staff, past and present, for creating a homely yet intellectually-stimulating research environment. A special thanks goes to Drs. Charl Bezuidenhout, Prem Lama, Varvara Nikolayenko, Leigh Loots, and Alan Eaby for their support both socially and scientifically. Lastly I would like to give special thanks to Wesley Feldmann for always having the time and willingness to help, while keeping me motivated when the going gets tough.

This would also not have been possible without the love and support from my family and friends, for which I am eternally grateful. Finally, I would like to thank the University of Stellenbosch for providing me with the necessary facilities and the NRF and Sasol for funding.

Abstract

The study of flexible MOFs or soft porous crystals is an exciting and fast-expanding area of MOF research. These materials respond dynamically to external stimuli, including temperature, mechanical pressure, guest sorption or light. Flexible MOFs are prime candidates for gas separation and storage, catalysis and sensing applications. Thus far the focus has largely been on the creation of new MOFs. However, focusing on fine-tuning and controlling the properties of these materials can produce advanced materials with potential applications in several areas of industry. This study investigates the structure-property relationships of three related flexible MOFs to explore ways in which to tune and control their response to specific stimuli. The effects of guest inclusion, temperature and light on the structure of the material are studied. The first two studies place special focus on photochemical cycloaddition and exploring means with which to control the outcome of the reaction.

We describe the use of guest exchange as a means to control the position of photochemical [2+2] cycloaddition between bpeb ligands in a new Cd (II) MOF. The selective synthesis of one of two different isomeric products is demonstrated by exchanging one solvent in the channels of the MOF for another. The nature of the guest controls the conformation of the organic linker (bpeb) within the framework, which has a direct effect on the regioselectivity of the cycloaddition reaction. The study demonstrates how a response to different guests in a flexible MOF can be utilised as a synthetic tool and is the first example of the synthesis of both isomers of the cyclized bpeb dimer in the same framework.

In the second study temperature change is employed as a stimulus control regioselectivity of the photochemical cycloaddition reaction in the same Cd(II) MOF. The isomeric product formed depends on the temperature at which irradiation is carried out. A rare temperature-induced phase transition alters the conformation of the bpeb ligand in the MOF, and thereby the position at which cycloaddition occurs. The phase transition is fully described and characterised using variable temperature X-ray diffraction techniques. This work also highlights the multistimulus responsive nature of this Cd(II) MOF, which responds to temperature as well as solvent exchange and light.

The final section describes a new highly flexible four-fold interpenetrated fluorinated MOF that undergoes breathing and subnetwork displacement modes of flexibility to give interesting gas sorption behaviour. The effect of fluorinated substituents on the gas sorption behaviour is investigated by comparing it to the non-fluorinated isoreticular analogue. Sorption analysis reveals significant changes in gate-opening pressure as well as the degree of hysteresis observed between the two frameworks. *In situ* SCXRD techniques and computational analysis are employed to describe and identify the interactions responsible for the change in behaviour. This study shows that fluorination of pillar linkers is a viable pathway to developing frameworks that exhibit favourable sorption profiles for future studies.

These studies improve the understanding of how to control or fine-tune MOFs that change their properties in response to particular stimuli.

Opsomming

Die bestudering van buigsame MOFs of sagte poreuse kristalle is 'n opwindende en vinnig-uitbreidende gebied van MOF-navorsing. Hierdie materiale reageer dinamies op eksterne stimuli, insluitend temperatuur, meganiese druk, sorpsie of lig. Buigsame MOFs is belangrike kandidate vir gasskeiding en opberging, katalise en sensortoepassings. Die fokus was dus grotendeels op die voorbereiding van nuwe MOFs, maar met die fokus op die fynstelling en die beheer van die eienskappe van hierdie materiale, kan gevorderde materiale met potensiële toepassings op verskillende bedryfsgebiede vervaardig word. Hierdie studie ondersoek die verhouding tussen struktuur-eienskap verhoudings en drie verwante buigsame MOFs om maniere te bepaal hoe hulle op spesifieke stimuli reageer en dus beheer. Die gevolge van die opname van gas, temperatuur en lig op die struktuur van die materiaal word bestudeer. Die eerste twee studies fokus veral op fotochemiese sikloaddisie en eksplorasie van middele om die uitkoms van die reaksie te beheer.

Ons beskryf die gebruik van gaswisseling as 'n middel om die posisie van fotochemiese [2 + 2] sikloaddisie tussen bpeb ligande in 'n nuwe Cd (II) MOF te beheer. Die selektiewe sintese van een van twee verskillende isomeer produkte word gedemonstreer deur een oplosmiddel in die kanale van die MOF vir 'n ander te ruil. Die aard van die gas beheer die konformasie van die organiese skakelaar (bpeb) binne die raamwerk, wat 'n direkte effek op die gebiedselektiwiteit van die sikloaddisie -reaksie het. Die studie demonstreer hoe 'n respons op verskillende gaste in 'n buigsame MOF as 'n sintetiese instrument gebruik kan word en is die eerste voorbeeld van die sintese van beide isomere van die gesikliseerde bpeb-dimer in dieselfde raamwerk.

In die tweede studie word temperatuurverandering aangewend as die stimulus om gebiedselektiwiteit van die fotochemiese sikloaddisie-reaksie in dieselfde Cd (II) MOF te beheer. Die gevormde isomeriese produk wat gevorm word hang af van die temperatuur waarteen bestraling plaasvind. 'n Seldsame temperatuur-geïnduseerde fase-oorgang verander die konformasie van die bpeb-ligand in die MOF, en sodoende die posisie waar die sikloaddisie plaasvind. Die fase-oorgang word volledig beskryf en gekarakteriseer met behulp van X-straaldiffraksie tegnieke met veranderlike temperatuur. Hierdie werk beklemtoon ook die multistimulus responsiewe aard van hierdie Cd (II) MOF wat reageer op temperatuur sowel as oplosmiddeluitwisseling en lig.

Die slotgedeelte beskryf 'n nuwe hoogs buigsame, viervoudige-geïntegreerde gefluoreerde MOF wat asemhalings- en subnetwerkverskuiwing van buigsaamheid ondergaan om interessante gassorpsiegedrag te toon. Die effek van gefluoreerde substituente op die gassorpsiegedrag word ondersoek deur dit met die nie-gefluoreerde isoretiese analoog te vergelyk. Die sorpsie-ontleding onthul aansienlike veranderinge in die hek openingsdruk sowel as die mate van histerese wat tussen die twee raamwerke waargeneem is. In-situ SCXRD-tegnieke en rekenaaranalise word gebruik om die interaksies wat vir die gedragsverandering verantwoordelik is, te beskryf en te identifiseer. Hierdie studie toon dat

fluorering van pilaarskakelaars 'n uitvoerbare roete is om raamwerke vir toekomstige studies te ontwikkel wat gunstige sorpsieprofiele vertoon.

Hierdie studies verhef die begrip van die beheer van MOFs wat hul eienskappe verander na aanleiding van spesifieke stimuli.

Publications

1. Solvent-Mediated Synthesis of Cyclobutane Isomers in a Photoactive Cadmium(II) Porous Coordination Polymer
   Isabella E. Claassens, Varvara I. Nikolayenko, Delia A. Haynes, and Leonard J. Barbour
   Angew. Chem. Int. Ed. **2018**, 57, 15563 –15566
   Angew. Chem. 2018, 130, 15789 – 15792

2. A Multistimulus Responsive Porous Coordination Polymer: Temperature-Mediated Control of Solid-State [2+2] Cycloaddition
   Isabella E. Claassens, Leonard J. Barbour, and Delia A. Haynes
   J. Am. Chem. Soc. **2019**, 141, 11425−11429

3. Tuning gate-opening pressure and hysteresis in a highly flexible pillared-layered metal-organic framework by ligand fluorination
   Isabella E. Claassens, Wesley K. Feldmann, Charl X. Bezuidenhout, Catharine Esterhuysen, Delia A. Haynes and Leonard J. Barbour
   Submitted, **2019**

Conferences

1. **SACI Young Chemists' Symposium**
   Stellenbosch, Western Cape, South Africa, 2016
   Oral Presentation: Post-synthetic Modification of Metal-Organic Frameworks
   Awarded 2nd Prize

2. **ICCOSS 2017: 23rd International Conference on the Chemistry of the Organic Solid Sta**te
   Stellenbosch, Western Cape, South Africa, 2017
   Poster Presentation: Post-synthetic photochemical [2+2] cycloaddition in cadmium MOFs

3. **SACI Inorg 2017: Inorganic Chemistry Conference and Carman Physical Chemistry Symposium**
   Hermanus, South Africa, June 2017
   Flash oral and poster presentation: Solvent-dependent site-selective photochemical [2+2] cycloaddition in a cadmium MOF
   Awarded Gold prize for the flash oral presentation

4. **2nd Meeting on Porous Molecular Solids (POMOS2)**
   Vietri sul Mare, Italy, June 2018
   Flash oral presentation and poster: Stepped sorption behaviour in a highly porous four-fold interpenetrated zinc-based MOF
   Awarded ECA Young Scientist travel bursary to attend

5. **Gordon Research Seminar: Crystal Engineering (GRS)**
   Newry, ME, USA, June 2018
   Oral presentation: Solvent-Mediated Photoactivity in a Cadmium MOF

6. **Gordon Research Conference: Crystal Engineering (GRC)**
   Newry, ME, USA, June 2018
   Poster presentation: Solvent-mediated synthesis of cyclobutane isomers in a photoactive cadmium(II) metal organic framework

7. **European Crystallographic School (ECS 5)**
   Stellenbosch University, South Africa, July 2018
   Contribution: Tutor at practical sessions

8. **4th International Symposium on Macrocyclic and Supramolecular Chemistry (ISMSC 2019)**

   Lecce Italy, June 2019

   Poster: A Multi-Stimulus Responsive Porous Coordination Polymer: Temperature-Mediated Control of Solid-state [2+2] Cycloaddition

   Awarded IUCr travel bursary to attend

9. **10th Crystal Forms Convention**

   Poster: A Multi-Stimulus Responsive Porous Coordination Polymer: Temperature-Mediated Control of Solid-state [2+2] Cycloaddition

   Bologna, Italy, June 2019

   Awarded 1st Poster prize

10. **First International School on Advanced Porous Materials (MOFSchool)**

    Como, Italy, June 2019

    Poster: A Multi-Stimulus Responsive Porous Coordination Polymer: Temperature-Mediated Control of Solid-state [2+2] Cycloaddition

    Awarded (IUCr) Journals Poster Prize

Abbreviations

1D	One-dimensional
2D	Two-dimensional
3D	Three-dimensional
adc	Azobenzene-4,4'-dicarboxylic acid
ASU	Asymmetric unit
bdc	1,4-Benzenedicarboxylic acid
bipy	4,4′−Dipyridyl
bpeb	1,4-Bis[2-(4'-pyridyl)ethenyl]benzene
bpee	1,2-Bis(4-pyridyl)ethylene
BTB	1,3,5-Tris(4-carboxphenyl)benzene)
btc	1,4-Benzenetricarboxylic acid
CIF	Crystallographic information file
CSD	Cambridge Structural Database
DMA	N,N-dimethylacetamide
DMF	N,N-dimethylformamide
DMSO	Dimethyl sulfoxide
DSC	Differential scanning calorimetry
fbpeb	4,4-[(2,3,5,6-tetrafluoro-1,4-phenylene)-2,1-ethenediyl]bis-pyridine
HKUST	Hong Kong University of Science and Technology
IR	Infrared
IUPAC	International Union of Pure and Applied Chemistry
MIL	Material of Institut Lavoisier
MOF	Metal-organic framework
NMR	Nuclear magnetic resonance
oba	4,4′-Oxybis(benzoic acid)
PCP	Porous Coordination Polymer
PGDSC	Pressure-gradient differential scanning calorimetry
PL-MOF	Pillared-layer metal-organic framework
PXRD	Powder X-ray diffraction

SBU	Secondary building unit
SCXRD	Single-crystal X-ray diffraction
TGA	Thermogravimetric analysis
UV	Ultraviolet
ZIF	Zeolitic imidazolate framework

Atom colour key

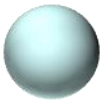

Hydrogen

Carbon

Oxygen

Nitrogen

Fluorine

Metal

Table of Contents

Chapter 1

Introduction

1.1 Supramolecular chemistry and crystal engineering

In 1978, Nobel Laureate J. M. Lehn defined supramolecular chemistry as the "chemistry beyond the molecule". He further explained it to be the chemistry of complex structures that result from the association of two or more chemical species held together by intermolecular interactions.[1] According to Dunitz, a crystal is "a supermolecule par excellence" which describes it as an assembly of millions of molecules self-crafted by mutual recognition at an "amazing level of precision".[2] Research in supramolecular chemistry aims at developing highly complex chemical systems from components interacting through non-covalent intermolecular forces.[3] The field encompasses many disciplines alongside chemistry, including areas such as condensed matter physics, materials science and the biological sciences.[4] The work described herein will focus on host-guest chemistry but this is just one aspect of supramolecular chemistry; the supramolecular field includes all aspects of self-assembly and pre-organisation. The evolution of the field can be traced back from the elementary solid-state "clathrate" model to the molecular host-guest inclusion model, and finally to the self-assembly paradigm.[5]

As stated by Desiraju, crystal engineering is "*the understanding of intermolecular interactions in the context of crystal packing and the utilization of such understanding in the design of new solids with desired physical and chemical properties*".[6] It relies on the use of supramolecular building blocks, often referred to as supramolecular synthons. These synthons are assembled in such a way that their interactions are used to direct the packing of molecules in the solid state.[7,8]

Corey introduced the term *synthon* in 1967 as "*structural units within molecules which can be formed and/or assembled by known or conceivable synthetic operations*".[9] Desiraju applied this to crystal engineering and defined the supramolecular synthon as "*structural units within supermolecules which can be formed and/or assembled by known or conceivable synthetic operations involving intermolecular interactions*".[7] A supramolecular synthon is therefore a pattern of groups and functionalities interacting by strong and/or directional interactions (Figure 1). These patterns can be used to design and predict the solid-state arrangements of molecules with similar functionalities.[10]

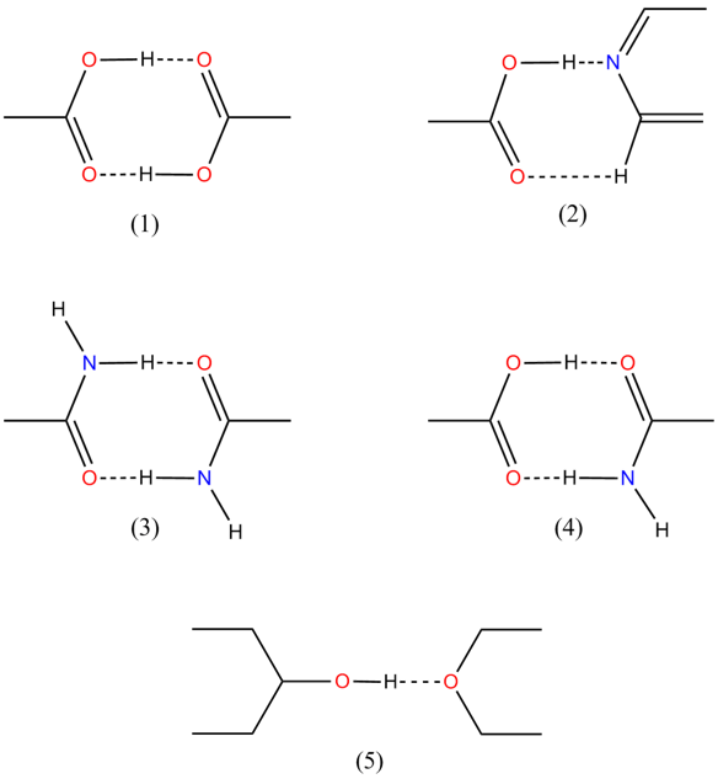

Figure 1 Commonly used supramolecular synthons in crystal engineering.[7, 119]

1.2 The tools of crystal engineering

A variety of supramolecular interactions and concepts are used in the solid state. The most important of these are described below.

1.2.1 Close packing and self-assembly

The principle of close packing in crystals refers to the tendency of molecules to pack as efficiently as possible to reach the maximum packing efficiency of 74%. This is achieved by optimising their mutual orientations so as to promote favourable intermolecular interactions.[11] There is a trade-off between electrostatic interactions until an energetically favourable state is reached. Hydrocarbons are good examples of the application of this model as their interactions are mainly isotropic, which results in packing arrangements that often resemble the stacked and herringbone geometries.[10] It is important to note that favourable or structure-directing interactions often work against achieving optimum packing efficiency. In the case of porous materials, crystal engineering employs favourable interactions as tools to produce less efficiently packed materials. Metal-organic frameworks, which make use of strong coordination bonds, have been a great success in reliably producing porous structures.

Self-assembly is also a vital concept in supramolecular chemistry. It is closely associated with molecular recognition, which is a key concept in the construction of supramolecular compounds.[5]

Although there are many classes and definitions of self-assembly, the most applicable to supramolecular chemistry is the one reported by Whitesides *et al.*, who define it as "*the spontaneous assembly of molecules into structured, stable, non-covalently joined aggregates*".[12] The structural integrity of the self-assembled structure remains, as it will be the most thermodynamically stable product. As the process of self-assembly relies on weaker non-covalent bonds, it is possible for molecules to associate and disassociate in a reversible manner through a process of "self-correction" until the most stable structure is obtained.[5]

1.2.2 Hydrogen bonding

The hydrogen bond is one of the most important interactions in supramolecular chemistry due to its strongly directional nature. It is seen as the master-key interaction in the field and several supramolecular synthons utilise it.[7] It was first described by Pauling in 1935, when he attributed the unusual properties of ice to the hydrogen bond.[13] The hydrogen bond is defined by Arunan *et al.* as "*an attractive interaction between a hydrogen atom from a molecule or a molecular fragment X–H in which X is more electronegative than H, and an atom or a group of atoms in the same or a different molecule, in which there is evidence of bond formation*".[14] The typical hydrogen bond is a directional interaction between a donor, X-H, and an acceptor, Y. The classical view suggested that the hydrogen bonding interaction arises as a result of the large difference in electronegativity between X and Y, which is considered "strong" or "conventional" and have energies usually 20-40 kJ mol^{-1}.[15] However if both X and Y are moderate to weakly electronegative, for example, C–H· · ·O, the hydrogen bond is considered "weak" or "nonconventional" and has energies 2–20 $kJmol^{-1}$.[16] The electronegative atoms (X and Y) polarise the X-H bond, thereby resulting in the electrostatic attraction between H and the electronegative atom Y.[10] Hydrogen bonding can be divided into three categories depending on strength and directionality. Strong hydrogen bonds have energies in the range of 63 – 167 kJ mol^{-1}, moderate in the range of 17 – 63 kJ mol^{-1} and the weak hydrogen bonds less than 17 kJ mol^{-1}.[17,18,19]

1.2.3 π–π interactions

π–π interactions are weak and non-directional interactions which fall in the energy range of 8 – 42 kJ mol^{-1}.[4] Computational studies have found that π–π interactions usually adopt two types of arrangements. The *edge-to-face* interaction is where a hydrogen atom from one aromatic ring interacts with the centre of another ring in a perpendicular fashion. In the *face-to-face* interaction, two arrangements are possible: one is parallel and another is offset. In case of offset, an interaction takes

place between the centre of one ring and the edge of another with a separation of about 3.5 Å between the planes.[20] These interactions facilitate the crystallisation of polynuclear aromatic hydrocarbons in four possible packing motifs, namely herringbone, sandwich-herringbone, γ- or β-structures.[21] The benzene dimer is an excellent example of this as it can adopt all four motifs (Figure 2).[22]

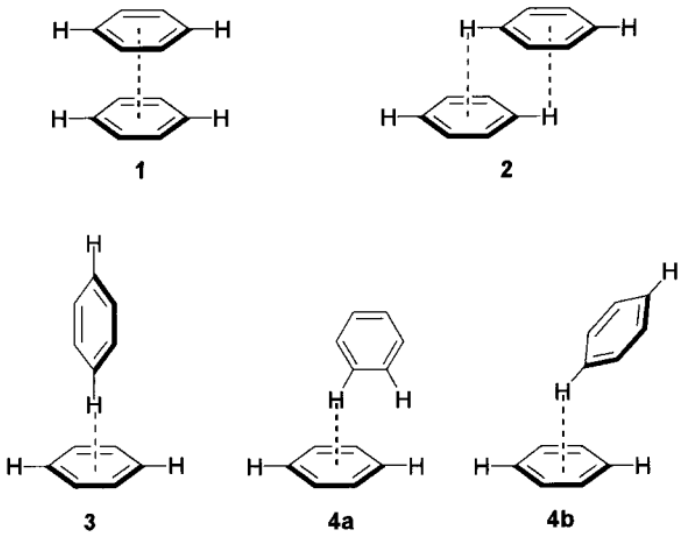

Figure 2 Structures of the benzene dimer.[22] **1** and **2** illustrate parallel and offset face-to-face interactions, respectively. **3**, **4a** and **4b** illustrate the edge-to-face interaction geometries, which include the T-shaped and the two tilted T-shaped structures.

1.2.4 Coordination bonds

The coordination bond takes place between a ligand donor atom and a metal atom. It usually involves the donation of a lone pair of electrons from an organic ligand, acting as a Lewis base, to the vacant site of a metal ion, which thereby acts as a Lewis acid.[23] The coordination bond is weaker than a covalent bond but stronger than a hydrogen bond, with energies in the range of 100 – 300 kJ mol^{-1}.[5] It is a key interaction in supramolecular chemistry, that allows the supramolecular assembly to undergo self-correction until the thermodynamically favoured product is achieved.[5] Due to its strong and labile nature, this bond is crucial in the formation of metal-organic frameworks through self-assembly.[24]

1.2.5 van der Waals interactions

The term “van der Waals interactions” refers to the sum of stabilising interactions, with the exclusion of hydrogen bonding, as well as any other anisotropic interactions.[10] They arise as a result of a change in the distribution of electrons which results in the formation of instantaneous dipoles within molecules

that are in close proximity to one another. These interactions generally have an energy of less than 5 kJ mol^{-1}, which rapidly decreases as the distance between the molecules increases.[20] van der Waals interactions are weak and non-directional in nature, which is why they do not feature strongly in supramolecular design. Despite this, they are critical to the formation of all crystals.[25]

1.2.6 Halogen bonding

The halogen bond is a newly recognised synthon in supramolecular chemistry and crystal engineering. In 2013 IUPAC defined the halogen bond as a bond that occurs "*when there is evidence of a net attractive interaction between an electrophilic region associated with a halogen atom in a molecular entity and a nucleophilic region in another, or the same, molecular entity*". It is commonly denoted as XB.[26,27] The halogen bond donor is the moiety that carries the electrophilic halogen atom and the nucleophile is considered the halogen bond acceptor. The strength of the interaction is dependent on the donor and changes the order I > Br > Cl > F. The order can be explained through the increase of positive electrostatic potential which increases with the polarizability, and decreases with the electronegativity, of the halogen atom.[28] Although computational and gas-phase studies have suggested that halogen bonds can adopt a considerable range of strengths between 10 and 200 kJ mol^{-1},[29] the forces typically encountered in solids lie between 10 and 50 $kJmol^{-1}$.[30]

1.3 Metal-organic frameworks

Porous materials are an important class of materials due to their use in catalysis, separation and storage.[31] Some of the most well-known porous materials include zeolites which are inorganic 3-dimensional crystalline framework materials. They possess guest-accessible voids which are occupied by water molecules and metal ions. Once these are removed, a highly porous material is left behind.[32] Activated carbons have also been widely used as porous media, known for their large surface areas and robust nature. These compounds have since been surpassed by a class of crystalline materials known as porous coordination polymers (PCPs). PCPs self-assemble through coordination bonds between metal cations and inorganic or organic ligands to form networks or "inorganic and organic hybrid polymers", with potential guest-accessible space. The properties of PCPs include ultrahigh porosity (up to 90% free volume), vast internal surface areas, extending beyond 6 000 m^2/g, and tunable pore sizes and surface properties.[33] These properties, together with the extraordinary degree of variability and regular topologies of PCP, resulted in a large increase in PCP research in the 1990s, yielding early examples of functional microporous materials.[34] Fujita *et al.* reported the catalytic properties of [Cd(4,4′-bpy)$_2$]

(bpy=bipyridine) in 1994.[35], while in 1995, Yaghi *et al.* and Moore *et al.* studied the adsorption of aromatic solvent molecules in PCPs.[36, 37] This was followed by gas sorption analysis at ambient temperatures by Kitagawa *et al.* in 1997.[38] The possible framework architectures that could be constructed by combining different metal node (connectors) and organic ligand (linkers) were further summarised by Kitagawa et al.[39] This highlighted the modular nature of PCPs that allows for the formation of one-, two- and three-dimensional (1D, 2D and 3D) framework architectures.

Yaghi *et al.* introduced the term "Metal-Organic Framework" (MOF) to describe a material that consists of organic ligands coordinated to metal ions to yield a permanently porous framework.[36,40] Although there is little distinction between the definitions of PCPs and MOFs, IUPAC guidelines state that a MOF is an extended coordination network (2D and 3D frameworks) whereas PCP describes frameworks in all dimensionalities.[41]

MOFs are often designed according to the principle of "*reticular synthesis"*. Yaghi *et al.* describe this as the "*process of assembling judiciously designed rigid molecular building blocks into predetermined ordered structures (networks), which are held together by strong bonding*".[42] The framework consists of metal-containing nodes, known as secondary building units (SBUs), with organic ligands acting as linkers between nodes (Figure 3). The SBU is the main factor in predicting the topology and geometry of the framework. Yaghi and co-workers have reported several well-known SBUs.[43] A large catalogue of known SBUs was published by Tranchemontagne *et al.* with SBUs ranging from three to sixty-six points of extension (Figure 4).[44] SBUs are linked by organic ligands to form two- or three-dimensional structures with open pores (Figure 3 and 4). These pores can be tuned by introducing suitable functional groups on the ligand unit that can lead to favourable host-guest interactions.

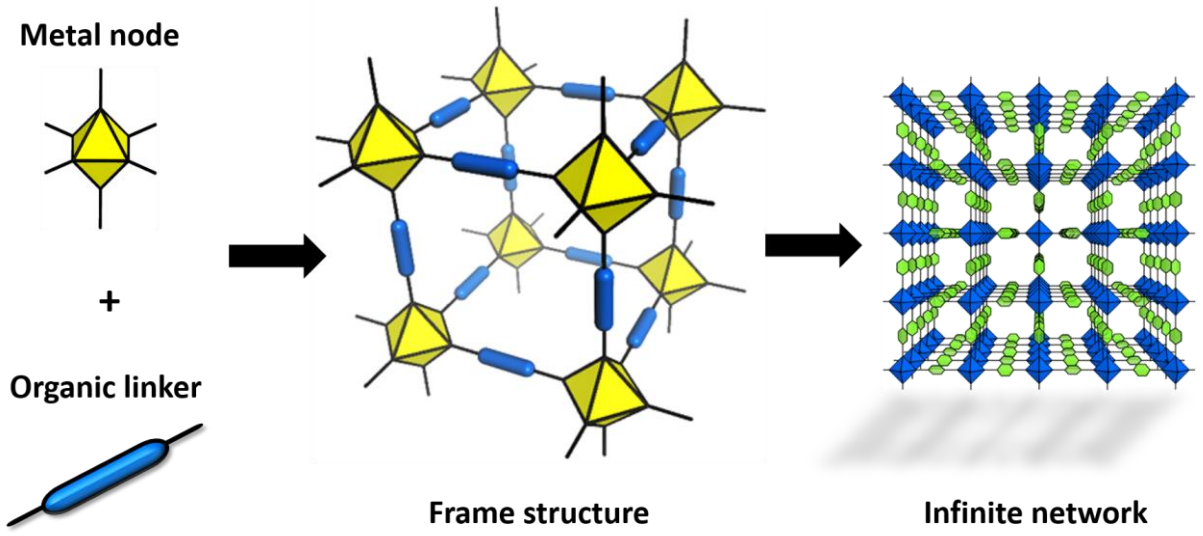

Figure 3 Synthesis of MOFs from organic ligands coordinated to metal clusters or nodes to form an infinite framework structure.

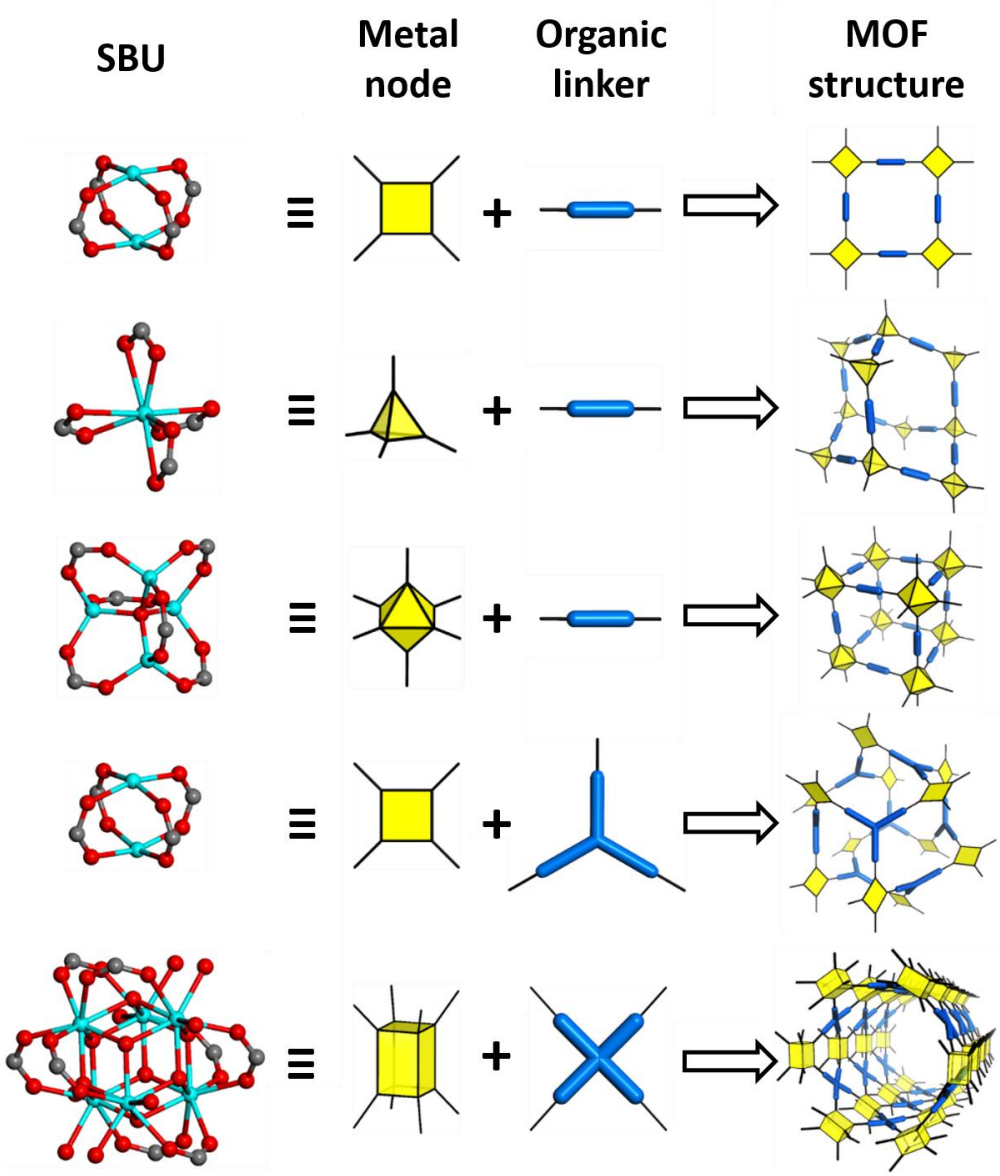

Figure 4 Diagram to show some of the different topologies that can be made using different SBUs and organic linkers. The SBUs on the left are constructed from the metal ions (light blue) coordinated to carboxylate groups (red) from the organic linker which creates the points of extension that can be seen as the central carbon (grey) of the carboxylate group. These points of extension are highlighted in the metal node as lines coming from the yellow geometry.

MOFs are generally synthesised using hydrothermal or solvothermal methods. MOFs such as MOF-5 ($Zn_4O(bdc)_3$, bdc = 1,4- benzenedicarboxylate) and HKUST-1 ($Cu_3(btc)_2$,btc = 1,3,5-benzenetricarboxylate) were landmarks in supramolecular chemistry with their high thermal stability and robust porosity.[45] Post-synthetic modification is also a common method of functionalising/modifying MOFs that would otherwise not be possible through the usual synthetic procedures.[46] Post-synthetic modification of a framework is the *in-situ* synthetic modification of the functional groups present on the organic linkers after the framework has already been formed.[47]

The channels and pores that are present in MOFs allow them to act as excellent adsorption, separation and purification materials. They have shown good catalytic properties, especially when compared to zeolites, the current industrial standard.[45] Due to the porous nature of MOFs they can encapsulate solvent, gas or other small molecules as guests in their channels and/or voids. Some MOFs exhibit interesting properties such as magnetism or luminescence that can be useful in designing chemical sensors and switches.[48] A large part of this study will focus on flexible MOFs (discussed in section 1.7), which is a new class of frameworks which exhibit dynamic responses to stimuli such as gas pressure, temperature and light.

1.4 Interpenetration

Interpenetration is the entanglement of two or more networks with one another. Although the interpenetrated networks are not covalently bonded, they cannot be separated without bond breakage (Figure 5).[49] MOFs are designed to be highly porous and these porous materials often undergo interpenetration to increase the stability of the framework so as to also achieve a higher packing efficiency. This usually occurs if the pore space of an individual net is sufficiently large to accommodate an additional network.[50] Interpenetration often occurs when using longer linkers, as often demonstrated in the literature.[51] Interpenetration in a framework has often been believed to be disadvantageous due to the decrease in pore size that leads to low uptake of guest molecules. However, several interpenetrated frameworks have shown an increase in the selectivity of gases and vapours due to the presence of smaller spaces.[45] An excellent example is $Zn(adc)(bpee)_{0.5}$ which has a triply-interpenetrated structure. The reduced pore size in the framework led to high selective uptake of hydrogen over nitrogen and carbon monoxide, as well as a selective sorption of carbon dioxide over methane gas at low temperatures.[52]

Although interpenetration can lead to MOFs having favourable properties, several methods have been proposed to control the degree of interpenetration. It has been observed that higher temperatures and concentrations often lead to interpenetrated frameworks.[53] Template molecules in the form of organic ligands and solvents can also be employed to prevent interpenetration.[54] Modification of the organic ligand with bulkier pendant groups can result in a reduction in void space, thereby preventing another net from passing through the space, thus controlling interpenetration.[55]

As previously mentioned, it is usually believed that a change in interpenetration can only be achieved through the breaking of bonds, which would result in a disintegration of the framework structure. However, in a recent article by Aggarwal *et al*., the degree of interpenetration of a MOF was

altered from two-fold to three-fold, which resulted in a decrease in porosity, without framework disintegration.[56]

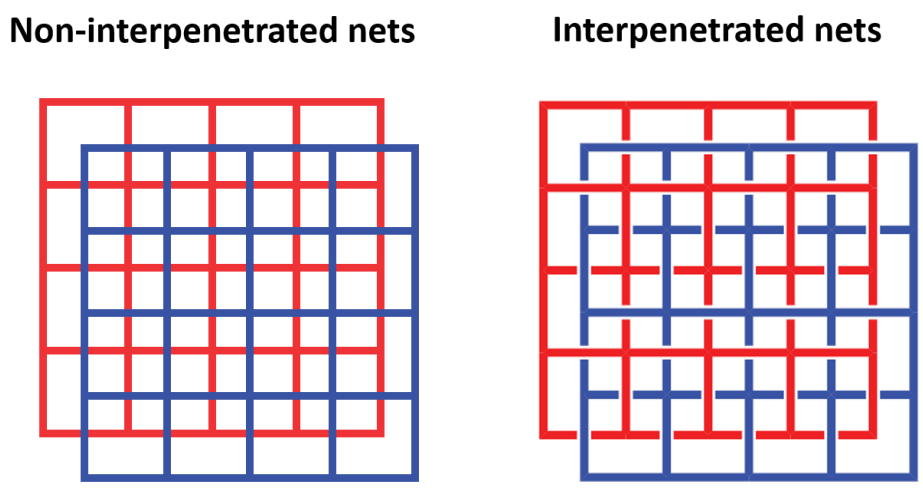

Figure 5 Schematic to show non-interpenetrated (left) and interpenetrated nets (right). In the non-interpenetrated nets the bonds do not overlap between the two nets as they are stacked upon one another whereas the interpenetrated nets are intertwined with overlapping bonds.

1.5 Porosity

A material is considered to be porous if it allows the transport of another material, into, out of, within, or through itself in a dynamic manner.[49] In other words, a structure is porous if the voids within the structure can be filled with guest molecules. In order to prove that a material is porous, *permeability* of the host must be demonstrated. With regard to MOFs, permeability refers to the exchange of the guest molecules in the pores or channels of the framework. The term "porosity" must also apply to a specific host phase and the structure of the host framework should therefore remain largely unaffected by the uptake and removal of guests. Barbour[57] proposes three distinct categories when discussing crystal porosity. These include conventional porosity, porosity "without pores" and virtual porosity.

Conventional porosity is when the guest molecules within the host are either completely removed or exchanged without a significant structural change or collapse.[57] This category includes zeolites and rigid MOFs. Porosity "without pores" applies to structures that do not contain distinct voids or pores but can facilitate the transport of guest molecules through the structure in a dynamic fashion. This is coupled to a change in the structure of the host to allow accommodation and passage of the guest molecules. As a result, these materials do not conform to the conventional definition of porosity discussed above. An example of this is the *p*-tert-butylcalix[4]arene.[58,59] The crystal structure contains discrete voids when exposed to vinyl-bromide results in a host-guest complex where vinyl bromide is trapped within the crystal lattice.[60,61]

Virtual porosity is essentially the concept of potential porosity. It is by no means true porosity and is created *in silico* by the deletion of solvent molecules within the voids of the host to give a porous appearance. Packing diagrams with capped-stick or ball-and-stick modes can also convey a false appearance of porosity. Space-filling mode includes the van der Waals radii of the atoms resulting in a more accurate depiction of the available space within the void. This is especially important with the measurement of pores and channels.[57]

Kitagawa *et al.* classified porosity according to dimensionality of the pores. Zero-dimensional pores are isolated or cut-off voids within the host framework. One-dimensional porosity describes non-intersecting channels running through the structure. Two-dimensional porosity exists between separate layers, and three-dimensional porosity refers to a system of intersecting channels (Figure 6).[39] Pores are further classified according to size. Ultramicropores are the smallest with a diameter of less than 5 Å. Micropores fall in the range of 5 – 20 Å, while mesopores have diameters in the range of 20 – 500 Å. Macropores are the largest, with diameters of more than 500 Å.[39] The degree of porosity can be conventionally established experimentally by analysis of the BET (Brunauer-Emmett-Teller) surface area. This is routinely carried out using nitrogen sorption at 77 K.[62] It is however important to note that this method is only effective if the material exhibits porosity for nitrogen at 77 K. Flexible MOFs are often a challenge to characterise using this method as many do not exhibit porosity under these conditions. Sorption analysis is often performed with bulkier gases such as butane (up to 1 bar) at ambient temperature to trigger the structural transformation.[63]

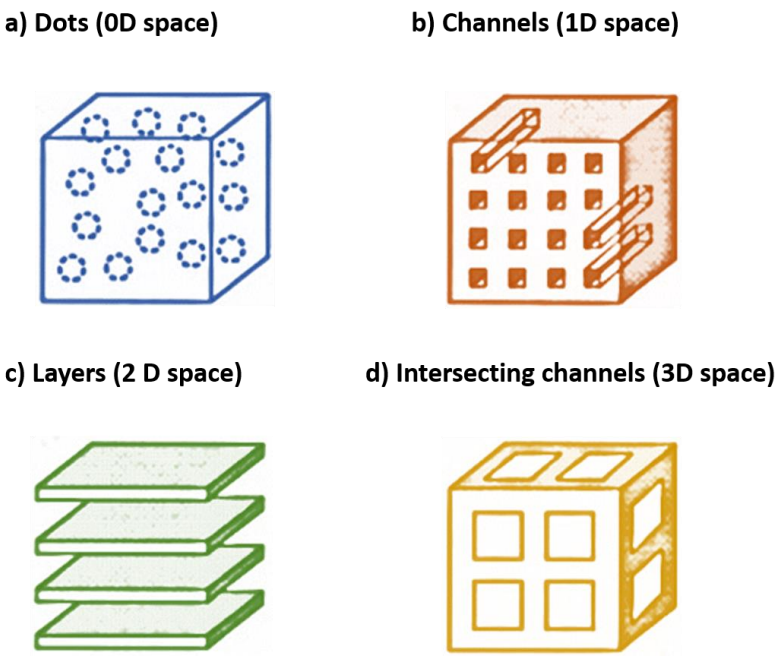

Figure 6 Schematic representation of the classes of pores based on special dimensions. Reproduced from an article by Kitagawa *et al.*[120]

1.6 Sorption

The generic term sorption is defined as the process whereby a liquid or gaseous substance (the sorbate) is taken up (sorbed) by a solid material. There are two categories of sorption: absorption and adsorption.[49] Absorption refers to the penetration of the guest molecules within the mass of the absorbing phase beyond the sorbent surface. Adsorption is the retention of molecules on the surface of the sorbate. Adsorption is further divided into two subclasses, *chemisorption* which involves retention of the gases through chemical bond formation, and *physiosorption* which relies on intermolecular interactions of gases with the sorbate.[49]

The IUPAC has classified six characteristic isotherms typically observed in gas sorption (Figure 7).[64] Type I isotherms are indicative of microporous solids with small external surfaces, such as zeolites and activated carbons. Type II is characteristic of non-porous or macroporous substances and represents monolayer-multilayer adsorption. Type III isotherms are rarely observed and have the distinct concave curvature that is indicative of adsorbate-adsorbate interactions. The isotherms IV and VI have previously been associated with stepped or gated sorption in MOFs which result from structural transformation of the host due to a pressure-induced gate-opening event, after which the sorption loading increases.[65] However, type IV and VI are actually due to capillary action and therefore, although the isotherm profile matches that of gated or stepped sorption it cannot be associated with this process. Type V is uncommon and is related to a system where guest-guest interactions are more favourable than guest-host interactions. The shapes of the isotherms are influenced by several factors, including pore size, host-

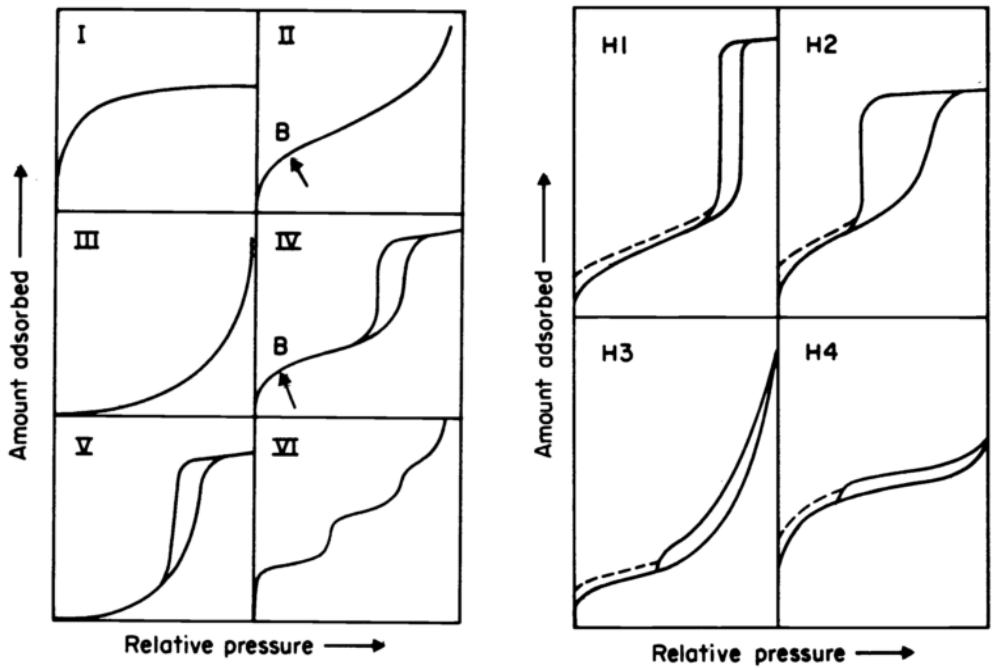

Figure 7 Six characteristic isotherms typically observed in gas sorption and the four categories for hysteresis loops in gas sorption isotherms classified by IUPAC. Figure reproduced from an article by Sing *et al*.[64]

guest interactions and the interactions between the guests themselves. MOFs have heterogeneous surfaces created from linker functionalities which may promote favourable host-guest interactions. Depending on the strength of the interactions, hysteresis may occur.[66] Hysteresis is when the adsorption and desorption isotherm curves do not follow the same path. This may be as a result of framework flexibility, a phase transition, capillary condensation or gas trapping in pore openings.[64,67] Figure 7 displays the four IUPAC categories for hysteresis loops in gas sorption isotherms.[64] Examples of frameworks exhibiting large hysteresis include MIL-53(Cr)[68] and LaBTB[69] (Figure 8).

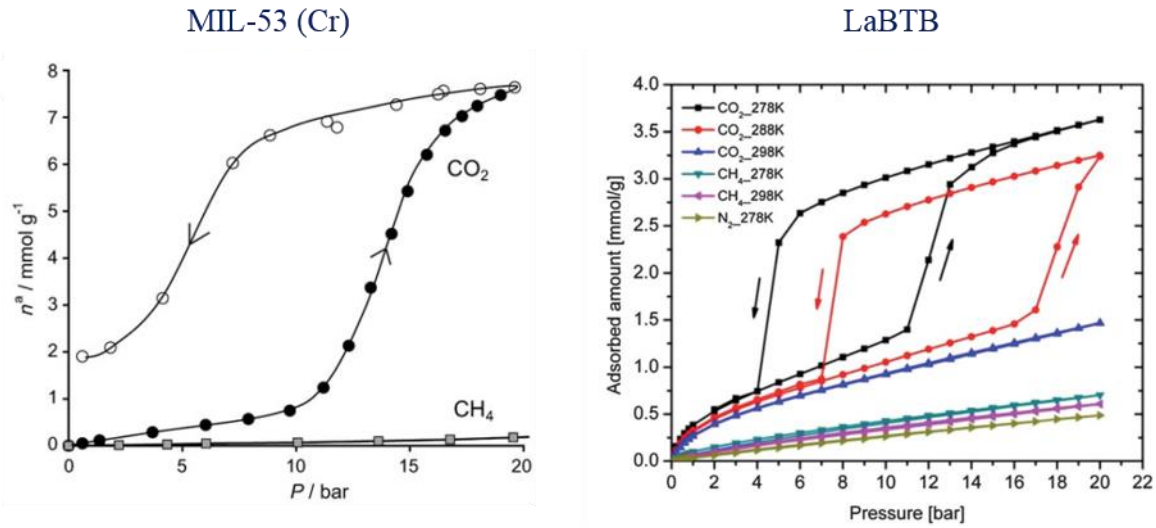

Figure 8 Gas sorption isotherms of MIL-53 (Cr) and LaBTB. Large hysteresis is seen in the sorption and desorption of CO_2 in both MIL-53 and LaBTB in comparison to the other gases analysed.

Flexible MOFs exhibit a structural change which is challenging to describe using the conventional isotherm profiles. There is a need for a more in-depth classification system to further describe the profile of the steps within the isotherm. Zaworotko and co-workers have proposed such a classification system, illustrated in Figure 9, with profiles ranging from type F-I to F-V describing the gradient of the step and finally the phenomenon of shape memory (Type F-V).[70] Type F-IV is without a doubt the most rarely observed isotherm profile for flexible MOFs, although it may lead to the most efficient working capacity.

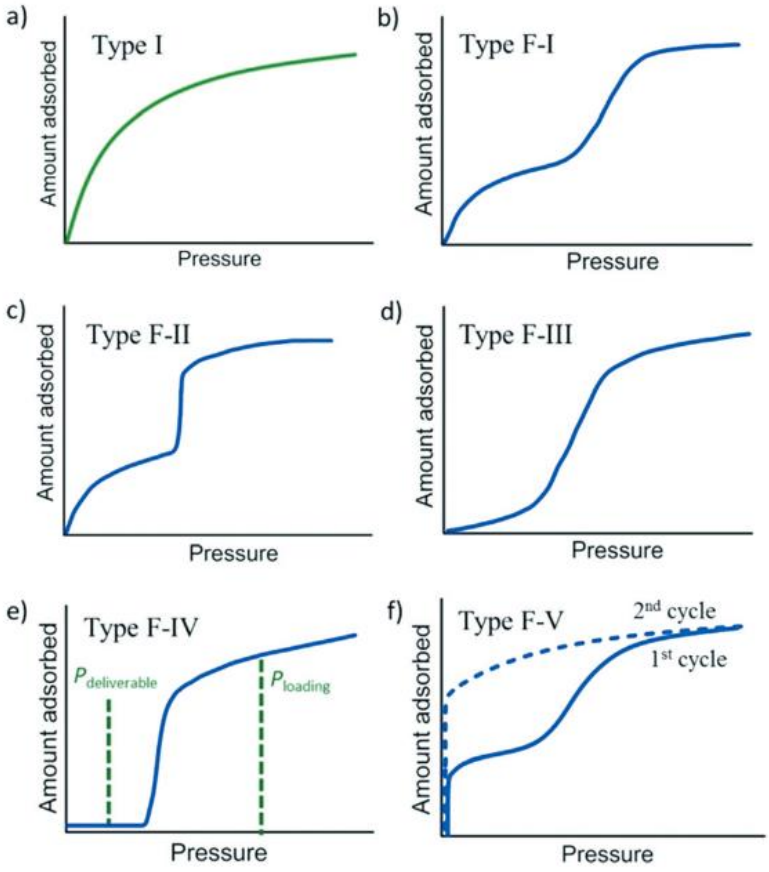

Figure 9 Proposed classification system for flexible microporous materials. Isotherms range from F-I to F-V type and depend on the rate at which the framework opens from a less or non-porous phase to an open porous phase.

1.7 Stimulus-responsive flexible MOFs

The study of flexible MOFs or soft porous crystals is an exciting and fast expanding area of MOF research. These materials respond dynamically to external stimuli of a physical or chemical nature; temperature changes, mechanical pressure, guest sorption or light exposure may induce transformations in flexible MOFs.[71] Flexible MOFs are prime candidates for gas separation and storage, catalysis and sensing applications.[72]

1.7.1 Guest and pressure induced flexibility

Kitagawa *et al.* classified these materials under three generations, according to the framework response upon guest removal (Figure 10).[73] First generation compounds collapse and lose structural integrity when the guest is removed. Second generation materials are permanently porous after guest removal and are similar to zeolitic materials. The third generation compounds undergo reversible

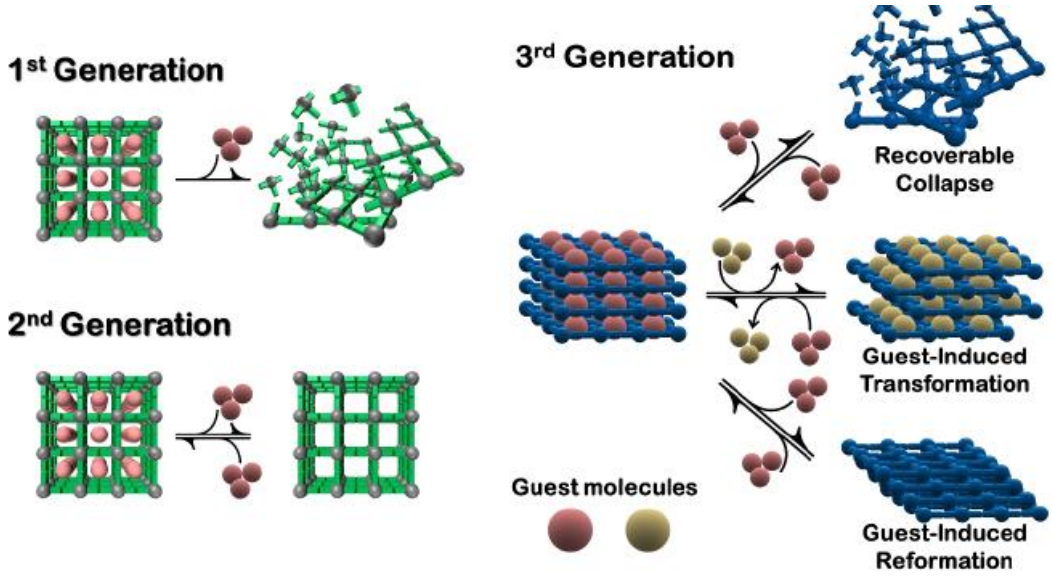

Figure 10 Schematic representation of first, second and third generation porous coordination polymers and MOFs as described by Kitagawa *et al*.[73]

transformations upon guest removal, uptake or exchange. There are four modes of flexibility which include breathing, swelling, linker rotation and subnetwork displacement (Figure 11). These modes have a significant effect on the gas sorption behaviour, resulting in stepped sorption or F-type isotherms (Figure 9).[70] The process is reversible, albeit commonly with hysteresis, depending on the strength of the guest-host interaction involved, or on guest-host trapping.[67] The breathing mode is one of the most well-studied and interesting of these phenomena. Breathing was particularly well defined by Schneemann *et al*. as the *"(reversible) transitions of metal-organic frameworks, during which the (substantial) displacement of atoms of the framework is accompanied by a change in the unit cell volume (ΔV≠0)"*.[74] Breathing in a MOF usually involves the structural transformation from a narrow pore (**np**) to a large or open pore (**lp**) form or phase (Figure 11 (a)). The MIL-53 family is the initial and an excellent example of a series of flexible MOFs exhibiting typical breathing behaviour upon hydration-dehydration.[75,76]

Subnetwork displacement is the shifting of individual nets relative to one another, creating guest-accessible space, without breaking any covalent or coordination bonds. This usually takes place in 3D interpenetrated or 2D interdigitated structures. A prime example of this is [Cu(dhbc)2(bipy)] which undergoes a gate-opening event at a threshold pressure for nitrogen, oxygen or methane through sub-network displacement to include additional guests within the host structure.[77] Other types of **np**-**lp** transformations include conformational isomerism of the organic ligands by irradiation with light[78] or temperature[79] and breaking/reformation of metal-ligand coordination bonds.[65]

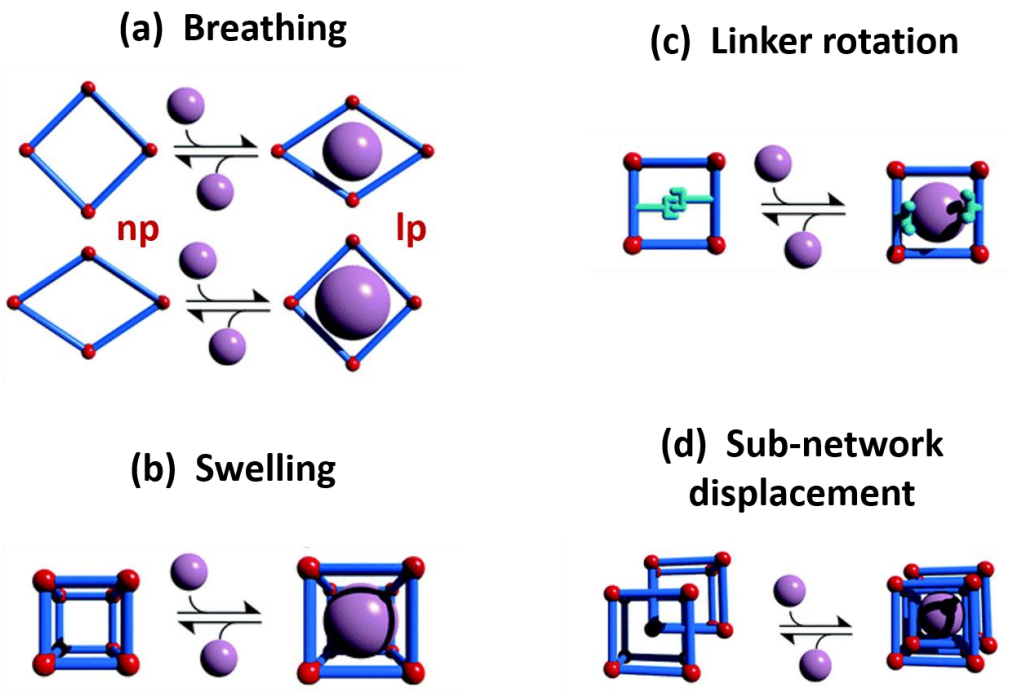

Figure 11 Four different modes of flexibility as described by Schneemann *et al.*[74]

1.8 Temperature- and light-induced flexibility

Thermoresponsive MOFs are confined to frameworks which show a reversible transformation when exposed to different temperatures without alteration to their molecular composition. Most materials containing solvent guests are excluded from this class as their exposure to elevated temperatures results in a loss of guest, and is therefore classified as a guest-induced transformation.[74] Anomalous thermal expansion, including negative (NTE) and anisotropic thermal expansion (ATE) are some of the interesting ways in which MOFs have exhibited flexibility in response to changes in temperature. MOFs such as HKUST-1[80] and MOF-5[81] are known to exhibit NTE, with UiO-66(Hf)[82] showing colossal NTE.[83] MOFs showing ATE with large contrasting positive and negative thermal expansions have also been reported[84,85] and few studies have even optimised such thermal responses through ligand functionalisation.[79] MOFs which exhibit temperature-driven first-order structural transitions are very rare in the literature.[71] Aside from the MIL-53 collection, only few have been reported.[86,87]

Photoresponsive MOFs are flexible frameworks which undergo a structural transformation in response to light. Most reported cases of photoresponsive frameworks can be classified into three generations, and are mainly classified based on where the photosensitive moiety is located.[71] Generation one involves MOFs with an extrinsic response as the pores are loaded with the photoactive guest. An example of this is the change in gas sorption capacity of an azobenzene-loaded MOF published by Yanai

et al., where the *trans-cis* isomerisation of the guest changes the pore capacity of the host framework.[88] The second generation is the most investigated category, where the photoresponsive moiety is incorporated as side chains on the organic linkers of the framework.[89] Some of these materials have demonstrated a change in CO_2 uptake after exposure to light and also displayed light-driven release of encapsulated dye compounds.[90,91] The third generation incorporates the photoresponsive moiety directly into the "backbone" of the framework through the organic linker. These MOFs are considered to be the most promising owing to their large stimulus responses, but are difficult to synthesise and characterise.[71] One of the early success stories was a framework reported by Hill and coworkers which appears to undergo a 'squeezing' effect upon irradiation with light, such that the adsorbed species can be rapidly desorbed.[92]

Ultraviolet light-induced [2+2] cycloaddition within MOFs is a key concept in this work. It is therefore important to note that a framework undergoing this reaction is not strictly considered a "photoresponsive MOF" but rather a framework that responds to light as a stimulus or "photoreactive". This is due to the fact that cycloaddition is by nature a reaction and is not always reversible unlike the phenomena describes previously in photoresponsive MOFs.

1.9 Photochemical [2+2] cycloaddition

Photochemical reactions are well known and can be used to synthesise a number of complex organic intermediates. However they are an unpopular tool among synthetic chemists due to their notoriously low yields and selectivity.[93] Photochemical [2+2] cycloaddition reactions have become particularly valuable as a means to construct cyclobutane derivatives, known for their biological and catalytic abilities and properties.[94,95] Although a well-established reaction in solution, [2+2] cycloaddition in the solid state (crystal) has become increasingly popular as a method to synthesise regio- or stereoselective products that are not possible, or are low-yielding in solution.[96] In the 1960s, Schmidt postulated topochemical rules for [2+2] cycloaddition in the solid state.[97] During [2+2] cycloaddition two olefinic groups photodimerise, resulting in the formation of a cyclobutane ring (Figure 12). He found that for the reaction to be successful, the olefinic bonds must have a separation of 3.5 Å to 4.2 Å, and be aligned parallel with respect to one another. This allows the four p-orbitals of the C=C bonds to have the appropriate proximity and orientation to undergo cycloaddition.[97] Due to the unpredictable nature of self assembly in the solid state, it is challanging to correctly orient olefinic bonds in the crystal lattice that comply with Schmidt's topochemical rules for the cycloaddition reaction. Once achieved, reactions often take place rapidly with near quantitative yields.[98]

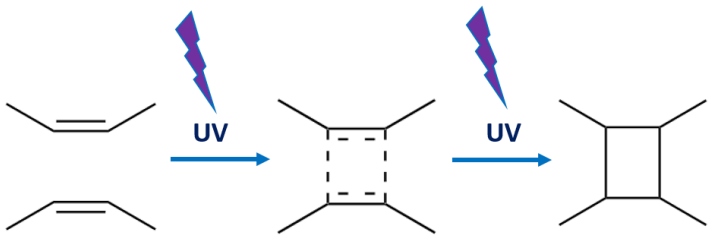

Figure 12 Photochemical [2+2] cycloaddition.

Several supramolecular design principles have been employed to control the packing of molecules to undergo photochemical cycloaddition in the solid state. MacGillivray has significantly advanced the field through the use of hydrogen-bond-driven self-assembly of template molecules with the target olefins. The template molecules correctly align the olefinic bonds in order to meet the topochemical requirements as displayed in Figure 13.[98] Functionalisation of the template molecules and olefins has also proven effective as a means to further control and direct the molecule into favourable positions. The presence of chloro-, fluoro-, alkoxyaryl, as well as electron donor/acceptor groups have all proven useful in promoting the alignment of the molecules to undergo photodimerisation in the solid state.[99,100] Recently the use of halogen bonding moieties as templates has also been investigated as a method of control.[101,102,103] There are also several examples of metal ions being employed as a means of directing molecules towards favourable packing in the solid state.[104,105,106]

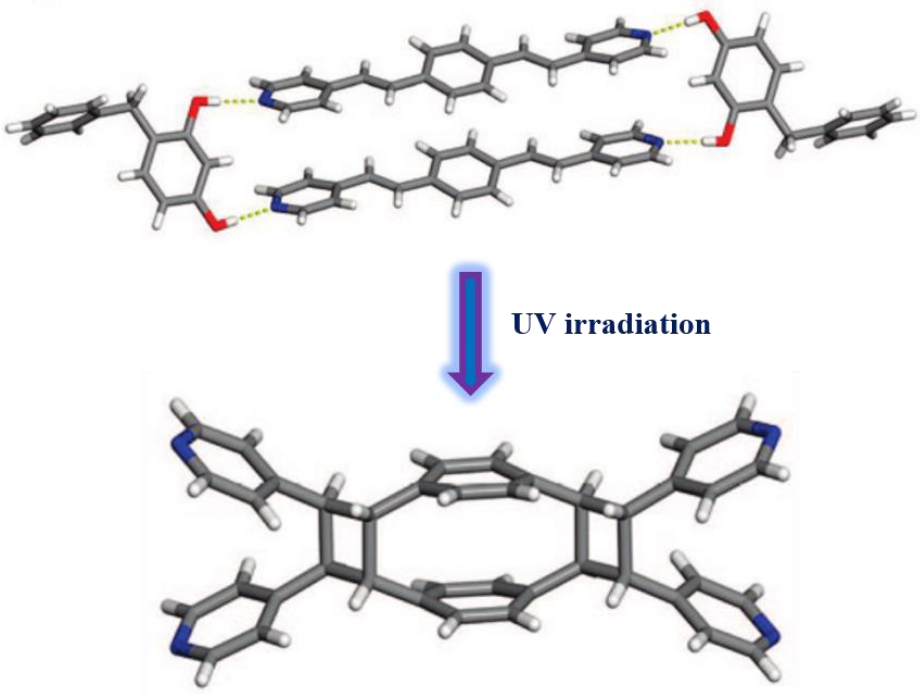

Figure 13 Co-crystal of 1,4-bpeb with 2-benzylresorcinol (above) undergoing photochemical cycloaddition resulting in the formation of 4,4'-tppcp (tetrakis(4-pyridyl)-1,2,9,10- diethano[2.2]). Figure reproduced from review article by MacGillivray *et al*.[98]

1.9.1 Photochemical [2+2] in MOFs

The geometrically versatile and predictable nature of MOFs make them excellent candidates to control molecular arrangement in the solid state.[98] MOFs can be exploited to facilitate favourable alignment of olefinic bonds through incorporation of an organic linker in the framework or even as a guest molecule within the channels or pores.[107, 108, 109] Frameworks which undergo cycloaddition in the solid state have not merely produced synthetically challenging products but also displayed favourable gas sorption and separation, fluorescent-switching and nitro-sensing properties to name a few.[110,111,112,113,114,115]

The ligand 1,4-bis[2-(4-pyridyl)ethenyl]-benzene (bpeb, Figure 14, top) has two olefinic bonds and therefore features quite often in the synthesis of photoactive MOFs. Controlling the alignment and position of the bpeb ligand is crucial as the presence of two double bonds greatly increases the number of possible positions where cycloaddition can occur and thereby the different isomeric products that can form. Two bpeb ligands can align in either an out-of-phase or an in-phase fashion as displayed in Figure 14, which results in the formation of either one or two cyclobutane ring units (Figure 14).[116] Vittal and co-workers synthesized both isomers in two different MOFs as a result of different degrees of interpenetration of the frameworks.[117] Liu and co-workers also synthesised the two isomers through incorporation of the bpeb ligand as the organic spacer in different MOFs. [118] Previously each of the two isomers could only be selectively synthesised in distinctly different framework materials. Herein however, we discuss the use of framework flexibility towards stimuli as means to selectively tailor the outcome of the [2+2] cycloaddition reaction of two bpeb molecules in a single MOF.

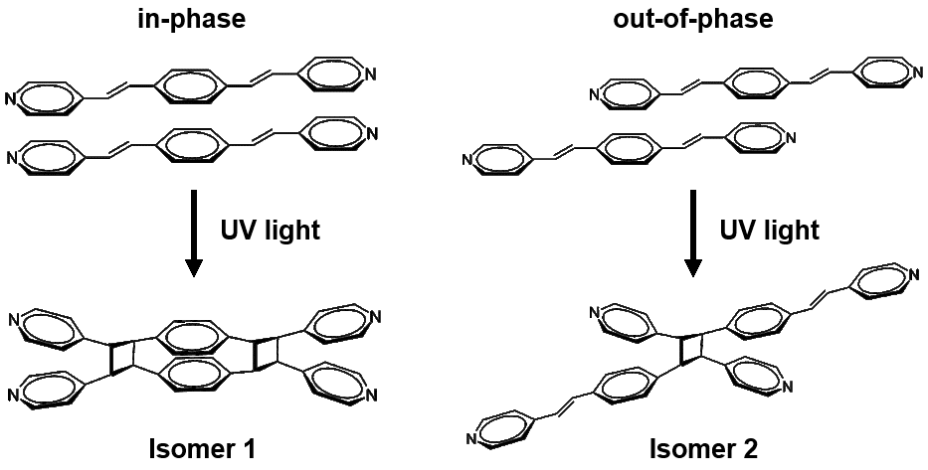

Figure 14 Two possible alignments of bpeb ligands in the solid state. In-phase alignment (left) results in the formation of Isomer 1 with two cyclobutane rings and out-of-phase alignment (right) results in the formation of Isomer 2 of the cyclized form with one cyclobutane ring.

1.10 Aims and objectives

The aim of this study was to investigate the structure-property relationships in two flexible MOFs to explore ways in which to tune and control their response to specific stimuli. The study is focused on the effect of guest-inclusion, temperature and light as stimuli. In the case of light, special focus was placed on photochemical cycloaddition and exploring means in which to control the outcome of the reaction. We aim to improve understanding, and thus control, of MOFs that change their properties in response to particular stimuli. The focus was in two areas; the stimulus-response in relation to cycloaddition with a Cd(II) MOF and the stimulus-response in relation to gas sorption with a Zn(II) flexible MOF.

Initial objectives in the cycloaddition studies focused on assessing and investigating the Cd (II) MOF's ability to undergo cycloaddition between the bpeb linkers in the backbone. The next objectives were to probe the response of the framework to a different guest molecule by means of solvent exchange. Upon observation of a change in ligand isomerisation, cycloaddition studies were pursued on the new form which revealed a change in regioselectivity of the reaction. Following objectives included full characterisation of the new products, as well as an investigation on the effect of a range of different guest molecules on the framework and subsequently the outcome of cycloaddition. Additional objectives included developing a method to isolate the different isomers from the material as we propose using the framework as a synthetic tool for the synthesis of these isomers

As part of the first study, observations suggested that the framework undergoes a phase transition at a low temperature. The objective was therefore to study the structural transition, as these types of transitions are rare in MOF literature, and fully to characterise the new phase. Once the new phase was better understood, the objective was to investigate the regioselectivity of cycloaddition in the new phase.

The second part of the study focussed on gas as a stimulus for responsive MOF materials. The first objective was to fully characterise the framework and explore activation conditions. As activation resulted in a non-porous material, the gas sorption behaviour of several gases was analysed so as to potentially induce a structural change to a porous phase. This proved successful with several gases. The next objective was to analyse gas sorption behaviour on several platforms and attempt to gain further insight into the mechanism of sorption by *in-situ* X-ray diffraction techniques. Due to the interesting behaviour exhibited by the fluorinated framework, further objectives were to synthesise the non-fluorinated analogue to compare the gas sorption behaviour.

1.11 Thesis outline

This dissertation is presented as three manuscripts. Two manuscripts have been published in high-impact journals (**Chapters 2 and 3**) and the last manuscript is formatted for submission to a journal in article format (**Chapter 4**).

Chapter 2 describes the use of solvent exchange as a means to control the position of photochemical [2+2] cycloaddition between bpeb ligands in a new Cd (II) MOF. The work shows how one of two different isomeric products can be obtained from cycloaddition by exchanging one solvent in the channels of the MOF for another. The nature of the guest controls the conformation of the organic linker (bpeb) within the framework, which has a direct effect on the regioselectivity of the cycloaddition reaction. This work shows the selective synthesis of both bpeb dimer isomers in the same PCP by changing the conformation of the olefinic bonds in the bpeb ligand via a simple exchange of guest. This is an example of how the guest-responsive nature of a flexible MOF can be utilised as a synthetic tool.

Chapter 3 focuses on temperature as a stimulus response of the same Cd(II) as a means to control regioselectivity of the photochemical cycloaddition reaction and thereby the isomeric products formed from the bpeb linkers. Herein the isomer formed depends on the temperature at which irradiation takes place. A rare temperature-induced phase transition alters the conformation of the bpeb ligand in the MOF, and thereby the position at which cycloaddition occurs. The phase transition is fully described and characterised using variable temperature X-ray diffraction techniques. This work also highlights the multistimulus responsive nature of this MOF that responds to temperature, as well as solvent exchange and light.

Chapter 4 discusses a new highly flexible four-fold interpenetrated fluorinated MOF that undergoes breathing and subnetwork displacement modes of flexibility to give interesting gas sorption behaviour. The study investigates the effect of the fluorinated substituents on the gas sorption behaviour by comparing it to the non-fluorinated isoreticular analogue. The sorption analysis reveals significant changes in gate-opening pressure as well as the degree of hysteresis observed between the two frameworks. *In-situ* SCXRD techniques and computational analysis are employed to describe and identify the interactions responsible for the change in behaviour. Flexible frameworks are still a relatively new field and few studies have discussed means to tune gate-opening pressure and hysteresis. This work also shows how the response to guest as a stimulus can easily be altered by ligand functionalisation.

Finally, **Chapter 5** summarises this work and presents some concluding remarks.

1.12 References

1 J.-M. Lehn, *Angew. Chem. Int. Ed.*, 1988, **27**, 89–112.

2 J. D. Dunitz, *Pure Appl. Chem.*, 1991, **63**, 177–185.

3 J.-M. Lehn, *Proc. Natl. Acad. Sci.*, 2002, **99**, 4763–4768.

4 J. L. Atwood and J. W. Steed, Eds., *Encyclopedia of Supramolecular Chemistry*, Marcel Dekker Inc, New York, 2004, vol. 1.

5 P. A. Gale and J. W. Steed, Eds., *Supramolecular Chemistry: from Molecules to Nanomaterials*, John Wiley & Sons, Chichester, 2012.

6 G. R. Desiraju, *Crystal engineering: the design of organic solids*, Elsevier, Amsterdam, 1989, vol. 54.

7 G. R. Desiraju, *Angew. Chem. Int. Ed.*, 1995, **34**, 2311–2327.

8 L. R. MacGillivray, *CrystEngComm*, 2002, **4**, 37–41.

9 E. J. J. Corey, *Pure Appl. Chem.*, 1967, **14**, 19–37.

10 G. R. Desiraju, J. J. Vittal and R. Arunachalam, *Crystal Engineering: A Textbook*, World Scientific Publishing Co. Pte. Ltd., Singapore, 1st edn., 2011.

11 A. I. Kitaigorodsky, *Physical Chemistry: Molecular Crystals and Molecules*, New York : Academic Press, New York, 1973.

12 G. M. Whitesides, J. P. Mathias and C. T. Seto, *Science*, 1991, **254**, 1312–1319.

13 L. Pauling, *J. Am. Chem. Soc.*, 1935, **57**, 2680–2684.

14 E. Arunan, G. R. Desiraju, R. A. Klein, J. Sadlej, S. Scheiner, I. Alkorta, D. C. Clary, R. H. Crabtree, J. J. Dannenberg, P. Hobza, H. G. Kjaergaard, A. C. Legon, B. Mennucci and D. J. Nesbitt, *Pure Appl. Chem.*, 2011, **83**, 1619–1636.

15 G. R. Desiraju, *Nature*, 2001, 412, 397–400.

16 J. W. Steed, J. L. Atwood and P. A. Gale, in *Definition and Emergence of Supramolecular Chemistry*, John Wiley & Sons, Ltd, Chichester, UK, 2012.

17 W. Saenger and G. A. Jeffrey, *Hydrogen bonding in biological structures*, Springer-Verlag, Berlin, 1991.

18 G. R. Desiraju and T. Steiner, *The weak hydrogen bond: in structural chemistry and biology*, Oxford University Press, Oxford, United Kingdom, 2001, vol. 9.

19 J. Emsley, *Chem. Soc. Rev.*, 1980, **9**, 91–124.

20 J. W. Steed, K. J. Wallace and D. R. Turner, *Core Concepts in Supramolecular Chemistry and Nanochemistry*, John Wiley & Sons, Chichester, 1st edn., 2007.

21 L. Loots and L. J. Barbour, *CrystEngComm*, 2012, **14**, 300–304.

22 W. B. Jennings, B. M. Farrell and J. F. Malone, *Acc. Chem. Res.*, 2001, **34**, 885–894.

23 A. Y. Robin and K. M. Fromm, *Coord. Chem. Rev.*, 2006, **250**, 2127–2157.

24 S. L. James, *Chem. Soc. Rev.*, 2003, **32**, 276–2288.

25 J. W. Steed and J. L. Atwood, *Supramolecular Chemistry*, John Wiley & Sons, Chichester, 2000.

26 G. R. Desiraju, P. Shing Ho, L. Kloo, A. C. Legon, R. Marquardt, P. Metrangolo, P. Politzer, G. Resnati and K. Rissanen, *Pure Appl. Chem.*, 2013, **85**, 1711–1713.

27 D. Bulfield and S. M. Huber, *Chem. Eur. J.*, 2016, **22**, 14434–14450.

28 H. Wang, H. K. Bisoyi, A. M. Urbas, T. J. Bunning and Q. Li, *Chem. Eur. J.*, 2019, **25**, 1369–1378.

29 P. Metrangolo, F. Meyer, T. Pilati, G. Resnati and G. Terraneo, *Angew. Chem. Int. Ed.*, 2008, **47**, 6114–6127.

30 R. B. Walsh, C. W. Padgett, P. Metrangolo, G. Resnati, T. W. Hanks and W. T. Pennington, *Cryst. Growth Des.*, 2001, **1**, 165–175.

31 P. B. Venuto, *Microporous Mater.*, 1994, **2**, 297–411.

32 J. V. Smith, *Chem. Rev.*, 1988, **88**, 149–182.

33 H. C. Zhou, J. R. Long and O. M. Yaghi, *Chem. Rev.*, 2012, 112, 673–674.

34 H. Furukawa, K. E. Cordova, M. O'Keeffe and O. M. Yaghi, *Science*, 2013, **341**, 1230444–1230444.

35 M. Fujita, Y. Jung Kwon, S. Washizu and K. Ogura, *Preparation, Clathration Ability, and Catalysis of a Two-Dimensional Square Network Material Composed of Cadmium(II) and 4,4'-Bipyridine*, 1994, vol. 116.

36 O. M. Yaghi, G. Li and H. Li, *Nature*, 1995, **378**, 703–706.

37 D. Venkataraman, J. S. Moore, G. B. Gardner and S. Lee, *J. Am. Chem. Soc.*, 1995, **117**, 11600–11601.

38 M. Kondo, T. Yoshitomi, H. Matsuzaka, S. Kitagawa and K. Seki, *Angew. Chem. Int. Ed.*, 1997, **36**, 1725–1727.

39 S. Kitagawa, R. Kitaura and S. Noro, *Angew. Chemie Int. Ed.*, 2004, **43**, 2334–2375.

40 H. Li, M. Eddaoudi, M. O'Keeffe and O. M. Yaghi, *Nature*, 1999, **402**, 276–279.

41 S. R. Batten, N. R. Champness, X. M. Chen, J. Garcia-Martinez, S. Kitagawa, L. Öhrström, M. O'Keeffe, M. P. Suh and J. Reedijk, *CrystEngComm*, 2012, **14**, 3001–3004.

42 O. M. Yaghi, M. O'Keeffe, N. W. Ockwig, H. K. Chae, M. Eddaoudi and J. Kim, *Nature*, 2003, **423**, 705–714.

43 A. Schoedel, M. Li, D. Li, M. O'Keeffe and O. M. Yaghi, *Chem. Rev.*, 2016, **116**, 12466–12535.

44 D. J. Tranchemontagne, J. L. Mendoza-Cortés, M. O'Keeffe and O. M. Yaghi, *Chem. Soc. Rev.*, 2009, **38**, 1257–1283.

45 J. Li, J. Sculley and H. Zhou, *Chem. Rev.*, 2012, **112**, 869–932.

46 T. R. Cook, Y.-R. Zheng and P. J. Stang, *Chem. Rev.*, 2013, **113**, 734–777.

47 Z. Wang and S. M. Cohen, *Chem. Soc. Rev.*, 2009, **38**, 1315–1329.

48 H.-C. Zhou and S. Kitagawa, *Chem. Soc. Rev.*, 2014, **43**, 5415–5418.

49 L. J. Barbour, D. Das, T. Jacobs, G. O. Lloyd and V. J. Smith, in *Concepts and Nomenclature in Chemical Crystallography*, John Wiley & Sons, Chichester, 2011, pp. 2869–2903.

50 H. Jiang, T. A. Makal and H. Zhou, *Coord. Chem. Rev.*, 2013, **257**, 2232–2249.

51 Y.-N. Gong, D.-C. Zhong and T.-B. Lu, *CrystEngComm*, 2016, **18**, 2596–2606.

52 B. Chen, S. Ma, E. J. Hurtado, E. B. Lobkovsky and H. Zhou, *Inorg. Chem.*, 2007, **46**, 8490–8492.

53 J. Zhang, L. Wojtas, R. W. Larsen, M. Eddaoudi and M. J. Zaworotko, *J. Am. Chem. Soc.*, 2009, **131**, 17040–17041.

54 S. Ma, D. Sun, M. Ambrogio, J. A. Fillinger, P. Sean and H.-C. Zhou, *J. Am. Chem. Soc.*, 2007, **129**, 1858–1859.

55 R. Kitaura, K. Seki, G. Akiyama and S. Kitagawa, *Angew. Chem. Int. Ed.*, 2003, **42**, 428–431.

56 H. Aggarwal, R. K. Das, P. M. Bhatt and L. J. Barbour, *Chem. Sci.*, 2015, **6**, 4986–4992.

57 L. J. Barbour, *Chem. Commun.*, 2006, 1163–1168.

58 J. L. Atwood, L. J. Barbour and A. Jerga, *Chem. Commun.*, 2002, 2952–2953.

59 J. L. Atwood, L. J. Barbour, G. O. Lloyd and P. K. Thallapally, *Chem. Commun.*, 2004, 922–923.

60 J. L. Atwood, L. J. Barbour, A. Jerga and B. L. Schottel, *Science*, 2002, **298**, 1000–1002.

61 J. W. Steed, *Science*, 2002, **298**, 976–977.

62 K. S. W. Sing, *Adv. Colloid Interface Sci.*, 1998, **76**–**77**, 3–11.

63 V. Bon, N. Kavoosi, I. Senkovska and S. Kaskel, *ACS Appl. Mater. Interfaces*, 2015, **7**, 22292–22300.

64 K. S. W. Sing, D. H. Everett, R. a. W. Haul, L. Moscou, R. a. Pierotti, J. Rouquérol and T. Siemieniewska, *Pure Appl. Chem.*, 1985, **57**, 603–619.

65 J. Seo, C. Bonneau, R. Matsuda, M. Takata and S. Kitagawa, *J. Am. Chem. Soc.*, 2011, **133**, 9005–9013.

66 A. J. Fletcher, K. M. Thomas and M. J. Rosseinsky, *J. Solid State Chem.*, 2005, **178**, 2491–2510.

67 J. T. Culp, M. R. Smith, E. Bittner and B. Bockrath, *J. Am. Chem. Soc.*, 2008, **130**, 12427–12434.

68 P. L. Llewellyn, S. Bourrelly, C. Serre, Y. Filinchuk and G. Férey, *Angew. Chemie Int. Ed.*, 2006, **45**, 7751–7754.

69 B. Mu, F. Li, Y. Huang and K. S. Walton, *J. Mater. Chem.*, 2012, **22**, 10172–10178.

70 Q.-Y. Yang, P. Lama, S. Sen, M. Lusi, K.-J. Chen, W.-Y. Gao, M. Shivanna, T. Pham, N. Hosono, S. Kusaka, J. J. Perry, S. Ma, B. Space, L. J. Barbour, S. Kitagawa and M. J. Zaworotko, *Angew. Chem. Int. Ed.*, 2018, **57**, 5684–5689.

71 F.-X. Coudert, *Chem. Mater.*, 2015, **27**, 1905–1916.

72 Z. Chang, D. H. Yang, J. Xu, T. L. Hu and X. H. Bu, *Adv. Mater.*, 2015, **27**, 5432–5441.

73 S. Horike, S. Shimomura and S. Kitagawa, *Nat. Chem.*, 2009, **1**, 695–704.

74 A. Schneemann, V. Bon, I. Schwedler, I. Senkovska, S. Kaskel and R. A. Fischer, *Chem. Soc. Rev.*, 2014, **43**, 6062–6096.

75 T. Loiseau, C. Serre, C. Huguenard, G. Fink, F. Taulelle, M. Henry, T. Bataille and G. Férey, *Chem. Eur. J.*, 2004, **10**, 1373–1382.

76 A. Boutin, F.-X. Coudert, M.-A. Springuel-Huet, A. V Neimark, G. Férey and A. H. Fuchs, *J. Phys. Chem. C*, 2010, **114**, 22237–22244.

77 T. K. Maji, R. Matsuda and S. Kitagawa, *Nat. Mater.*, 2007, **6**, 142–148.

78 A. Modrow, D. Zargarani, R. Herges and N. Stock, *Dalt. Trans.*, 2011, **40**, 4217–4222.

79 I. Grobler, V. J. Smith, P. M. Bhatt, S. A. Herbert and L. J. Barbour, *J. Am. Chem. Soc.*, 2013, **135**, 6411–6414.

80 Y. Wu, A. Kobayashi, G. J. Halder, V. K. Peterson, K. W. Chapman, N. Lock, P. D. Southon and C. J. Kepert, *Angew. Chem. Int. Ed.*, 2008, **47**, 8929–8932.

81 W. Zhou, H. Wu, T. Yildirim, J. R. Simpson and A. R. H. Walker, *Phys. Rev. B*, 2008, **78**, 054114.

82 M. J. Cliffe, J. A. Hill, C. A. Murray, F. X. Coudert and A. L. Goodwin, *Phys. Chem. Chem. Phys.*, 2015, **17**, 11586–11592.

83 A. L. Goodwin, M. Calleja, M. J. Conterio, M. T. Dove, J. S. O. Evans, D. A. Keen, L. Peters and M. G. Tucker, *Science*, 2008, **319**, 794–797.

84 L. D. Devries, P. M. Barron, E. P. Hurley, C. Hu and W. Choe, *J. Am. Chem. Soc.*, 2011, **133**, 14848–14851.

85 P. Lama, R. K. Das, V. J. Smith and L. J. Barbour, *Chem. Commun.*, 2014, **50**, 6464–6467.

86 Y. Liu, J.-H. Her, A. Dailly, A. J. Ramirez-Cuesta, D. A. Neumann and C. M. Brown, *J. Am. Chem. Soc.*, 2008, **130**, 11813–11818.

87 J.-P. Zhang, Y.-Y. Lin, W.-X. Zhang and X.-M. Chen, *J. Am. Chem. Soc.*, 2005, **127**, 14162–14163.

88 N. Yanai, T. Uemura, M. Inoue, R. Matsuda, T. Fukushima, M. Tsujimoto, S. Isoda and S. Kitagawa, *J. Am. Chem. Soc*, 2012, **134**, 4501–4504.

89 R. D. Mukhopadhyay, V. K. Praveen and A. Ajayaghosh, *Mater. Horizons*, 2014, **1**, 572–576.

90 J. Park, D. Yuan, K. T. Pham, J. R. Li, A. Yakovenko and H. C. Zhou, *J. Am. Chem. Soc.*, 2012, **134**, 99–102.

91 J. W. Brown, B. L. Henderson, M. D. Kiesz, A. C. Whalley, W. Morris, S. Grunder, H. Deng, H. Furukawa, J. I. Zink, J. F. Stoddart and O. M. Yaghi, *Chem. Sci.*, 2013, **4**, 2858–2864.

92 R. Lyndon, K. Konstas, B. P. Ladewig, P. D. Southon, P. C. J. Kepert and M. R. Hill, *Angew. Chem. Int. Ed.*, 2013, **52**, 3695–3698.

93 V. Ramamurthy and J. Sivaguru, *Chem. Rev.*, 2016, **116**, 9914–9993.

94 T. Seiser, T. Saget, D. N. Tran and N. Cramer, *Angew. Chemie Int. Ed.*, 2011, **50**, 7740–7752.

95 M. A. Beniddir, L. Evanno, D. Joseph, A. Skiredj and E. Poupon, *Nat. Prod. Rep.*, 2016, 33, 820–842.

96 G. R. Desiraju, *Endeavour*, 1984, **8**, 201–206.

97 G. M. J. Schmidt, *Pure Appl. Chem.*, 1971, **27**, 647–678.

98 L. R. MacGillivray, G. S. Papaefstathiou, T. Friščić, T. D. Hamilton, D.-K. Bučar, Q. Chu, D. B. Varshney and I. G. Georgiev, *Acc. Chem. Res.*, 2008, **41**, 280–291.

99 C. Schalley, F. Vogtle and K. Dotz, *Templates in Chemistry I*, Springer Berlin Heidelberg, Berlin, Heidelberg, 2004, vol. 248.

100 K. Vishnumurthy, T. N. G. Row and K. Venkatesan, *J. Chem. Soc. Perkin Trans. 2*, 1997, 615–620.

101 T. Caronna, R. Liantonio, T. A. Logothetis, P. Metrangolo, T. Pilati and G. Resnati, *J. Am. Chem. Soc.*, 2004, **126**, 4500–4501.

102 M. A. Sinnwell and L. R. MacGillivray, *Angew. Chem. Int. Ed.*, 2016, **55**, 3477–3480.

103 E. Bosch, S. J. Kruse, E. W. Reinheimer, N. P. Rath and R. H. Groeneman, *CrystEngComm*,

2019, **21**, 6671–6675.

104 G. S. Papaefstathiou, Z. Zhong, L. Geng and L. R. MacGillivray, *J. Am. Chem. Soc.*, 2004, **126**, 9158–9159.

105 C. Li, G. Campillo-Alvarado, D. C. Swenson and L. R. MacGillivray, *Inorg. Chem.*, 2019, **58**, 12497–12500.

106 J. F. Eubank, V. C. Kravtsov and M. Eddaoudi, *J. Am. Chem. Soc.*, 2007, **129**, 5820–5821.

107 R. Medishetty, I.-H. Park, S. S. Lee and J. J. Vittal, *Chem. Commun.*, 2016, **52**, 3989–4001.

108 W. J. Shi, L. Y. Du, H. Y. Yang, K. Zhang, L. Hou and Y. Y. Wang, *Inorg. Chem.*, 2017, **56**, 10090–10098.

109 N. Y. Li, D. Liu and J. P. Lang, *Chem. Asian J.*, 2019, **14**, 3635–3641.

110 A. Hazra, S. Bonakala, K. K. Bejagam, S. Balasubramanian and T. K. Maji, *Chem. Eur. J.*, 2016, **22**, 7792–7799.

111 M. L. Foo, R. Matsuda, Y. Hijikata, R. Krishna, H. Sato, S. Horike, A. Hori, J. Duan, Y. Sato, Y. Kubota, M. Takata and S. Kitagawa, *J. Am. Chem. Soc.*, 2016, **138**, 3022–3030.

112 F. F. Li, L. Zhang, L. Le Gong, C. S. Yan, H. Y. Gao and F. Luo, *Dalt. Trans.*, 2017, **46**, 338–341.

113 N. Y. Li, D. Liu, Z. G. Ren, C. Lollar, J. P. Lang and H. C. Zhou, *Inorg. Chem.*, 2018, **57**, 849–856.

114 I.-H. Park, H. Ju, K. Kim, S. S. Lee and J. J. Vittal, *IUCrJ*, 2018, **5**, 182–189.

115 N.-Y. Li, D. Liu, B. F. Abrahams and J.-P. Lang, *Chem. Commun.*, 2018, **54**, 5831–5834.

116 R. Medishetty, I. Park, S. S. Lee and J. J. Vittal, *Chem. Commun.*, 2016, **52**, 3989–4001.

117 I.-H. Park, R. Medishetty, J.-Y. Kim, S. S. Lee and J. J. Vittal, *Angew. Chemie Int. Ed.*, 2014, **53**, 5591–5595.

118 D. Liu, Z. Ren, H.-X. Li, J. Lang, N. Li and B. F. Abrahams, *Angew. Chemie Int. Ed.*, 2010, **49**, 4767–4770.

Chapter 2

Solvent-Mediated Synthesis of Cyclobutane Isomers in a Photoactive Cadmium(II) Porous Coordination Polymer

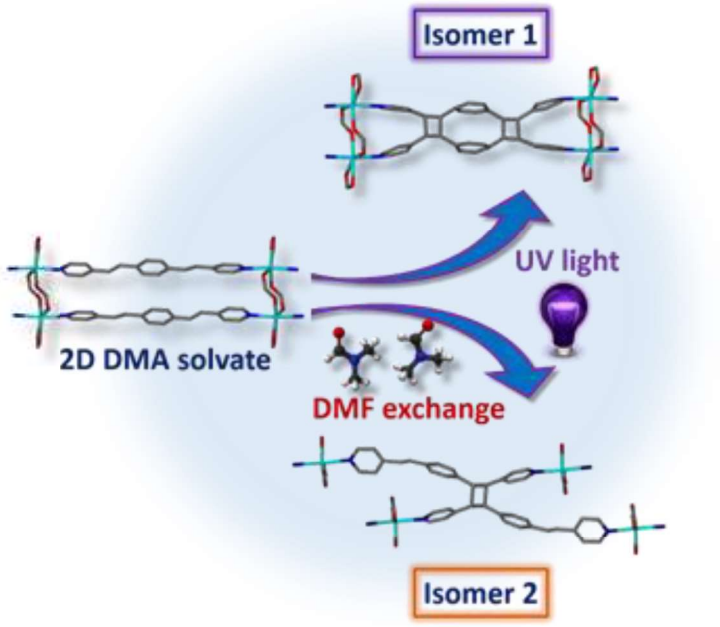

2.1 Communication in Angewandte Chemie

The framework was first prepared by Dr Varvara Nikolayenko and initial irradiation experiments on the DMA solvate were carried out with her assistance. Prem Lama gave advice regarding modification of the synthetic procedure for the bpeb ligand. The author is responsible for all further contributions, including:

- Design of project
- Synthesis of ligand and MOF (including all solvent exchange experiments)
- Collection of single-crystal X-ray data, solution and refinement of single-crystal X-ray structures
- Collection and analysis of powder X-ray data, IR spectra and TGA thermograms
- Design and execution of UV irradiation experiments
- Development and execution of digestion procedure and analysis and processing of NMR data
- Interpretation of results
- Writing the first draft of the article

Single-Crystal Cycloadditions Hot Paper

International Edition: DOI: 10.1002/anie.201809050
German Edition: DOI: 10.1002/ange.201809050

Solvent-Mediated Synthesis of Cyclobutane Isomers in a Photoactive Cadmium(II) Porous Coordination Polymer

Isabella E. Claassens, Varvara I. Nikolayenko, Delia A. Haynes, and Leonard J. Barbour**

Abstract: *Photochemical [2+2] cycloaddition of 1,4-bis[2-(4-pyridyl)ethenyl]benzene, carried out in a Cd^{II} porous coordination polymer (PCP), produces different isomeric products depending on the guest solvent present in the PCP during irradiation. The nature of the included guest influences the conformation of the ligand, and thus the outcome of the cycloaddition reaction. We demonstrate controlled production of the two isomers from the same PCP by simple exchange of solvent.*

Porous coordination polymers, PCPs, are polymeric network structures, constructed from established coordination bonding motifs.[1,2] PCPs are particularly appealing because modular design strategies can be applied to yield networks with specific properties. Owing to the diversity of organic ligands, metal ions and solvents available, topology, pore shape, size and surface nature can all be tailored.[2,3] In addition, some PCPs exhibit flexible and dynamic structural responses to external stimuli such as temperature, pressure, irradiation, mechanical force and guest exchange.[4–10] In particular, soft porous crystals are flexible coordination polymers that undergo structural transformations triggered by guest exchange.[11]

Solid-state photochemical [2+2] cycloaddition reactions have attracted attention as an alternative approach to synthesizing regio- or stereoselective products that are generally low yielding or impossible to obtain in solution.[12] According to the topochemical postulates proposed by Schmidt, carbon–carbon double bonds should be separated by less than 4.2 Å and aligned parallel to each other in order to undergo [2+2] cycloaddition in the solid state.[13] It is an ongoing challenge to control the packing of olefinic molecules to meet these topochemical requirements. The use of template molecules has proven especially effective in controlling [2+2] cycloaddition in the solid state.[14–16] Metal-organic frameworks (MOFs) and coordination polymers (CPs) have been widely used to control the arrangement of organic molecules in the solid state due to their versatile but highly predictable geometries.[17–25] Frameworks that undergo photodimerization through cycloaddition have also displayed favorable gas separation, fluorescence-switching and nitro-sensing properties.[26–31]

The ligand 1,4-bis[2-(4-pyridyl)ethenyl]benzene (bpeb, Scheme 1) is often used in the synthesis of photoactive

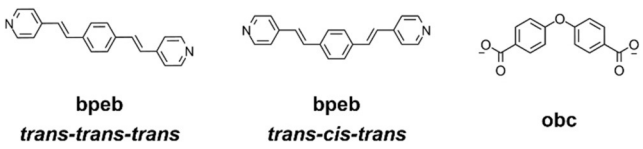

Scheme 1. Chemical structures of 1,4-bis[2-(4-pyridyl)ethenyl]benzene (bpeb) and 4,4′-oxybis(benzoic acid) (obc). Bpeb can assume either the *trans-trans-trans* or *trans-cis-trans* conformation.

MOFs since it has two C=C olefinic bonds. Two bpeb ligands can align in either an out-of-phase or an in-phase fashion.[20] If Schmidt's topochemical postulates are satisfied in a crystal containing either arrangement, this could result in the formation of either one or two cyclobutane ring units, respectively, and thus lead to the synthesis of two isomeric cycloaddition products (Scheme 2).[13]

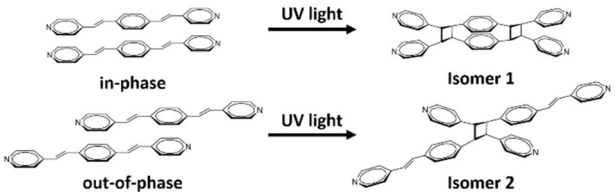

Scheme 2. Two possible alignments of bpeb ligands in the solid state. In-phase alignment (above) results in the formation of **Isomer 1** and out-of-phase alignment (below) results in the formation of **Isomer 2** of the cyclized form.

MacGillivray and co-workers have synthesized two isomers of the cyclized bpeb dimer in the solid state using template molecules to correctly align the ligands through hydrogen bonding.[32] Vittal and co-workers also synthesized two cyclobutane isomers in two different CPs as a result of different degrees of interpenetration of the frameworks.[33] Liu and co-workers synthesized the two isomers depicted in Scheme 2 in the solid state through incorporation of the bpeb ligand as the organic spacer in different CPs.[34] Herein we report the selective synthesis of both bpeb dimer isomers in the same PCP by changing the conformation of the olefinic bonds in the bpeb ligand via a simple exchange of guest.

Large yellow rhomboid crystals of **CdPCP·DMA** ([Cd(bpeb)(obc)]·2 DMA, where obc is 4,4′-oxybis(benzoic acid)) (Scheme 1) were obtained in 69% yield through the solvo-

[*] I. E. Claassens, Dr. V. I. Nikolayenko, Prof. D. A. Haynes, Prof. L. J. Barbour
Department of Chemistry and Polymer Science
Stellenbosch University
P. Bag X1, Matieland, 7602, Stellenbosch (South Africa)
E-mail: ljb@sun.ac.za
dhaynes@sun.ac.za

Supporting information and the ORCID identification number(s) for the author(s) of this article can be found under: https://doi.org/10.1002/anie.201809050.

thermal reaction of $Cd(NO_3)_2 \cdot 4H_2O$, H_2obc, and bpeb in a $1^1/_2$:1:1 molar ratio dissolved in a mixture of dimethylacetamide (DMA), water and dimethyl sulfoxide (DMSO) in a 3:1:1 volume ratio. Single-crystal X-ray diffraction (SCXRD) analysis revealed that the resulting material is two-dimensional and consists of interdigitated sheets, which are stacked in a slipped fashion as illustrated in Figure 1. The

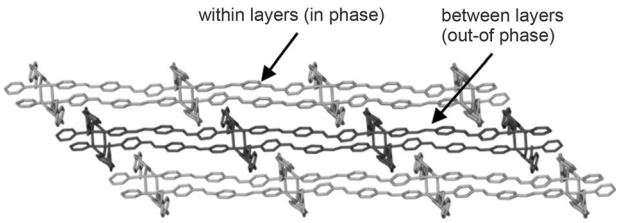

Figure 1. Two-dimensional interdigitated layers in **CdPCP·DMA** stacked in a slipped fashion. Distinct adjacent layers are shaded light and dark. Solvent molecules and hydrogen atoms have been omitted for clarity.

framework has **3,5L2** and **sql** topology, in standard and cluster representations, respectively.[35] The geometry of the secondary building unit aligns two photoactive bpeb ligands within a sheet such that both double bonds within one ligand are correctly positioned to undergo cycloaddition with a second ligand molecule. The two sets of symmetry-equivalent double bonds have a separation of 4.204(4) Å at 298 K, which is at the proposed limit for photochemical [2+2] cycloaddition. The slip-stacked packing of the 2D sheets also results in two bpeb ligands being aligned in the out-of-phase manner between adjacent interdigitated 2D layers, with a separation of 4.242(5) Å between double bonds, which falls just outside the photochemical limit (Figure 2). Two DMA molecules are present per asymmetric unit (ASU), as confirmed by thermogravimetric analysis, which also shows that **CdPCP·DMA** is stable to 275 °C (see the Supporting Information, Figure S6).

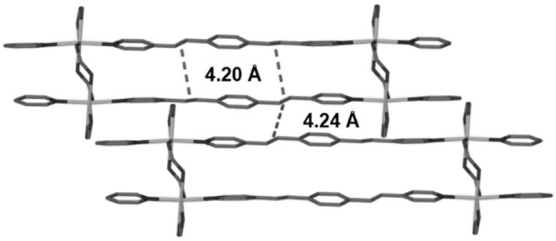

Figure 2. The two potentially photoactive positions in **CdPCP·DMA** based on parallel bond alignment.

Irradiation of **CdPCP·DMA** with a 365 nm UV-LED at 298 K resulted in cycloaddition between two bpeb ligands at both double bond positions within the two-dimensional layer to yield **Isomer 1**, as revealed by SCXRD analysis (Figure 3). The topology of the new framework is **3,4,5L7**.[35] A maximum yield of 60% cycloaddition product was observed in the SCXRD analysis, but irradiation time was limited in these

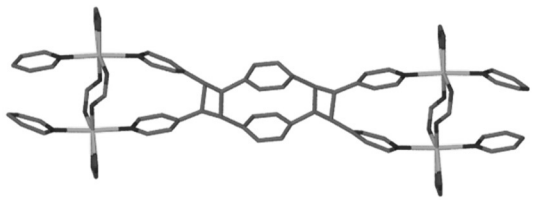

Figure 3. Structure of **CdPCP·DMA** after irradiation. All hydrogen atoms and solvent molecules are omitted for clarity and only the major component of disorder is displayed.

experiments to maintain single crystal integrity. After prolonged irradiation of a bulk sample the peak corresponding to the ligand olefinic bonds was no longer discernible in the FT-IR spectrum of the product (Figure S13). The irradiated framework was digested and the resulting solution subjected to NMR analysis. This confirmed the synthesis of **Isomer 1**, and also suggests near 100% conversion as no signals corresponding to the non-cyclized bpeb ligand are observed in the ^{1}H NMR spectrum (Figure S16). The formation of **Isomer 1** in **CdPCP·DMA** was shown to be reproducible by recording SCXRD data before and after cycloaddition for several different samples. This also confirmed that the yield, as determined by SCXRD, is dependent on the duration of exposure to irradiation.

It has been suggested that the type of solvent included in a particular framework may affect the conformation of the olefinic bonds in the bpeb ligand by inducing a pedal-like motion in the ligand.[19] This can reversibly change the conformation of the ligand from *trans-trans-trans* to *trans-cis-trans* (Scheme 1). It follows from Schmidt's postulates that the conformation of the double bonds in bpeb will affect the photoreactivity of any framework containing this ligand. In light of this, solvent-exchange experiments were carried out on **CdPCP·DMA** by immersing crystals in dimethylformamide (DMF). This yielded **CdPCP·DMF,** in which the two DMA molecules in the ASU are replaced by two DMF molecules and one H_2O molecule (confirmed by TGA, see Figure S10). SCXRD analysis revealed that the bpeb ligand changes from the *trans-trans-trans* to the *trans-cis-trans* conformation upon exchange of DMA for DMF (Figure S2). The olefinic bonds between the bpeb ligands within the 2D layer are now photoinactive as they no longer have a parallel alignment with respect to one another. However, the out-of-phase bpeb ligand pair between the 2D layers now has both the correct alignment for the one set of parallel double bonds, and a separation of 3.712(8) Å. This falls well within the photochemical limit, making this position favorable for cycloaddition.

As expected, irradiation of **CdPCP·DMF** results in cycloaddition between the out-of-phase aligned bpeb ligands in adjacent two-dimensional sheets, yielding **Isomer 2** of the bpeb dimer (Figure 4).

Cycloaddition between the ligands in this position also results in cross-linking of the two-dimensional sheets, thus transforming the framework into a new three-dimensional MOF (Figure 5). The new framework has a **3,4,5T3** and **fsc** topology.[35] SCXRD analysis confirmed near-quantitative conversion to the cyclized form but the amorphous nature of

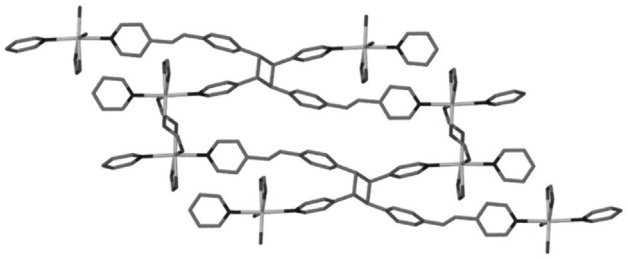

Figure 4. Structure of **CdPCP·DMF** after irradiation where cyclization has taken place between the out-of-phase bpeb ligands between 2D layers, resulting in the formation of **Isomer 2**.

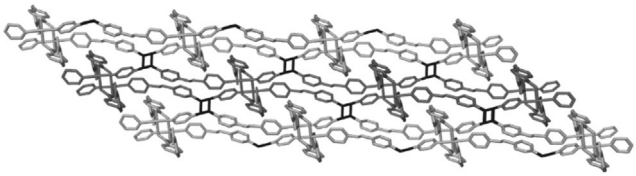

Figure 5. Structure of the 3D framework resulting from **CdPCP·DMF** after UV irradiation where cycloaddition has taken place between the 2D layers. Cyclobutane rings are shown in a darker shade.

the bulk sample after prolonged irradiation made further characterization difficult. The required duration of exposure to UV irradiation in order to achieve cyclization is shorter for **CdPCP·DMF** than for **CdPCP·DMA**, which may be due to much shorter distances between the reacting double bonds in the latter. Modelling of the DMF and water molecules in the channels of **CdPCP·DMF** was not possible after irradiation, and thermal analysis suggests that some solvent loss occurs during irradiation. SCXRD analysis of several different samples showed that cyclization upon irradiation in **CdPCP·DMF** is reproducible.

Both **CdPCP·DMA** and **CdPCP·DMF** were digested after irradiation, and cycloaddition products **Isomer 1** and **Isomer 2**, respectively were precipitated by altering the pH of the solution. Both products were characterized using NMR spectroscopy, confirming that either isomer can be synthesized, extracted and isolated from the same PCP (see Figures S16, S17, and S21).

Repeated exchange of solvent within the framework was carried out on a single crystal of **CdPCP·DMA**. The solvent was exchanged between DMA and DMF, and the crystal analyzed by SCXRD after each step, confirming the reversible nature of the guest exchange from DMA to DMF. An intermediate structure was also obtained in which one DMA, one DMF and one water molecule are present per ASU, showing that the more disordered DMA guest in the center of the channel in **CdPC·DMA** was replaced by DMF. The conformation of the bpeb ligand in this intermediate structure is similar to that in **CdPCP·DMA** (see the Supporting Information for details on possible minor disorder in the ligand in both structures).

Further solvent-exchange experiments using **CdPCP·DMA** were also carried out with THF, 1,4-dioxane, benzene, toluene, chloroform and carbon tetrachloride. In all cases it was clear from SCXRD analysis that exchange of solvent had occurred. SCXRD analysis was used to investigate the effect each solvent has on the conformation of the double bonds in the bpeb linker, as well as the effect on the distances between the potentially photoactive bonds. The bpeb ligand in **CdPCP·DMA** has the *trans-trans-trans* conformation in which all the double bonds have parallel alignment with respect to one another, both within and between the 2D sheets. The bpeb linker in **CdPCP·DMF** has the *trans-cis-trans* conformation in which only the double bonds between the 2D layers have a parallel alignment. Table 1 lists the conformation of the bpeb linker in the various solvates, as well as the distance between the double bonds within the 2D layers and between the 2D sheets. A small amount of disorder of the ligand is observed in most cases; only the major component of disorder was considered in generating the data in Table 1, which was used to predict the position of cyclization within the framework (see the Supporting Information for details).

Irradiation experiments were carried out on single crystals of **CdPCP·*x*** (where x = solvent) for all solvents listed in Table 1, and SCXRD analysis was used to determine the position of cyclization in each case where this was possible. Cyclization between the 2D layers in the framework was observed for THF and 1,4-dioxane, where both the confor-

Table 1: Predicted locations of cycloaddition upon UV-irradiation of the different solvates of **CdPCP·*x***. The distances between double bonds, as well as within the 2D layers, are given. The conformation of the bpeb ligand is either *trans-trans-trans* (T-T-T) or *trans-cis-trans* (T-C-T).

Solvent	Conformation of bpeb	Distance within 2D layer	Distance between 2D layers	Predicted position of cyclization (isomer)[a]	Observed position of cyclization (isomer)
DMA	T-T-T	4.204(4)	4.242(5)	within (**1**)	within (**1**)
DMF	T-C-T	3.995(4)	3.712(8)	between (**2**)	between (**2**)
THF	T-T-T	4.199(4)	3.701(8)	between (**2**)	between (**2**)
1,4-dioxane	T-T-T	4.200(2)	3.710(5)	between (**2**)	between (**2**)
toluene	T-C-T/T-T-T	3.84(1)	4.047(8)	between (**1** or **2**, **1** more likely)	both (**1** and **2**)
carbon tetrachloride	T-C-T	3.808(3)	4.243(3)	between (**2**)	no cycloaddition observed[b]
benzene	T-C-T	3.878(8)	3.818(6)	between (**2**)	crystal quality too poor
chloroform	T-C-T	3.858(9)	3.88(1)	between (**2**)	crystal quality too poor

[a] Predicted position of cyclization depends on both ligand conformation and distances between double bonds. In the T-T-T conformation, both the bonds within and between the layers are correctly aligned for cyclization. In these cases, the possibility with the shorter distance between double bonds was chosen as the more likely position to undergo cycloaddition. If the ligand is in the T-C-T conformation, only the double bonds between layers are correctly aligned for cyclization. [b] Cracking of the crystal occurred upon irradiation, which may be indicative of some cycloaddition taking place on the surface. No cycloaddition is observed in the SCXRD structure determined after irradiation.

mation of the ligand and the distance between olefinic bonds in the non-irradiated framework indicated that this would be the case. The toluene solvate is an interesting case. Analysis of the crystal structure of the solvate indicates that cycloaddition could take place either within or between the layers. A structure determined after irradiation indicates that cycloaddition has taken place in both positions, although the quality of the crystal was poor. For the CCl_4 solvate, SCXRD indicated that cycloaddition would take place between the layers but no cycloaddition was observed, despite repeated attempts.

Irradiation experiments were also attempted for the benzene and chloroform solvates, but SCXRD analysis of the product was not possible due to loss of crystal integrity. It is nonetheless clear from these results that the included solvent affects the position and conformation of the bpeb ligands, and thus controls the outcome of the cycloaddition reaction.

In conclusion, two isomers of a cyclized bpeb dimer have been isolated through UV-induced cycloaddition within the same material by exchanging the type of solvent included in the PCP channels. The nature of the guest affects the conformation of the bpeb linker, which in turn changes the photoreactivity of the crystals. A change in the position of the cyclization transformed the 2D interdigitated PCP into a three-dimensional MOF. The choice of included solvent thus offers a precise degree of control over the outcome of the photochemical cycloaddition reaction in this PCP.

Experimental Section

CCDC 1860392, 1860393, 1860394, 1860395, 1860396, 1860397, 1860398, 1860399, 1860400, 1860401, 1860402, 1860403, 1860404, 1860405, and 1860406 contain the supplementary crystallographic data for this paper. These data can be obtained free of charge from The Cambridge Crystallographic Data Centre.

Acknowledgements

We thank the National Research Foundation of South Africa, Stellenbosch University, and SASOL for funding.

Conflict of interest

The authors declare no conflict of interest.

Keywords: coordination polymers · cycloaddition · photochemistry · single-crystal to single-crystal · stimulus response

How to cite: *Angew. Chem. Int. Ed.* **2018**, *57*, 15563–15566
Angew. Chem. **2018**, *130*, 15789–15792

[1] S. Kitagawa, M. Kondo, *Bull. Chem. Soc. Jpn.* **1998**, *71*, 1739.
[2] H. Furukawa, K. E. Cordova, M. O'Keeffe, O. M. Yaghi, *Science* **2013**, *341*, 1230444.
[3] J.-P. Zhang, H.-L. Zhou, D.-D. Zhou, P.-Q. Liao, X.-M. Chen, *Natl. Sci. Rev.* **2017**, *4*, 1.
[4] R. Kitaura, K. Fujimoto, S.-I. Noro, M. Kodo, S. Kitagawa, *Angew. Chem. Int. Ed.* **2002**, *41*, 133; *Angew. Chem.* **2002**, *114*, 141.
[5] K. Uemura, S. Kitagawa, M. Kondo, K. Fukui, R. Kitaura, H.-C. Chang, T. Mizutani, *Chem. Eur. J.* **2002**, *8*, 3586.
[6] C. Serre, F. Millange, C. Thouvenot, *J. Am. Chem. Soc.* **2002**, *124*, 13519.
[7] S. Kitagawa, R. Kitaura, S. Noro, *Angew. Chem. Int. Ed.* **2004**, *43*, 2334; *Angew. Chem.* **2004**, *116*, 2388.
[8] K. Uemura, R. Matsuda, S. Kitagawa, *J. Solid State Chem.* **2005**, *178*, 2420.
[9] G. Férey, C. Serre, *Chem. Soc. Rev.* **2009**, *38*, 1380.
[10] W. Cai, A. Gładysiak, M. Anioła, V. J. Smith, L. J. Barbour, A. Katrusiak, *J. Am. Chem. Soc.* **2015**, *137*, 9296.
[11] S. Horike, S. Shimomura, S. Kitagawa, *Nat. Chem.* **2009**, *1*, 695.
[12] G. R. Desiraju, *Endeavour* **1984**, *8*, 201.
[13] G. M. J. Schmidt, *Pure Appl. Chem.* **1971**, *27*, 647.
[14] L. R. MacGillivray, J. L. Reid, J. A. Ripmeester, *J. Am. Chem. Soc.* **2000**, *122*, 7817.
[15] T. Friščić, L. R. MacGillivray, *Chem. Commun.* **2003**, 1306.
[16] L. R. MacGillivray, G. S. Papaefstathiou, T. Friščić, D. B. Varshney, T. D. Hamilton, *Top. Curr. Chem.* **2004**, *248*, 201.
[17] L. R. MacGillivray, G. S. Papaefstathiou, T. Friščić, T. D. Hamilton, D. K. Bučar, Q. Chu, D. B. Varshney, I. G. Georgiev, *Acc. Chem. Res.* **2008**, *41*, 280.
[18] K. Biradha, R. Santra, *Chem. Soc. Rev.* **2013**, *42*, 950.
[19] I.-H. Park, S. S. Lee, J. J. Vittal, *Chem. Eur. J.* **2013**, *19*, 2695.
[20] R. Medishetty, I. Park, S. S. Lee, J. J. Vittal, *Chem. Commun.* **2016**, *52*, 3989.
[21] I.-H. Park, C. E. Mulijanto, H.-H. Lee, Y. Kang, E. Lee, A. Chanthapally, S. S. Lee, J. J. Vittal, *Cryst. Growth Des.* **2016**, *16*, 2504.
[22] I.-H. Park, R. Medishetty, H. H. Lee, C. E. Mulijanto, H. S. Quah, S. S. Lee, J. J. Vittal, *Angew. Chem. Int. Ed.* **2015**, *54*, 7313; *Angew. Chem.* **2015**, *127*, 7421.
[23] D. Liu, J. Lang, *CrystEngComm* **2014**, *16*, 76.
[24] G. K. Kole, J. J. Vittal, *Chem. Soc. Rev.* **2013**, *42*, 1755.
[25] J. J. Vittal, H. S. Quah, *Dalton Trans.* **2017**, *46*, 7120.
[26] A. Hazra, S. Bonakala, K. K. Bejagam, S. Balasubramanian, T. K. Maji, *Chem. Eur. J.* **2016**, *22*, 7792.
[27] M. L. Foo, R. Matsuda, Y. Hijikata, R. Krishna, H. Sato, S. Horike, A. Hori, J. Duan, Y. Sato, Y. Kubota, et al., *J. Am. Chem. Soc.* **2016**, *138*, 3022.
[28] F. F. Li, L. Zhang, L. Le Gong, C. S. Yan, H. Y. Gao, F. Luo, *Dalton Trans.* **2017**, *46*, 338.
[29] N. Y. Li, D. Liu, Z. G. Ren, C. Lollar, J. P. Lang, H. C. Zhou, *Inorg. Chem.* **2018**, *57*, 849.
[30] I.-H. Park, J. Huiyeong, K. Kihwan, S. S. Lee, J. J. Vittal, *IUCrJ* **2018**, *5*, 182.
[31] N.-Y Li, D. Liu, B. F. Abrahams, J.-P Lang, *Chem. Commun.* **2018**, *54*, 5831.
[32] T. Friščić, L. R. MacGillivray, *Aust. J. Chem.* **2006**, *59*, 613.
[33] I.-H. Park, R. Medishetty, J.-Y. Kim, S. S. Lee, J. J. Vittal, *Angew. Chem. Int. Ed.* **2014**, *53*, 5591; *Angew. Chem.* **2014**, *126*, 5697.
[34] D. Liu, Z.-G. Ren, H.-X. Li, J.-P. Lang, N.-Y. Li, B. F. Abrahams, *Angew. Chem. Int. Ed.* **2010**, *49*, 4767; *Angew. Chem.* **2010**, *122*, 4877.
[35] TOPOSPro free structure determination service, http://www.topospro.com; V. A. Blatov, A. P. Shevchenko, D. M. Proserpio, *Cryst. Growth Des.* **2014**, *14*, 3576.

Manuscript received: August 6, 2018
Accepted manuscript online: September 25, 2018
Version of record online: October 23, 2018

Angewandte Chemie
Eine Zeitschrift der Gesellschaft Deutscher Chemiker

Supporting Information

Solvent-Mediated Synthesis of Cyclobutane Isomers in a Photoactive Cadmium(II) Porous Coordination Polymer

Isabella E. Claassens, Varvara I. Nikolayenko, Delia A. Haynes, and Leonard J. Barbour**

anie_201809050_sm_miscellaneous_information.pdf

Table of Contents

Experimental Procedures

Instrument details

Nuclear magnetic resonance spectroscopy (NMR)

^{1}H and ^{13}C nuclear magnetic resonance spectra were recorded at 25 °C on a 400 MHz or a 600 MHz Varian Unity Inova using deuterated DMSO or $CHCl_3$ as solvents.

Thermogravimetric analysis (TGA)

Thermogravimetric analyses were carried out on a TA Instruments Q500 analyzer. The instrument records weight loss as a function of temperature. Samples ranging in mass from 2 – 4 mg were placed in an aluminum pan and heated from room temperature to 600 °C at a rate of 10 °C min^{-1} under N_2 flow of 50 mL min^{-1}. Data Analysis was carried out using the Universal Analysis 2000 (TA Instruments, Version 4.5A) software.

Powder X-ray diffraction (PXRD)

PXRD data were recorded on a benchtop Bruker D2 PHASER. It is equipped with a Lynxeye 1D detector and uses Ni-filtered Cu Kα radiation (λ = 1.5418 Å) with generator power settings of 30 kV and 10 mA. The X-ray beam is restricted by a 1.0 mm divergence slit and a 2.5 mm Söller collimator. Powder samples were evenly distributed on a zero-background holder after being ground with a mortar and pestle to minimize the effects of preferred orientation. Data analysis was carried out using X'Pert HighScore Plus[1] (Version 2.2e). Powder patterns were simulated from SCXRD structures using Mercury[2].

Single-crystal X-ray diffraction (SCXRD)

Suitable single crystals were selected and attached to a MiTeGen MicroLoop™ mount using Paratone®N oil. SCXRD data were recorded on three different instruments. Routine data collections were carried out on a Bruker SMART APEX-II and an APEX-II DUO diffractometer, both of which utilize APEX-II CCD area-detectors, and Oxford Cryosystems 700Plus cryostats to control the temperature. X-rays were generated from a sealed tube (MoKα radiation λ = 0.71073 Å) fitted with a multilayer monochromator on the SMART APEX-II, while the APEX-II DUO uses an Incoatec IμS microfocus source fitted with a multilayer monochromator. Specialized experiments were carried out on a Bruker D8 Venture equipped with a Photon II CPAD detector, which has a multilayer monochromator with MoKα radiation (λ = 0.71073 Å) from an Incoatec IμS microfocus source. An Oxford Cryostreams 800Plus cryostat was used to control the temperature. Specialized experiments include variable-temperature and UV-irradiation studies.
Data reduction was carried out with the Bruker SAINT[3] software package. The absorption corrections and the correction of other systematic errors were carried out with SADABS[4]. Structures were solved using the X-Seed[5],[6] interface by direct methods using SHELXS[7] or by intrinsic phasing using SHELXT[8]. Structure refinement was carried out using SHELXL[7]. Hydrogen atom positions were assigned using riding models.

PLATON[9] SQUEEZE[10] was used to determine the total electron count per unit cell of guest molecules within the structures. These counts were then used to determine occupancy of the guest molecules within the channels of the PCPs. Graphics were generated with POV-Ray [11] and CIF files were edited in Olex2.[12]

Infrared Spectroscopy

IR analysis was carried out on a Bruker Alpha II FTIR infrared spectrometer with a QuickSnap™ Platinum ATR module. Solid-state samples were ground before analysis.

Irradiation

Photoirradiation was carried out using a hand held UV-Groebel UV-LED SOLO photodiode emitting UV light of wavelength 365 nm at 4 200 mW cm^{-2}. Single crystals in Paratone®N oil on a glass slide were irradiated for between 5 and 15 minutes. Samples were irradiated for as long as possible whilst maintaining crystal integrity. In most cases irradiation was continuous; in some cases irradiation was interrupted to check crystal quality before further irradiation was carried out. Powder samples were irradiated between two glass slides. Further details are given in the synthesis section below.

TOPOSPro[13] was used to determine the topology of the framework through the website service at topospro.org.

Synthesis

Chemicals and solvents were obtained from Sigma-Aldrich and used as received. Nitrogen was passed through a Drierite™ drying column before use.

Synthesis of 1,4-bis[2-(4'-pyridyl)ethenyl]benzene (bpeb)
The synthetic procedure (Scheme S1) was adapted from that reported by Bhowmik *et al*.[14]

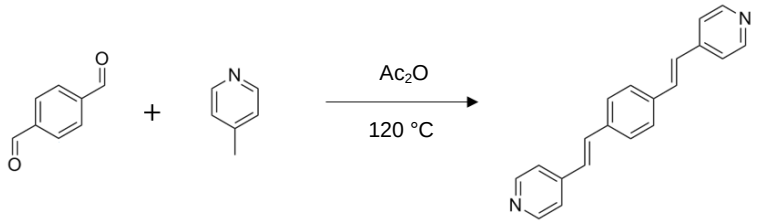

Scheme S1 Synthesis of 1,4-bis[2-(4'-pyridyl)ethenyl]benzene (bpeb) from terepthaldehyde and 4-picoline.

Terepthaldehyde (3.35 g, 24.9 mmol) was added to 4-picoline (9.7 mL, 0.10 mol) in 30 mL acetic anhydride under inert conditions. The mixture was heated to 70 °C and stirred for an hour, until the solution turned a deep brown color. After the addition of anhydrous $ZnBr_2$ (12.35 g, 54.84 mmol), the reaction was heated to 120 °C and allowed to reflux for 3 hours under inert conditions. The mixture was refluxed for a further 48 hours under inert conditions, during which time an orange precipitate formed. The orange precipitate was filtered off, washed four times with acetic anhydride and allowed to dry for 24 hours under ambient conditions. The mixture was then washed with 100 mL hot ethanol (70 °C) in small batches. It was then allowed to dry once more, after which it was washed a final time with ether (4-5 times). The dried product was then recrystallized from pyridine. The resulting powder was filtered and washed with copious amounts of diethyl ether to ensure that all of the pyridine was removed. NMR confirmed successful synthesis and purity of the product. The percentage yield was 34.0% (2.40 g).

1H-NMR (CDCl3, 400 MHz): δ 7.04 (2H, d, CHethelyne), 7.29 (2H, d, CHethelyne), 7.36 (4H, dd, CHpyridine), 7.55 (4H, s, CHbenzene), 8.58 (4H, dd, CHpyridine).

Synthesis of CdPCP·DMA
$Cd(NO_3)_2 \cdot 4H_2O$ (26 mg, 0.084 mmol), 4,4'-oxybis(benzoic acid) (18 mg, 0.070 mmol) and bpeb (20 mg, 0.070 mmol) were dissolved in a mixed solvent system consisting of 3 mL DMA, 2 mL H_2O and 1 mL DMSO with the assistance of a heat gun. The solution was then heated in a 20 mL scintillation vial in an oven at 100 °C for 48 hours, resulting in the formation of rhombohedral-shaped clear yellow crystals. Post synthesis, the crystals were placed in pure DMA to avoid their dissolution in the mother liquor. Yield 38.4 mg (74% yield based on bpeb).

Solvent-exchange experiments
Single crystals of **CdPCP·DMA** were immersed in approximately 2 mL of solvent for 2 days in a dark cupboard at room temperature. The solvent was replenished after 24 hours.

Digestion of irradiated CdPCP·DMA
Single crystals of **CdPCP·DMA** (65 mg) were finely ground and irradiated for 2 hours between two glass slides with frequent mixing to ensure even irradiation of the sample. The powder was then transferred to a 25 mL round-bottomed flask with 5 mL of 3 M HCl. The mixture was allowed to stir at ambient conditions for 15 minutes after which the yellow precipitate was filtered and the filtrate was discarded. The precipitate was then washed with 2 x 3 mL distilled water to remove obc. The pH of the filtrate was adjusted to between 7 and 8 with 1 M NaOH, at which point **Isomer 1** precipitated. The precipitate was filtered and washed with ethanol. ^1H and ^{13}C NMR analysis was performed on the precipitate in d-DMSO (see Figures S15 and S16).

Digestion of irradiated CdPCP·DMF

Single crystals of **CdPCP·DMF** (43 mg) were finely ground and irradiated for 2 hours between two glass slides with frequent mixing to ensure even irradiation of the sample. The powder was then transferred to a 25 mL round-bottomed flask with 5 mL of 3 M HCl. The mixture was allowed to stir at ambient conditions for 15 minutes after which the yellow precipitate was filtered and the filtrate was discarded. The precipitate was then washed with 2 x 3 mL slightly acidic distilled water to remove obc. The pH of the filtrate was adjusted to between 7 and 8 with 1 M NaOH, at which point **Isomer 2** precipitated. The precipitate was filtered and washed with ethanol. ^1H NMR analysis was performed on the precipitate in d-DMSO (see Figure 20).

Results

Single-crystal X-ray diffraction
Details of refinement of structures are given below.

The asymmetric units of **CdPCP·DMA** and **CdPCP·DMF** are shown in Figures S1 and S2. Selected crystallographic data for all structures are given in Table S1.

Details regarding crystal structure refinement

CdPCP·DMA
Two residual density peaks of 0.7-0.8 e $Å^{-3}$ appear close to one bpeb double bond. All attempts to model this as minor disorder of the ligand were unsuccessful. The occupancy factor of the bpeb ligand as modelled refines to 1. We have therefore not modelled any disorder in the ligand, although a minor component may be present.

CdPCP·DMA (irradiated)
The geometry of the cycloaddition product is strained. Attempts to model a full unreacted ligand were unsuccessful – both ligands had to be refined isotropically in order to keep the refinement stable, and the geometry of neither ligand was improved by this model. We have therefore modelled only partial disorder in the reacted and unreacted ligand. Solvent molecules in the channels are highly disordered. The reported model was the best of several attempts, and was only obtained by using FRAG and SAME commands.

CdPCP·DMF
The solvent molecules in the channels could not be modelled satisfactorily. The SQUEEZE procedure was therefore employed. SCXRD on a crystal from the same batch at 100 K confirmed the presence of two DMF molecules and one partially occupied water molecule in the channels of the PCP. The unit cell of this 100 K structure is a different setting of the same reduced cell that arises due to changes in the cell angles on decreasing the temperature.

The data for the following structures were collected at 100 K to improve resolution of the solvent molecules wherever possible. The unit cells of all crystals were also checked at room temperature to confirm that there are no significant changes in the structure on cooling.

CdPCP·DMF (irradiated)
The solvent molecules in the channels could not be modelled. SQUEEZE was therefore employed. The crystal quality was very poor due to cracking of the crystal on cycloaddition. The best of many crystals tested was chosen.

CdPCP·DMA_DMF
This structure also has indications of disorder in the bpeb double bond position (residual density peaks of 1.32 and 1.71 e $Å^{-3}$). As with **CdPCP·DMA**, all attempts to model this as minor disorder of the ligand were unsuccessful, and we have therefore not modelled any disorder in the ligand, although a minor component may be present.

CdPCP·THF
Attempts to model the minor component of disorder in the ligand were unsuccessful. The second solvent molecule is highly disordered. This has been modelled as far as possible.

CdPCP·THF (irradiated)
The cycloaddition product is the minor component of the disorder in this structure. Models with two complete ligands (one reacted, one unreacted) were not good (both ligands had to be refined isotropically for any stability in the refinement) and did not improve the geometry of either ligand noticeably. For this reason, only part of the cycloaddition product has been modelled. The second THF molecule could not be well modelled, and residual electron density has been removed using SQUEEZE.

CdPCP·dioxane
There were no issues with the refinement of this structure.

CdPCP·dioxane (irradiated)
Only the two carbon atoms (with associated hydrogens) that have undergone [2+2] cycloaddition have been modelled as a separate PART from the unreacted ligand. Attempts to model the entire cyclobutane ligand led to unstable refinements, and the positions of the ayrl and pyridyl rings were displaced only very slightly from the positions of their equivalents in the unreacted ligand.

CdPCP·bezene
Only the major ligand position could be modelled anisotropically. No [2+2] cycloaddition was observed in these crystals, despite several attempts.

CdPCP·toluene
Only the major ligand position could be modelled anisotropically. There is disorder in the solvent molecules, but this could not be modelled.

CdPCP·toluene (irradiated)
The best model for this data shows partial [2+2] cycloaddition at two different position – both between and within the layers. As with other structures, any attempts to model the cycloaddition product further led to unsatisfactory or unstable requirements. The solvent in the channels is highly disordered and SQUEEZE has been applied.

CdPCP·$CHCl_3$
Only one solvent molecule could be satisfactorily modelled.

CdPCP·CCl_4
The solvent molecules are highly disordered, although a satisfactory model has been obtained.

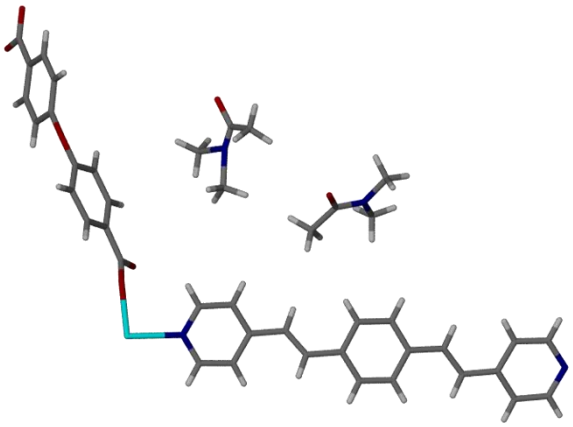

Figure S1. ASU of **CdPCP·DMA** at 298 K.

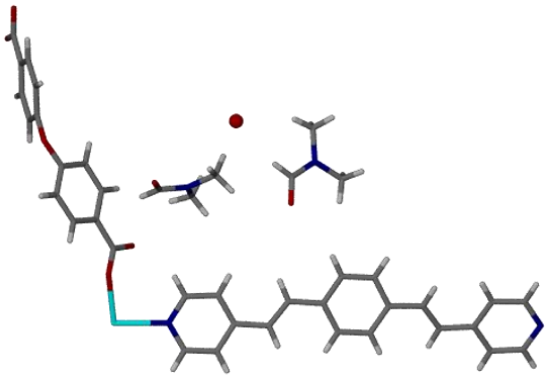

Figure S2. ASU of **CdPCP·DMF** at 298 K.

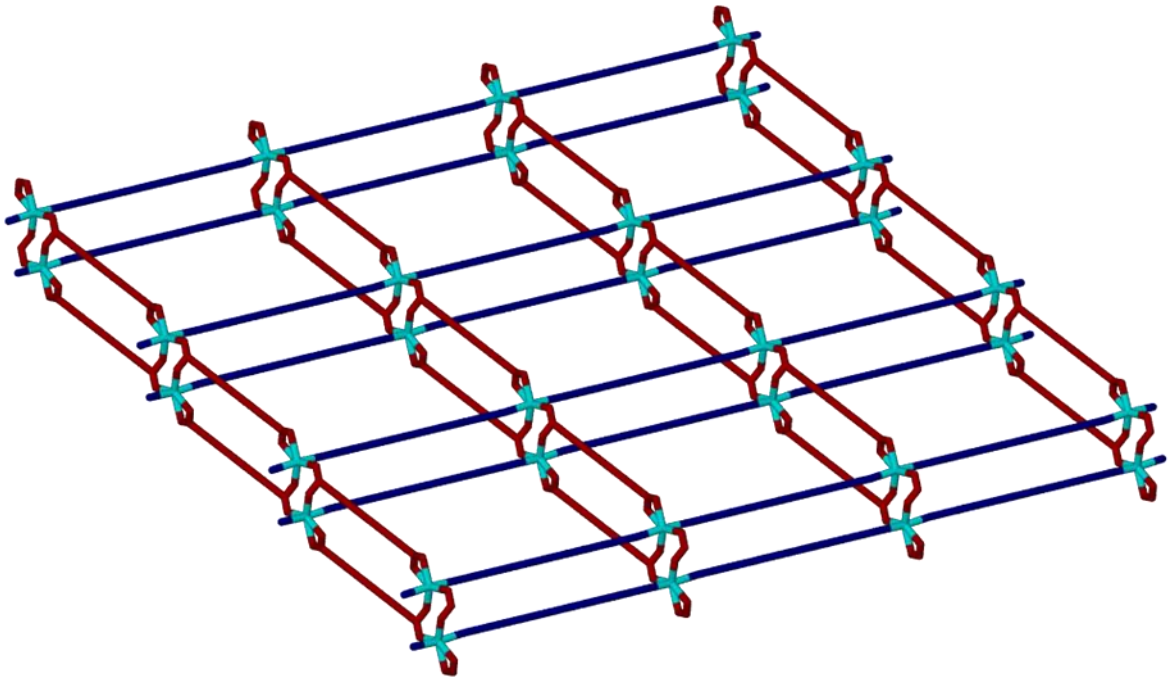

Figure S3. Connectivity diagram of **CdPCP·DMA** – the 2D net is (4,4) connected. The bpeb linker is represented by the blue lines and the obc linker by the red lines.

Table S1 Selected crystallographic data for structures reported in this manuscript.

	CdPCP_DMA_298 K	**CdPCP_DMF_100K**	**CdPCP_DMF_298K**	**DMA irrad**	**CdPCP_DMF_irrad**	**CdPCP_DMA_DMF**	**CdPCP_1,4 dioxane**	**CdPCP_1,4 dioxane_irrad**
Empirical formula	$C_{42}H_{42}CdN_4O_7$	$C_{40}H_{38}CdN_4O_{7.68}$	$C_{34}H_{24}CdN_2O_5$	$C_{39.49}H_{25}CdN_{3.22}O_{7.22}$	$C_{34}H_{20}CdN_2O_5$	$C_{39.50}H_{36.50}CdN_{3.50}O_{7.50}$	$C_{42}H_{40}CdN_2O_9$	$C_{42}H_{40}CdN_2O_9$
Formula weight	827.19	809.70	652.95	772.57	648.92	792.62	829.16	829.16
Temperature (K)	298(2)	100(2)	298(2)	100(2)	100(2)	100(2)	100(2)	100(2)
Wavelength (Å)	0.71073	0.71073	0.71073	0.71073	0.71073	0.71073	0.71073	0.71073
Crystal system	triclinic	triclinic	triclinic	triclinic	triclinic	triclinic	triclinic	triclinic
Space group	*P*-1	*P*-1	*P*-1	*P*-1	*P*-1	*P*-1	*P*-1	*P*-1
Unit cell dimensions (Å, °)	*a* = 9.6855(4)	*a* = 9.7310(8)	*a* = 9.7993(14)	*a* = 9.474(4)	*a* = 10.745(9)	*a* = 9.7227(4)	*a* = 9.5847(4)	*a* = 9.6174(5)
	b = 15.4863(7)	*b* = 15.0552(13)	*b* = 15.380(2)	*b* = 15.348(7)	*b* = 12.783(11)	*b* = 15.3764(7)	*b* = 15.0858(6)	*b* = 15.0715(9)
	c = 15.7346(6)	*c* = 15.3749(13)	*c* = 15.417(2)	*c* = 15.705(10)	*c* = 15.272(13)	*c* = 15.4683(7)	*c* = 15.4851(6)	*c* = 15.4876(9)
	α = 113.0560(10)	α = 60.829(3)	α = 115.155(2)	α = 117.730(4)	α = 104.653(11)	α = 116.0490(10)	α = 61.0490(10)	α = 109.612(2)
	β = 106.2370(10)	β = 78.282(3)	β = 107.383(2)	β = 103.661(6)	β = 109.205(10)	β = 107.705(2)	β = 72.1680(10)	β = 107.370(2)
	γ = 94.835(2)	γ = 71.869(3)	γ = 95.086(2)	γ = 93.977(4)	γ = 104.051(11)	γ = 92.276(2)	γ = 75.8990(10)	γ = 104.537(2)
Volume (Å^3)	2034.16(15)	1865.5(3)	1943.5(5)	1921.0(17)	1790(3)	1938.22(15)	1852.84(13)	1857.86(19)
Z	2	2	2	2	2	2	2	2
Calculated density (g cm^{-3})	1.351	1.441	1.116	1.336	1.204	1.358	1.486	1.482
Absorption coefficient (mm^{-1})	0.589	0.642	0.596	0.619	0.646	0.616	0.650	0.648
F_{000}	852	831	660	781	652	812	852	852
Crystal size (mm^3)	0.230 × 0.140 × 0.128	0.244 × 0.076 × 0.027	0.659 × 0.217 × 0.092	0.360 × 0.291 × 0.176	0.192 × 0.155 × 0.074	0.410 × 0.195 × 0.106	0.922 × 0.202 × 0.123	0.449 × 0.153 × 0.110
θ range for data collection (°)	2.233 to 27.181	2.206 to 27.142	1.581 to 26.517	1.533 to 23.528	2.711 to 30.466	2.232 to 28.224	2.247 to 26.410	2.250 to 25.540
Miller index ranges	-12 ≤ *h* ≤ 12, -19 ≤ *k* ≤ 19, -20 ≤ *l* ≤ 20	-12 ≤ *h* ≤ 12, -19 ≤ *k* ≤ 19, -19 ≤ *l* ≤ 18	-12 ≤ *h* ≤ 12, -19 ≤ *k* ≤ 19, -19 ≤ *l* ≤ 19	-10 ≤ *h* ≤ 10, -17 ≤ *k* ≤ 17, -17 ≤ *l* ≤ 17	-15 ≤ *h* ≤ 14, -17 ≤ *k* ≤ 17, -21 ≤ *l* ≤ 21	-12 ≤ *h* ≤ 12, -20 ≤ *k* ≤ 20, -14 ≤ *l* ≤ 20	-11 ≤ *h* ≤ 11, -18 ≤ *k* ≤ 18, -18 ≤ *l* ≤ 19	-11 ≤ *h* ≤ 11, -18 ≤ *k* ≤ 18, -18 ≤ *l* ≤ 17
Reflections collected	39587	19255	31307	11432	48176	27416	22167	26046
Independent reflections	9008 [R_{int} = 0.0309]	8217 [R_{int} = 0.0461]	8053 [R_{int} = 0.0438]	5543 [R_{int} = 0.0407]	10175 [R_{int} = 0.2232]	9506 [R_{int} = 0.0588]	7538 [R_{int} = 0.0282]	6869 [R_{int} = 0.0371]
Completeness to θ_{max} (%)	0.994	0.991	0.997	0.970	0.934	0.993	0.992	0.990
Max. and min. transmission	0.870 and 1	0.900 and 1	0.861 and 1	0.842 and 1	0.742 and 1	0.868 and 1	0.883 and 1	0.876 and 1
Refinement method	Full-matrix least-squares on F^2	Full-matrix least-squares on F^2	Full-matrix least-squares on F^2	Full-matrix least-squares on F^2	Full-matrix least-squares on F^2	Full-matrix least-squares on F^2	Full-matrix least-squares on F^2	Full-matrix least-squares on F^2
Data / restraints / parameters	9008 / 0 / 485	8217 / 0 / 483	8053 / 0 / 380	5543 / 14 / 456	10175 / 0 / 380	9505 / 0 / 486	7538 / 0 / 487	6869 / 0 / 506
Goodness-of-fit on F^2	1.058	1.089	1.053	1.057	0.888	1.062	1.051	1.319
Final *R* indices [$I > 2\sigma(I)$]	*R*1 = 0.0353, *wR*2 = 0.0905	*R*1 = 0.0552, *wR*2 = 0.1009	*R*1 = 0.0370, *wR*2 = 0.0977	*R*1 = 0.0722, *wR*2 = 0.1894	*R*1 = 0.0835, *wR*2 = 0.1917	*R*1 = 0.0637, *wR*2 = 0.1465	*R*1 = 0.0263, *wR*2 = 0.0597	*R*1 = 0.0691, *wR*2 = 0.1584
R indices (all data)	*R*1 = 0.0418, *wR*2 = 0.0960	*R*1 = 0.0732, *wR*2 = 0.1104	*R*1 = 0.0519, *wR*2 = 0.1034	*R*1 = 0.0995, *wR*2 = 0.2084	*R*1 = 0.2297, *wR*2 = 0.2604	*R*1 = 0.0909, *wR*2 = 0.1663	*R*1 = 0.0302, *wR*2 = 0.0621	*R*1 = 0.0735, *wR*2 = 0.1604
Largest diff. peak and hole (e Å^{-3})	0.772 and -0.383	0.650 and -0.875	0.593 and -0.566	0.868 and -0.737	0.650 and -1.463	1.715 and -1.295	0.604 and -0.345	1.436 and -2.063

Table S1 (cont.).

	CdPCP_THF	**CdPCP_THF_irrad**	**CdPCP_toluene**	**CdPCP_toluene_irrad**	**CdPCP_benzene**	**CdPCP_CCl4**	**CdPCP_CHCl3**
Empirical formula	$C_{37.56}H_{31.11}CdN_2O_{5.89}$	$C_{43}H_{32}CdN_2O_6$	$C_{43.49}H_{29.73}CdN_2O_5$	$C_{33.74}H_{23.74}CdN_2O_5$	$C_{46}H_{36}CdN_2O_5$	$C_{36}H_{24}CdCl_8N_2O_5$	$C_{35}H_{25}CdCl_3N_2O_5$
Formula weight	788.87	725.05	779.50	650.21	809.17	960.57	772.35
Temperature (K)	100(2)	100(2)	100(2)	100(2)	100(2)	100(2)	100(2)
Wavelength (Å)	0.71073	0.71073	0.71073	0.71073	0.71073	0.71073	0.71073
Crystal system	triclinic	triclinic	triclinic	triclinic	triclinic	triclinic	triclinic
Space group	*P*-1	*P*-1	*P*-1	*P*-1	*P*-1	*P*-1	*P*-1
Unit cell dimensions (Å, °)	*a* = 9.6392(5)	*a* = 9.6593(19)	*a* = 9.5678(5)	*a* = 9.5814(10)	*a* = 9.5801(4)	*a* = 9.645(2)	*a* = 9.5930(7)
	b = 14.8831(8)	*b* = 14.740(3)	*b* = 15.3835(8)	*b* = 15.3003(17)	*b* = 15.3589(6)	*b* = 15.248(4)	*b* = 15.2765(13)
	c = 15.3355(8)	*c* = 15.457(5)	*c* = 15.6500(7)	*c* = 15.3822(16)	*c* = 15.4666(6)	*c* = 15.742(4)	*c* = 15.3888(12)
	α = 61.569(2)	α = 109.442(9)	α = 114.6920(10)	α = 118.062(3)	α = 62.7320(10)	α = 117.169(3)	α = 62.252(3)
	β = 72.137(2)	β = 107.649(9)	β = 107.159(2)	β = 94.660(3)	β = 72.1580(10)	β = 105.715(3)	β = 72.124(3)
	γ = 77.103(2)	γ = 103.653(6)	γ = 93.499(2)	γ = 104.809(3)	γ = 87.8040(10)	γ = 93.321(3)	γ = 88.794(3)
Volume (Å^3)	1833.60(17)	1833.3(8)	1954.13(17)	1869.4(3)	1911.51(13)	1937.6(8)	1879.5(3)
Z	2	2	2	2	2	2	2
Calculated density (g cm^{-3})	1.429	1.313	1.325	1.155	1.406	1.646	1.366
Absorption coefficient (mm^{-1})	0.648	0.641	0.604	0.619	0.621	1.160	0.834
F_{000}	811	740	797	659	828	956	778
Crystal size (mm^3)	0.601 × 0.171 × 0.104	0.563 × 0.200 × 0.110	0.496 × 0.186 × 0.118	0.139 × 0.097 × 0.022	0.357 × 0.115 × 0.083	0.344 × 0.199 × 0.128	0.456 × 0.355 × 0.150
θ range for data collection (°)	2.229 to 26.427	2.237 to 25.260	2.253 to 26.417	2.263 to 25.257	2.250 to 26.439	1.536 to 26.466	2.254 to 26.436
Miller index ranges	-12 ≤ *h* ≤ 12, -18 ≤ *k* ≤ 18, -19 ≤ *l* ≤ 17	-11 ≤ *h* ≤ 11, -17 ≤ *k* ≤ 17, -18 ≤ *l* ≤ 18	-11 ≤ *h* ≤ 11, -19 ≤ *k* ≤ 18, -19 ≤ *l* ≤ 19	-11 ≤ *h* ≤ 11, -18 ≤ *k* ≤ 18, -18 ≤ *l* ≤ 17	-11 ≤ *h* ≤ 11, -19 ≤ *k* ≤ 19, -19 ≤ *l* ≤ 19	-12 ≤ *h* ≤ 12, -19 ≤ *k* ≤ 19, -19 ≤ *l* ≤ 19	-12 ≤ *h* ≤ 11, -19 ≤ *k* ≤ 19, -19 ≤ *l* ≤ 18
Reflections collected	33575	33815	35137	34202	36700	46198	27320
Independent reflections	7529 [R_{int} = 0.0352]	6559 [R_{int} = 0.0653]	7991 [R_{int} = 0.0355]	6739 [R_{int} = 0.0809]	7837 [R_{int} = 0.0332]	7944 [R_{int} = 0.0413]	7693 [R_{int} = 0.0277]
Completeness to θ_{max} (%)	0.998	0.984	0.997	0.994	0.998	0.996	0.996
Max. and min. transmission	0.839 and 1	0.716 and 1	0.859 and 1	0.83711 and 1	0.925 and 1	0.907 and 1	0.765 and 1
Refinement method	Full-matrix least-squares on F^2	Full-matrix least-squares on F^2	Full-matrix least-squares on F^2	Full-matrix least-squares on F^2	Full-matrix least-squares on F^2	Full-matrix least-squares on F^2	Full-matrix least-squares on F^2
Data / restraints / parameters	7529 / 1 / 513	6559 / 3 / 368	7991 / 139 / 573	6739 / 1 / 401	7837 / 121 / 706	7944 / 31 / 599	7693 / 0 / 416
Goodness-of-fit on F^2	1.053	1.077	1.157	1.040	1.092	1.141	1.008
Final *R* indices [$I > 2\sigma(I)$]	*R*1 = 0.0375, *wR*2 = 0.0810	*R*1 = 0.0839, *wR*2 = 0.2011	*R*1 = 0.0517, *wR*2 = 0.1352	*R*1 = 0.0575, *wR*2 = 0.1331	*R*1 = 0.0289, *wR*2 = 0.0614	*R*1 = 0.0336, *wR*2 = 0.0790	*R*1 = 0.0734, *wR*2 = 0.2046
R indices (all data)	*R*1 = 0.0433, *wR*2 = 0.0848	*R*1 = 0.1021, *wR*2 = 0.2142	*R*1 = 0.0567, *wR*2 = 0.1385	*R*1 = 0.0950, *wR*2 = 0.1489	*R*1 = 0.0338, *wR*2 = 0.0638	*R*1 = 0.0362, *wR*2 = 0.0804	*R*1 = 0.0786, *wR*2 = 0.2106
Largest diff. peak and hole (e Å^{-3})	1.488 and -0.554	2.279 and -1.343	1.179 and -0.995	0.652 and -0.647	0.432 and -0.438	0.730 and -0.559	8.036 and -2.007

Characterisation of CdPCP·DMA

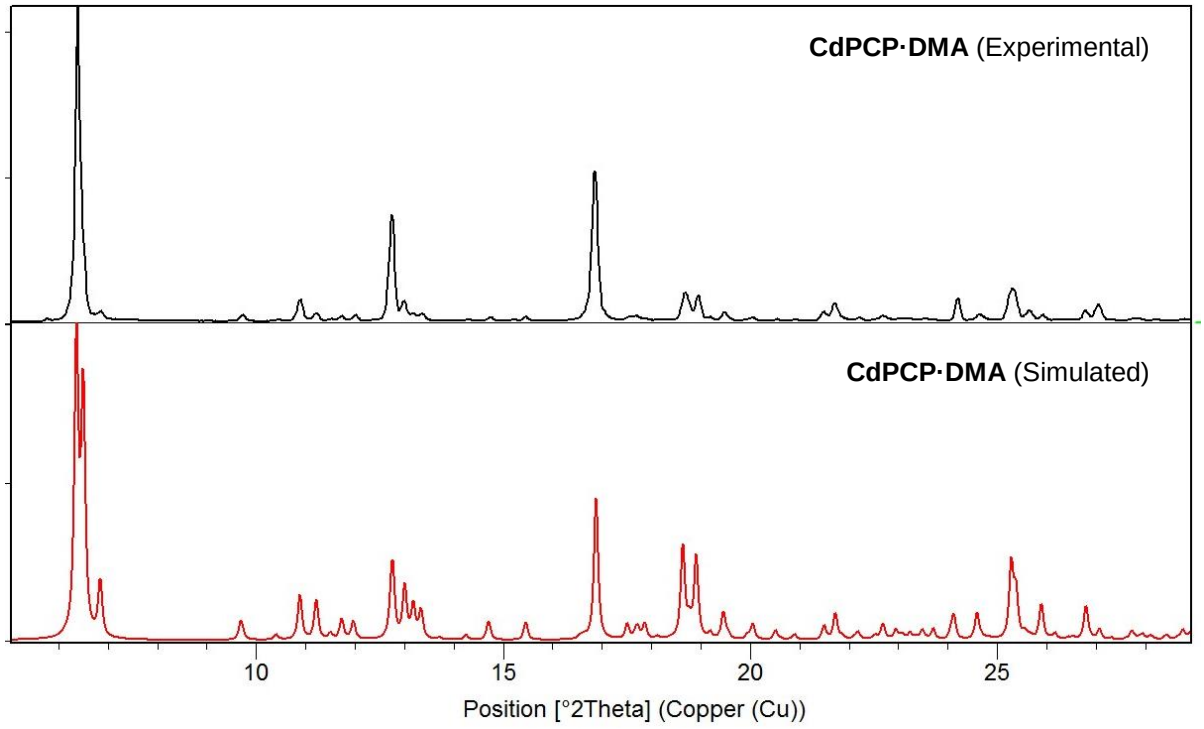

Figure S4 Comparison of the experimental powder pattern of **CdPCP·DMA** with the pattern simulated from the structure of **CdPCP·DMA** at 298 K.

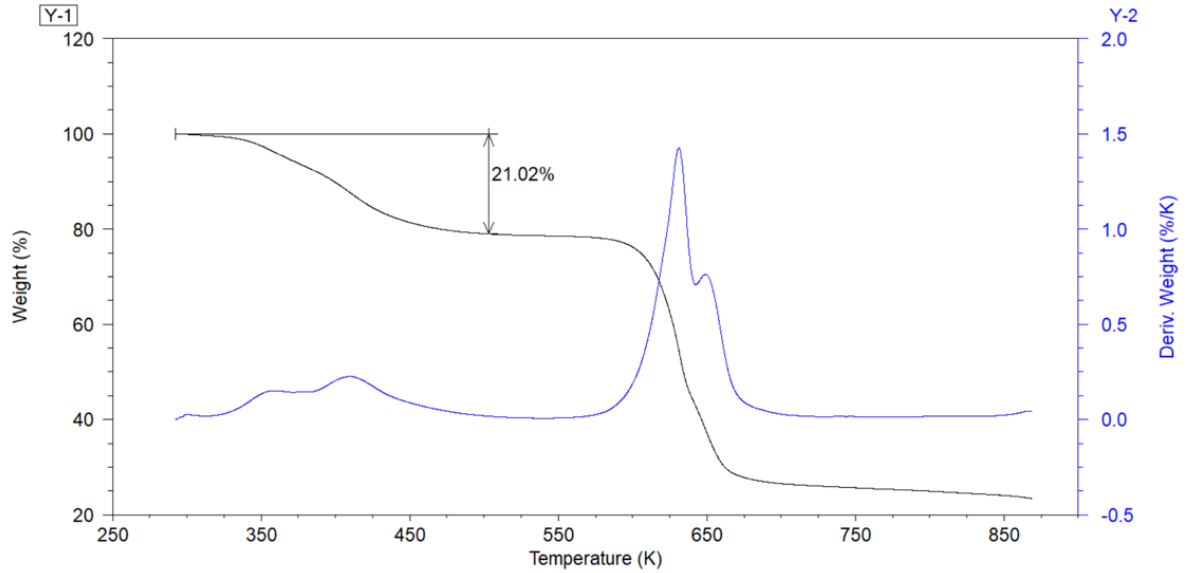

Figure S5 TGA thermogram of **CdPCP·DMA** showing 21.02% solvent loss. This compares well to the calculated value of 21.00% for 2 DMA molecules per cadmium ion.

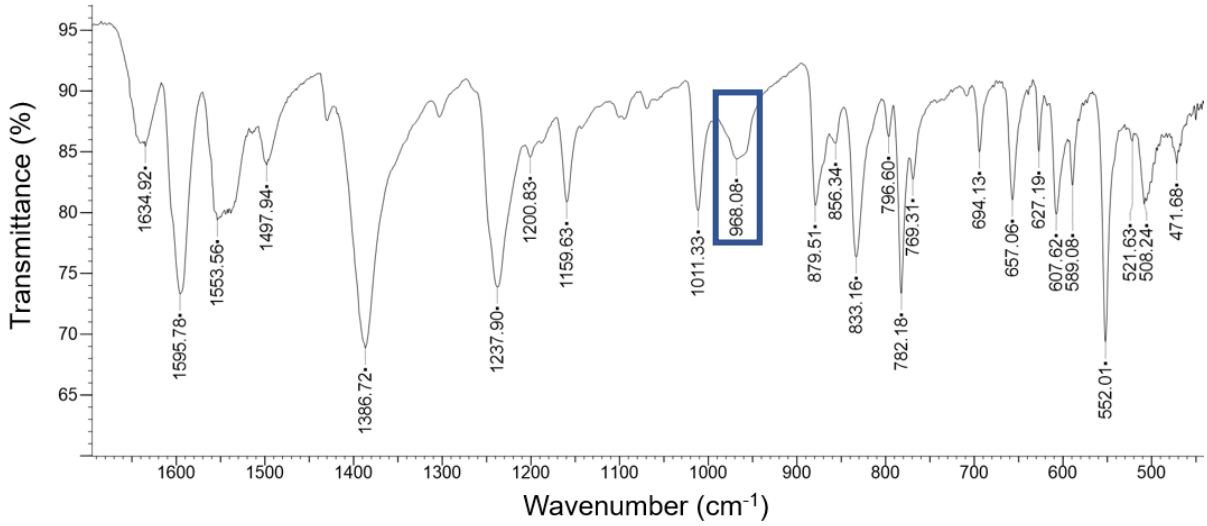

Figure S6 IR spectrum of **CdPCP·DMA.** The CH=CH stretch arising from the bpeb ligand can be seen at 968.08 cm^{-1}.

Characterisation of CdPCP·DMF

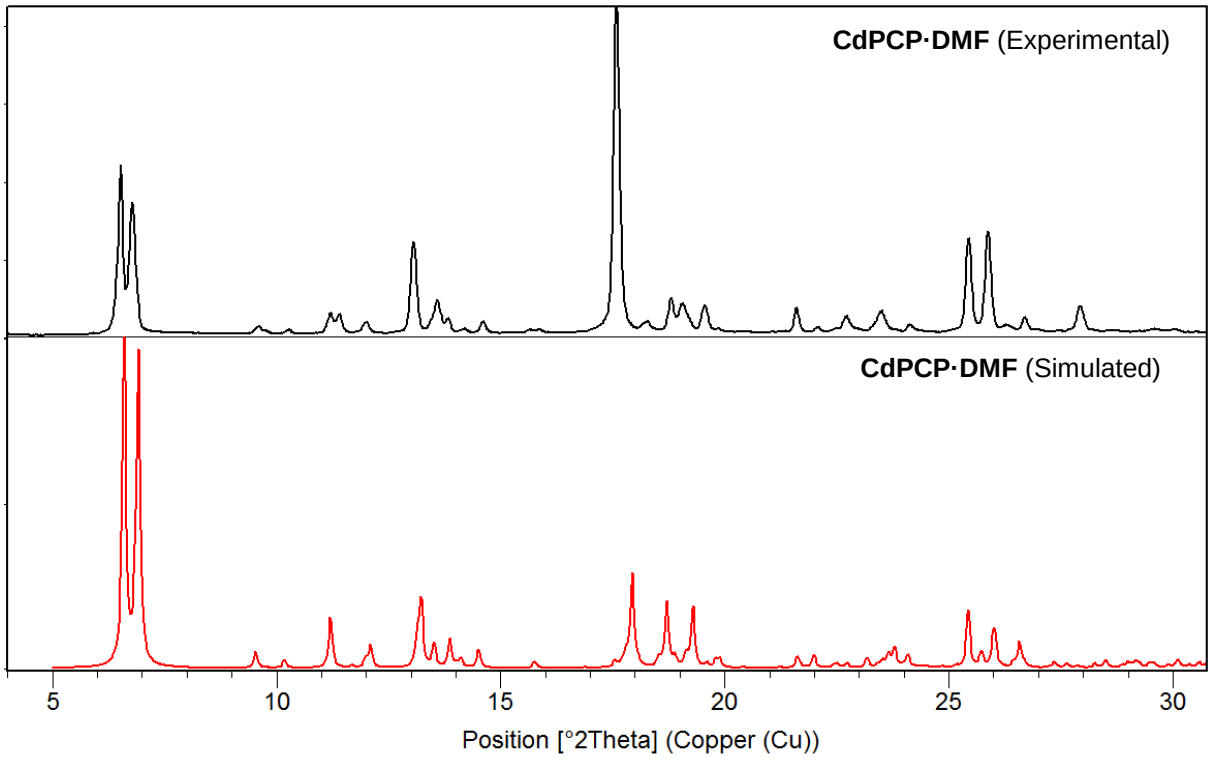

Figure S7 Comparison of the experimental powder pattern of **CdPCP·DMF** with the pattern simulated from the structure of **CdPCP·DMF** at 100 K

Comparison of CdPCP·DMA and CdPCP·DMF

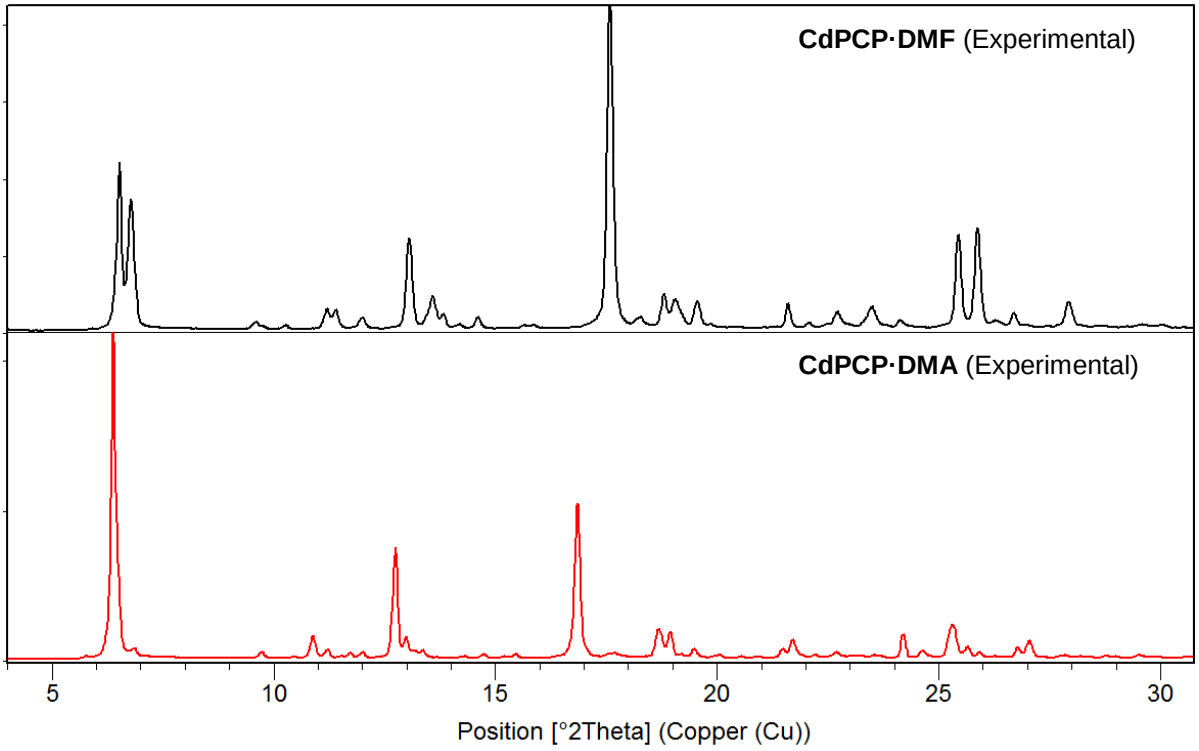

Figure S8. Comparison of the experimental powder pattern of **CdPCP·DMA** (298 K) with the experimental pattern of **CdPCP·DMF** (100 K)

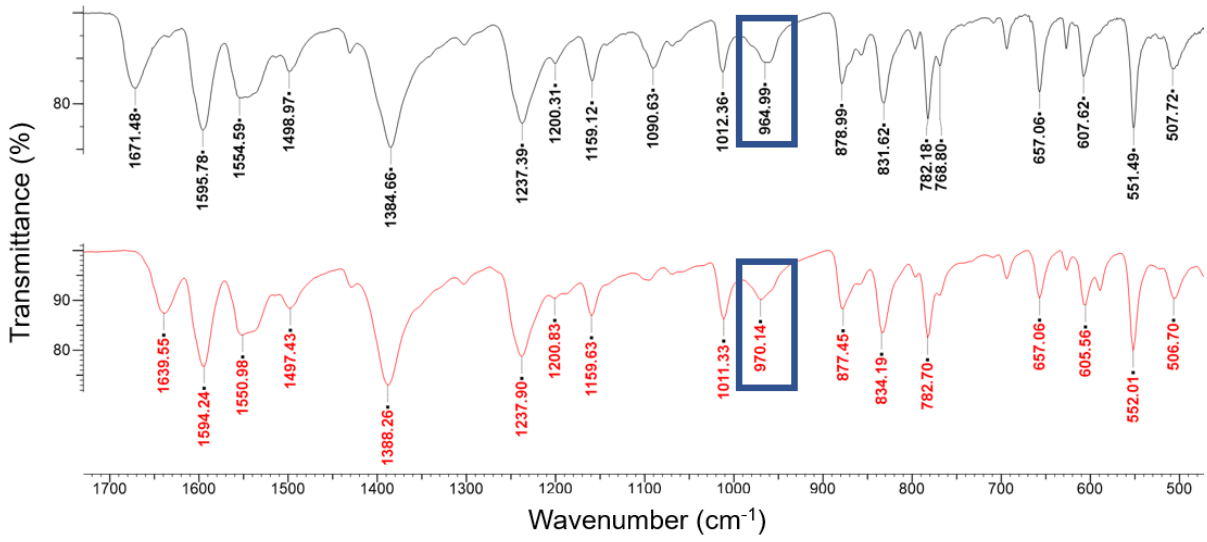

Figure S9. IR spectra of **CdPCP·DMA** (above, black) and **CdPCP·DMF** (below, red). The double bond stretches of the bpeb linker are indicated by the blue box.

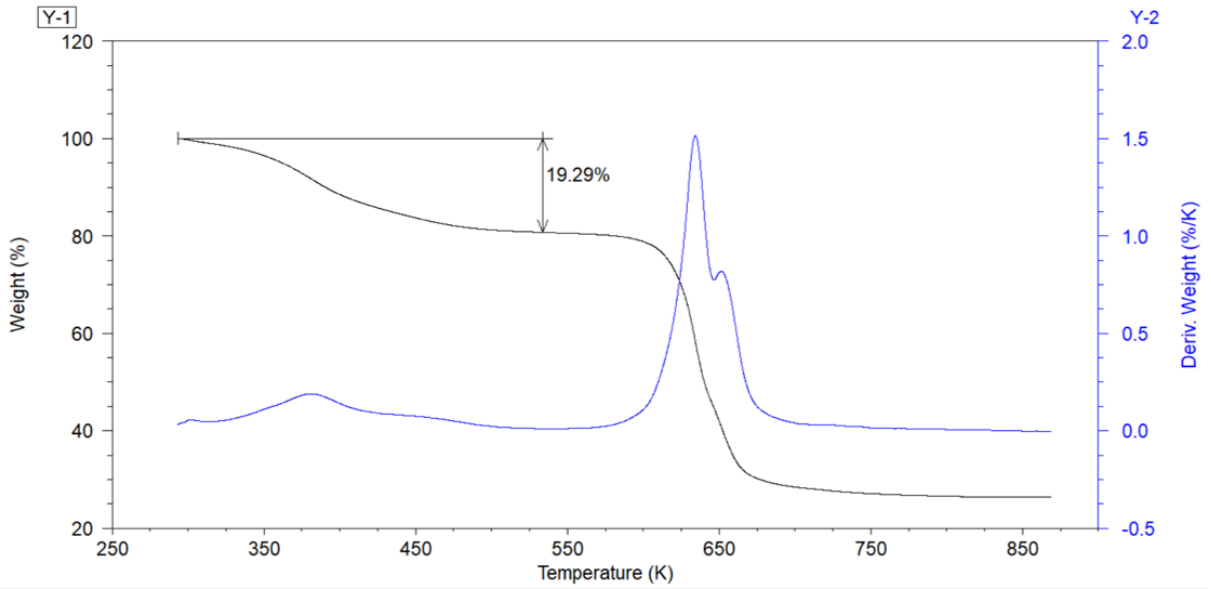

Figure S10. TGA thermogram of **CdPCP·DMF** showing 19.29% solvent loss. This compares well to the calculated value of 20.00% for 2 DMF molecules and one water molecule per cadmium ion.

CdPCP·DMA after irradiation and cycloaddition

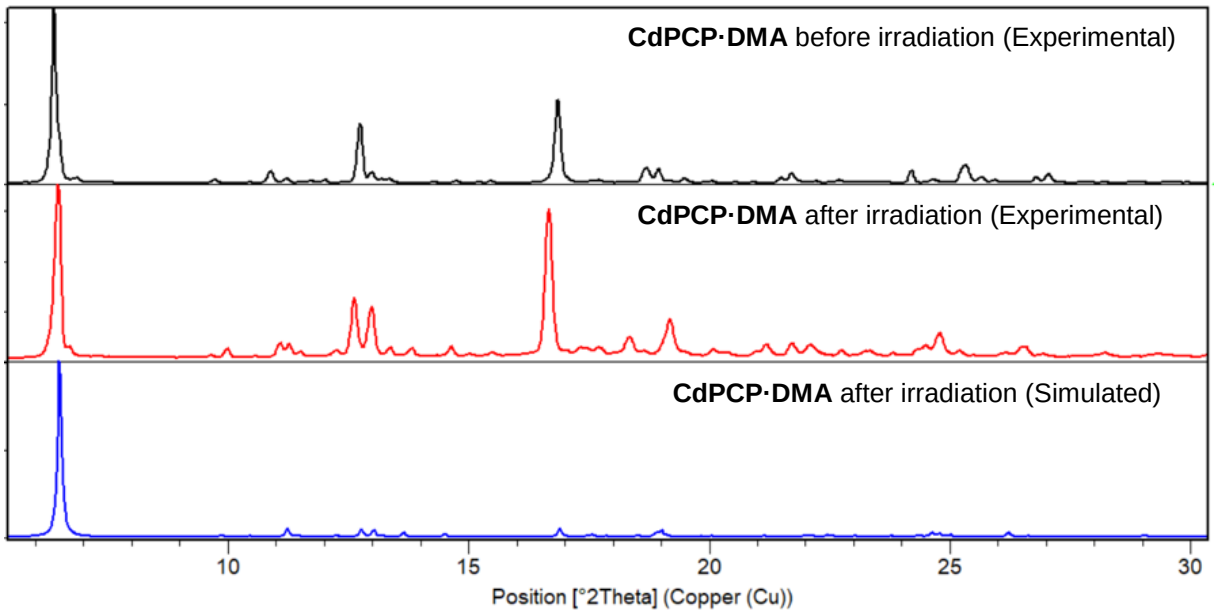

Figure S11. Comparison of the powder patterns of **CdPCP·DMA** before and after irradiation with the pattern simulated from a SCXRD structure of **CdPCP·DMA** with a 50% conversion to the cyclised form. See Figure S12 for comparison of the same patterns for 2θ above 10 ^{0} .

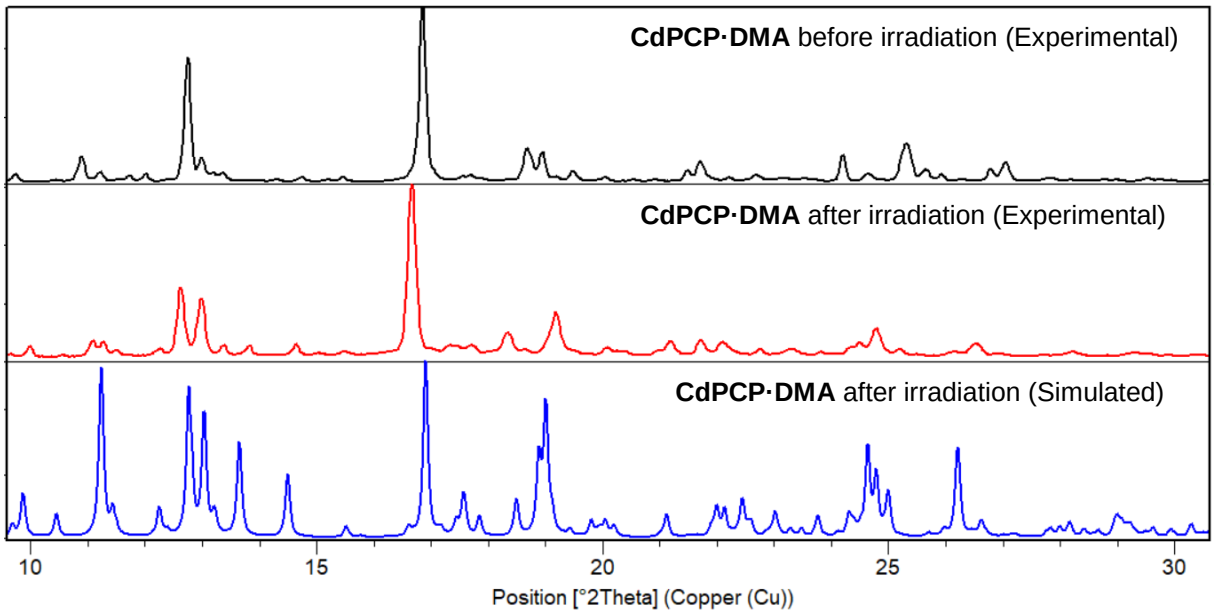

Figure S12. Comparison of the powder patterns of **CdPCP·DMA** before and after irradiation and a pattern simulated from a SCXRD structure of **CdPCP·DMA** with a 50% conversion to the cyclised form with peaks before 10 ° 2θ omitted.

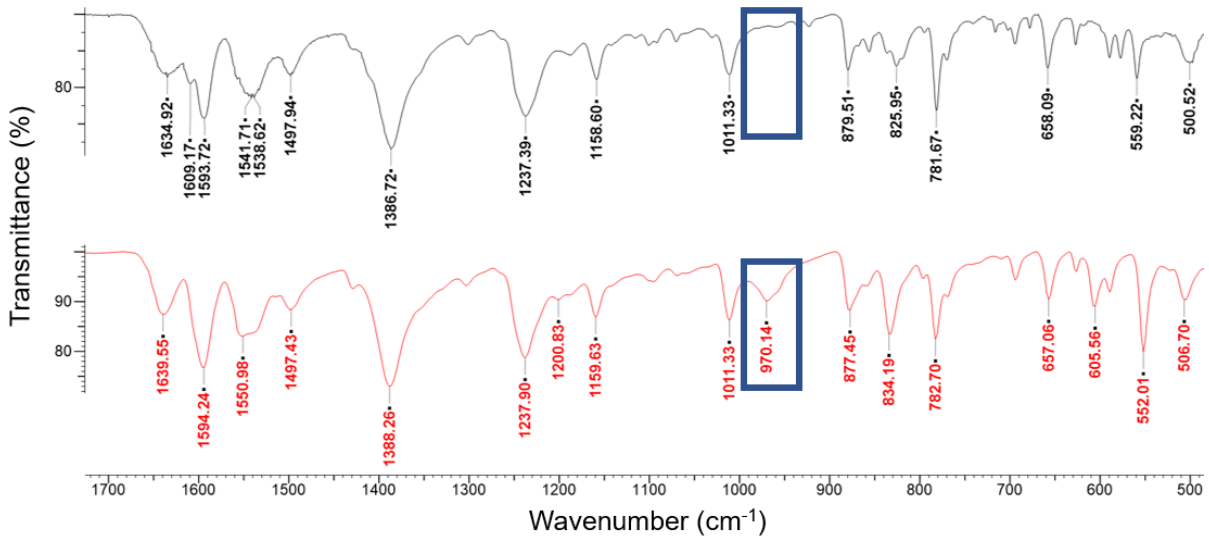

Figure S13. IR spectra of **CdPCP·DMA** after irradiation (above, black) and **CdPCP·DMA** before irradiation (below, red). After irradiation the double bond stretches disappear, as indicated by the blue box.

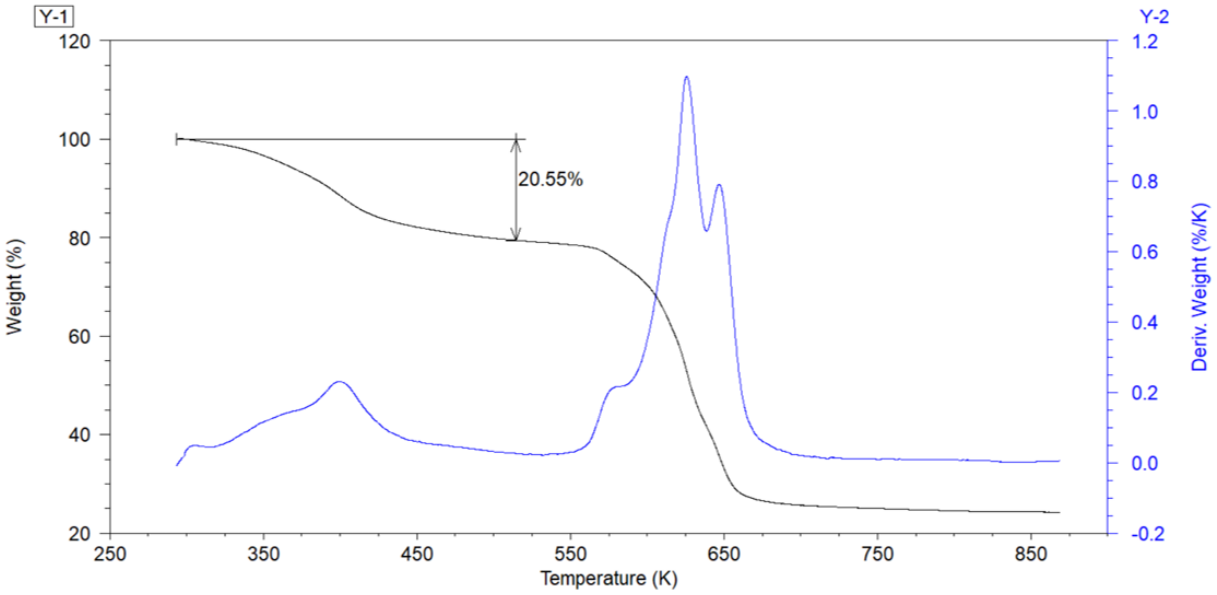

Figure S14. TGA thermogram of **CdPCP·DMA** after irradiation showing 20.55% solvent loss. This compares well to the calculated value of 21.00% for 2 DMA molecules per cadmium ion, clearly showing that there is no solvent loss on irradiation.

Digestion of CdPCP·DMA and isolation of Isomer 1

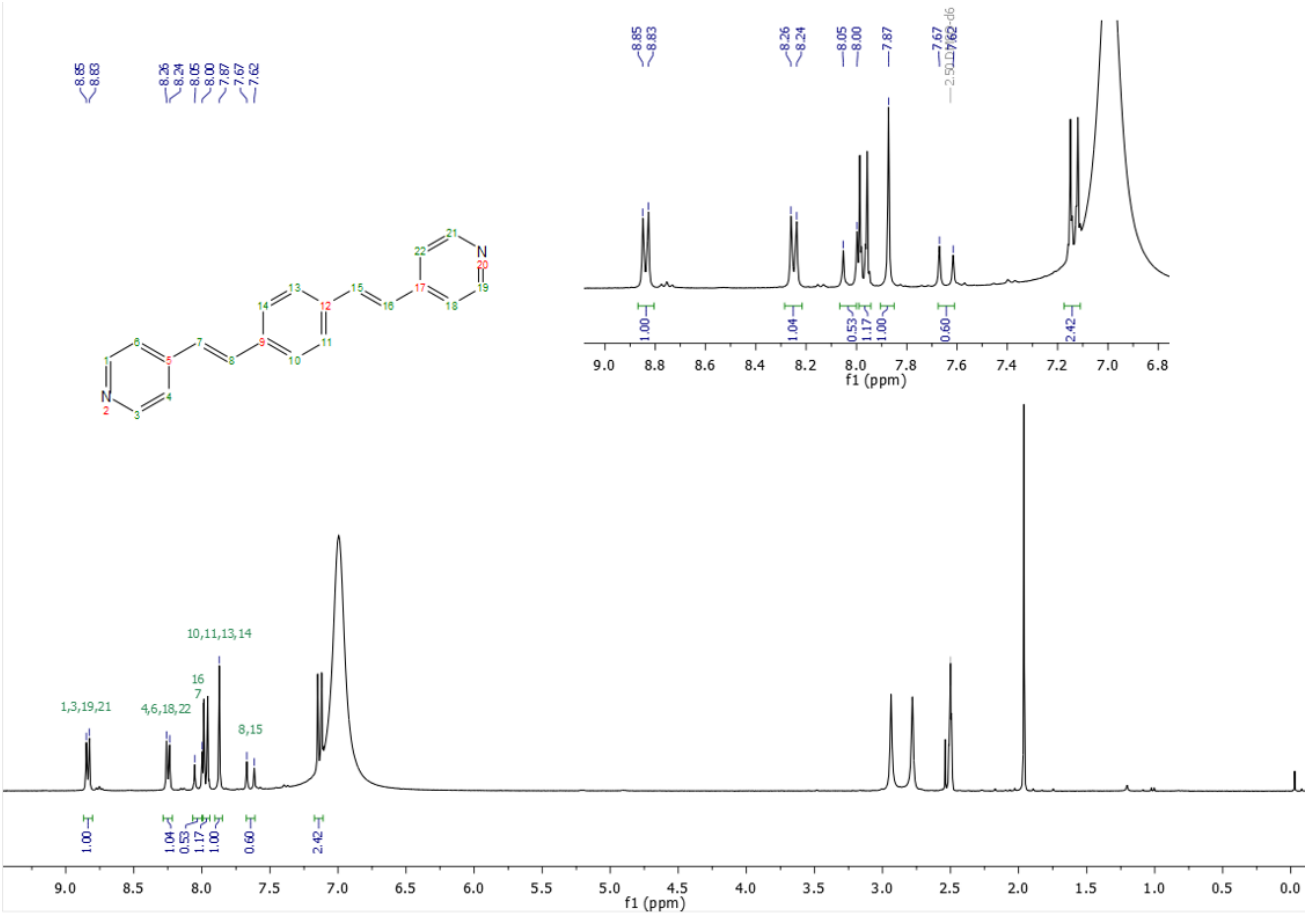

Figure S15. ^{1}H NMR of resulting mixture after digestion of **CdPCP·DMA** using a drop of deuterated sulphuric acid. Peaks for the bpeb linker are clearly visible.

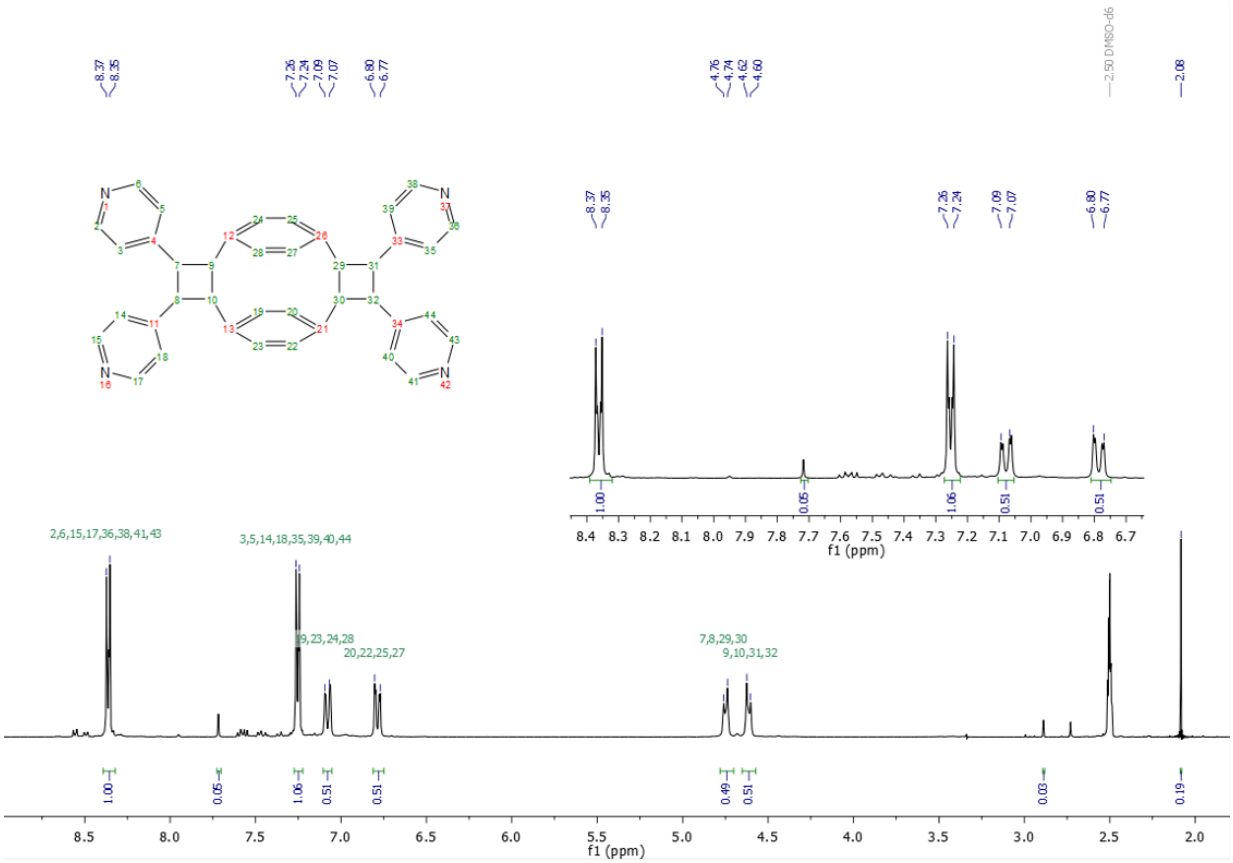

Figure S16. ^{1}H NMR of **Isomer 1** after extraction from the irradiated **CdPCP·DMA**.

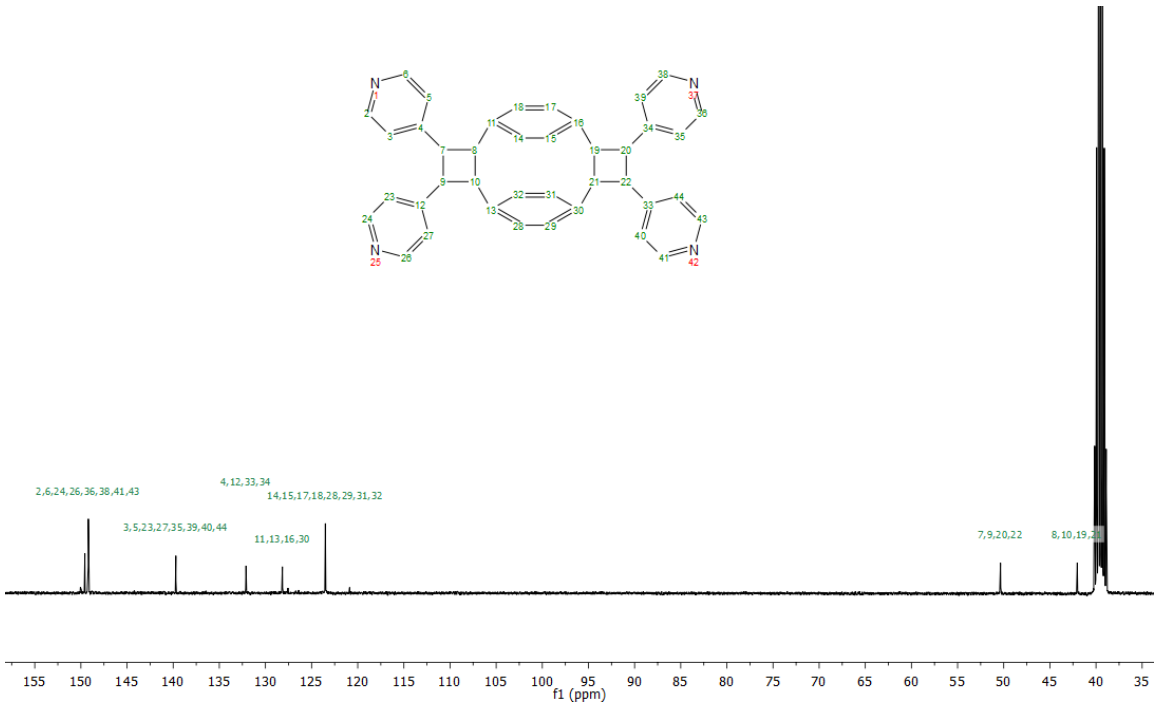

Figure S17. ^{13}C NMR of **Isomer 1** after extraction from irradiated **CdPCP·DMA**.

Characterisation of CdPCP·DMF after irradiation

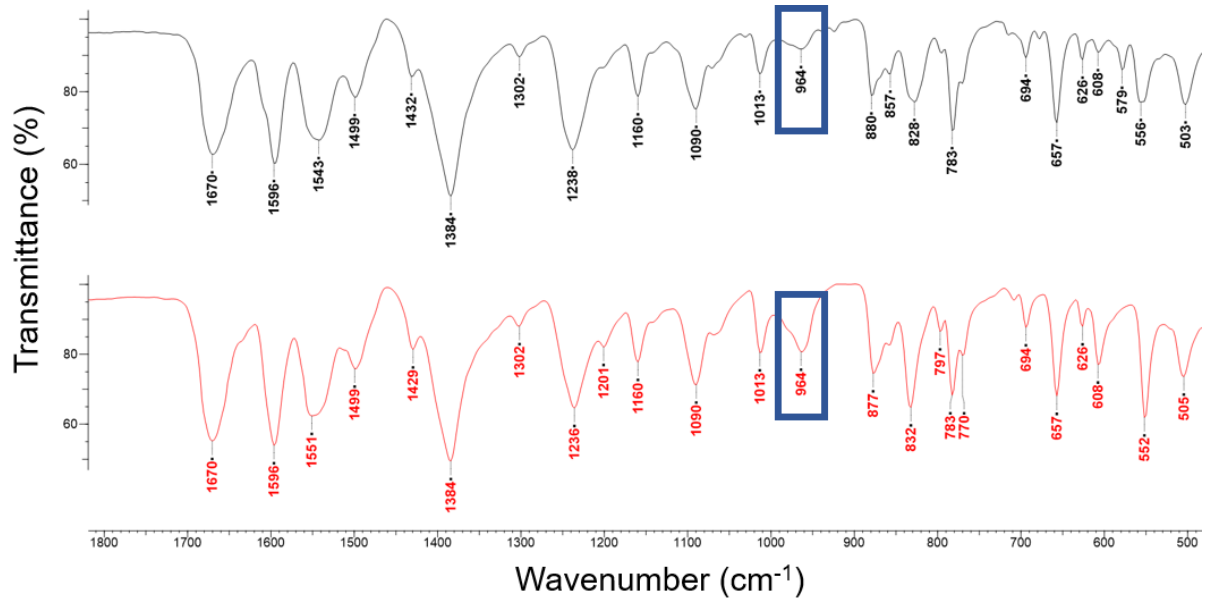

Figure S18. IR spectra of **CdPCP·DMF** before irradiation (above, black) and after irradiation (below, red). After irradiation there is a reduction in the peak at 964 cm^{-1} corresponding to the olefinic C=C bonds in the bpeb ligand, as indicated by the blue box.

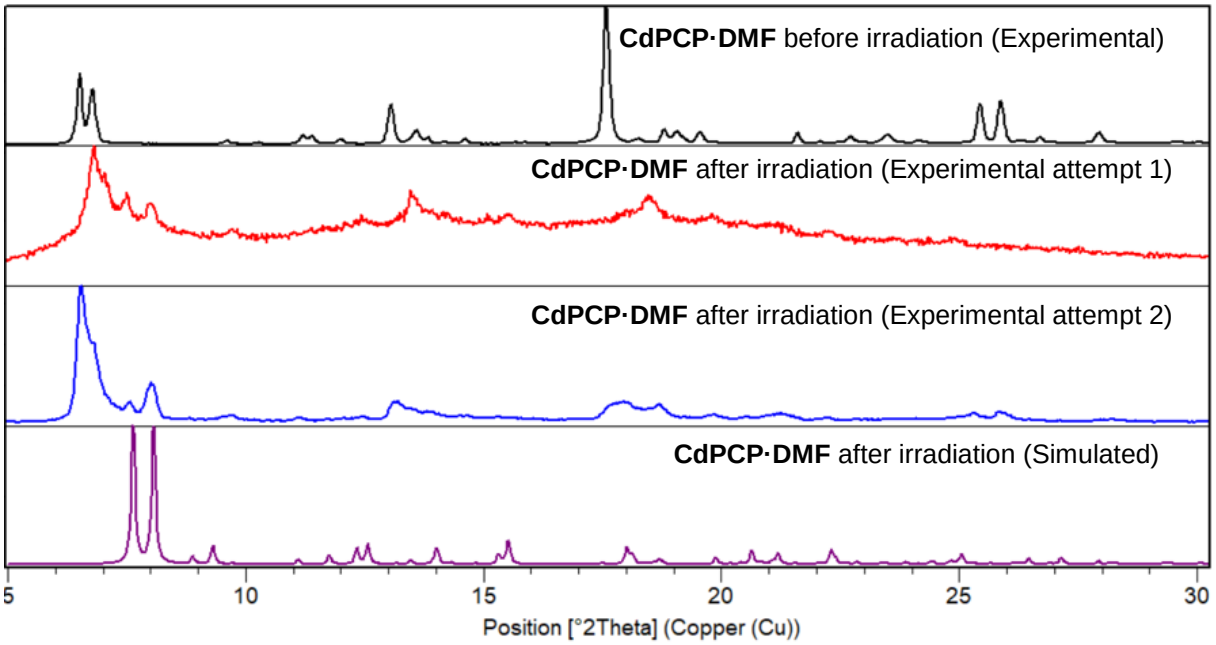

FigureS19. Powder diffractograms of bulk samples of **CdPCP·DMF** before and after irradiation, and the pattern simulated from the SCXRD structure of the fully cyclised form.

Although SCXRD experiments were carried out several times on the irradiated **CdPCP·DMF**, PXRD shows that the material loses crystallinity after prolonged irradiation. The above patterns only display partial conversion to the cyclized form. SCXRD analysis of the cyclized form was successful as the irradiation time of a single crystal is much shorter than a powdered bulk sample.

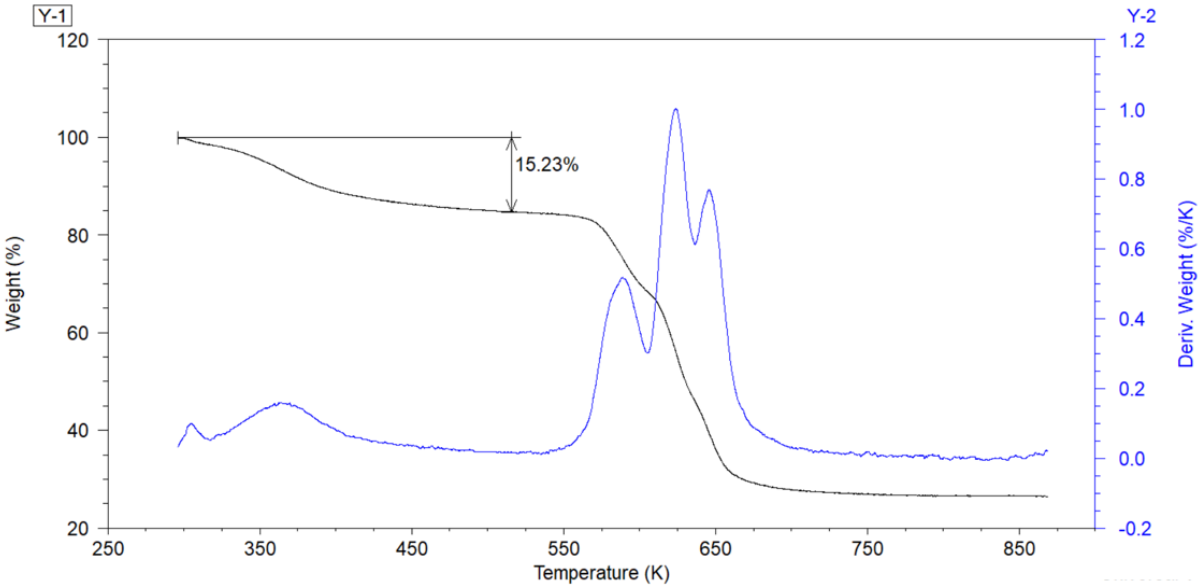

Figure S20. TGA thermogram of **CdPCP·DMF** after irradiation showing 15.23% solvent loss. This indicates a loss of approximately 5% of the solvent during the irradiation process. The degree of solvent loss varies with each experiment.

Digestion of CdPCP·DMF and isolation of isomer 2

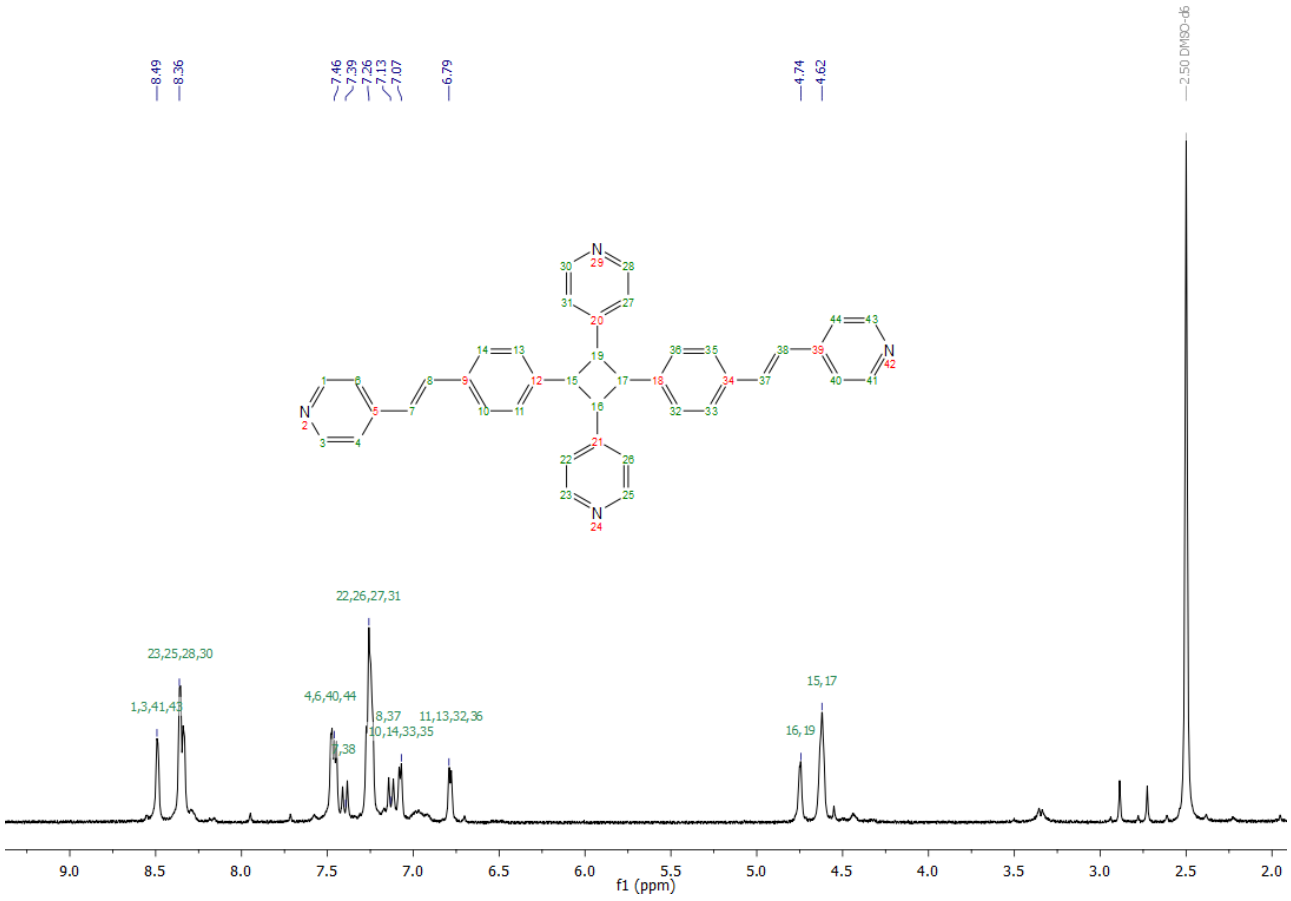

Figure S21. ^{1}H NMR of isomer 1 after extraction from the irradiated **CdPCP·DMF.** Integration of signal peaks was not performed due to the uneven nature of the baseline, which is due to the small sample size. The two signals between 2.7 and 3.0 ppm correspond to residual DMF.

Solvent exchange experiments

Solvent-exhange experiments were carried out on **CdPCP·DMA** with the following solvents:

dimethylformamide, tetrahydrofuran, toluene, benzene, 1,4-dioxane, chloroform, carbon tetrachloride.

SCXRD structures after UV-irradiation could only be obtained for DMF, THF, toluene and 1,4-dioxane.

Photographs of the crystals after exchange are shown below.

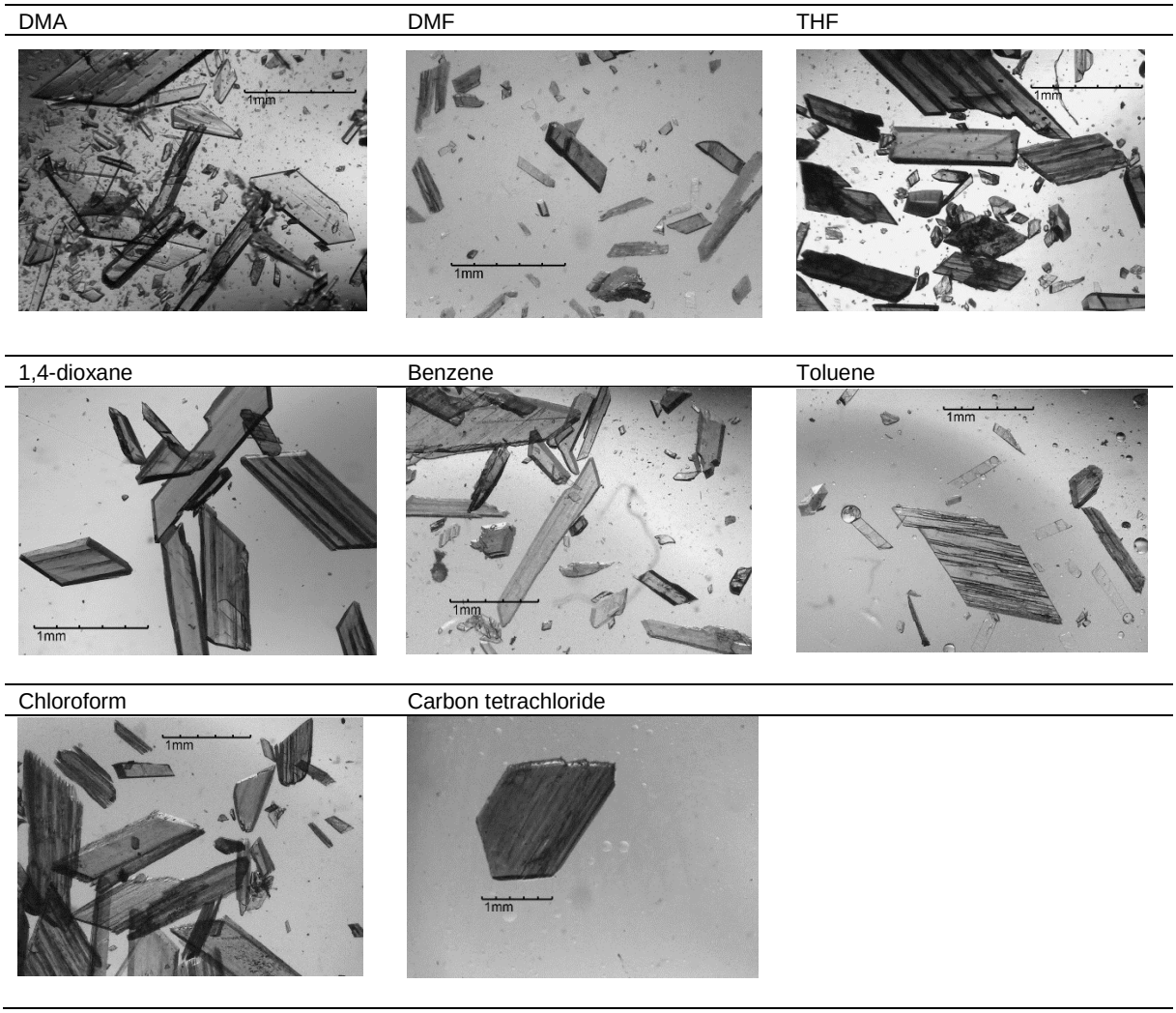

Figure S22. Photographs of crystals obtained after exchange of DMA in **CdPCP·DMA** with various solvents.

References

[1] T. Degen, M. Sadki, E. Bron, U. König, G. Nénert, *Powder Diffr*. **2014**, *29*, S13.
[2] C. F. Macrae, I. J. Bruno, J. A. Chisholm, P. R. Edgington, P. McCabe, E. Pidcock, L. Rodriguez-Monge, R. Taylor, J. van de Streek, P. A. Wood, *J. Appl. Crystallogr*. **2008**, *41*, 466.
[3] Bruker (2012). SAINT. Bruker AXS Inc., Madison, Wisconsin, USA.
[4] Bruker (2001). SADABS. Bruker AXS Inc., Madison, Wisconsin, USA.
[5] L. J. Barbour, *J. Supramol. Chem.* **2001**, *1*, 189.
[6] J. Atwood, L. J. Barbour, *Cryst. Growth Des.* **2003**, *3*, 3.
[7] G. M. Sheldrick, *Acta Crystallogr. Sect. A* **2008**, *64*, 112.
[8] G. M. Sheldrick, *Acta Crystallogr. Sect. A* **2015**, *71*, 3.
[9] A. L. Spek, *Acta Crystallogr. Sect. D* **2009**, *65*, 148.
[10] A. L. Spek, *Acta Crystallogr. Sect. C* **2015**, *71*, 9.
[11] Persistence of Vision Pty. Ltd. (2004). POV-Ray. Persistence of Vision Pty. Ltd., Williamstown, Victoria, Australia.
[12] O. V. Dolomanov, L. J. Bourhis, R. J. Gildea, J. A. K. Howard, H. Puschmann, *J. Appl. Crystallogr.* **2009**, *42*, 339.
[13] V. A. Blatov, A. P. Shevchenko, D. M. Proserpio, *Cryst. Growth Des.* **2014**, *14*, 3576.
[14] P. K. Bhowmik, A. K. Nedeltchev, H. Han, *Tetrahedron Lett.* **2007**, *48*, 5383.

Chapter 3

A Multi-Stimulus Responsive Porous Coordination Polymer: Temperature-Mediated Control of Solid-state [2+2] Cycloaddition

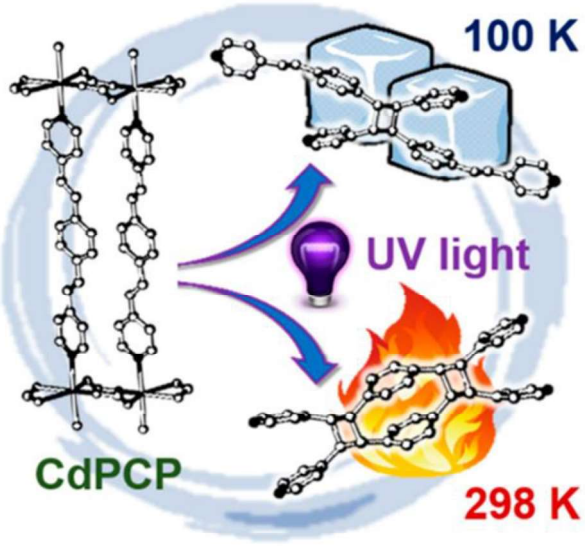

3.1 Communication in the Journal of the American Chemical Society

The framework was first reported in the previous publication (Chapter 2). The author is responsible for all further contributions, including:

- Design of project
- Synthesis of ligand and MOF
- Collection of variable-temperature single-crystal X-ray data, solution and refinement of single-crystal X-ray structures
- Collection and analysis of powder X-ray data, IR spectra and DSC thermograms, hot-stage DSC microscopy
- Design and execution of ambient and low temperature UV irradiation experiments
- Interpretation of results
- Writing the first draft of the article

JACS JOURNAL OF THE AMERICAN CHEMICAL SOCIETY
Cite This: J. Am. Chem. Soc. 2019, 141, 11425−11429
Communication
pubs.acs.org/JACS

A Multistimulus Responsive Porous Coordination Polymer: Temperature-Mediated Control of Solid-State [2+2] Cycloaddition

Isabella E. Claassens, Leonard J. Barbour,* and Delia A. Haynes*

Department of Chemistry and Polymer Science, Stellenbosch University, P. Bag X1, Matieland, 7602 Stellenbosch, South Africa

Supporting Information

ABSTRACT: Either of two different isomeric products can be selectively obtained by photochemical [2+2] cycloaddition of 1,4-bis[2-(4-pyridyl)ethenyl]-benzene within a porous coordination polymer (PCP). The cycloaddition product obtained depends on the temperature at which irradiation occurs. A rare temperature-induced phase transition alters the conformation of the photoactive ligand in the PCP, and thereby the positions at which cycloaddition occurs. We show that the multistimulus responsive nature of this particular PCP is due to the flexibility of the ligands employed.

Over the past 20 years porous coordination polymers (PCPs) have emerged as an exciting new class of diverse functional materials, often exhibiting extremely high porosity and very large surface areas.[1] These polymeric network structures are constructed through modular design from established bonding motifs.[1,2] Their pore size, shape and chemical functionality can be tailored, thus leading to possible applications in areas such gas storage and separation, enantioselective separations, heterogeneous catalysis, chemical sensing and drug delivery.[2,3] In recent years there has been an emerging focus on flexibility in PCPs, and particularly on stimulus-responsive framework materials.[4,5] Stimuli that induce dynamic transformations can be of a physical or chemical nature, for example guest removal or exchange, gas pressure, mechanical force, irradiation or temperature.[6−14] Although numerous PCPs show heat-induced structural transitions where the transition is driven by guest removal, only very few exhibit solely temperature-induced crystal-to-crystal phase transitions.[4,5,15] Here we describe a multistimulus responsive PCP that responds to temperature, as well as solvent exchange and light.

Photochemical [2+2] cycloaddition reactions in PCPs have generated much interest as a means to synthesize regio- or stereoselective products that are generally low yielding or impossible to obtain in solution.[16] Solid-state [2+2] cycloaddition reactions are governed by several topochemical postulates, which state that the reacting carbon−carbon double bonds must be separated by no more than 4.2 Å, and must be aligned parallel to one another.[17] Control of the packing of olefinic molecules in the solid state to meet these topochemical requirements remains a challenge. MacGillivray and coworkers demonstrated the use of template molecules to be especially effective in controlling [2+2] cycloaddition reactions in the solid state.[18−20] Metal−organic frameworks (MOFs), a subclass of PCPs, have also proven to be prime candidates for the alignment of olefinic molecules as a result of their flexible yet predictable geometries.[21−29] Favorable properties such as increased gas selectivity, fluorescence-switching and nitro-sensing have been observed in PCPs that have undergone [2+2] cycloaddition.[30−35]

The ligand 1,4-bis[2-(4-pyridyl)ethenyl]-benzene (bpeb, Figure 1 top) has two olefinic bonds and therefore features prominently in the synthesis of photoactive PCPs.[36] Two bpeb ligands can be aligned either out-of-phase or in-phase, resulting in the formation of one or two cyclobutane rings on cycloaddition, respectively (Figure 1 bottom).[24] This allows for the selective synthesis of one of two possible isomeric products, depending on ligand alignment. We previously demonstrated the selective synthesis of either **Isomer 1** or **Isomer 2** in the same PCP.[37] This was achieved by a single-crystal to single-crystal exchange of the guest, which changed the conformation of the bpeb ligands and altered the position of cycloaddition. Herein we demonstrate the selective synthesis of both isomers in this same PCP, **CdPCP**, by carrying out the cycloaddition reaction at different temperatures. Changing the

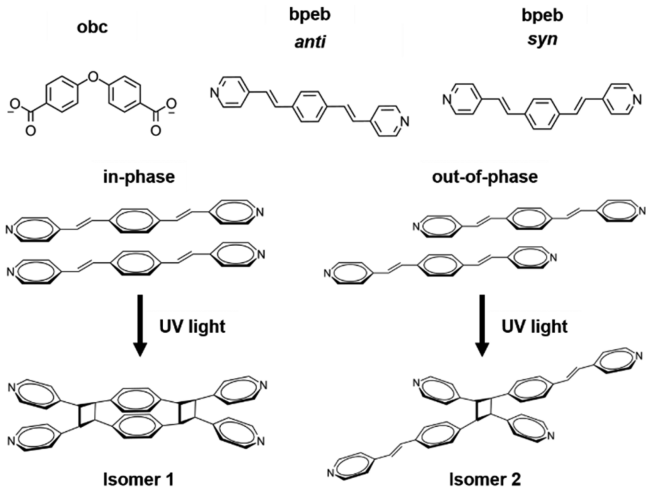

Figure 1. (top) Schematic diagrams of 1,4-bis[2-(4-pyridyl)ethenyl]-benzene (bpeb) and 4,4′-oxybis(benzoic acid) (obc); (bottom) in-phase and out-of-phase alignment of bpeb ligands, resulting in the formation of **Isomer 1** (left) and **Isomer 2** (right) during irradiation with UV light.

Received: June 4, 2019
Published: July 16, 2019

DOI: 10.1021/jacs.9b05961
J. Am. Chem. Soc. 2019, 141, 11425−11429

temperature results in a rare temperature-induced phase transition without loss of guest solvent, which alters the ligand conformation in the crystalline PCP. We thus demonstrate the multistimulus responsive nature of **CdPCP**.

Large pale-yellow rhomboid crystals of **CdPCP-P1** ([Cd(bpeb)(obc)]·2DMA) were synthesized according to the published procedure.[37] As previously reported, single-crystal X-ray diffraction (SCXRD) analysis reveals that **CdPCP-P1** crystallizes in the triclinic space group $P\bar{1}$. The asymmetric unit (ASU) consists of a cadmium ion coordinated to one bpeb ligand in the *trans-anti-trans* (*anti*) conformation and one 4,4′-oxybisbenzoate (obc) ligand. Two dimethylacetamide (DMA) solvent molecules per ASU are included within the one-dimensional channels that propagate along [100]. The framework is two-dimensional, with interdigitated sheets stacked in a slipped manner, and has **3,5L2** and **sql** topology in standard and cluster representations, respectively (Figure 2a).[38] Each cadmium ion is coordinated to four oxygen and two nitrogen atoms in a distorted octahedral geometry. The secondary building unit (SBU) consists of two cadmium ions bridged by two obc ligands. Each of the metal ions then further coordinates to an obc ligand in a bidentate fashion, and each SBU is connected to two neighboring SBUs by means of two obc ligands to form chains that propagate along [010]. The SBUs are also linked by bpeb ligands coordinated to the cadmium ions in the two axial positions to form chains along [10-1], thus producing a double-pillar layered structure (Figure 2b). The geometry of the SBU results in in-phase alignment of two adjacent bpeb ligands within layers at a distance that is at the proposed limit for photochemical [2+2] cycloaddition. Owing to slipped stacking of interdigitated layers, the bpeb ligands of adjacent layers are aligned out-of-phase at a distance just longer than the limit (Figure 2a).

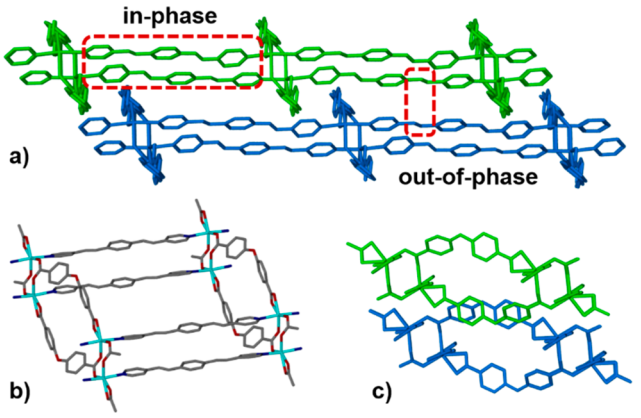

Figure 2. (a) Two-dimensional interdigitated layers in **CdPCP-P1** stacked in a slipped fashion. Adjacent layers are colored green and blue. Positions where in-phase or out-of-phase cycloaddition could potentially occur are highlighted. (b) Double-pillar layered structure in **CdPCP-P1** with four SBUs shown. Repeating units form the 2D sheets. (c) Interdigitated layers of **CdPCP-P1** viewed along [10-1]. The image is rotated by 90° with respect to that in panel a such that the view is along the bpeb molecules. Solvent molecules and hydrogen atoms have been omitted for clarity.

We previously showed[37] that irradiation of **CdPCP-P1** with a 365 nm UV light-emitting diode at 298 K results in cycloaddition taking place exclusively between the two double bond pairs within a 2D layer, resulting in the formation of **Isomer 1** (Figure 3a). Near-quantitative conversion was confirmed with infrared and nuclear magnetic resonance analysis of the digested framework after prolonged irradiation.[37]

During SCXRD analysis of **CdPCP-P1**, we noted a doubling of the crystallographic *a* axis on cooling from 298 to 100 K. The consistent observation of this phenomenon made it clear that **CdPCP-P1** undergoes a reversible temperature-induced structural transition to yield **CdPCP-P2**. Comparison of the crystal structures reveals that all of the bpeb ligands of **CdPCP-P1** are in the *anti* conformation whereas they alternate between the *anti* and *trans-syn-trans* (*syn*) conformation along a chain in **CdPCP-P2** (Figure 4). Aside from the conformation of the ligand, the space group remains unchanged and the structures of the two phases are very similar (Figures S3 and S4).

Conversion of bulk material from **CdPCP-P1** to **CdPCP-P2** was confirmed using variable-temperature powder X-ray diffraction (PXRD) analysis; the diffractograms at 298 and 100 K closely match those simulated from the SCXRD structures determined at 298 and 100 K, respectively (Figure S25). The temperature was cycled between 298 and 100 K several times for both powdered samples and single crystals, and it was confirmed that the structural change is reversible in both cases (see Table S2 and Figures S11, S26−S28).

Although there is a clear distinction between the structures of **CdPCP-P1** at 298 K and **CdPCP-P2** at 100 K, determining the precise transition temperature proved challenging. Variable-temperature unit cell determination for a single crystal showed that there is a 10−15 K range on both cooling and heating where domains of both **CdPCP-P1** and **CdPCP-P2** are present (reflections can be separated into two groups, each of which can be indexed to yield one of the two unit cells; see SI for further details, Figures S5−S10). The occurrence of a biphasic crystal, where domains corresponding to both phases are observed, is not merely due to inadequate equilibration time allowed for the transition. Exposure of several single crystals to a temperature within the transition range for 6−8 h gave the same result. It has recently been reported that flash cooling kinetically traps a particular phase of an organic cocrystal containing olefinic bonds by "freezing out" the pedal motion of the moeity.[39] Both flash cooling and slow cooling experiments were carried out on **CdPCP-P1**, but the same results were obtained in both cases. Experiments at various temperatures also confirmed that **CdPCP-P2** is not a disordered phase of **CdPCP-P1**; the fraction of each conformation remains constant at 50% as the temperature is changed, and the change in conformation (resulting in halving or doubling of the crystallographic *a* axis) is an abrupt rather than a gradual change. It would also be surprising to see an increase in pedal motion on decreasing the temperature. It is clear that **P1**and **P2** are distinct phases, or polymorphs, of **CdPCP**.

The structural transition was further investigated using differential scanning calorimetry (DSC; details in the SI), which showed that both thermal cycling and aging of samples resulted in the phase transition occurring at lower temperatures. It has been suggested that an increase in crystal defects may result in phase transitions occurring at lower temperatures.[40] This is consistent with our DSC analysis of **CdPCP**, which also shows that ground samples produce smoother peak profiles and often have a lower onset temperature for the transition on both heating and cooling. Hot-stage DSC analysis revealed that **CdPCP** is thermosalient. Upon cooling from 298

DOI: 10.1021/jacs.9b05961
J. Am. Chem. Soc. 2019, 141, 11425−11429

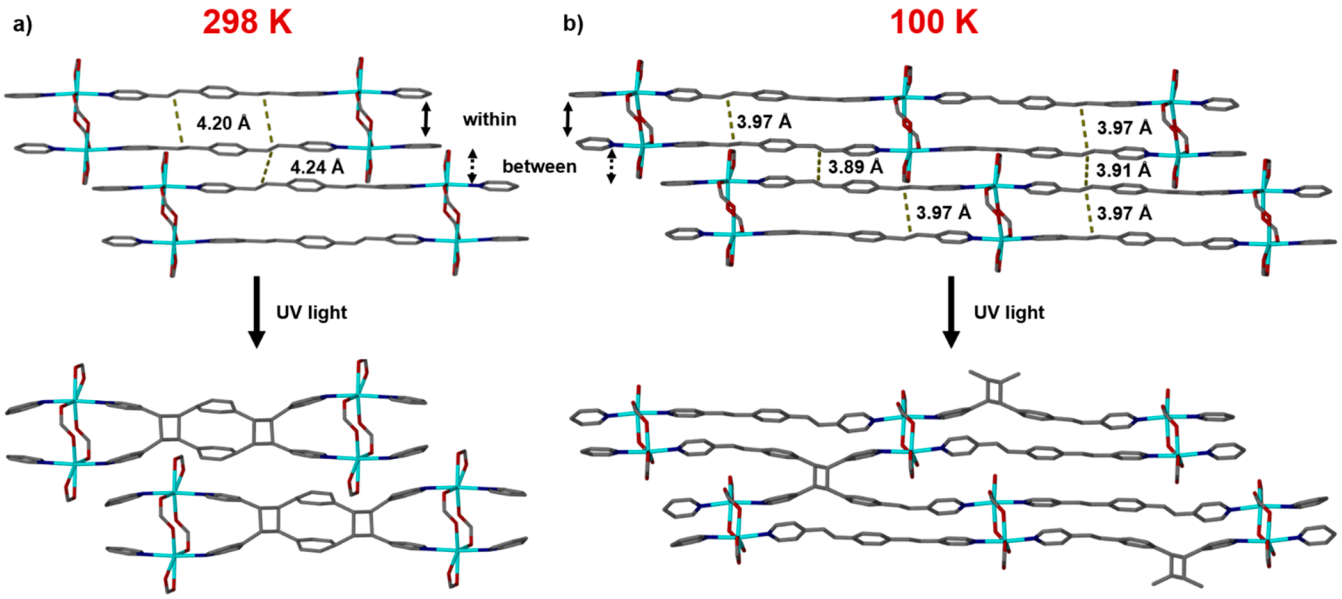

Figure 3. (a) Potentially photoactive positions in **CdPCP-P1** (top) and the structure of **CdPCP-P1** after irradiation at 298 K (bottom). (b) Potentially photoactive positions in **CdPCP-2** (top) and the structure of **CdPCP-2** after irradiation at 100 K (bottom). Hydrogen atoms and solvent molecules are omitted for clarity.

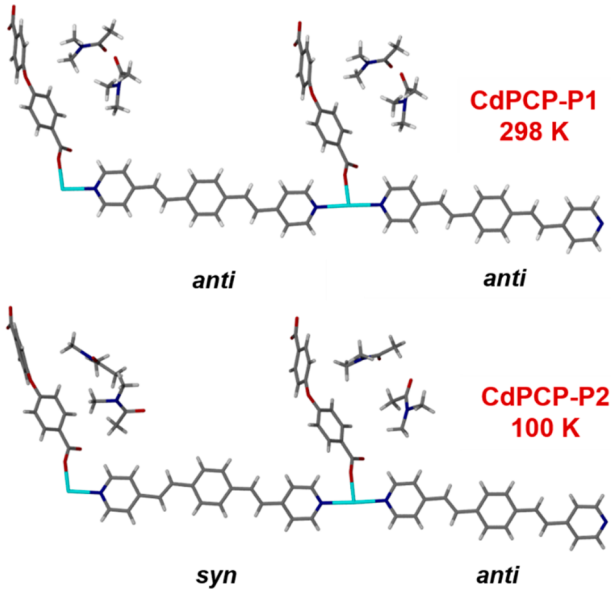

Figure 4. Comparison of the conformation of the bpeb linker in **CdPCP-P1** (top) and **CdPCP-P2** (bottom). Two ASUs of **CdPCP-P1** are displayed to facilitate comparison to the ASU of **CdPCP-P2**.

to 100 K, single crystals moved significantly in the temperature range where the phase transition takes place (see supplementary videos). Soon after the phase transition, several crystals jumped; this thermosalient behavior appears to be highly size-dependent with only the smallest crystallites undergoing the popping motion. This is not unusual, and several reports suggest a link between particle size and thermosalient effects.[41]

We have previously demonstrated how the conformation of the bpeb ligand in **CdPCP** directly determines the outcome of photochemical reactions in this material.[37] The temperature-induced conformational change in the bpeb ligand from **CdPCP-P1** to **CdPCP-P2** similarly alters the relative positions and alignment of the olefinic bonds of the bpeb ligands in the framework. In **CdPCP-P1**, cycloaddition occurs within the 2D layers, exclusively forming **Isomer 1** on irradiation at room temperature. In **CdPCP-P2**, the synthesis of **Isomer 1** is no longer possible because one of the olefinic bond pairs between the two bpeb ligands within a 2D layer becomes photoinactive (the bonds are no longer in parallel alignment with respect to each other). However, several other double bond pairs still meet the distance and alignment requirements to potentially undergo cycloaddition (Figure 3b).

Irradiation of **CdPCP-P2** at 100 K results in cycloaddition between alternate pairs of the out-of-phase aligned bpeb ligands between adjacent two-dimensional sheets, yielding **Isomer 2** (Figure 3b). SCXRD analysis revealed complete cycloaddition in this position, resulting in linking of the two-dimensional sheets, thus transforming the framework to a three-dimensional MOF with **sqc124** topology.[38] Reproducibility of this behavior was confirmed by irradiating several different single crystals of **CdPCP-P2** at 100 K. In all cases cycloaddition occurred between alternate pairs of out-of-phase bpeb ligands. The distinct behavior of **CdPCP-P1** and **CdPCP-P2** on irradiation confirms that these two phases can be described as polymorphs.

Cycloaddition in **CdPCP-P2** only takes place at alternate positions between the layers. Inspection of the structure reveals that the unreacted double bond pairs meet the topochemical requirements for [2+2] cycloaddition, with a distance of 4.003(4) Å between the bonds, yet no ring closure is observed even after prolonged irradiation at 100 K. SCXRD of the irradiated structure at 298 K revealed that the distance between the unreacted double bonds in the irradiated structure is 4.172(7) Å. Continued irradiation of the sample at 298 K in an attempt to induce cycloaddition at the unreacted position gave ambiguous results due to a loss in crystallinity preventing definitive determination of whether cycloaddition had taken place.

In summary, **CdPCP-P1** undergoes a temperature-induced first-order phase transition to yield **CdPCP-P2**. This structural transition results in a change in the conformation of the bpeb

DOI: 10.1021/jacs.9b05961
J. Am. Chem. Soc. 2019, 141, 11425−11429

linker, altering the position at which cycloaddition occurs. In **CdPCP-P1** cycloaddition takes place within the layer, resulting in exclusive formation of **Isomer 1**. Irradiation of **CdPCP-P2** at 100 K results in exclusive formation of **Isomer 2**. **CdPCP** thus undergoes structural changes in response to both solvent exchange and changes in temperature, in both cases allowing for selective synthesis of different isomers upon irradiation. The structural change on cooling to 100 K is subtle, but nevertheless significant in terms of the response of the resultant material to irradiation. **CdPCP** is an example of the importance of polymorphism in PCPs, which is probably frequently undetected.[42] It seems likely that other PCPs might undergo similar subtle structural changes with changes in temperature, and our results show that simple temperature-induced phase transitions can also be exploited for targeted solid-state synthesis of isomers.

■ ASSOCIATED CONTENT

Supporting Information

The Supporting Information is available free of charge on the ACS Publications website at DOI: 10.1021/jacs.9b05961.

Experimental details, crystallographic data, unit cells at various temperatures, DSC, PXRD, thermal expansion (PDF)

Crystallographic data in cif format (CIF)

Video of hot stage DSC analysis upon cooling (AVI)

Video of hot stage DSC analysis upon heating (AVI)

■ AUTHOR INFORMATION

Corresponding Authors

*dhaynes@sun.ac.za

*ljb@sun.ac.za

ORCID

Leonard J. Barbour: 0000-0002-6453-8331

Delia A. Haynes: 0000-0002-8390-5432

Notes

The authors declare no competing financial interest.

■ ACKNOWLEDGMENTS

We thank the National Research Foundation of South Africa, Stellenbosch University and SASOL for funding. The authors declare no conflict of interest.

■ REFERENCES

(1) Kitagawa, S.; Kondo, M. Functional Micropore Chemistry of Crystalline Metal Complex-Assembled Compounds. *Bull. Chem. Soc. Jpn.* **1998**, *71*, 1739−1753.

(2) Furukawa, H.; Cordova, K. E.; O'Keeffe, M.; Yaghi, O. M. The chemistry and applications of metal-organic frameworks. *Science* **2013**, *341*, 1230444.

(3) Zhang, J.-P.; Zhou, H.-L.; Zhou, D.-D.; Liao, P.-Q.; Chen, X.-M. Controlling flexibility of metal−organic frameworks. *Natl. Sci. Rev.* **2018**, *5*, 907−919.

(4) Coudert, F.-X. Responsive Metal−Organic Frameworks and Framework Materials: Under Pressure, Taking the Heat, in the Spotlight, with Friends. *Chem. Mater.* **2015**, *27*, 1905−1916.

(5) He, W.-W.; Li, S.-L.; Lan, Y.-Q. Liquid-free single-crystal to single-crystal transformations in coordination polymers. *Inorg. Chem. Front.* **2018**, *5*, 279−300.

(6) Kitaura, R.; Fujimoto, K.; Noro, S.-I.; Kondo, M.; Kitagawa, S. A Pillared-Layer Coordination Polymer Network Displaying Hysteretic Sorption: $[Cu_2(pzdc)_2(dpyg)]_n$ (pzdc= Pyrazine-2,3-dicarboxylate; dpyg = 1,2-Di(4-pyridyl)glycol). *Angew. Chem., Int. Ed.* **2002**, *41*, 133−135.

(7) Uemura, K.; Kitagawa, S.; Kondo, M.; Fukui, K.; Kitaura, R.; Chang, H. C.; Mizutani, T. Novel Flexible Frameworks of Porous Cobalt(II) Coordination Polymers That Show Selective Guest Adsorption Based on the Switching of Hydrogen-Bond Pairs of Amide Groups. *Chem. - Eur. J.* **2002**, *8*, 3586−3600.

(8) Serre, C.; Millange, F.; Thouvenot, C.; Noguès, M.; Marsolier, G.; Louër, D.; Férey, G. Very Large Breathing Effect in the First Nanoporous Chromium(III)-Based Solids: MIL-53 or $Cr^{III}(OH)\cdot\{O_2C\text{-}C_6H_4\text{-}CO_2\}\cdot\{HO_2C\text{-}C_6H_4\text{-}CO_2H\}_x\cdot H_2O_y$. *J. Am. Chem. Soc.* **2002**, *124*, 13519−13526.

(9) Kitagawa, S.; Kitaura, R.; Noro, S. Functional Porous Coordination Polymers. *Angew. Chem., Int. Ed.* **2004**, *43*, 2334−2375.

(10) Uemura, K.; Matsuda, R.; Kitagawa, S. Flexible microporous coordination polymers. *J. Solid State Chem.* **2005**, *178*, 2420−2429.

(11) Férey, G.; Serre, C. Large breathing effects in three-dimensional porous hybrid matter: facts, analyses, rules and consequences. *Chem. Soc. Rev.* **2009**, *38*, 1380−1399.

(12) Horike, S.; Shimomura, S.; Kitagawa, S. Soft porous crystals. *Nat. Chem.* **2009**, *1*, 695−704.

(13) Cai, W.; Gładysiak, A.; Anioła, M.; Smith, V. J.; Barbour, L. J.; Katrusiak, A. Giant Negative Area Compressibility Tunable in a Soft Porous Framework Material. *J. Am. Chem. Soc.* **2015**, *137*, 9296−9301.

(14) Shivanna, M.; Yang, Q.-Y.; Bajpai, A.; Patyk-Kazmierczak, E.; Zaworotko, M. J. A dynamic and multi-responsive porous flexible metal−organic material. *Nat. Commun.* **2018**, *9*, 3080.

(15) Chang, Z.; Yang, D. H.; Xu, J.; Hu, T. L.; Bu, X. H. Flexible Metal−Organic Frameworks: Recent Advances and Potential Applications. *Adv. Mater.* **2015**, *27*, 5432−5441.

(16) Desiraju, G. R. Carrying out organic chemistry within crystalline solids. *Endeavour* **1984**, *8*, 201−206.

(17) Schmidt, G. M. J. Photodimerization in the solid state. *Pure Appl. Chem.* **1971**, *27*, 647−678.

(18) MacGillivray, L. R.; Reid, J. L.; Ripmeester, J. A. Supramolecular Control of Reactivity in the Solid State Using Linear Molecular Templates. *J. Am. Chem. Soc.* **2000**, *122*, 7817−7818.

(19) Friščić, T.; MacGillivray, L. R. 'Template-switching': a supramolecular strategy for the quantitative, gram-scale construction of a molecular target in the solid state. *Chem. Commun.* **2003**, *2*, 1306−1307.

(20) MacGillivray, L. R.; Papaefstathiou, G. S.; Friščić, T.; Varshney, D. B.; Hamilton, T. D. Template-Controlled Synthesis in the Solid-State. *Top. Curr. Chem.* **2005**, *248*, 201−221.

(21) Macgillivray, L. R.; Papaefstathiou, G. S.; Friščić, T.; Hamilton, T. D.; Bučar, D. K.; Chu, Q.; Varshney, D. B.; Georgiev, I. G. Supramolecular Control of Reactivity in the Solid State: From Templates to Ladderanes to Metal−Organic Frameworks. *Acc. Chem. Res.* **2008**, *41*, 280−291.

(22) Biradha, K.; Santra, R. Crystal engineering of topochemical solid state reactions. *Chem. Soc. Rev.* **2013**, *42*, 950−967.

(23) Park, I.-H.; Lee, S. S.; Vittal, J. J. Guest-Triggered Supramolecular Isomerism in a Pillared-Layer Structure with Unusual Isomers of Paddle-Wheel Secondary Building Units by Reversible Single-Crystal-to-Single-Crystal Transformation. *Chem. - Eur. J.* **2013**, *19*, 2695−2702.

(24) Medishetty, R.; Park, I.-H.; Lee, S. S.; Vittal, J. J. Solid-state polymerisation via [2+2] cycloaddition reaction involving coordination polymers. *Chem. Commun.* **2016**, *52*, 3989−4001.

(25) Park, I.-H.; Ju, H.; Herng, T. S.; Kang, Y.; Lee, S. S.; Ding, J.; Vittal, J. J. Supramolecular Isomerism and Polyrotaxane-Based Two-Dimensional Coordination Polymers. *Cryst. Growth Des.* **2016**, *16*, 7278−7285.

(26) Park, I.-H.; Medishetty, R.; Lee, H. H.; Mulijanto, C. E.; Quah, H. S.; Lee, S. S.; Vittal, J. J. Formation of a Syndiotactic Organic Polymer Inside a MOF by a [2+2] Photo-Polymerization Reaction. *Angew. Chem., Int. Ed.* **2015**, *54*, 7313−7317.

(27) Liu, D.; Lang, J. Regiospecific photodimerization reactions of an unsymmetrical alkene in two coordination compounds. *CrystEngComm* **2014**, *16*, 76−81.
(28) Kole, G. K.; Vittal, J. J. Solid-state reactivity and structural transformations involving coordination polymers. *Chem. Soc. Rev.* **2013**, *42*, 1755−1775.
(29) Vittal, J. J.; Quah, H. S. Photochemical reactions of metal complexes in the solid state. *Dalton Trans* **2017**, *46*, 7120−7140.
(30) Hazra, A.; Bonakala, S.; Bejagam, K. K.; Balasubramanian, S.; Maji, T. K. Host−Guest [2+2] Cycloaddition Reaction: Postsynthetic Modulation of CO_2 Selectivity and Magnetic Properties in a Bimodal Metal−Organic Framework. *Chem. - Eur. J.* **2016**, *22*, 7792−7799.
(31) Foo, M. L.; Matsuda, R.; Hijikata, Y.; Krishna, R.; Sato, H.; Horike, S.; Hori, A.; Duan, J.; Sato, Y.; Kubota, Y.; Takata, M.; Kitagawa, S. An Adsorbate Discriminatory Gate Effect in a Flexible Porous Coordination Polymer for Selective Adsorption of CO_2 over C_2H_2. *J. Am. Chem. Soc.* **2016**, *138*, 3022−3030.
(32) Li, F. F.; Zhang, L.; Gong, L. L.; Yan, C. S.; Gao, H. Y.; Luo, F. Reversible photo/thermoswitchable dual-color fluorescence through single-crystal-to-single-crystal transformation. *Dalton Trans* **2017**, *46*, 338−341.
(33) Li, N. Y.; Liu, D.; Ren, Z. G.; Lollar, C.; Lang, J. P.; Zhou, H. C. Controllable Fluorescence Switching of a Coordination Chain Based on the Photoinduced Single-Crystal-to-Single-Crystal Reversible Transformation of a syn-[2.2]Metacyclophane. *Inorg. Chem.* **2018**, *57*, 849−856.
(34) Park, I.-H.; Ju, H.; Kim, K.; Lee, S. S.; Vittal, J. J. Isomerism in double-pillared-layer coordination polymers − structures and photoreactivity. *IUCrJ* **2018**, *5*, 182−189.
(35) Li, N.-Y.; Liu, D.; Abrahams, B. F.; Lang, J.-P. Covalent switching, involving divinylbenzene ligands within 3D coordination polymers, indicated by changes in fluorescence. *Chem. Commun.* **2018**, *54*, 5831−5834.
(36) Medishetty, R.; Park, I.-H.; Lee, S. S.; Vittal, J. J. Solid-state polymerisation via [2+2] cycloaddition reaction involving coordination polymers. *Chem. Commun.* **2016**, *52*, 3989−4001.
(37) Claassens, I. E.; Nikolayenko, V. I.; Haynes, D. A.; Barbour, L. J. Solvent-Mediated Synthesis of Cyclobutane Isomers in a Photoactive Cadmium(II) Porous Coordination Polymer. *Angew. Chem., Int. Ed.* **2018**, *57*, 15563−15566.
(38) Blatov, V. A.; Shevchenko, A. P.; Proserpio, D. M. Applied Topological Analysis of Crystal Structures with the Program Package ToposPro. *Cryst. Growth Des.* **2014**, *14*, 3576−3586.
(39) Crawford, A. W.; Groeneman, R. H.; Unruh, D. K.; Hutchins, K. M. Cooling-rate dependent single-crystal-to-single-crystal phase transition in an organic co-crystal. *Chem. Commun.* **2019**, *55*, 3258−3261.
(40) Sahoo, S. C.; Panda, M. K.; Nath, N. K.; Naumov, P. Biomimetic Crystalline Actuators: Structure−Kinematic Aspects of the Self-Actuation and Motility of Thermosalient Crystals. *J. Am. Chem. Soc.* **2013**, *135*, 12241−12251.
(41) Commins, P.; Desta, I. T.; Karothu, D. P.; Panda, M. K.; Naumov, P. Crystals on the move: mechanical effects in dynamic solids. *Chem. Commun.* **2016**, *52*, 13941−13954.
(42) Aulakh, D.; Varghese, J. R.; Wriedt, M. The Importance of Polymorphism in Metal−Organic Framework Studies. *Inorg. Chem.* **2015**, *54*, 8679−8684.

DOI: 10.1021/jacs.9b05961
J. Am. Chem. Soc. 2019, 141, 11425−11429

A Multistimulus Responsive Porous Coordination Polymer: Temperature-Mediated Control of Solid-state [2+2] Cycloaddition

Isabella E. Claassens,† Leonard J. Barbour,*,† and Delia A. Haynes*,†

†Department of Chemistry and Polymer Science, Stellenbosch University, P. Bag X1, Matieland, 7602, Stellenbosch, South Africa

Supplementary Information

Experimental Procedures

Instrumental details

Powder X-ray diffraction (PXRD)

PXRD data were recorded on a benchtop Bruker D2 PHASER. It is equipped with a Lynxeye 1D detector and uses Ni-filtered Cu Kα radiation (λ = 1.5418 Å) with generator power settings of 30 kV and 10 mA. The X-ray beam is restricted by a 1.0 mm divergence slit and a 2.5 mm Soller collimator. Powder samples were evenly distributed on a zero-background holder after being ground with a mortar and pestle to minimise the effects of preferred orientation. Variable-temperature PXRD data were recorded using a PANalytical X'Pert PRO diffractometer using the capillary spinner configuration and a short-nozzle Oxford Cryostream 700Plus cooling system. Powdered samples were placed in a 0.5 mm Lindemann glass capillary, which was spun during data collection over a range of 5° - 40° 2θ. Data analysis was carried out using X'Pert HighScore Plus[1] (Version 2.2e). Powder patterns were simulated from SCXRD structures using Mercury.[2]

Single-crystal X-ray diffraction (SCXRD)

Suitable single crystals were attached to a MiTeGen MicroLoopTM mount using Paratone®N oil. SCXRD experiments were carried out on a Bruker D8 Venture equipped with a Photon II CPAD detector, which has a multilayer monochromator with MoKα radiation (λ = 0.71073 Å) from an Incoatec IμS microfocus source. An Oxford Cryostreams 800Plus cryostat was used to control the temperature of the crystal.

Data reduction was carried out with the Bruker SAINT[3] software package. The absorption corrections and the correction of other systematic errors were carried out with SADABS.[4] Structures were solved by direct methods using SHELXS[5] or by intrinsic phasing using SHELXT[6] in the X-Seed[7,8] interface. Structure refinement was carried out using SHELXL.[5] Hydrogen atom positions were assigned using riding models.

PLATON[10] SQUEEZE[11] was used to determine the total electron count per unit cell of guest molecules within the structures. These counts were then used to determine occupancy of the guest molecules within the channels of the porous coordination polymer PCP. Graphics were generated with POV-Ray [12] in the X-Seed interface[7,8], and CIF files were edited in Olex2 [13] and EnCIFer.

Irradiation

Photoirradiation was carried out using a hand held UV-Groebel UV LED SOLO photodiode emitting UV light of wavelength 365 nm at 4 200 mW cm^{-2}. Single crystals were irradiated for between 45 and 120 minutes on a mount on the diffractometer under the cryostream. Samples were irradiated for as long as possible whilst maintaining crystal integrity. In most cases irradiation was continuous; in some cases irradiation was interrupted to check crystal quality before further irradiation was carried out.

Differential scanning calorimetry (DSC)

DSC was performed on a TA instruments Q20 analyser. Samples ranging in size from 0.9 - 5.0 mg were placed in an aluminium pan. The pan was then either covered with an aluminium lid (with a pin hole) and crimped to seal the edges or it was left with no lid. Initially both methods were employed to investigate the effect of the lid but this did not influence the results. The reference pan was subjected to the same protocol as the sample pan. The sample was then cooled and heated in cycles at a rate of 5 °C min^{-1}. A nitrogen flow rate of 50 ml min^{-1} was used to purge the system. Data analysis was carried out on the Universal Analysis 2000 software (TA Instruments, Version 4.5A).

Hot-stage DSC

Hot-stage microscopy experiments were carried out using a Linkam DSC-600 system, equipped with a Meiji MS-45D Unicam zoom microscope and a PixelLink digital camera. Single crystals or polycrystalline samples were placed in a sapphire DSC pan and cooled, using a liquid nitrogen cooling attachment, at a rate of 5 K min^{-1}.

Topology

TOPOSPro[14] was used to determine the topology of the frameworks through the online service at topospro.org.

Synthesis

Chemicals and solvents were obtained from Sigma-Aldrich and used as received. Nitrogen was passed through a Drierite™ drying column before use. Both the 1,4-bis[2-(4'-pyridyl)ethenyl]benzene (bpeb) ligand and **CdPCP-P1** were synthesised according to the previously published procedures.[15]

Results

CdPCP_P2_100K	**CdPCP-P2** at 100 K
CdPCP_P2_irrad_100K	**CdPCP-P2** after irradiation at 100 K
CdPCP_P2_irrad_100K_298K	**CdPCP-P2** irradiated at 100 K then warmed to 298 K

Details regarding crystal structure refinement

To facilitate a direct comparison of the following structures with the published structure of **CdPCP-P1**, the unit cells for each structure were transformed to a non-standard setting using the transformation matrix (0 0 -1, 0 -1 0, -1 0 0).

CdPCP_P2_100K
Four DMA solvent molecules per asymmetric unit (ASU) were modelled. We were unable to refine the minor component (O115 – C120) of one of the DMA solvent molecules anisotropically or with hydrogen atoms.

CdPCP_P2_irrad_100K
Two of the four DMA solvent molecules in the channels could not be modelled satisfactorily. The SQUEEZE procedure was therefore employed. The residual unmodelled electron density is consistent with the presence of two further DMA molecules. SQUEEZE analysis reveals 99 electrons per ASU. The expected value for two DMA solvent molecules is 96 electrons per ASU.

Small residual electron density peaks were observed around the cyclobutane ring. These could be modelled as partially occupied, but no further atoms from unreacted ligand could be modelled. Allowing the occupancy of the cyclobutane to refine yielded an occupancy of 100 %. This, combined with the small size of the residual electron density peaks, indicates that there is unlikely to be a significant amount of unreacted bpeb, so we have not attempted to model this.

CdPCP_P2_irrad_100K_298K
Two of the four DMA solvent molecules in the channels could not be modelled satisfactorily. The SQUEEZE procedure was therefore employed. The residual unmodelled electron density is consistent with the presence of the expected additional two DMA molecules. SQUEEZE analysis yields 98 electrons per ASU. The expected value for two DMA solvent molecules is 96 electrons per ASU. We were also unable to anisotropically refine the disordered components of one of the two remaining DMA solvent molecules in the ASU.

As with the 100 K structure, small residual density peaks are present around the cyclobutane moeity. Again, the small residual peaks, as well as the occupancy of the ligand refining to 1, indicate that there is no significant amount of unreacted ligand.

Asymmetric units (ASU)

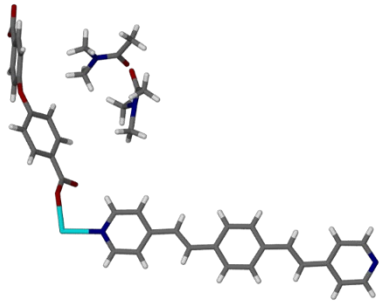

Figure S1 ASU of **CdPCP-P1** at 298 K.

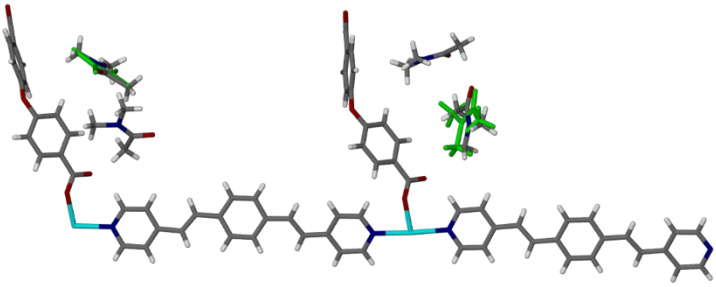

Figure S2 ASU of **CdPCP-P2** at 100 K. The minor components of the disordered DMA solvent molecules are coloured green.

Table S1. Selected crystallographic data for structures reported in this manuscript, as well as the previously published structure, **CdPCP-P1**[15].

	CdPCP_P1	**CdPCP_P2_100K**	**CdPCP_P2_irrad_100K**	**CdPCP_P2_irrad_100K_298K**
Empirical formula	$C_{42}H_{42}CdN_4O_7$	$C_{84}H_{84}Cd_2N_8O_{14}$*	$C_{84}H_{84}Cd_2N_8O_{14}$*	$C_{84}H_{84}Cd_2N_8O_{14}$*
Formula weight	827.19	1654.46*	1654.46*	1654.46*
Temperature (K)	298(2)	100(2)	100(2)	298(2)
Wavelength (Å)	0.71073	0.71073	0.71073	0.71073
Crystal system	triclinic	triclinic	triclinic	triclinic
Space group	*P*-1	*P*-1	*P*-1	*P*-1
Unit cell dimensions (Å, °)	*a* = 9.6855(4)	*a* = 19.4978(9)	*a* = 19.811(2)	*a* = 20.0731(12)
	b = 15.4863(7)	*b* = 15.4920(8)	*b* = 15.4443(16)	*b* = 15.4449(9)
	c = 15.7346(6)	*c* = 15.3385(7)	*c* = 15.0786(14)	*c* = 15.1647(8)
	α = 113.056(1)	*α* = 116.236(2)	*α* = 115.954(3)	*α* = 114.710(2)
	β = 106.237(1)	*β* = 108.509(2)	*β* = 108.416(3)	*β* = 107.275(2)
	γ = 94.835(2)	*γ* = 93.369(2)	*γ* = 94.546(3)	*γ* = 95.625(2)
Volume (Å)	2034.16(15)	3831.4(3)	3805.6(7)	3942.3(4)
Z	2	2	2	2
Calculated density (g cm^{-3})	1.351	1.432	1.292	1.247
Absorption coefficient (mm^{-1})	0.589	0.626	0.619	0.598
F_{000}	852	1700	1512	1512
Crystal size (mm^3)	0.230 × 0.140 × 0.128	0.328 × 0.121 × 0.066	0.328 × 0.121 × 0.066	0.328 × 0.121 × 0.066
θ range for data collection (°)	2.233 to 27.181	2.290 to 26.786	2.197 to 24.456	2.180 to 25.105
Miller index ranges	$-12 \le h \le 12$, $-19 \le k \le 19$, $-20 \le l \le 20$	$-21 \le h \le 24$, $-19 \le k \le 19$, $-19 \le l \le 19$	$-23 \le h \le 23$, $-17 \le k \le 17$, $-17 \le l \le 17$	$-23 \le h \le 23$, $-18 \le k \le 18$, $-18 \le l \le 18$
Reflections collected	39587	43736	77064	66025
Independent reflections	9008 [R_{int} = 0.0309]	16234 [R_{int} = 0.0388]	12551 [R_{int} = 0.0610]	13961 [R_{int} = 0.0623]
Completeness to θ_{max} (%)	0.994	0.991	0.996	0.994

Max. and min. transmission	0.870 and 1	0.9357 and 1	0.8589 and 1	0.9000 and 1
Refinement method	Full-matrix least-squares on F^2	Full-matrix least-squares on F^2	Full-matrix least-squares on F^2	Full-matrix least-squares on F^2
Data / restraints / parameters	9008 / 0 / 485	16234 / 0 / 1063	12551 / 0 / 895	13961 / 0 / 866
Goodness-of-fit on F^2	1.058	1.039	1.025	1.017
Final R indices [$I>2\sigma(I)$]	$R1$ = 0.0353, $wR2$ = 0.0905	$R1$ = 0.0393, $wR2$ = 0.0774	$R1$ = 0.0426, $wR2$ = 0.0956	$R1$ = 0.0569, $wR2$ = 0.1180
R indices (all data)	$R1$ = 0.0418, $wR2$ = 0.0960	$R1$ = 0.0554, $wR2$ = 0.0865	$R1$ = 0.0552, $wR2$ = 0.1015	$R1$ = 0.0905, $wR2$ = 0.1330
Largest diff. peak and hole (e Å^{-3})	0.772 and -0.383	0.767 and -0.702	0.753 and -0.745	0.605 and -0.622

* These formulae and formula masses have been corrected to include solvent molecules that have not been fully modelled.

Structural overlays

In order to assess the similarity of the structures, parts of each structure were overlaid in Materials Studio.[16] The RMS difference was estimated as 1.04 Å and 0.48 Å when including and omitting DMA, respectively.

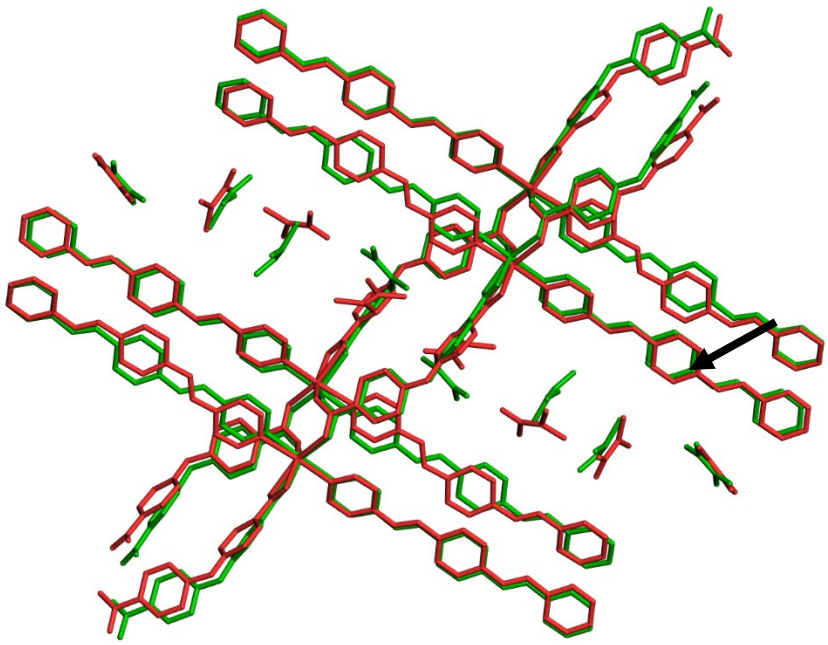

Figure S3 Overlay of **CdPCP-P**1 (298 K, green) and **CdPCP-P2** (100 K, red). The position of the bpeb conformational change is indicated by an arrow. Hydrogen atoms are omitted for clarity.

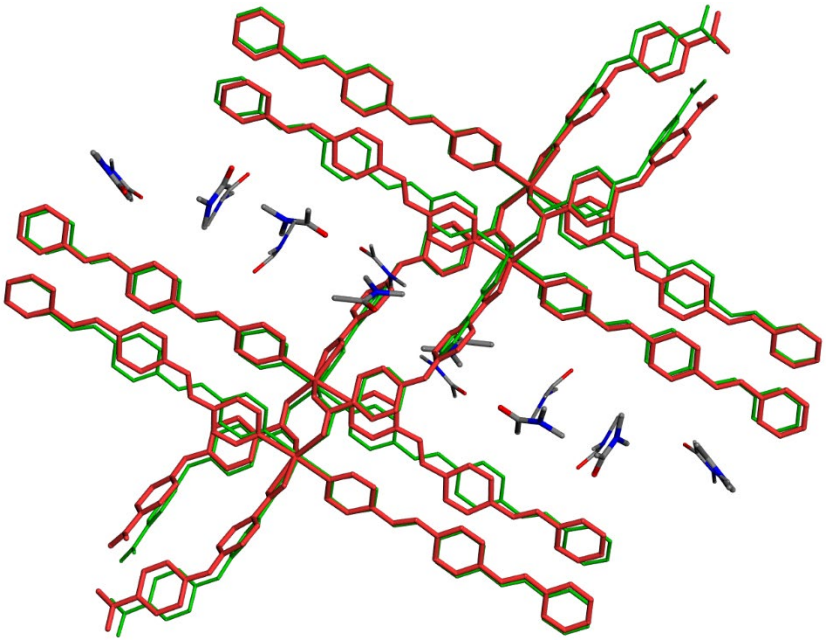

Figure S4 Overlay of **CdPCP-P1** (298 K, green) and **CdPCP-P2** (100 K, red). The DMA molecules belonging to **CdPCP-P1** are indicated by a thinner bond width. Hydrogen atoms are omitted for clarity. The DMA solvent molecules are displayed in CPK colours to reveal the position of the oxygen atom in the DMA molecules.

Variable-temperature SCXRD unit cell analysis

SCXRD unit cell analysis was carried out on several crystals of **CdPCP-P1**. The results from two single crystals are shown below. Unit cell data were recorded at 5 K intervals from 298 to 100 K upon cooling and 100 and 298 K upon heating. The equilibration time was set to 15 minutes at each temperature.

Variable-temperature unit cell determination for a single crystal indicated that **CdPCP-P1** persists from 298 to 248 K. The crystal then undergoes a transition between 248 and 238 K where domains of both **CdPCP-P1** and **CdPCP-P2** are present. At 238 K the transition appears to be complete since the unit cell parameters of **CdPCP-P2** are exclusively obtained. Further cooling to 100 K revealed gradual changes in the unit cell parameters in accordance with the expected thermal contraction of the material. Upon re-heating, the phase transition occurred between 238 and 253 K and the unit cell parameters of **CdPCP-P1** were exclusively obtained from 258 to 298 K. The transition temperature range therefore appears to be 248 – 238 K upon cooling and 238 – 253 K upon heating for this particular crystal (Figure S5).

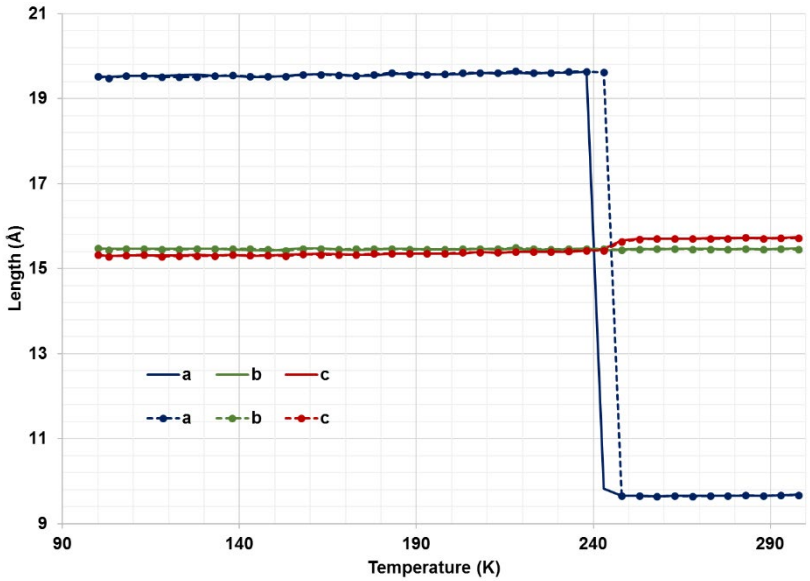

Figure S5 Unit cell length from 298 to 100 K upon cooling and heating from 100 to 298 K for crystal 1. The solid lines correspond to cooling and the dotted lines to heating of the crystal.

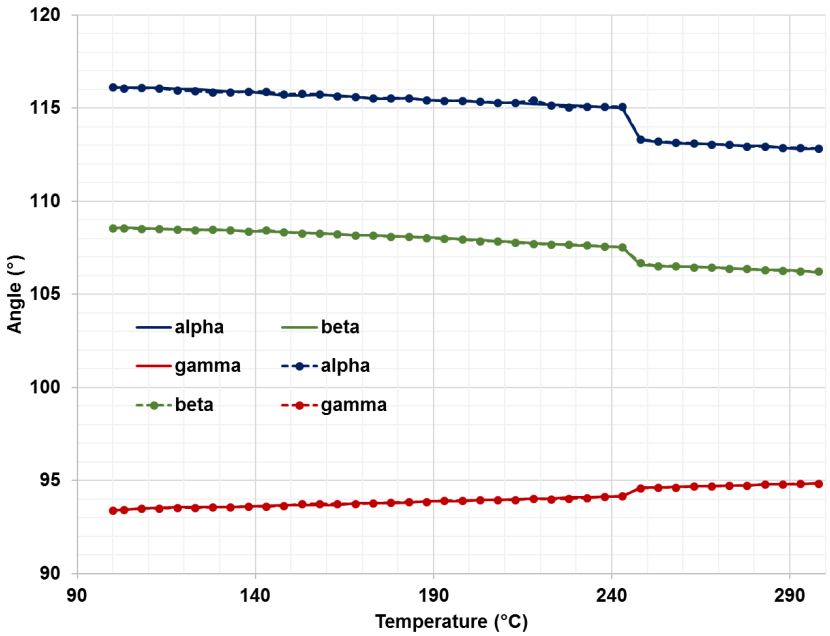

Figure S6 Unit cell angles from 298 to 100 K upon cooling and heating from 100 to 298 K for crystal 1. The solid lines correspond to cooling and the dotted lines to heating of the crystal.

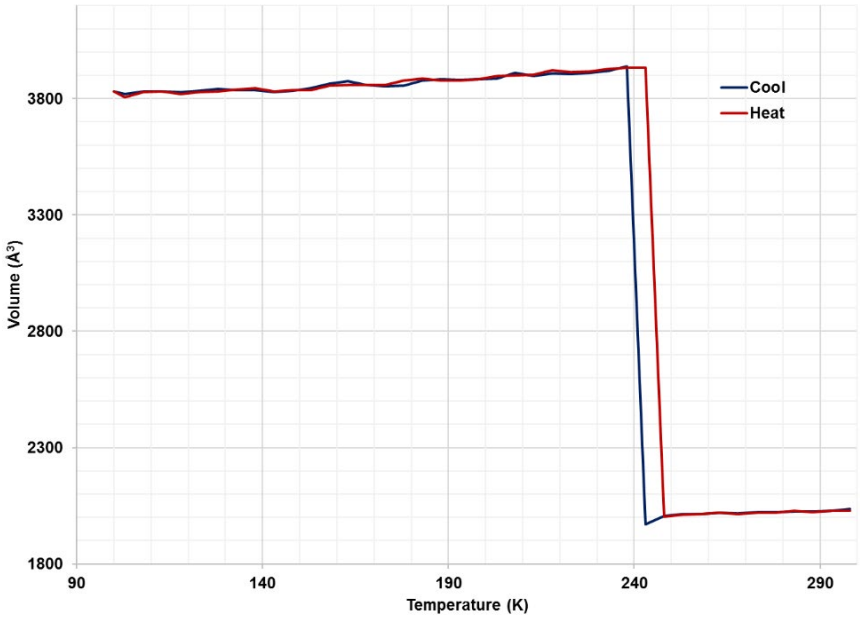

Figure S7 Unit cell volume from 298 to 100 K upon cooling and heating from 100 to 298 K for crystal 1.

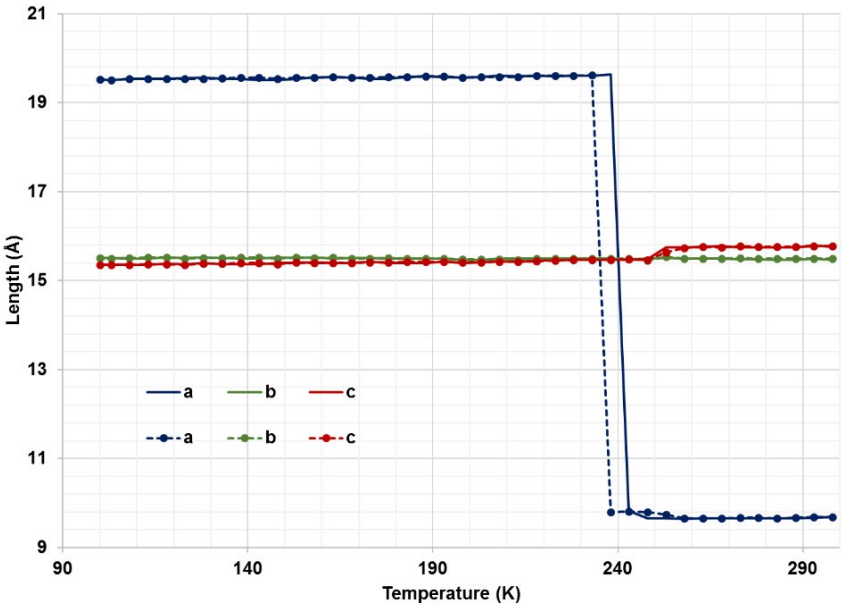

Figure S8 Unit cell length from 298 to 100 K upon cooling and heating from 100 to 298 K for crystal 2. The solid lines correspond to cooling and the dotted lines to heating of the crystal.

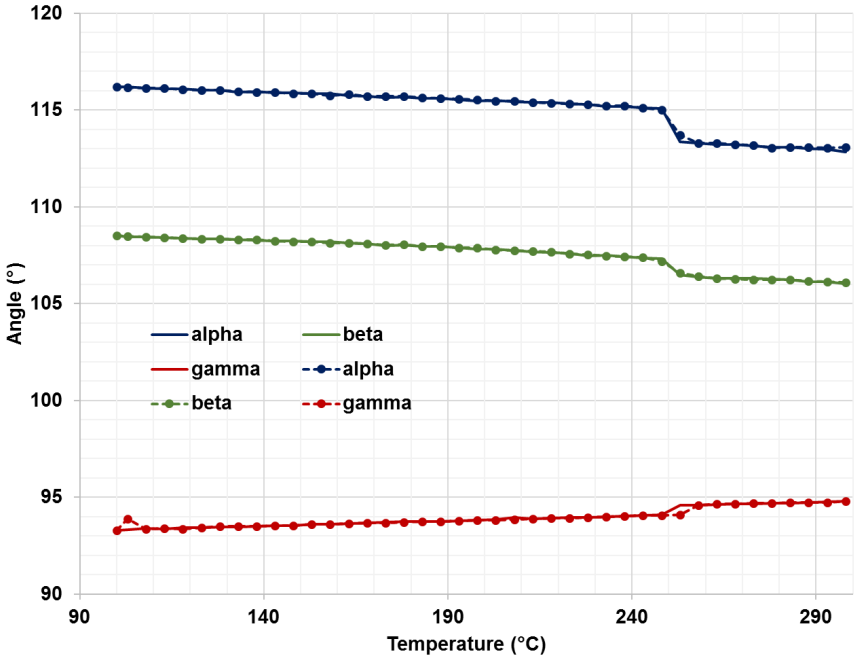

Figure S9 Unit cell angles from 298 to 100 K upon cooling and heating from 100 to 298 K for crystal 2. The solid lines correspond to cooling and the dotted lines to heating of the crystal.

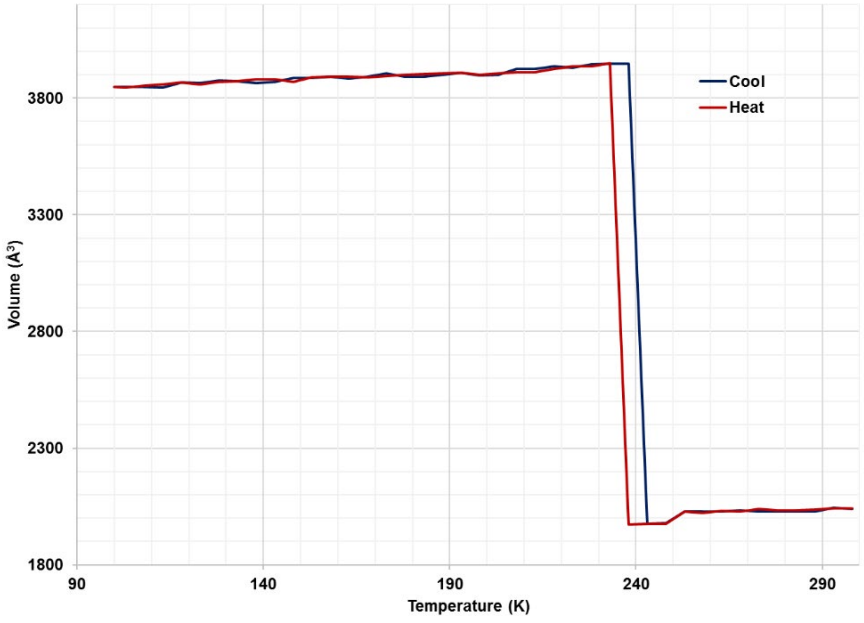

Figure S10 Unit cell volume from 298 to 100 K upon cooling and heating from 100 to 298 K for crystal 2.

SCXRD cycling of temperature

The temperature of a single crystal of **CdPCP-P1** was repeatedly cycled between 298 and 100 K. Extended unit cell data collection strategies were employed for each unit cell (>2500 reflections with I/σ of 12 was used to determine each unit cell). Equilibration time was set to 1 hour at each temperature. Unit cell parameters are tabulated in Table S2.

Table S2 Unit cell parameters of a single crystal of **CdPCP** as it is consecutively cycled from 298 to 100 K.

Cycle	Temperature (K)	a (Å)	b (Å)	c (Å)	α (°)	β (°)	γ (°)	V (Å^3)
1	298	9.70	15.46	15.72	112.95	106.34	94.73	2034
2	100	19.56	15.48	15.30	116.04	108.71	93.39	3832
3	298	9.69	15.46	15.70	112.98	106.32	94.76	2029
4	100	19.54	15.47	15.29	116.03	108.72	93.37	3824
5	298	9.70	15.47	15.72	112.99	106.35	94.74	2033
6	100	19.56	15.48	15.30	116.02	108.69	93.40	3832
7	298	9.69	15.46	15.71	113.02	106.36	94.71	2030
8	100	19.56	15.48	15.30	116.02	108.69	93.39	3834
9	298	9.69	15.46	15.71	113.00	106.31	94.75	2031
10	100	19.56	15.48	15.30	116.02	106.69	93.39	3832
11	298	9.69	15.46	15.71	113.00	106.37	94.67	2030
12	100	19.57	15.49	15.32	116.08	108.73	93.39	3840
13	298	9.70	15.47	15.71	113.00	106.34	94.67	2034

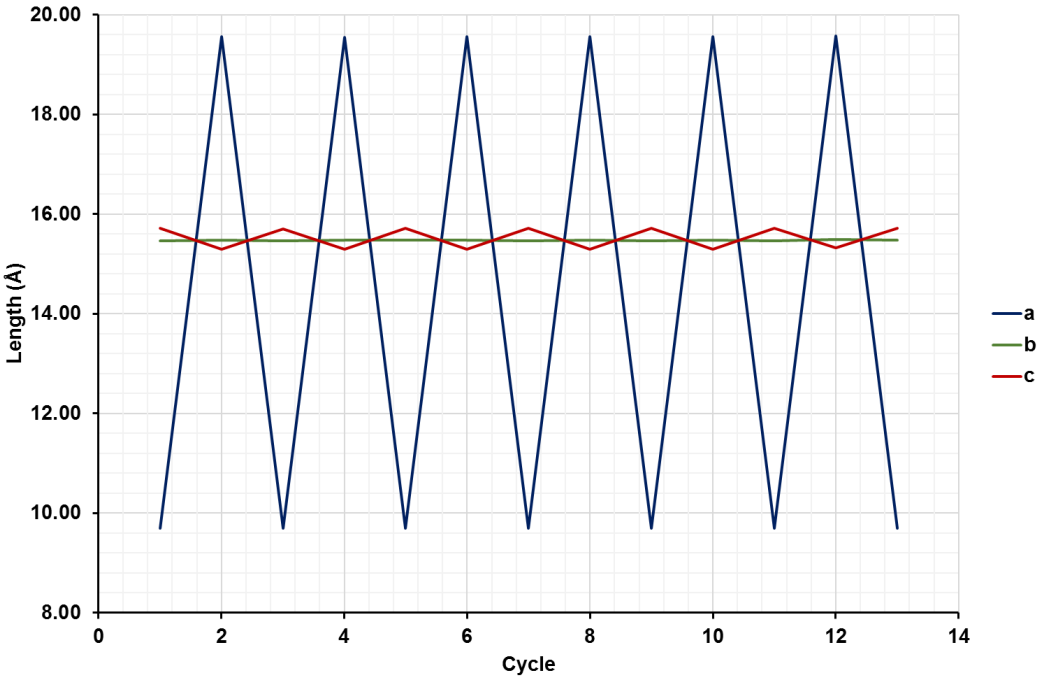

Figure S11 Plot of the change in unit cell lengths for a single crystal of **CdPCP** as it is cycled between 298 and 100 K, showing the reversible transition between **CdPCP-P1** and **CdPCP-P2**.

Unit cell analysis on crystals ranging in size

To assess the effect of crystal size on the onset temperature of the phase change, SCXRD analysis was carried out on several crystals ranging in size. No clear correlation could be established between crystal size and the onset temperature of the phase change (Table S3).

SCXRD analysis was carried out on a number of single crystals ranging in size and age. Unit cell data were collected at 5 K intervals in the range 298 to 218 K on cooling and 218 to 298 K on heating. Extended unit cell data collection strategies were employed for each unit cell and equilibration time was set to 15 minutes at each temperature. As stated in the manuscript, there appears to be little correlation between onset temperature or the length of the transition period and the size of the crystal. It was however noted that older crystals generally had a lower onset temperature than recently synthesised crystals as indicated in Table S4, where crystals from newly synthesised batches and those from aged batches are shaded differently.

Table S3 Onset temperatures of the transition period as **CdPCP** undergoes the phase change are displayed for cooling and heating. The length of the transition period is noted, as well as the size of the single crystal for which the data were collected. Entries are ordered by volume of the crystals.

Sample size				Cooling			Heating		
Dimensions (mm)			Volume (10^3 mm^3)	Onset (K)	End (K)	Range (K)	Onset (K)	End (K)	Range (K)
0.030	0.056	0.171	0.29	263	258	5	263	273	10
0.049	0.102	0.122	0.61	258	228	30	238	253	15
0.040	0.127	0.130	0.66	253	248	5	253	253	0
0.045	0.108	0.178	0.87	253	248	5	243	248	5
0.038	0.084	0.277	0.88	258	253	5	258	258	0
0.040	0.107	0.244	1.04	243	223	20	238	253	15
0.040	0.124	0.242	1.20	273	263	10	268	283	15
0.059	0.104	0.200	1.23	253	253	0	253	253	0
0.074	0.102	0.213	1.61	248	248	0	248	258	10
0.078	0.094	0.255	1.87	263	253	10	258	263	5
0.052	0.128	0.338	2.25	263	253	10	258	258	0
0.073	0.128	0.288	2.69	248	238	10	238	243	5
0.046	0.179	0.369	3.04	253	253	0	253	253	0
0.070	0.192	0.446	5.99	248	248	0	248	248	0
0.097	0.244	0.297	7.03	248	248	0	253	253	0

Table S4 Onset temperatures of the transition period as **CdPCP** undergoes the phase change on both cooling and heating. Entries are ordered by onset temperature of the phase change upon cooling. Newly synthesised samples are shaded in blue whereas the single crystals from much older batches are shaded in orange.

Sample size				Cooling			Heating		
Dimensions (mm)			Volume (10^3 mm^3)	Onset (K)	End (K)	Range (K)	Onset (K)	End (K)	Range (K)
0.040	0.107	0.244	1.04	243	223	20	238	253	15
0.074	0.102	0.213	1.61	248	248	0	248	258	10
0.073	0.128	0.288	2.69	248	238	10	238	243	5
0.097	0.244	0.297	7.03	248	248	0	253	253	0
0.040	0.127	0.13	0.66	253	248	5	253	253	0
0.045	0.108	0.178	0.87	253	248	5	243	248	5
0.059	0.104	0.2	1.23	253	253	0	253	253	0
0.046	0.179	0.369	3.04	253	253	0	253	253	0
0.030	0.056	0.171	0.29	263	258	5	263	273	10
0.078	0.094	0.255	1.87	263	253	10	258	263	5
0.052	0.128	0.338	2.25	263	253	10	258	258	0
0.040	0.124	0.242	1.20	273	263	10	268	283	15

Older sample batches **Freshly synthesised**

DSC analysis

The temperature range of the transition in DSC experiments is similar to that observed with SCXRD, but reproducibility of the DSC trace proved problematic. The onset temperatures of both the endotherm and exotherm differed between samples, as did the peak profiles. In order to probe the source of this variation between samples, hot-stage DSC analysis was carried out with a view to visualising the thermal events that occur during cooling and heating (see videos). DSC analysis was carried out on several different samples of **CdPCP-P1**. These samples ranged in both particle size and age of the sample. A selection of the thermograms can be seen below. The sample size is indicated on the thermogram in each case.

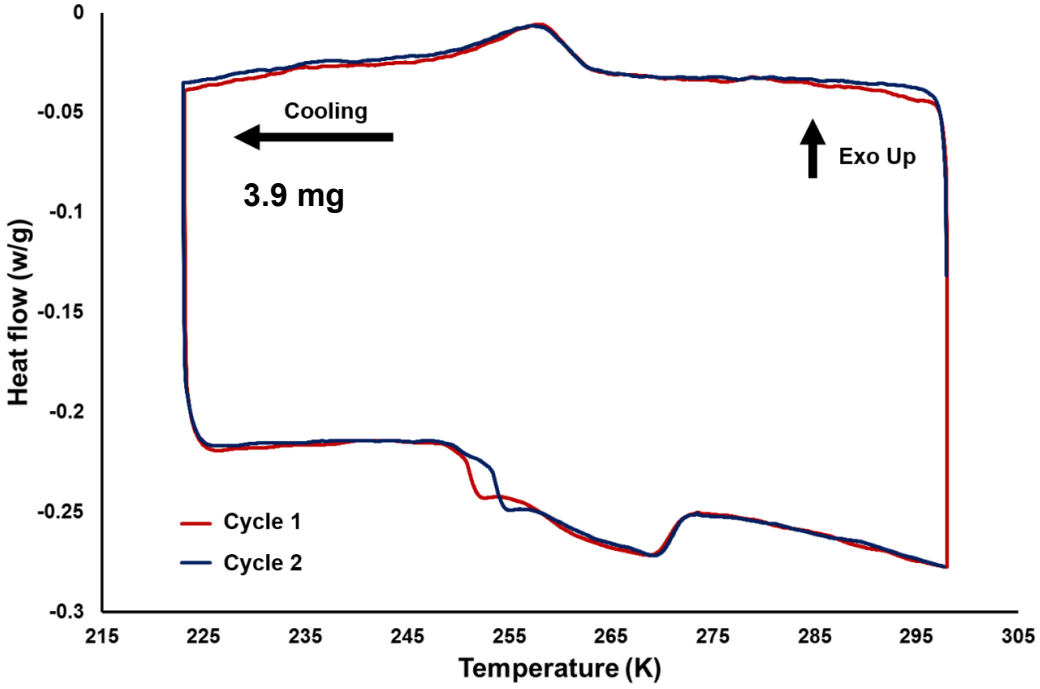

Figure S12 DSC thermogram of single crystals of **CdPCP-P1**. Two cycles were carried out. A lowering of the onset temperature for the phase transition on heating is observed in the second cycle.

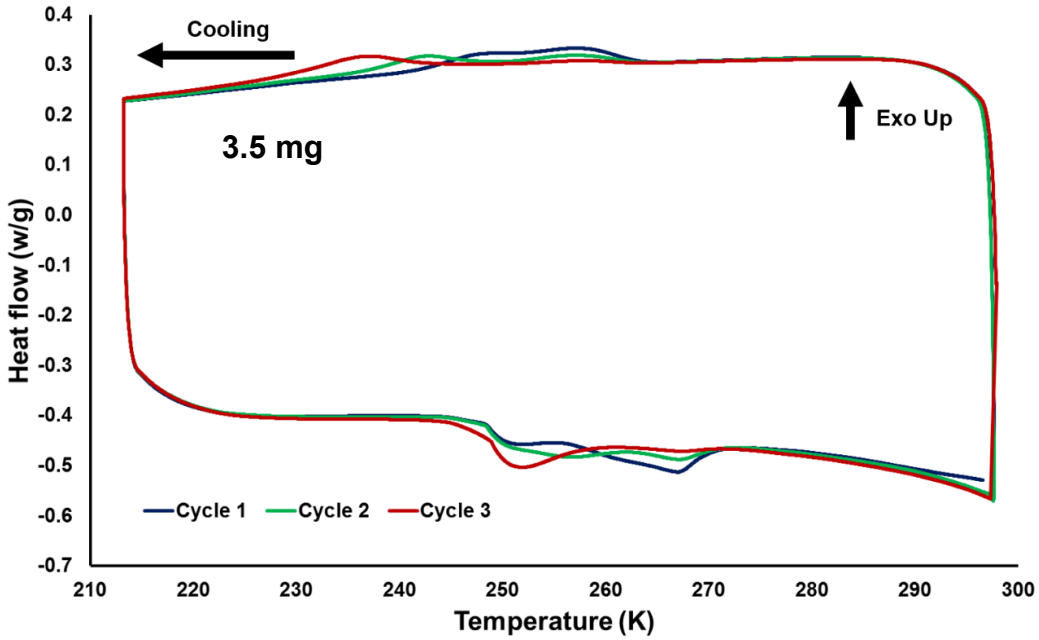

Figure S13 DSC thermogram of large single crystals of **CdPCP-P1**.

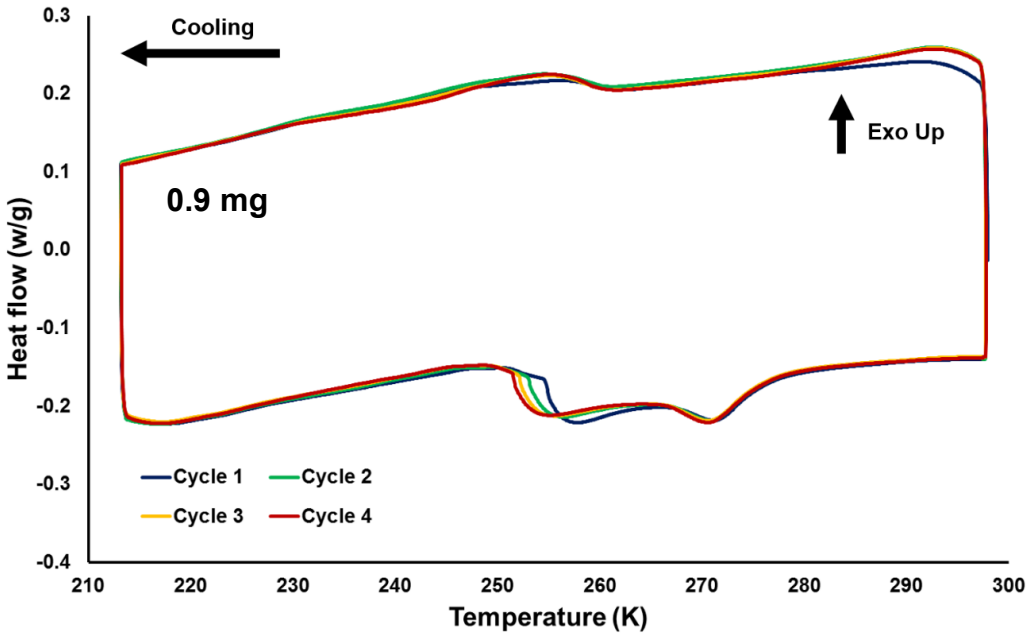

Figure S14 DSC thermogram of single crystals of **CdPCP-P1**. A lowering in the onset temperature for the phase transition is observed on heating with consecutive cycles.

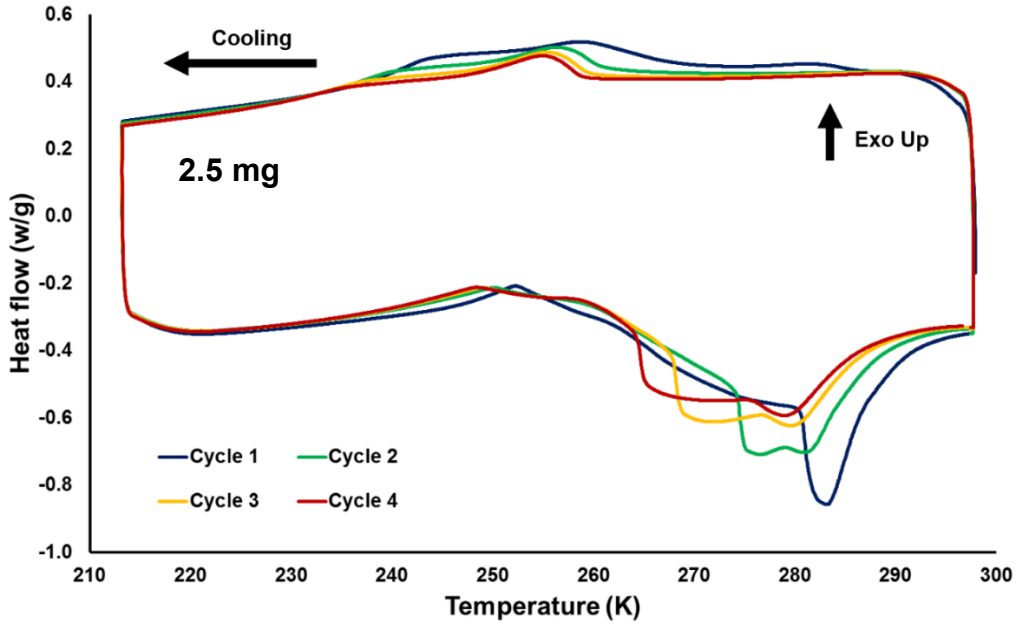

Figure S15 DSC thermogram of freshly synthesied single crystals of **CdPCP-P1**. A lowering in the onset temperature for the phase transition is observed on heating and cooling with consecutive cycles.

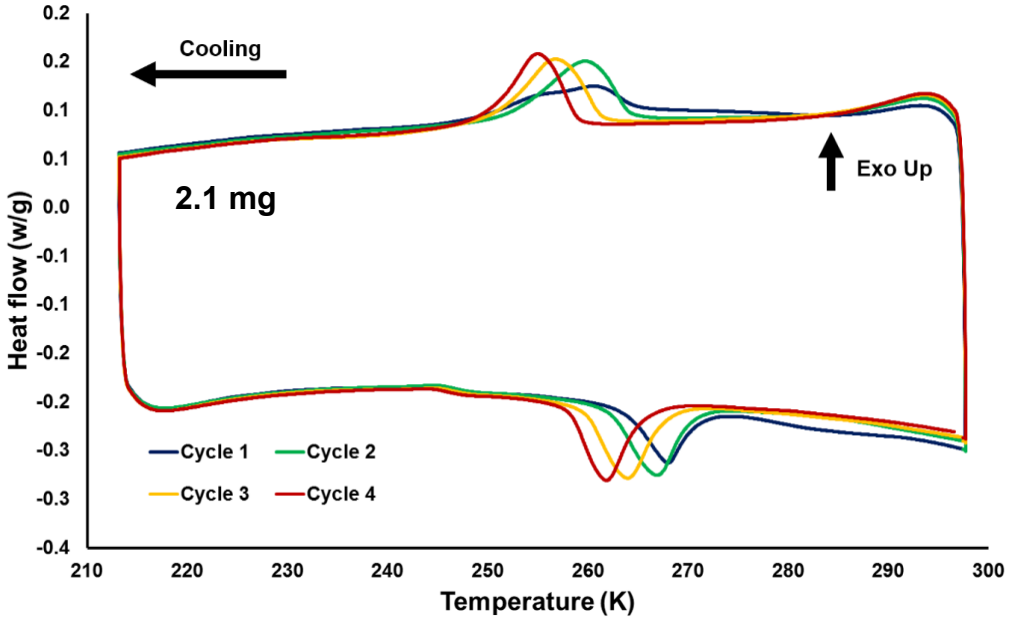

Figure S16 DSC thermogram of a polycrystalline sample of **CdPCP-P1**. A lowering in the onset temperature for the phase transition is observed on heating and cooling with consecutive cycles.

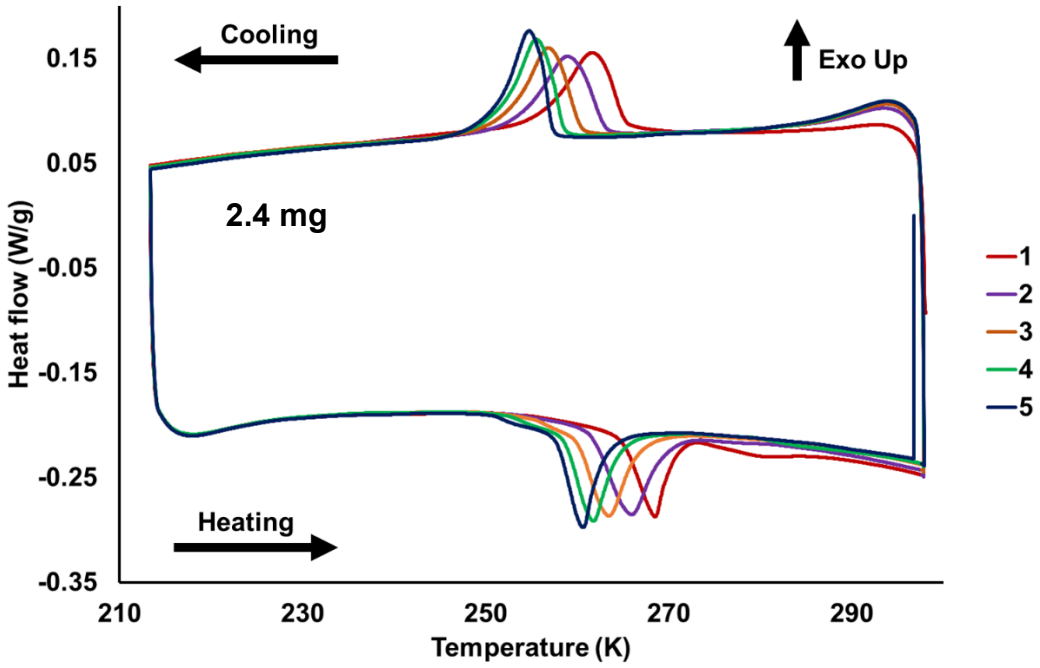

Figure S17 DSC thermograms of consecutive cooling and heating cycles of a polycrystalline sample of **CdPCP-P1**. A lowering in the onset temperature of the phase change is observed with each consecutive cycle.

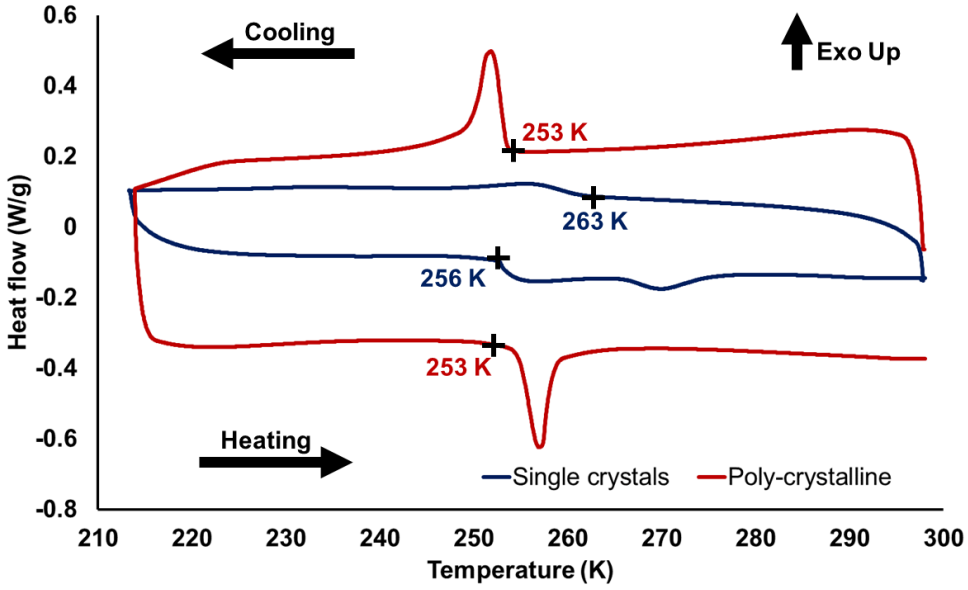

Figure S18 DSC thermogram of single crystals of CdPCP-P1 (blue) and a polycrystalline sample (red).

Thermal Expansion

Since the three crystallographic axes are not orthogonal to one another in **CdPCP**, the principal axis strain calculator PASCal[17] was used to determine the linear thermal expansion coefficients along the three principal axes, as well as the volumetric thermal expansion coefficient for both phases. The structure undergoes anomalous anisotropic thermal expansion, with positive linear thermal expansion along two principal axes and negative expansion along the third principal axis.

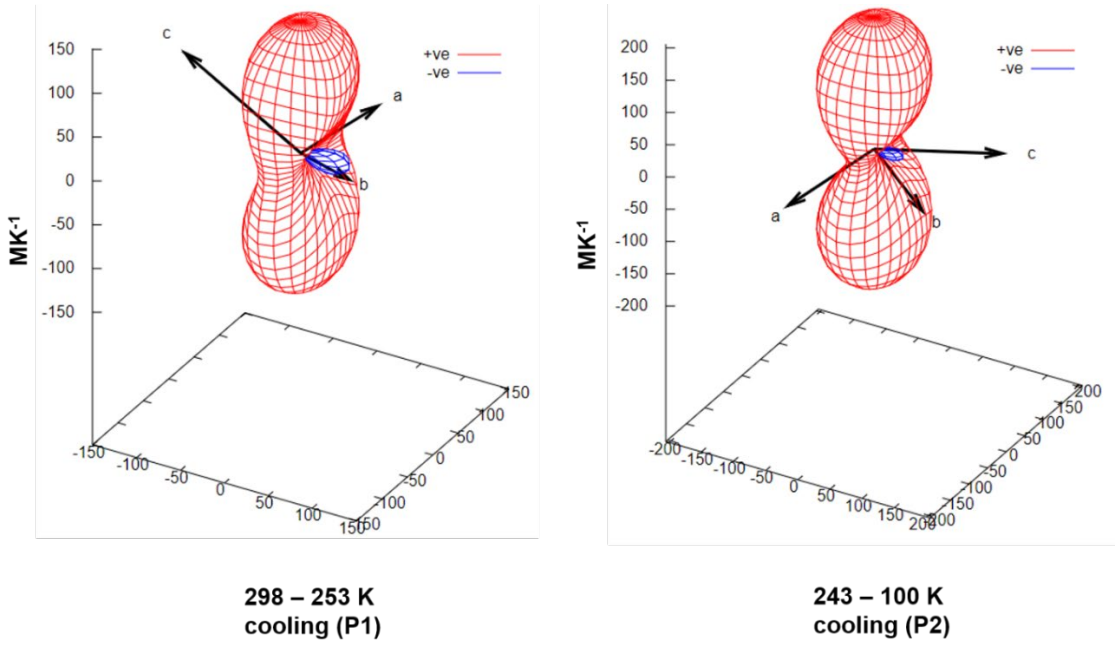

Figure S19 Expansivity indicatrix of **CdPCP-P1** (left) and **CdPCP-P2** (right) on cooling (298 to 100 K).

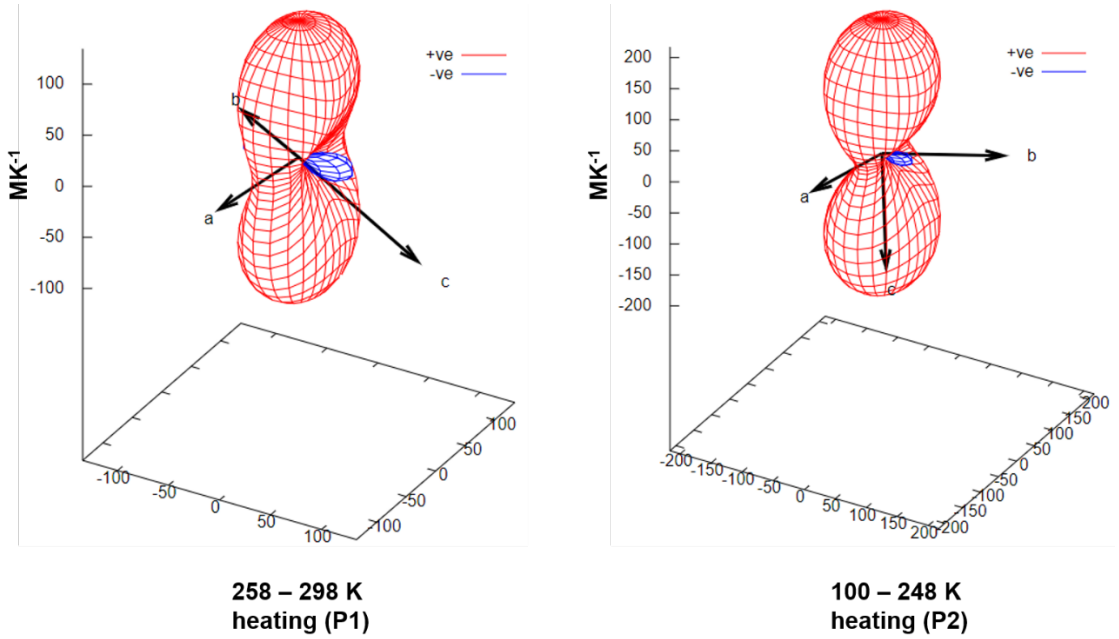

Figure S20 Expansivity indicatrix of **CdPCP-P1** and **CdPCP-P2** on heating (100 to 298 K).

Table S5 Thermal expansion coefficients α_{X1}, α_{X2}, and α_{X3} and volumetric thermal expansion coefficients (α_V) for **CdPCP-P1** and **CdPCP-P2** on cooling and heating.

Temperature range (K)	Phase	α_{X1} (MK^{-1})	α_{X2} (MK^{-1})	α_{X3} (MK^{-1})	α_V (MK^{-1})
298 - 253	P1	-56(6)	67(7)	150(8)	186(17)
243 - 100	P2	-45(2)	59(1)	205(5)	218(4)
100 - 248	P2	-48(2)	60(1)	216(5)	226(3)
258 - 298	P1	-53(6)	63(5)	135(8)	163(15)

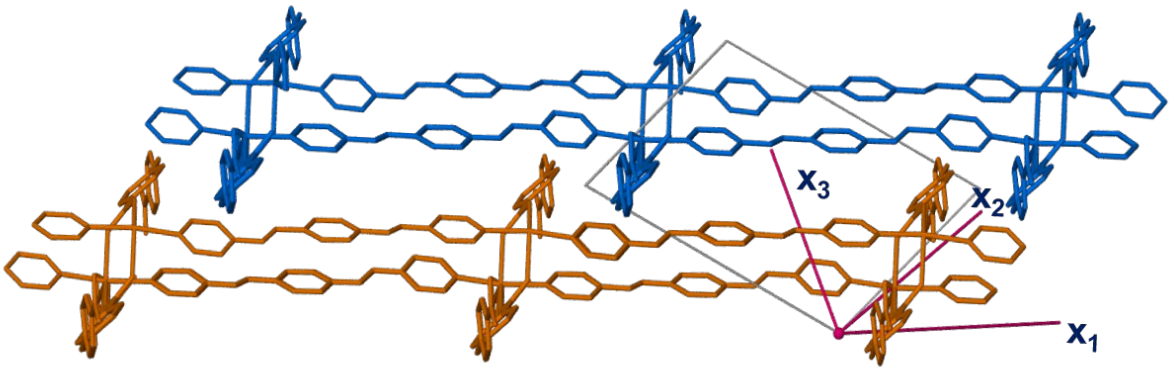

Figure S21 Principal axes for the coefficients of thermal expansion in **CdPCP-P1**. The largest coefficient of thermal expansion, α_{x3}, running along the x_3 principal axis, coincides with the expansion between the 2D layers.

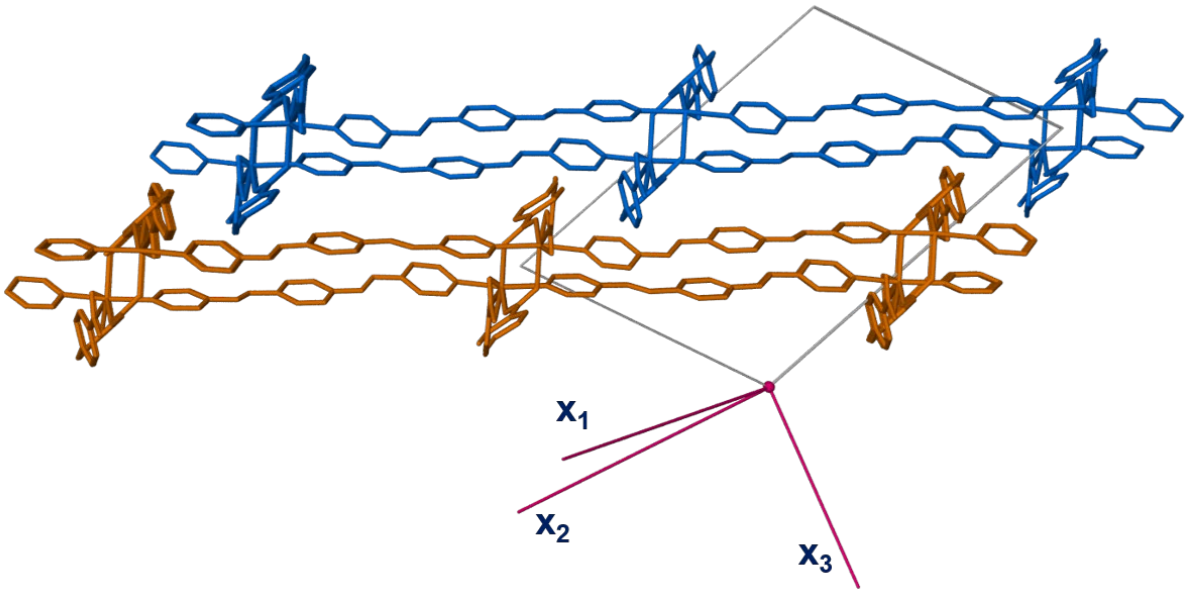

Figure S22 Principal axes for the coefficients of thermal expansion in **CdPCP-P2**. The largest coefficient of thermal expansion, α_{x3}, running along the x_3 principal axis, coincides with the expansion between the 2D layers.

SCXRD structures after irradiation at 100 K

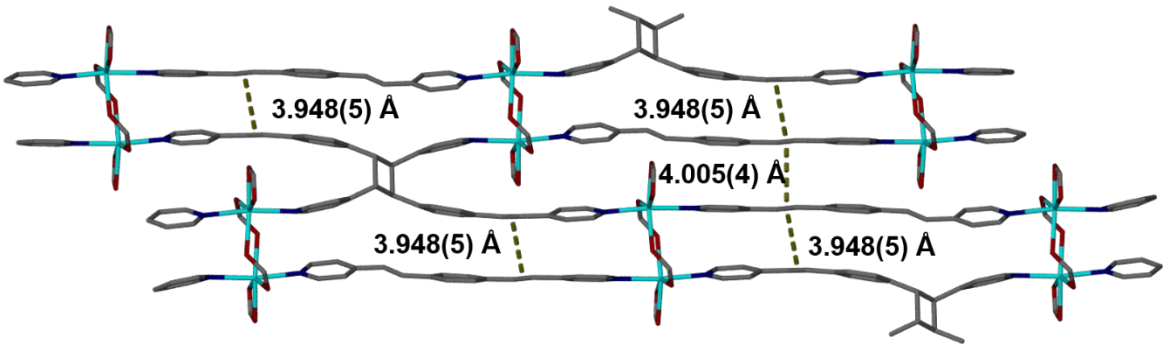

Figure S23 Potentially photoactive positions and distances between the olefinic bonds at 100 K in **CdPCP-P2** after irradiation at 100 K .Hydrogen atoms and solvent molecules are omitted for clarity.

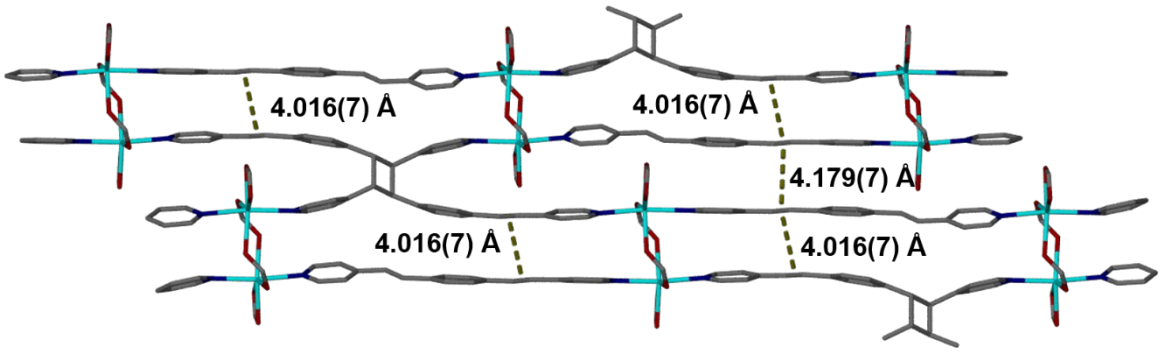

Figure S24 Potentially photoactive positions and distances between the olefinic bonds at 298 K in **CdPCP-P2** after irradiation at 100 K. Hydrogen atoms and solvent molecules are omitted for clarity.

PXRD

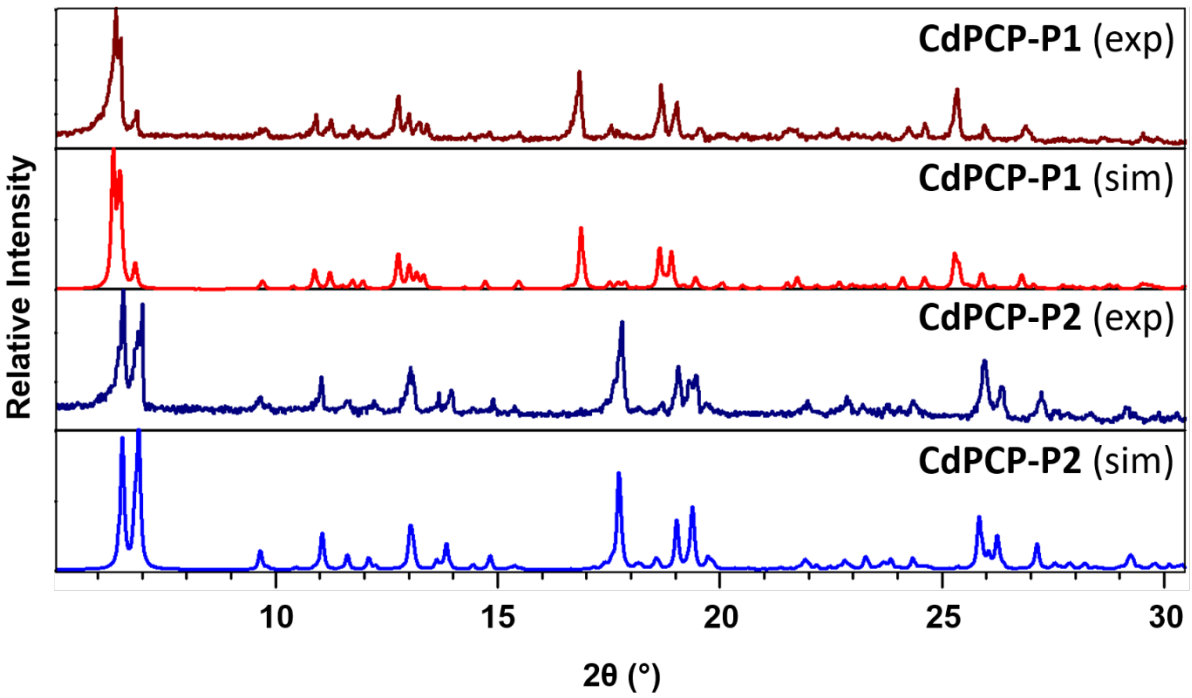

Figure S25 Experimental and simulated powder diffraction patterns of **CdPCP-P1** (298 K) and **CdPCP-P2** (100 K).

Variable-temperature PXRD

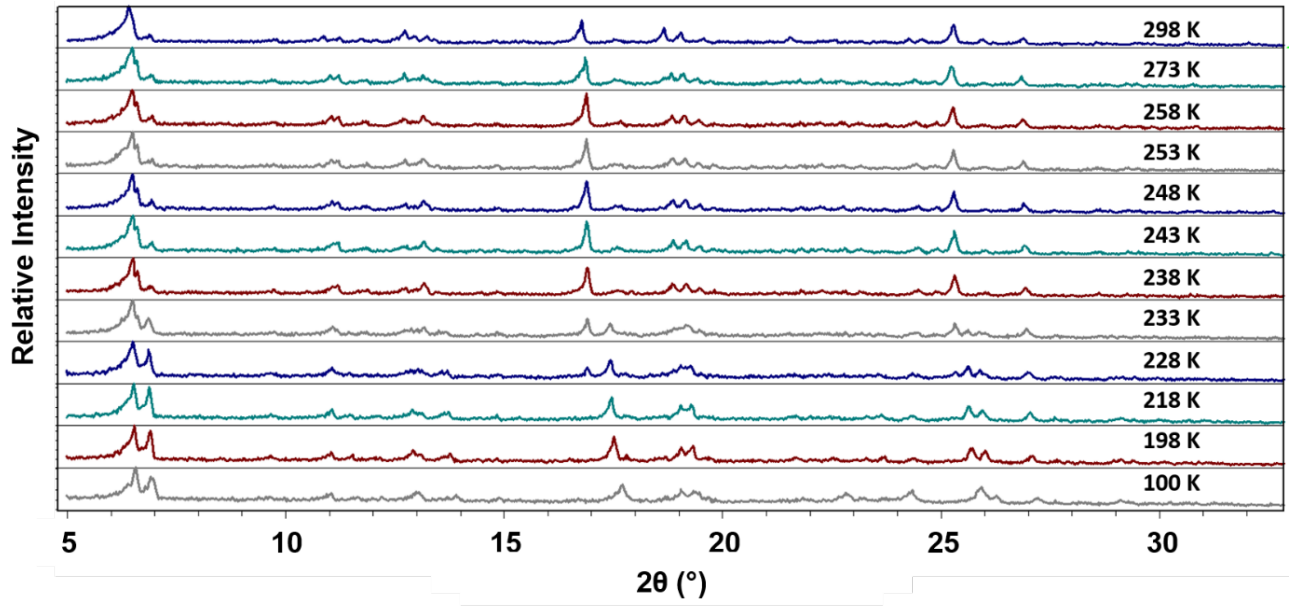

Figure S26 Variable-temperature PXRD of **CdPCP** from 298 to 100 K (cooling). The phase transition from **CdPCP-P1** to **CdPCP-P2** is observed in the 233 and 228 K diffractograms.

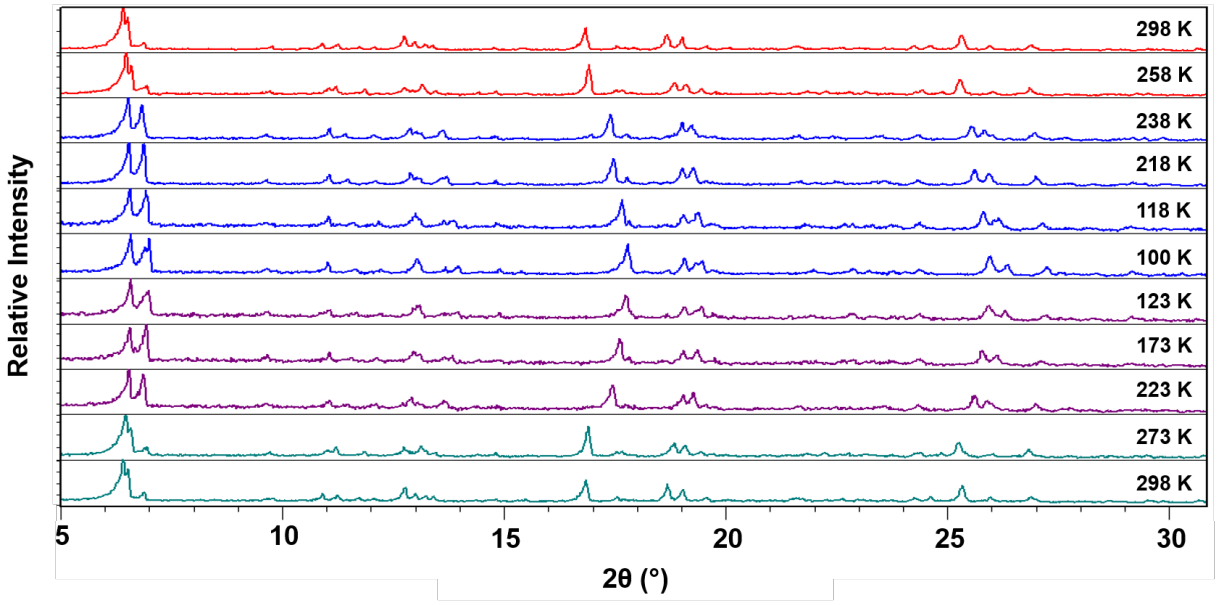

Figure S27 Powder diffractograms of **CdPCP** cooled from 298 to 100 K, followed by reheating to 298 K (top to bottom). The change from **CdPCP-P1** to **CdPCP-P2** and back can clearly be seen. The red colour indicates initial **CdPCP-P1**, whilst blue indicates **CdPCP-P2** obtained on cooling. The purple colour indicates **CdPCP-P2** which remains on heating from 100 to 223 K, and the teal colour indicates reconversion to **CdPCP-P1** on heating past 223 K.

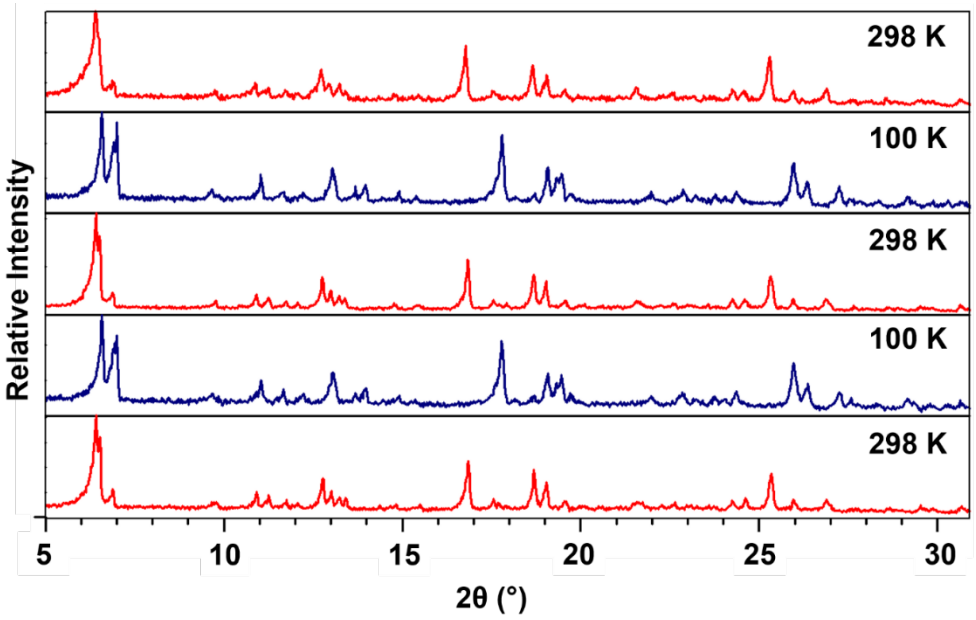

Figure S28 Variable-temperature PXRD of **CdPCP**. Consecutive cycles on the same sample are given to show the reversibility of the phase transition between **CdPCP-P1** and **CdPCP-P2**.

References

(1) Degen, T.; Sadki, M.; Bron, E.; König, U.; Nénert, G. The HighScore suite. *Powder Diffr.* **2014**, *29*, S13-S18.
(2) Macrae, C. F.; Bruno, I. J.; Chisholm, J. A.; Edgington, P. R.; McCabe, P.; Pidcock, E.; Rodriguez-Monge, L.; Taylor, R.; van de Streek, J.; Wood, P. A. Mercury CSD 2.0 - new features for the visualization and investigation of crystal structures. *J. Appl. Crystallogr.* **2008**, *41*, 466-470.
(3) Bruker (2012). SAINT. Bruker AXS Inc., Madison, Wisconsin, USA.
(4) Bruker (2001). SAINT. Bruker AXS Inc., Madison, Wisconsin, USA.
(5) Sheldrick, G. M. A short history of SHELX. *Acta Crystallogr. Sect. A* **2008**, *64*, 112-122.
(6) Sheldrick, G. M. Crystal structure refinement with SHELXL. *Acta Crystallogr. Sect. C* **2015**, *71*, 3-8.
(7) Barbour, L. J. X-Seed - A Software Tool for Supramolecular Crystallography. *J. Supramol. Chem.* **2001**, *1*, 189-191.
(8) Atwood, J. L.; Barbour, L. J. Molecular Graphics: From Science to Art. *Cryst. Growth Des.* **2003**, *3*, 3-8.
(9) Malaspina, L. A.; Edwards, A. J.; Woińska, M.; Jayatilaka, D.; Turner, M. J.; Price, J. R.; Herbst-Irmer, R.;. Sugimoto, K.; Nishibori, E.; Grabowsky, S. Predicting the Position of the Hydrogen Atom in the Short Intramolecular Hydrogen Bond of the Hydrogen Maleate Anion from Geometric Correlations. *Cryst. Growth Des*. **2017**, *17*, 3812-3825.
(10) Spek, A. L. Structure validation in chemical crystallography. *Acta Crystallogr. Sect. D* **2009**, *65*, 148-155.
(11) Spek, A. L. PLATON SQUEEZE: a tool for the calculation of the disordered solvent contribution to the calculated structure factors. *Acta Crystallogr. Sect. C* **2015**, *71*, 9-18.
(12) Persistence of Vision Pty. Ltd. (2004). POV-Ray. Persistence of Vision Pty. Ltd., Williamstown, Victoria, Australia.
(13) Dolomanov, O. V.; Bourhis, L. J.; Gildea, R. J.; Howard, J. A. K.; Puschmann, H. OLEX2: a complete structure solution, refinement and analysis program. *J. Appl. Crystallogr.* **2009**, *42*, 339-341.
(14) Blatov, V. A.; Shevchenko, A. P.; Proserpio, D. M. Applied Topological Analysis of Crystal Structures with the Program Package ToposPro. *Cryst. Growth Des.* **2014**, *14*, 3576-3586.
(15) Claassens, I. E.; Nikolayenko, V. I.; Haynes, D. A.; Barbour, L. J. Solvent-Mediated Synthesis of Cyclobutane Isomers in a Photoactive Cadmium(II) Porous Coordination Polymer. *Angew. Chemie Int. Ed.* **2018**, *57*, 15563-15566.
(16) *Dassault Systèmes BIOVIA Materials Studio*, Release 18, San Diego: Dassault Systèmes, **2017**.
(17) Cliffe, J.; Goodwin, A. L. PASCal: a principal axis strain calculator for thermal expansion and compressibility determination. *J. Appl. Crystallogr.*, **2012**, *45*, 1321-1329.

Chapter 4

Tuning gate-opening pressure and hysteresis in a highly flexible pillared-layered metal-organic framework by ligand fluorination

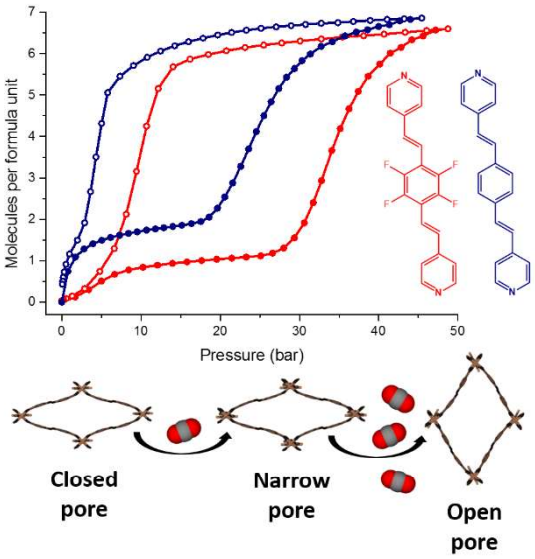

3.1 To be submitted

Both frameworks were first prepared by Dr Charl Bezuidenhout. Initial activation and volumetric sorption analysis of the fluorinated framework was carried out together with Bezuidenhout. Computational work was carried out by Prof Catharine Esterhuysen.The author is responsible for all further contributions, including:

- Design of project
- Synthesis of MOF and ligands with Charl Bezuidenhout
- Collection and analysis of volumetric sorption data
- Collection and analysis of PGDSC sorption data with Wesley Feldmann
- Collection of *in situ* variable pressure single-crystal X-ray data solution and refinement of single-crystal X-ray structures and collection and analysis of *in situ* variable-pressure powder X-ray data
- Collection of TGA thermograms
- Interpretation of results after discussions with Wesley Feldmann
- Computational work was carried out by Catharine Esterhuysen
- Writing the first draft of the article

ARTICLE

Tuning gate-opening pressure and hysteresis in a highly flexible pillared-layered metal-organic framework by ligand fluorination

Received 00th January 20xx,
Accepted 00th January 20xx

DOI: 10.1039/x0xx00000x

Isabella E. Claassens, Wesley K. Feldmann, Charl X. Bezuidenhout, Catharine Esterhuysen, Delia A. Haynes* and Leonard J. Barbour*

A new highly flexible four-fold interpenetrated fluorinated MOF, as well as the isoreticular non-fluorinated analogue, have been prepared. The isoreticular nature of these MOFs has allowed a detailed study of the effect of fluorination of the organic pillar linker on the properties of the resulting MOFs. Gas sorption analysis reveals significant changes in gate-opening pressure as well as the degree of hysteresis observed between the two framemworks. *In-situ* SCXRD techniques and computational analysis are emplyed to identify the interactions responsible for the change in behaviour.

Introduction

Metal-organic frameworks (MOFs) are a versatile class of crystalline materials known for their porosity and tunability.[1-3] Flexible MOFs or "soft porous crystals" are an exciting and rapidly growing subclass of frameworks that respond to external stimuli such as gas pressure, temperature or light.[4-9] Four modes of flexibility have been identified, namely breathing, swelling, linker rotation and subnetwork displacement.[5] As the material flexes, it undergoes a structural transition.[6,10,11] This often leads to a change in porosity, resulting in a 'stepped' gas sorption isotherm with a hysteresis loop, which increases the working capacity for gas uptake and release.[12] Flexible MOFs have potential applications in gas storage[12] and separation,[13,14] sensor technology[15,16] and catalysis.[17] To move towards designing commercially viable flexible systems, it is crucial to understand and thereby control the different modes of flexibility. Some recent studies have investigated means of tuning the onset pressure of the structural transition in flexible MOFs by means of ligand substitution and functionalisation,[18,19] metal substitution [20-22] and variation in particle size,[23,24] but the concept remains underexplored.[19] Hysteresis in gas sorption and desorption in a framework is another aspect of flexible MOFs that has not been investigated systematically. Hysteresis can lead to lower energy penalties for regeneration of the material, and often result in greater working capacities in terms of CO_2 storage and release.[25]

Many pillared-layered MOFs (PL-MOFs) are flexible. They are comprised of a 2D net formed by a metal cluster and one type of organic ligand, with a second ligand functioning as a pillar that links the nets to yield a three-dimensional framework. Here we report a new highly flexible PL-MOF that exhibits a stepped hysteretic isotherm profile with CO_2, C_2H_4 and C_3H_8. We also explore the effect of fluorine functionalisation of the pillaring ligand on both the gate-opening onset pressure and the degree of hysteresis. *In-situ* crystallographic techniques and density functional theory calculations were employed to provide insight into the intermolecular interactions governing the behaviour of the two MOFs during the gas sorption process.

Results and discussion

The hydrothermal reaction of 4,4'-[(2,3,5,6-tetrafluoro-1,4-phenylene)-2,1-ethenediyl]bis-pyridine (fbpeb), 4,4'-azodibenzoic acid ($adcH_2$) and $Zn(NO_3)_2{\cdot}4H_2O$ in DMF afforded orange-red petal-shaped crystals of $[Zn_2(adc)_2(fbpeb)]{\cdot}4DMF{\cdot}2H_2O$ (**1as**). Single crystal X-ray diffraction (SCXRD) revealed that **1as** crystallises in the monoclinic space group *C*2/*c*. The framework is comprised of dinuclear Zn(II) tetracarboxylate paddlewheel secondary building units (SBU) linked by adc ions to form a square lattice net propagating along (010). The nets are pillared along [101] by the flexible fbpeb linkers to afford a **pcu** topology. The structure is 4-fold interpenetrated with the interpenetrated nets forming large undulating channels along [101] that accommodate 4 DMF and 2 H_2O guest molecules per host formula unit (HFU). TGA analysis confirmed this host-guest stoichiometry, showing a mass loss of 22.0% (calc: 21.47%) up to 120 °C, with decomposition commencing at 320 °C.

The calculated guest-accessible volume of **1as** is 33.1%‡ and its bulk phase purity was confirmed by powder X-ray diffraction (PXRD) (Fig. S10). Heating **1as** at 125 °C under reduced pressure resulted in removal of the guest and formation of a closed-pore phase, **1cp**. SCXRD analysis revealed complete collapse of the 1D channels, resulting in 0% guest-accessible volume and no

Department of Chemistry and Polymer Science, University of Stellenbosch, Matieland, 7600, South Africa. E-mail: ljb@sun.ac.za
† Footnotes relating to the title and/or authors should appear here.
Electronic Supplementary Information (ESI) available: [details of any supplementary information available should be included here]. See DOI: 10.1039/x0xx00000x

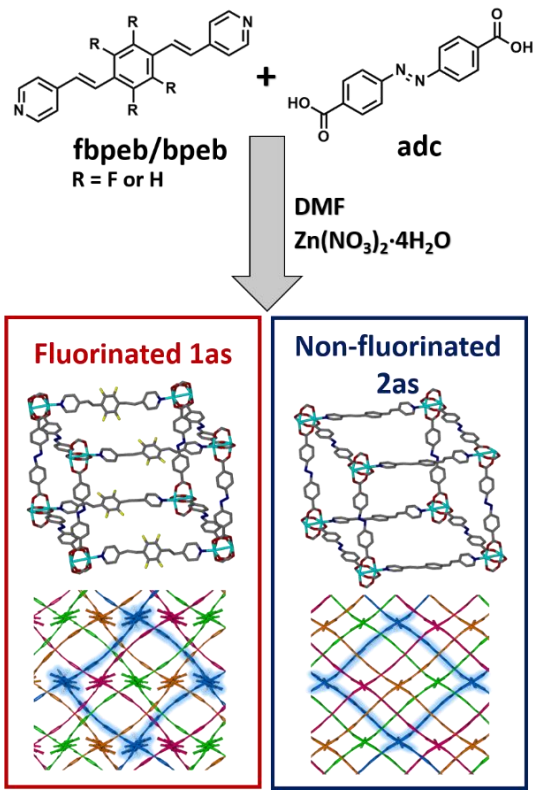

Fig.1 Schematic of the synthesis of a fluorinated flexible pillared-layered framework (**1as**) and its isoreticular non-fluorinated analogue (**2as**). Both the connectivity of the pillared-layered structure and the four-fold interpenetration are displayed for each framework.

residual electron density. The nets undergo a "closing" breathing motion with a slight subnetwork displacement between neighbouring nets. This is accompanied by a change in space group from *C*2/*c to C2/m* and an overall 28.1% reduction in unit cell volume.

Although **1cp** is seemingly non-porous, high-pressure gas sorption analyses using N_2, CH_4, C_2H_4, C_3H_8 and CO_2 were carried out at 298 K, since several seemingly non-porous frameworks have been shown to open with the appropriate stimulus or gas pressure.[26] These gases were selected to represent a range of different sizes and polarities. Uptake of N_2 and CH_4 was negligible (<0.5 mmol g^{-1}) up to 50 bar. On the other hand, the CO_2 sorption isotherm shows stepped uptake with exceptionally large hysteresis. Between 0 and ~23 bar, one molecule of CO_2 is included per HFU with a type I profile. Since **1cp** has no guest-accessible space, it is likely that it undergoes a small gate-opening event below ~23 bar to accommodate the guest, yielding a narrow-pore phase, **1np**. This probably occurs upon commencement of the measurement, which is why the characteristic inflection is not evident in the isotherm profile. The major gate-opening event has an onset pressure of approximately 23 bar, which is evidenced by an inflection in the sorption isotherm, indicating that the framework undergoes a phase change from **1np** to a highly porous phase, **1op** (open-pore). **1op** accommodates a further 5.8 molecules of CO_2 per HFU, resulting in a loading capacity of 6.8 molecules of CO_2 at 50 bar. Upon desorption, **1op** exhibits large hysteresis (52%) and 6 CO_2 molecules per HFU are retained within the framework until 15 bar, suggesting favourable host-guest interactions. Thereafter all of the CO_2 molecules are released and the structure reverts back to the closed-pore phase, **1cp**. Adsorption and desorption experiments were carried out in triplicate, yielding reproducible isotherm profiles.

The guest inclusion behaviour of **1cp** was further investigated using pressure-gradient differential scanning calorimetry (PGDSC).[27] CO_2 sorption (Fig. 2b) yields an exotherm between 0 and 15 bar, corresponding to the initial uptake of one molecule of CO_2 per HFU. Small peaks and shoulders are observed, indicating that the framework undergoes a subtle structural transition at these pressures, converting to **1np**. The

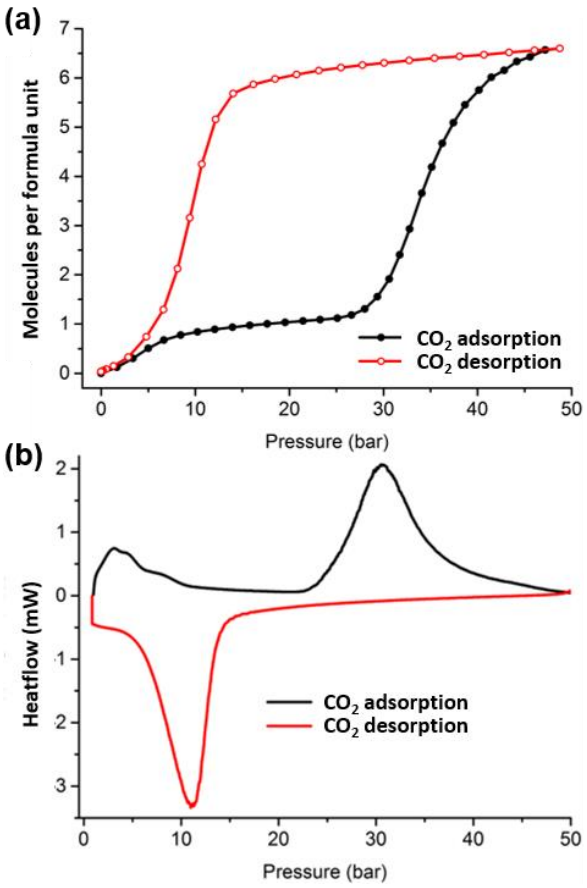

Fig. 2 (a) CO_2 adsorption (black) and desorption (red) isotherms for 1 recorded at 298 K. (b) PGDSC trace showing thermal events corresponding to inflections observed during adsorption (black) and desorption (red) in the isotherm.

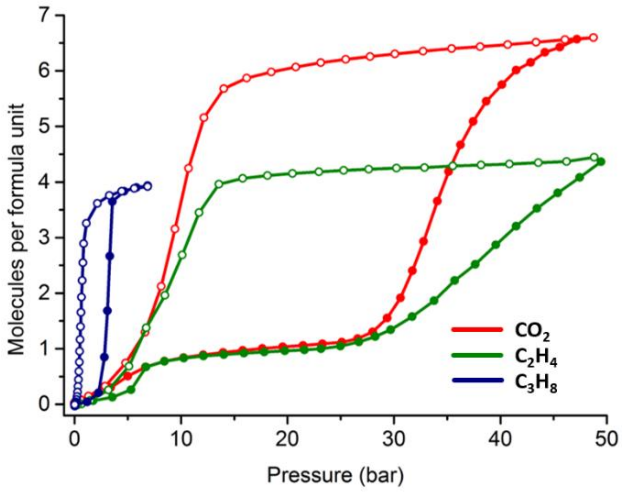

Fig. 3 Comparison of the sorption isotherms of **1** for CO_2 (red), C_2H_4 (green) and C_3H_8 (blue) at 298 K.

large adsorption exotherm (23 bar) and desorption endotherm (15 bar) correspond to the gate opening and closing events in the sorption profile (Fig. 2a), respectively.

The C_2H_4 adsorption profile is similar to that for CO_2, although the initial gate opening event from **1cp** to **1np** is observed at ~4 bar, with a similar onset pressure (22 bar) for the **1np** to **1op** transition. A maximum uptake of 4.45 molecules per HFU (3.8 mmol g^{-1}) was observed at 50 bar, with large hysteresis (53.5%) occurring upon desorption. Interestingly, propane (C_3H_8) shows no initial uptake up to 1 bar, whereupon it opens to accommodate a maximum of 4 molecules of propane per HFU (4 mmol g^{-1}). This F-IV-type isotherm,[26] exhibiting negligible uptake, is rarely observed in flexible frameworks and is highly desirable for pressure-swing adsorption and gas storage.[28]

The PGDSC thermogram for sorption of C_2H_4 and C_3H_8 by **1** exhibit exotherms and endotherms that correspond to the steps observed in the isotherms (Figs S20-S23). The C_2H_4 desorption profile shows a distinct endotherm at ~6 bar, corresponding to a structural change from **1np** to **1cp**, which cannot be clearly observed in the isotherm (Fig. S20). The thermogram for C_3H_8 confirms negligible gas uptake below 1 bar, and also shows large hysteresis, with propane retained within the material at ambient conditions.

In order to obtain further insight into the structural changes during CO_2 loading (as inferred from the sorption analyses) *in situ* variable-pressure SCXRD and PXRD analyses were carried out using environmental gas cells. Owing to the significant changes in structure, obtaining single crystals of all the phases was challenging. Nevertheless, we were ultimately able to obtain single-crystal structures for all of the phases. A fully activated single crystal of **1cp** (Fig. 4, absence of residual electron density) was exposed to 10 bar of CO_2 and allowed to equilibrate, during which time **1cp** transformed to **1np** (Fig. 4). SCXRD analysis of **1np** revealed a slight twisting of the paddlewheels, resulting in a small opening of the net. Discrete pockets of solvent-accessible space (259 $Å^3$) formed between the perfluorinated ring of the fbpeb linker and the metal node of a neighbouring net. Although the CO_2 molecule could not be modelled without extensive restraints, the residual electron density corresponds well to the measured loading of 1 CO_2 molecule per formula unit. The **1cp** → **1np** transformation is accompanied by a change in symmetry from monoclinic *C*2/*m* to *C*2/*c*. Both **1cp** and **1np** have side-on aryl-perfluoroaryl interactions between fbpeb ligands (Fig. S30-32 and *vide infra*).

SCXRD analysis of was carried out at 50 bar, yielding the structure of **1op**. The phase transition from **1np** to **1op** is coupled to a change in symmetry from monoclinic *C*2/*c* to $P2_1/c$ and an overall 32% increase in unit cell volume. The orientation

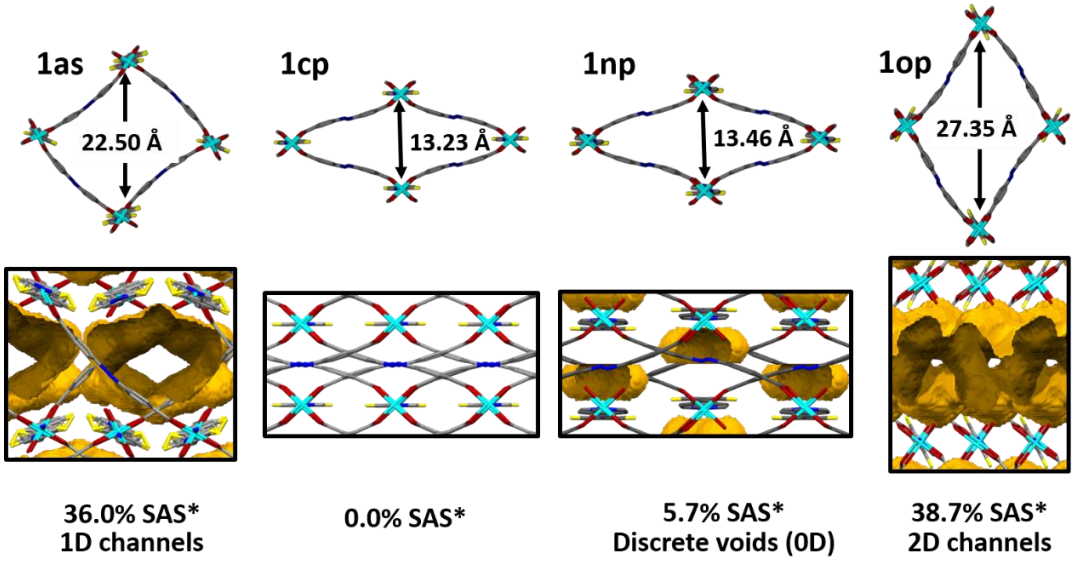

Fig. 4 Crystal structures of **1as**, **1cp**, **1np** and **1op** obtained during *in-situ* SXCRD analysis in a 10 bar and 50 bar CO_2 environment for **1np** and **1op** respectively. SAS* refers to the solvent accessible space as displayed below each structure.

of the fbpeb linkers changes, resulting in offset-stack interactions between aryl and perfluoroaryl moieties. The distance between the paddlewheels in a net increases from 13.46 to 27.35 Å in one direction and decreases from 30.73 to 20.19 Å in the other, in accordance with a large breathing motion. Surprisingly the phase transition from **1np** to **1op** takes place from single-crystal to single-crystal despite the significant structural changes that occur during this transition. Sub-network displacement also occurs as the interpenetrated nets shift relative to one another, allowing for the formation of large two-dimensional channels along [1 0 0] and [0 0 1] in which the CO_2 guest molecules are located. The solvent accessible space thereby increases from 5.5 % in **1np** to 38.8% in **1op**. The CO_2 guest molecules could not be modelled, but electron count analysis using Platon SQUEEZE revealed 7.4 molecules of CO_2 per formula unit. This corresponds well to the gas sorption isotherm, where CO_2 loading was 6.8 molecules at 50 bar.

In-situ variable-pressure PXRD studies on **1** were performed with C_2H_4, C_3H_8 and CO_2 over a range of pressures. The measured and simulated patterns were compared for the respective phases, and an excellent match was obtained for all phases observed during CO_2 sorption (Fig. S26). The PXRD patterns also confirm the subtle difference between **1cp** and **1np**. A distinct change in the PXRD pattern is observed corresponding to the transition from **1np** to **1op**. The PXRD patterns measured during the sorption of C_2H_4 and C_2H_8 closely match the simulated patterns for the CO_2-loaded structures, suggesting that the framework opens to yield the same phases independent of the guest used.

A few studies have investigated the effects of fluorination on host-guest interactions in PCPs.[29] We therefore synthesised a non-fluorinated structural equivalent to framework **1** to study the effect of fluorination for sorption applications. Fluorine functionalization is often used to promote electrostatic interactions between guest molecules, such as CO_2 and C_2H_4 and the host framework.

$[Zn_2(adc)_2(bpeb)]\cdot 4DMF$ (**2as**) was synthesised using the same synthetic procedure as **1as**, but the fluorinated fbpeb linker was replaced with with the non-fluorinated equivalent, 1,4-bis[2-(4-pyridyl)ethenyl]-benzene (bpeb). **2as** crystallised in the monoclinic space group *C2/c* with a pillared-layered structure isoreticular to **1as**. The framework is also four-fold interpenetrated with pcu topology. In **2as**, the solvent-accessible space constitutes 41.2% of the unit cell volume in the form of two-dimensional channels running along [0 1 0] and [0 0 1]. SQUEEZE[29] electron count and thermal analysis confirmed the presence in the channels of four DMF molecules per formula unit. Bulk phase purity of **2as** was confirmed with PXRD analysis (SI).

Activation of **2as** was carried out by heating at 160 °C under reduced pressure. SCXRD analysis showed that **2as** does not completely collapse upon guest removal, but transitions to a narrow-pore phase, **2np**. The nets undergo a closing breathing motion coupled to a minor subnetwork displacement between neighbouring nets. A 25% reduction in unit cell volume is observed, with no change to the space group upon activation. This is accompanied by a reduction in solvent-accessible space

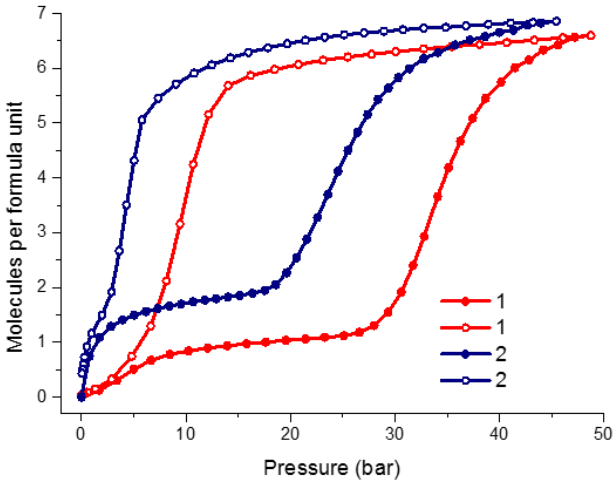

Fig 5 Comparison of the CO_2 adsorption and desorption isotherms of **1** (red) and **2** (blue) between 0 and 50 bar.

from 41.2 to 12.0%. Guest molecules are absent from the discrete pockets within the framework as confirmed by TGA and SQUEEZE[30] analysis of **2np**. The absence of the fluorine atoms is a potential reason for **2as** not collapsing completely to a closed-pore form. The possibility for C-F···H-C interactions between neighbouring nets is eliminated in **2**, making the completely closed form less favourable.

Gas sorption analysis was carried out in the same manner as with framework **1**. Sorption of N_2, CH_4, C_2H_4, C_3H_8 and CO_2 was analysed at 298 K to evaluate the effect of framework fluorination on gas sorption behaviour. **2np** showed minor uptake of N_2 and CH_4 up to 50 bar, with no opening of the structure. The adsorption of CO_2 resulted in a stepped isotherm, due to a structural opening (**2np** → **2op**) with an onset of ~13 bar. The maximum loading capacity for the material was 6.85 CO_2 guest molecules per formula unit. Compared to the fluorinated framework, the onset pressure in **2** is lowered considerably, from 23 to 13 bar. A comparison between the loading capacities for **1op** (6.8 molecules) and **2op** (6.85 molecules) shows a minor increase for **2op**. This may be due to the reduced size of hydrogen compared to the larger fluorine atoms, ultimately leading to a slight increase in accessible space for guest molecules in **2op**. The isotherms of both materials show hysteresis upon desorption, although **1** has a considerably larger degree of hysteresis, suggesting stronger host-guest interactions. The C_2H_4 sorption profile shows a distinct difference between the onset pressures of the gate-opening events **1np**→**1op** and **2np**→**2op**. The **2np**→**2op** transition (7 bar) occurs at a significantly lower pressure than **1np**→**1op** (25 bar), and the maximum loading capacity is greater in **2op** (4.5 molecules) when compared to **1op** (5.6 molecules). The C_3H_8 sorption profile also shows a distinct difference in the onset pressure for the gate-opening events **1cp**→**1op** and **2np**→**2op**. Once again, the **2np**→**2op** transition occurs at a much lower pressure (0.5 bar) than **1cp**→**1np/1op** (1.2 bar). Interestingly, **1cp** shows no uptake until a threshold pressure is reached, after

which it undergoes the changes to **1np** and **1op** in quick succession. In comparison, **2op** exhibits a rapid gate-opening with propane, which may be due to the large kinetic diameter (size) of propane pushing the framework open when no structure-directing interactions are keeping it locked in the closed pore form. The maximum capacity for **2op** (3.6 molecules) is only slightly less than that of **1op** (3.9 molecules). This is lower than the maximum capacity of both CO_2 and C_2H_4 due to the larger size of C_3H_8. PGDSC measurements were also carried out (SI), corroborating the analysis of the sorption isotherms in terms of gate opening events and adsorption and desorption onset pressures.

Unfortunately, variable pressure SCXRD analysis studies could not be performed on **2op** as the structural change resulted in disintegration of the single crystal with every attempt. Variable-pressure PXRD studies were thus carried out to give some structural information about the open-pore form of **2**. PXRD patterns confirm that **2op** for CO_2 (50 bar) and C_2H_4 (bar) have the same structure, as the patterns match very well. The patterns are almost identical to **2as**, suggesting the same framework structure. The PXRD pattern of the C_3H_8-included **2op** (at 7bar) also compares well, with some small differences that may be due to insufficient equilibration time.

Structurally, the important difference between **1** and **2** is the fluorination of the ligand in **1**. In order to attempt to explain the changes in gate-opening pressure and hysteresis between **1** and **2**, we have focussed on interactions involving the fbpeb ligands. In order to confirm that the aryl-perfluoroaryl intermolecular interactions have an important effect on the gate-opening pressures of **1**, we have calculated the interaction energies for these interactions at the PBE-D3/def2-TZVP level of theory in the various forms of **1**. In the structure of **1cp**, the fluorinated fbpep pillars are arranged alongside one another in a slipped manner, allowing for favourable side-on interactions between the fluorinated and non-fluorinated aryl rings of neighbouring molecules (Fig. S30-32). On increasing the pressure, the molecules move further apart, with a concomitant decrease in the energy of the interaction (Table S1). The structure of **1np**, which was determined at 10 bar, has these same side-on interactions at a very similar distance and thus a very similar energy. The structure of **1op** was determined at both 26 bar and 50 bar. In this phase, there are no longer side-on aryl-perfluoroaryl interactions. Instead, the opening up of the structure results in changes in orientation of the fbpep ligands. In **1op** the fbpep ligands are stacked on top of one another, resulting in offset π-π interactions between the aryl and perfluoroaryl moieties (Fig. S30-32). These interactions are energetically significantly more favourable than those in **1cp** and **1np**. We propose that it is this very favourable interaction that results in the large hysteresis in sorption exhibited by **1**.

We assume that similar interactions exist in the structures of **2**, but because the ligand is not fluorinated these interactions do not have the added favourable electrostatic component and are likely to be less stabilising.

Conclusions

The effect of fluorination on the gas sorption behaviour of a new flexible pillared-layer MOF (**1**) has been investigated by comparison to its non-fluorinated isoreticular analogue (**2**) Both new frameworks have been comprehensively characterised. *In-situ* SCXRD showed a complete collapse of the channels in **1** and a partial collapse of the channels in **2** on activation. Gas sorption analysis revealed an opening of the structures with CO_2, C_2H_4 and C_3H_8, but not with N_2 and CH_4, for both frameworks. The fluorinated framework exhibits greater hysteresis, but the onset pressure of the gate-opening event is quite substantially delayed in comparison to the non-fluorinated analogue: in the case of CO_2, the onset pressure of shifted from 13 bar in the non-fluorinated framework to 23 bar in the fluorinated MOF, with much larger hysteresis observed in the fluorinated framework. Similar trends were observed with C_2H_4 and C_3H_8. *In-situ* XRD as well as computational analysis demonstrated that the fluorination of the organic pillar linker promotes C-F…H-C interactions between linkers, which appear to hold the framework closed on increasing gas pressure. Conversely, the non-fluorinated MOF lacks these interactions, and has lower gate-opening pressures and narrower hysteresis. We thus demonstrate that fluorination of the pillar ligand is a simple and useful tool to tune both the gate-opening pressure and hysteresis in pillared-layered frameworks.

Conflicts of interest

There are no conflicts to declare.

Acknowledgements

We thank the National Research Foundation of South Africa and SASOL for financial support.

Notes and references

‡ Void space was calculated with a 1.4 Å probe radius and a grid spacing of 0.2 Å using Mercury.[27]

1 H. C. Zhou, J. R. Long and O. M. Yaghi, *Chem. Rev.*, 2012, **112**, 673.
2 S. Kitagawa and M. Kondo, *Bull. Chem. Soc. Jpn*., 1998, **71**, 1739.
3 H. Furukawa, K. E. Cordova, M. O'Keeffe and O. M. Yaghi, *Science*, 2013, 341, 1230444.
4 S. Horike, S. Shimomura and S. Kitagawa, *Nat. Chem.*, 2009, **1**, 695.
5 A. Schneemann, V. Bon, I. Schwedler, I. Senkovska, S. Kaskel and R. A. Fischer, *Chem. Soc. Rev.*, 2014, **43**, 6062.
6 Z. Chang, D. H. Yang, J. Xu, T. L. Hu and X. H. Bu, *Adv. Mater*., 2015, **27**, 5432.
7 R. E. Morris and L. Brammer, *Chem. Soc. Rev*., 2017, **46**, 5444.
8 S. K. Elsaidi, M. H. Mohamed, D. Banerjee and P. K. Thallapally, *Coord. Chem. Rev.*, 2018, **358**, 125.
9 F.-X. Coudert, *Chem. Mater.*, 2015, **27**, 1905.
10 T. Loiseau, C. Serre, C. Huguenard, G. Fink, F. Taulelle, M. Henry, T. Bataille, G.Férey. *Chem. Eur. J.*, 2004, **10**, 1373.

11 S. Bourrelly, P. L. Llewellyn, C. Serre, F. Millange, T. Loiseau, G. Férey, *J. Am. Chem. Soc.*, 2005, **127**, 13519.
12 J. A. Mason, J. Oktawiec, M. K. Taylor, M. R. Hudson, J. Rodriguez, J. E. Bachman, M. I. Gonzalez, A. Cervellino, A. Guagliardi, C. M. Brown, P. L. Llewellyn, N. Masciocchi and J. R. Long, *Nature*, 2015, **527**, 357.
13 B. Zornoza, A. Martinez-Joaristi, P. Serra-Crespo, C. Tellez, J. Coronas, J. Gascon and F. Kapteijn, *Chem. Commun.*, 2011, **47**, 9522.
14 A. Chakraborty, S. Roy, M. Eswaramoorthy and T. K. Maji, *J. Mater. Chem.* A, 2017, **5**, 8423.
15 P. Freund, I. Senkovska and S. Kaskel, *ACS Appl. Mater. Interfaces*, 2017, **9**, 43782.
16 A. Douvali, A. C. Tsipis, S. V. Eliseeva, S. Petoud, G. S. Papaefstathiou, C. D. Malliakas, I. Papadas, G. S. Armatas, I. Margiolaki and M. G. Kanatzidis, *Angew. Chem.*, 2015, **127**, 1671.
17 S. Yuan, L. Zou, H. Li, Y. P. Chen, J. Qin, Q. Zhang, W. Lu, M. B. Hall and H. C. Zhou, *Angew. Chem., Int. Ed.*, 2016, **55**, 10776.
18 M. K. Taylor, T. Runčevski, J. Oktawiec, M. I. Gonzalez, R. L. Siegelman, J. A. Mason, J. Ye, C. M. Brown and J. R. Long, *J. Am. Chem. Soc.*, 2016, **138**, 15019.
19 A.-X. Zhu, Q.-Y. Yang, S. Mukherjee, A. Kumar, C.-H. Deng, A. A. Bezrukov, M. Shivanna and M. J. Zaworotko, *Angew. Chemie Int. Ed*., 2019, DOI:10.1002/anie.201909977.
20 A. Schneemann, P. Vervoorts, I. Hante, M. Tu, S. Wannapaiboon, C. Sternemann, M. Paulus, D. C. F. Wieland, S. Henke and R. A. Fischer, *Chem. Mater.*, 2018, **30**, 1667.
21 J. Zhu, J. Chen, T. Qiu, M. Deng, Q. Zheng, Z. Chen, Y. Ling and Y. Zhou, *Dalt. Trans*., 2019, **48**, 7100.
22 A. Schneemann, R. Rudolf, S. J. Baxter, P. Vervoorts, I. Hante, K. Khaletskaya, S. Henke, G. Kieslich and R. A. Fischer, *Dalt. Trans.*, 2019, **48**, 6564.
23 H. Miura, V. Bon, I. Senkovska, S. Ehrling, S. Watanabe, M. Ohba and S. Kaskel, *Dalt. Trans.,* 2017, **46**, 14002.
24 Ehrling, I. Senkovska, V. Bon, J. D. Evans, P. Petkov, Y. Krupskaya, V. Kataev, T. Wulf, A. Krylov, A. Vtyurin, S. Krylova, S. Adichtchev, E. Slyusareva, M. S. Weiss, B. Büchner, T. Heine and S. Kaskel, *J. Mater. Chem. A*, 2019, **7**, 21459.
25 S. A. Sapchenko, M. O. Barsukova, R. V. Belosludov, K. A. Kovalenko, D. G. Samsonenko, A. S. Poryvaev, A. M. Sheveleva, M. V. Fedin, A. S. Bogomyakov, D. N. Dybtsev, M. Schröder and V. P. Fedin, *Inorg. Chem.*, 2019, **58**, 6811.
26 Q.-Y. Yang, P. Lama, S. Sen, M. Lusi, K.-J. Chen, W.-Y. Gao, M. Shivanna, T. Pham, N. Hosono, S. Kusaka, J. J. Perry, S. Ma, B. Space, L. J. Barbour, S. Kitagawa and M. J. Zaworotko, *Angew. Chemie Int. Ed.*, 2018, **57**, 5684.
27 W. K. Feldmann, K. White, C. X. Bezuidenhout, V. J. Smith, C. Esterhuysen and L. J. Barbour, ChemSusChem, 2019, DOI: 10.1002/cssc.201902990.
28 C. F. Macrae, I. J. Bruno, J. A. Chisholm, P. R. Edgington, P. McCabe, E. Pidcock, L. Rodriguez-Monge, R. Taylor, J. van de Streek, P. A. Wood*, J. Appl. Crystallogr.*, 2008, **41**, 466.
29 S. Noro and T. Nakamura, *NPG Asia Mater.,* 2017, **9**, e433.
30 A. L. Spek, *Acta Crystallogr. Sect. C*, 2015, **71**, 9.

Tuning gate-opening pressure and hysteresis in a highly flexible pillar-layered metal-organic framework by ligand fluorination

Isabella E. Claassens, Wesley K. Feldmann, Charl X. Bezuidenhout, Catharine Esterhuysen, Delia A. Haynes* and Leonard J. Barbour*

Supplementary Information

Experimental Procedures

Results

Experimental Procedures

Instrumental details

Powder X-ray diffraction (PXRD)

PXRD data were recorded on a benchtop Bruker D2 PHASER. It is equipped with a Lynxeye 1D detector and uses Ni-filtered Cu Kα radiation (λ = 1.5418 Å) with generator power settings of 30 kV and 10 mA. The X-ray beam is restricted by a 1.0 mm divergence slit and a 2.5 mm Soller collimator. Powder samples were evenly distributed on a zero-background holder after being ground with a mortar and pestle to minimise the effects of preferred orientation. Variable-pressure PXRD data were recorded using a PANalytical X'Pert PRO diffractometer using the capillary spinner configuration and a short-nozzle Oxford Cryostream 700Plus cooling system to maintain temperature at 298 K. Powdered samples were placed in a 0.3 mm Lindemann glass capillary (environmental gas cell), which was spun during data collection over a range of 5° - 40° 2θ. Data analysis was carried out using X'Pert HighScore Plus[1] (Version 2.2e). Powder patterns were simulated from SCXRD structures using Mercury.[2]

Single-crystal X-ray diffraction (SCXRD)

Suitable single crystals were attached to a MiTeGen MicroLoopTM mount using Paratone®N oil for standard data collections, or placed in an environmental gas cell during variable-pressure studies. SCXRD experiments were carried out on a Bruker D8 Venture equipped with a Photon II CPAD detector, which has a multilayer monochromator with MoKα radiation (λ = 0.71073 Å) from an Incoatec IμS microfocus source. An Oxford Cryostreams 800Plus cryostat was used to control the temperature of the crystal when required.

Data reduction was carried out with the Bruker SAINT[3] software package. The absorption corrections and the correction of other systematic errors were carried out with SADABS.[4] Structures were solved by direct methods using SHELXS[5] or by intrinsic phasing using SHELXT[6] in the X-Seed[7,8] interface. Structure refinement was carried out using SHELXL.[5] Hydrogen atom positions were assigned using riding models.[9]

PLATON[10] SQUEEZE[11] was used to determine the total electron count per unit cell of guest molecules within the structures. These counts were then used to determine occupancy of the guest molecules within the channels of the metal-organic framework. Graphics were generated with POV-Ray [12] in the X-Seed interface[7,8], and CIF files were edited in Olex2 [13] and EnCIFer.

Topology

TOPOSPro[14] was used to determine the topology of the frameworks through the online service at topospro.org.

Thermogravimetric analysis (TGA)

Thermogravimetric analyses were carried out on a TA Instruments Q500 analyser. The instrument records weight loss as a function of temperature. Samples ranging in mass from 1 – 5 mg were placed in an aluminium pan and heated from room temperature to 600 °C at a rate of 10 °C min^{-1} under N_2 flow of 50 mL min^{-1}. Data analysis was carried out using the Universal Analysis 2000 (TA Instruments, Version 4.5A) software.

Volumetric sorption analysis

A Setaram PCT Pro-E&E gas sorption analyser with a MicroDoser attachment was utilised to conduct high pressure gas sorption experiments with N_2, CH_4, CO_2, C_2H_4 and C_3H_8 at 298 K. The instrument utilises Sievert's volumetric method. The sample temperature was maintained to an accuracy of ±1 °C using a Grant refrigerated recirculation bath filled with antifreeze and water. A sample at known pressure and volume was connected to a reservoir of known volume and pressure through an isolation valve. The valve was opened, and the system allowed to equilibrate. The difference between the measured and calculated pressures was used to determine the amount of gas adsorbed. National Institute of Standards and Technology (NIST) software was used to calculate the thermodynamic corrections to account for the non- ideal behaviour of the gases at relatively high pressures. Adsorbent samples weighing around 70-100 mg were placed in the sample tube and activated *in situ* under vacuum for 2 hours at the activation temperature specified. The dead volume of the sample cells was measured using helium gas with 99.99% purity. Blank runs for each gas were recorded to further correct for any other residual systematic errors in the experiment. Figure preparation and data analyses were performed using Microsoft Excel and OriginPro[15].

Pressure-Gradient Differential Scanning Calorimetry (PGDSC)

PGDSC measurements were made using a Setaram µDSC7 Evo module equipped with a high pressure sample holder. The pressure gradient was controlled by a ProportionAir QPV1M pressure valve. The valve was controlled by software developed in-house. Data were recorded and analyzed using the Calisto software package from Setaram and OriginPro[15]. A detailed experimental set-up is reported by Feldmann *et al.*[16]

Synthesis

Chemicals and solvents were obtained from Sigma-Aldrich and used as received. Nitrogen was passed through a Drierite™ drying column before use.

Synthesis of 1,4-bis[2-(4'-pyridyl)ethenyl]benzene (bpeb)

The synthetic procedure (Scheme S1) was adapted from that reported by Bhowmik *et al*.[17]

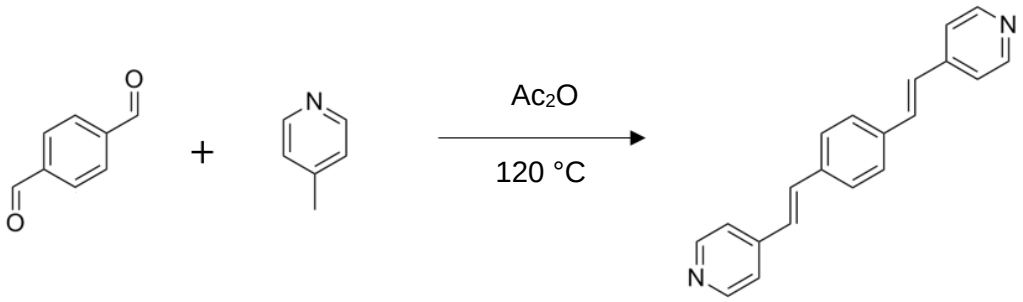

Scheme S1 Synthesis of 1,4-bis[2-(4'-pyridyl)ethenyl]benzene (bpeb) from terepthaldehyde and 4-picoline.

Terepthaldehyde (3.35 g, 24.9 mmol) was added to 4-picoline (9.7 mL, 0.10 mol) in 30 mL acetic anhydride under inert conditions. The mixture was heated to 70 °C and stirred for an hour, until the solution turned a deep brown color. After the addition of anhydrous $ZnBr_2$ (12.35 g, 54.84 mmol), the reaction was heated to 120 °C and allowed to reflux for 51 hours under inert conditions. During this time an orange precipitate formed. The orange precipitate was filtered off, washed four times with acetic anhydride and allowed to dry for 24 hours under ambient conditions. The mixture was then washed with 100 mL hot ethanol (70 °C) in small batches. It was then allowed to dry once more, after which it was washed a final time with ether (4-5 times). The dried product was then recrystallized from pyridine. The resulting powder was filtered and washed with copious amounts of diethyl ether to ensure that all of the pyridine was removed. NMR confirmed successful synthesis and purity of the product. The percentage yield was 34.0% (2.40 g).

^{1}H-NMR ($CDCl_3$, 400 MHz): δ 7.04 (2H, d, $CH_{ethelyne}$), 7.29 (2H, d, $CH_{ethelyne}$), 7.36 (4H, dd, $CH_{pyridine}$), 7.55 (4H, s, $CH_{benzene}$), 8.58 (4H, dd, $CH_{pyridine}$).

Synthesis of 4,4'-[(2,3,5,6-tetrafluoro-1,4-phenylene)-2,1-ethenediyl]bis-pyridine (fbpeb)

The synthetic procedure was adapted from that reported by Nielsen *et al*.[18]

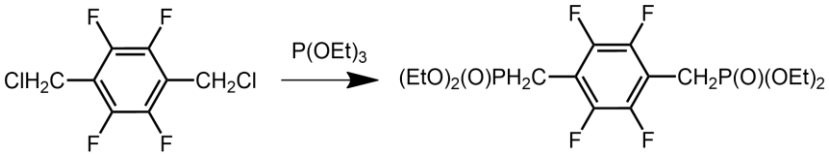

A **B** **92%**

Scheme S2 Synthesis of precursor compound **B** from **A**.

Compound **A** (5.0 g, 6.96 mmol) was refluxed in $P(OEt)_3$ (10 mL) for 1 h. After cooling to RT, the precipitate was filtered and washed with 2x 5 ml EtOH. The ethanol filtrate was cooled in a refrigerator to yield additional material totaling to 4.44 g (92 %) of **B** as a white powder.

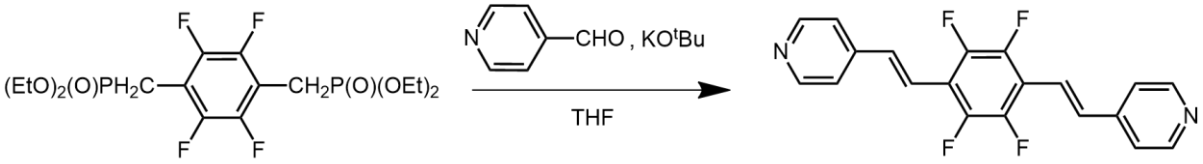

B **fpeb 27%**

Scheme S3 Synthesis of fbpeb from compound **B**.

KO^tBu (1.85 g, 16.5 mmol) was added step-wise to a solution of 4-pyridine carboxaldehyde (1.18 g, 11.0 mmol) and **B** (2.68 g, 5.0 mmol) in THF (150 mL in a 250 ml round bottom flask) under stirring at RT over a 5 min period. This was followed by stirring at RT for an additional 1 h. The reaction was quenched with diluted HCl (1 M, 75 mL) to remove unreacted KO^tBu. The crude product was then filtered and recrystallized from pyridine to yield 0.92 g (27 %) of an off-white light yellow powder.

Synthesis of 4,4'-azodibenzoic acid ($adcH_2$)

4,4'-azodibenzoic acid was synthesised according to the procedure reported by Peng *et al.* without modification.[19]

Preparation of $[Zn_2(adc)_2(fbpeb)]\cdot 4DMF\cdot 2H_2O$ (1as)

$Zn(NO_3)_2\cdot 4H_2O$ (26 mg, 0.01 mmol), 4,4'-azodibenzoic acid (27 mg, 0.01 mmol) and fbpeb (20 mg, 0.055 mmol) were dissolved 5 mL DMF with the assistance of a heat gun. The solution was then heated in a 20 mL scintillation vial in an oven at 120 °C for 24 hours, resulting in the formation of petal-shaped red-yellow crystals. Post synthesis, the crystals were placed in pure DMF to avoid their dissolution in the mother liquor.

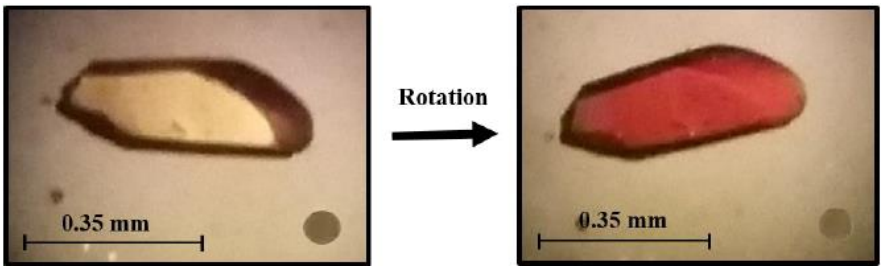

Figure S1 Colour change from yellow to bright red observed in the **1as** crystals upon rotation of the crystal under polarised light.

Preparation of $[Zn_2(adc)_2(bpeb)]\cdot 4DMF$ (2as)

$Zn(NO_3)_2\cdot 4H_2O$ (26 mg, 0.01 mmol), 4,4'-azodibenzoic acid (27 mg, 0.01 mmol) and bpeb (14.6 mg, 0.051 mmol) were dissolved 5 mL DMF with the assistance of a heat gun. The solution was then heated in a 20 mL scintillation vial in an oven at 120 °C for 24 hours, resulting in the formation of petal-shaped orange-yellow crystals. Post synthesis, the crystals were placed in pure DMF to avoid their dissolution in the mother liquor.

Results

Single-crystal X-ray diffraction analysis

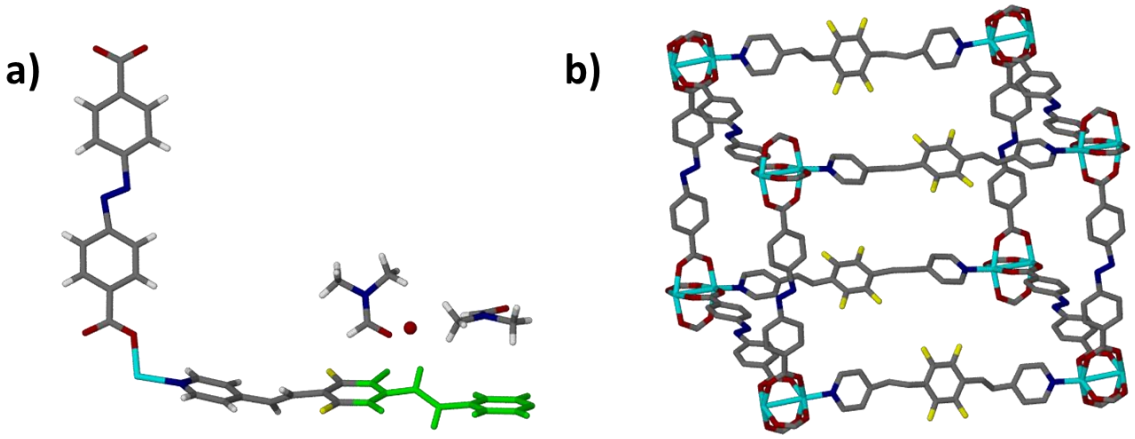

Figure S2 (a) Asymmetric unit of **1as**. The disordered part of the fbpeb linker is displayed as green and is on a special position (see figure SX below). The occupancy is 50%. (b) Pillar-layered structure of **1as** to show connectivity within a net. Solvent molecules and hydrogen atoms are omitted for clarity.

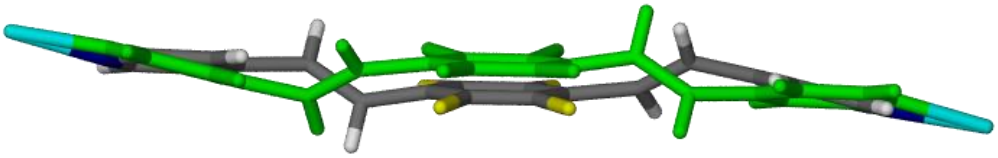

Figure S3 Disordered fbpeb ligand in **1as** viewed perpendicular to the (0 0 1) plane.

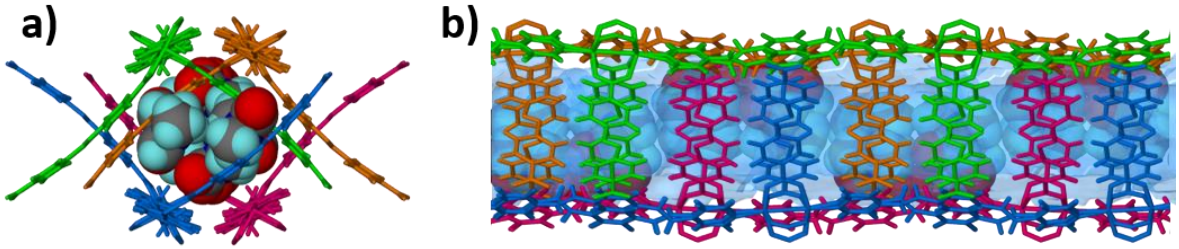

Figure S4 (a) View of channel in **1as** along [1 0 1] The four interpenetrating nets that form the channel are displayed in different colours. The DMF solvent molecules are housed within the channel. (b) View of the Connolly surface of the channel and the interweaving of the interpenetrated nets to form the 1 D channel.

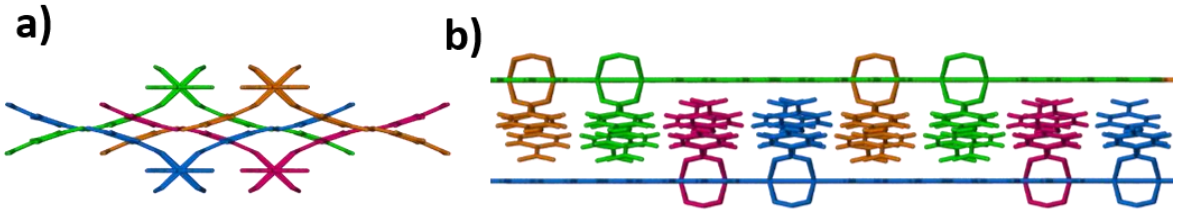

Figure S5 X View of channel in **1cp** after the solvent has been removed. The collapsed channel has no solvent-accessible space.

Thermogravimetric analysis (TGA)

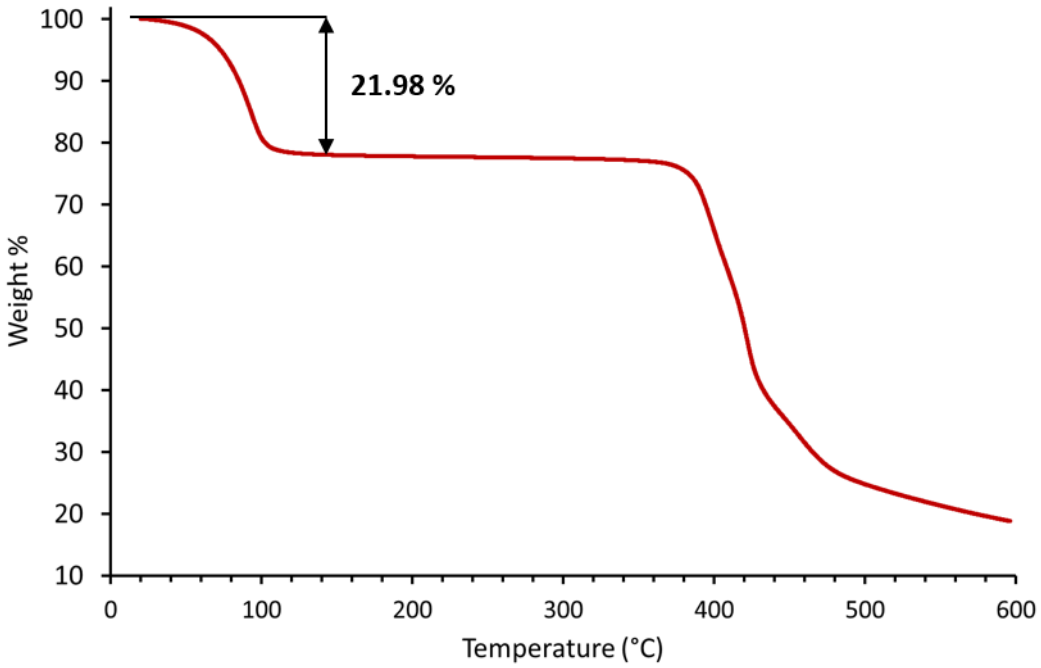

Figure S6 Thermogravimetric analysis of **1as** showing solvent mass loss of 21.98% up to 140°C. The mass loss equates to 4 DMF and 2 H_2O molecules per formula unit.

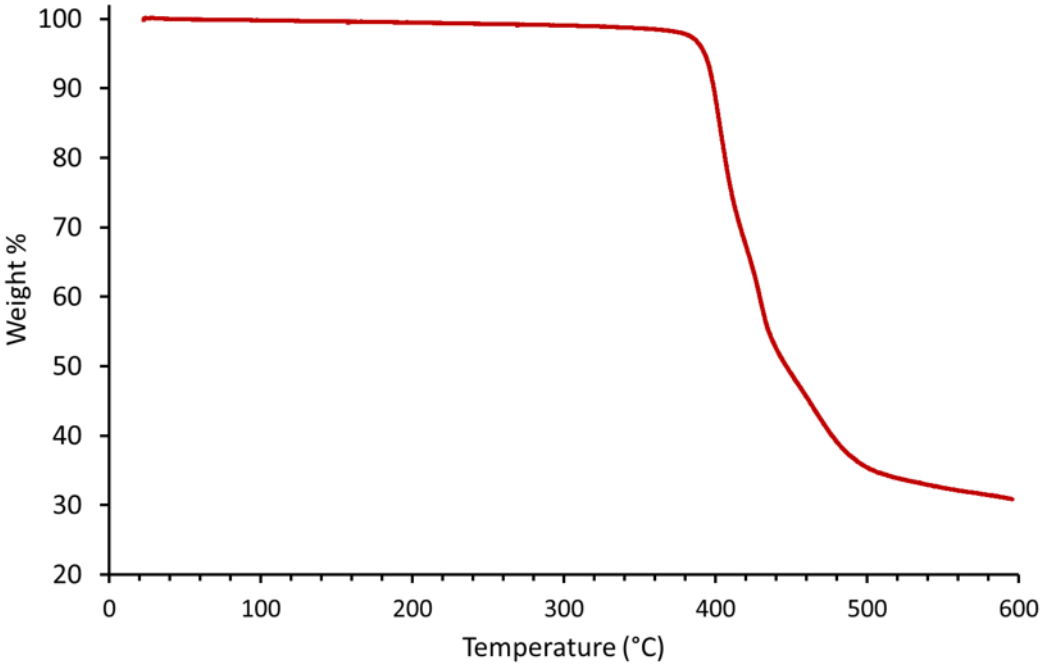

Figure S7 Thermogravimetric analysis of activated **1as**, **1cp** showing negligible mass loss.

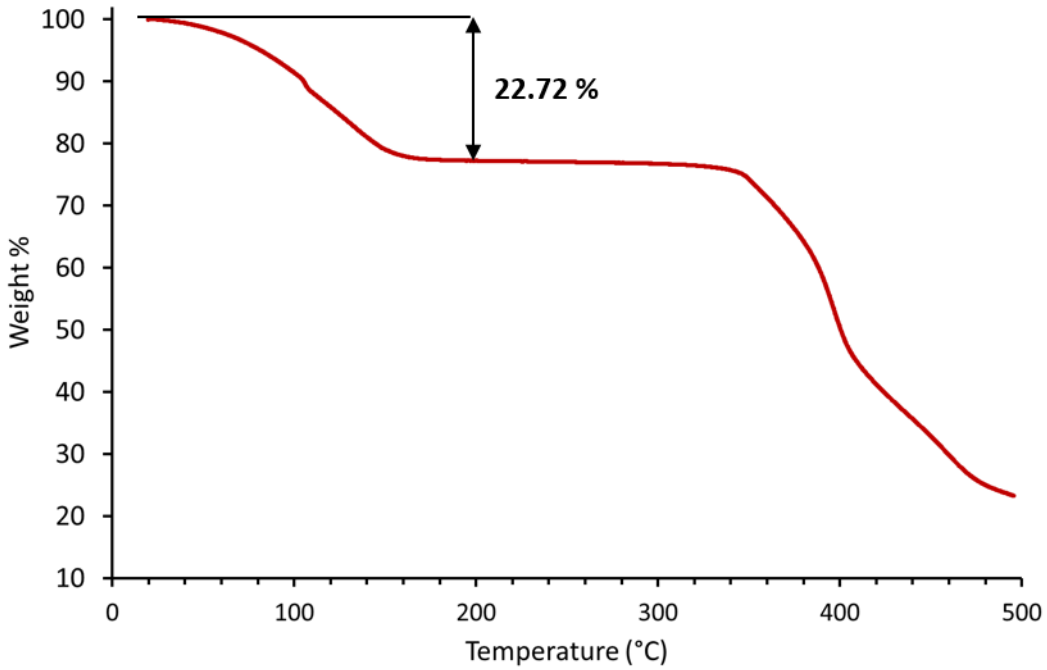

Figure S8 Thermogravimetric analysis of **2as** showing solvent mass loss of 22.72% up to 200°C. The mass loss equates to 4 DMF molecules per formula unit.

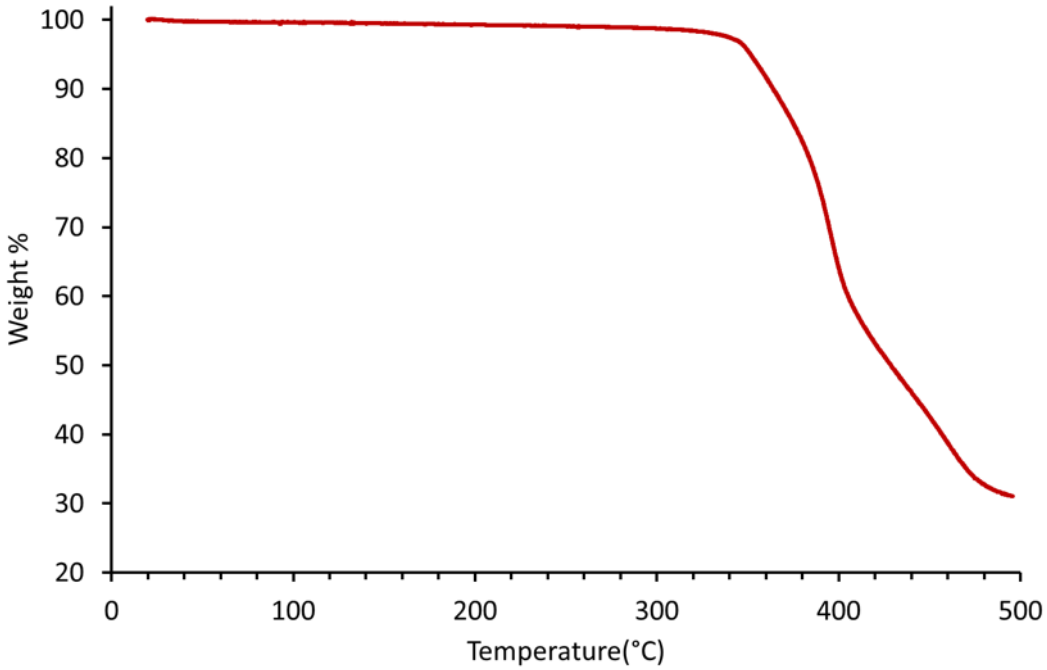

Figure S9 Thermogravimetric analysis of activated **2as**, **2np** showing negligible mass loss.

Powder X-ray diffraction (PXRD)

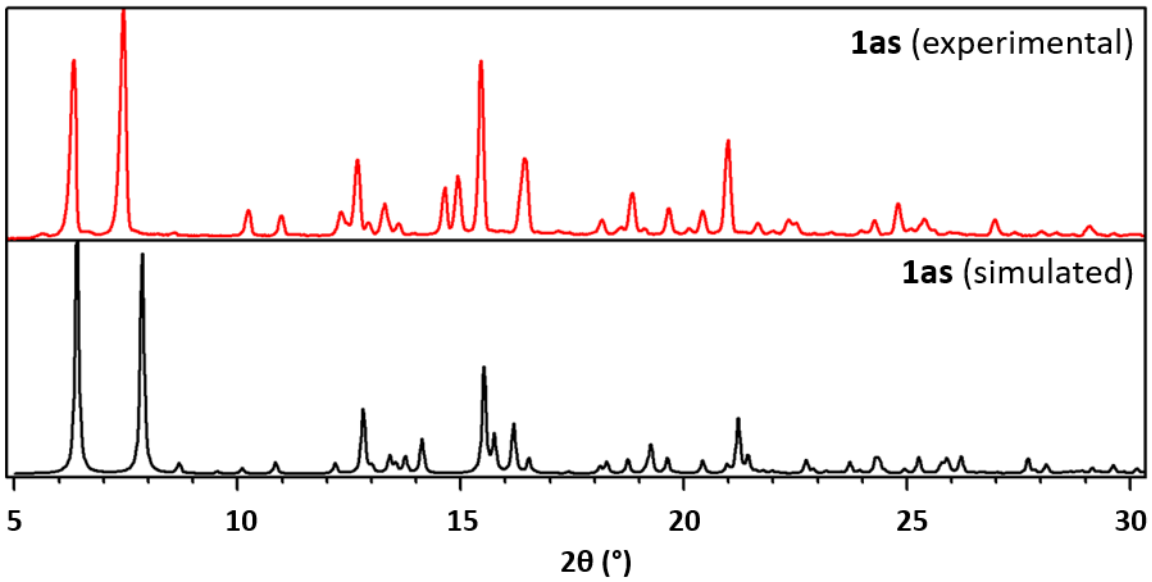

Figure S10 Experimental and simulated powder diffraction patterns of **1as**. Some peaks found in the experimental pattern do not coincide exactly with those in the simulated pattern. This is likely as a result of solvent loss in the diffractometer during analysis.

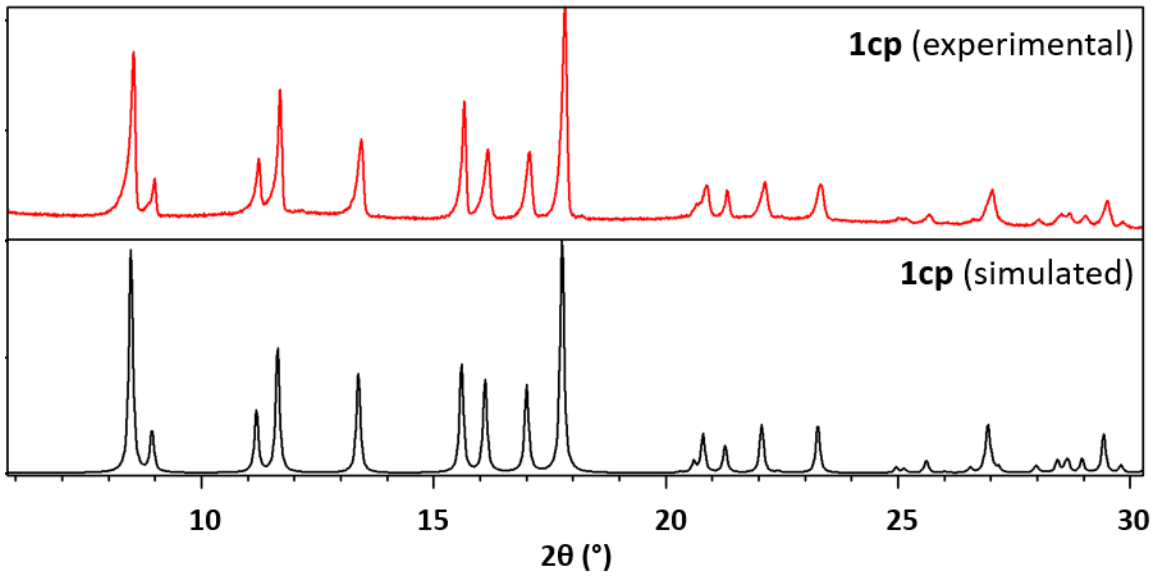

Figure S11. Experimental and simulated powder diffraction patterns of **1cp**.

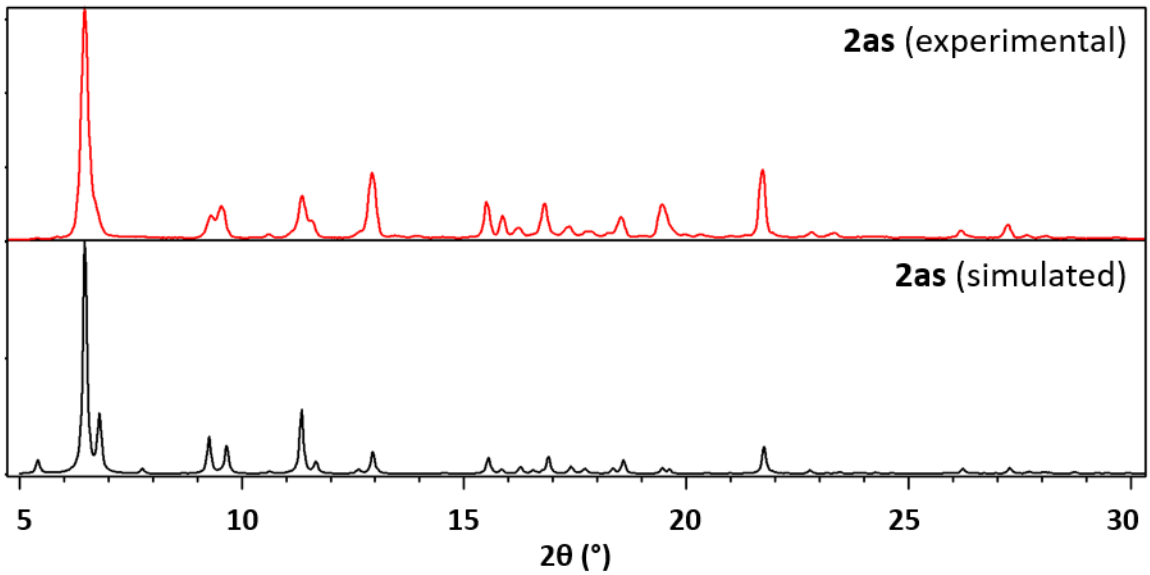

Figure S12 Experimental and simulated powder diffraction patterns of **2as**.

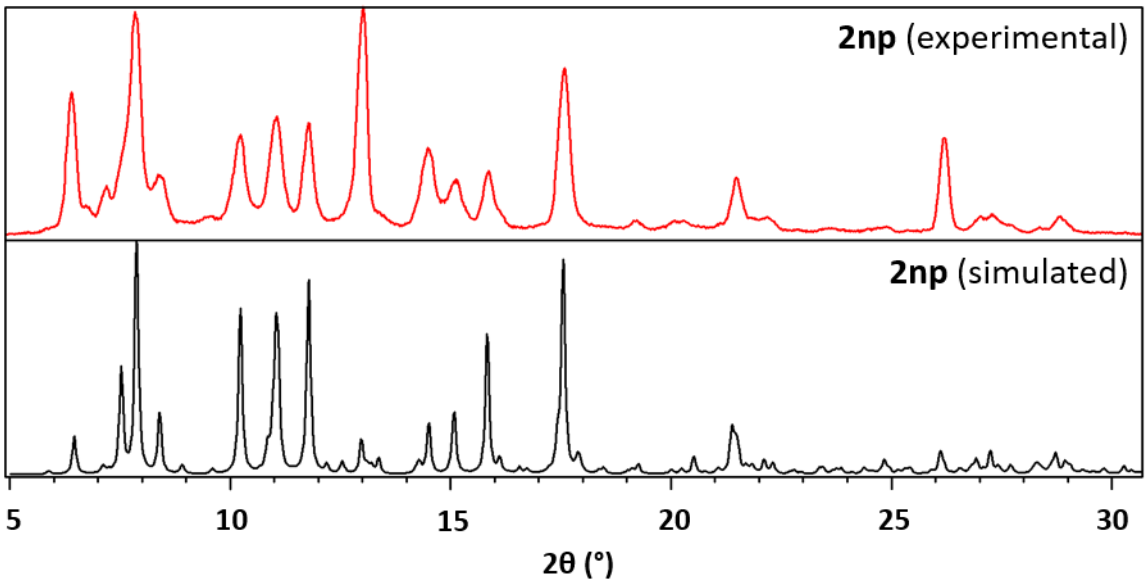

Figure S13 Experimental and simulated powder diffraction patterns of **2np**.

Volumetric sorption analysis and pressure-gradient differential scanning calorimetry measurements (PGDSC)

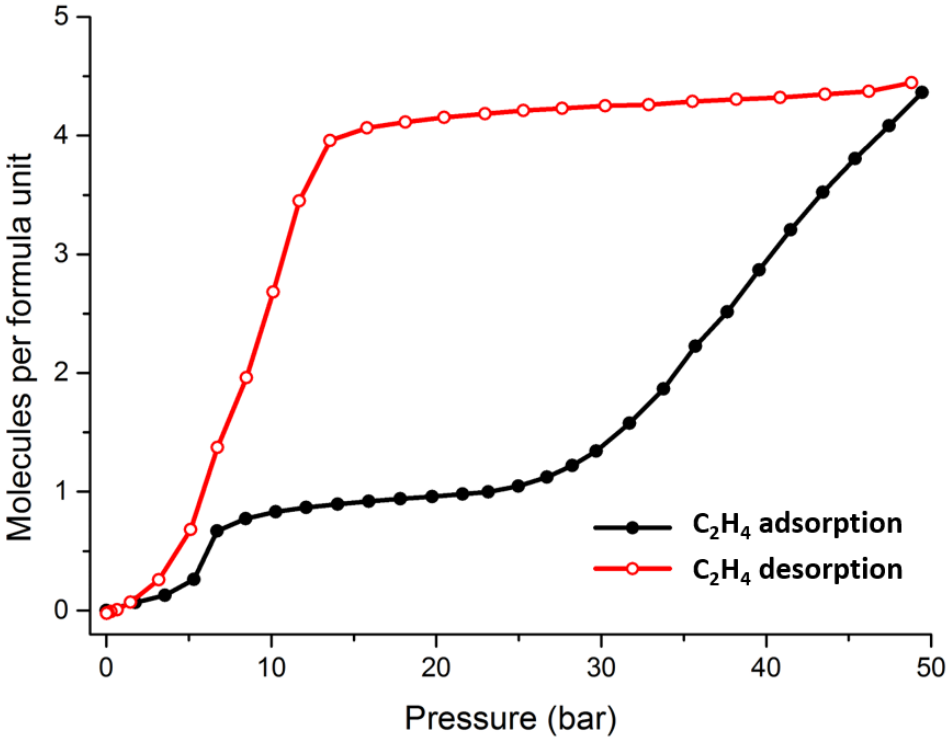

Figure S14 Adsorption (black) and desorption (red) isotherms for **1** measured at 298 K with C_2H_4.

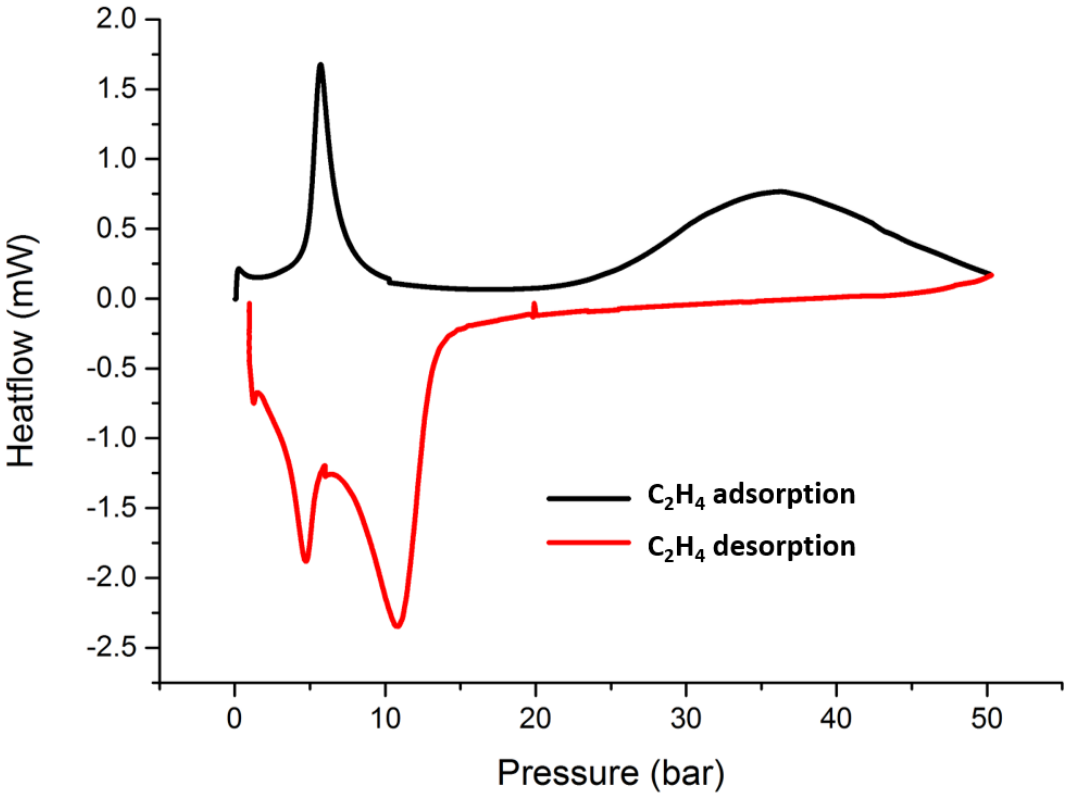

Figure S15 PGDSC trace of **1** showing thermal events during adsorption (black) and desorption (red) of C_2H_4.

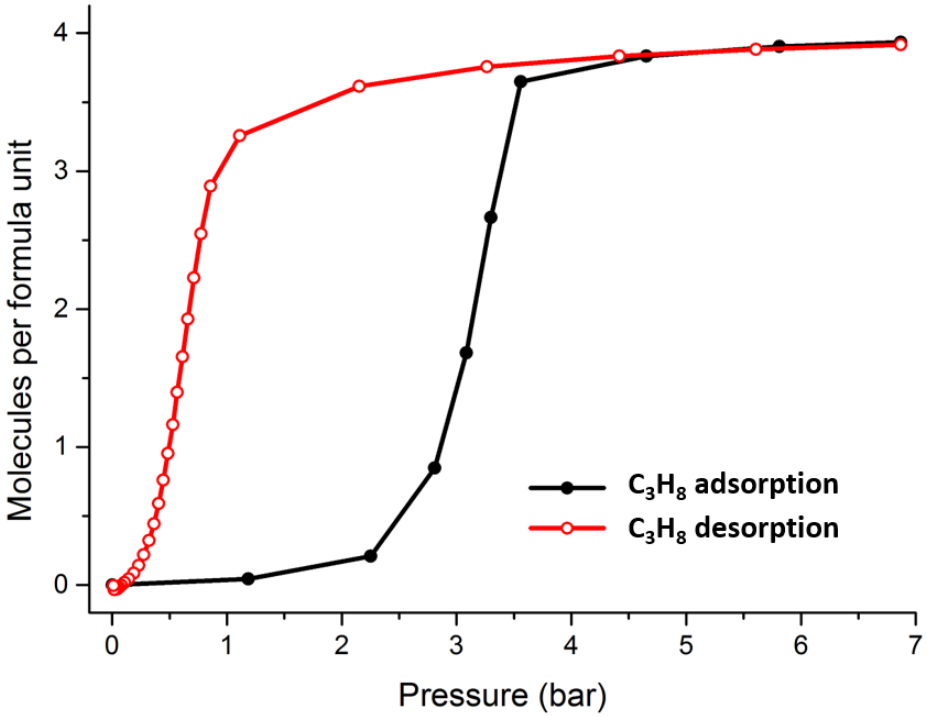

Figure S16 Adsorption (black) and desorption (red) isotherms for **1** measured at 298 K with C_3H_8.

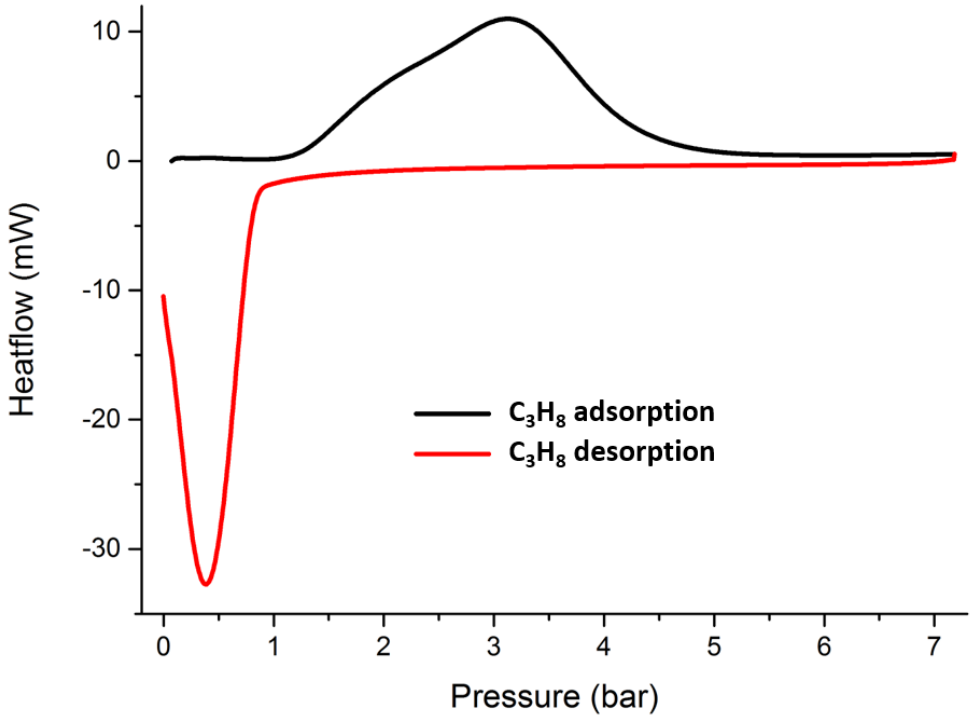

Figure S17 PGDSC trace of **1** showing thermal events during adsorption (black) and desorption (red) of C_3H_8.

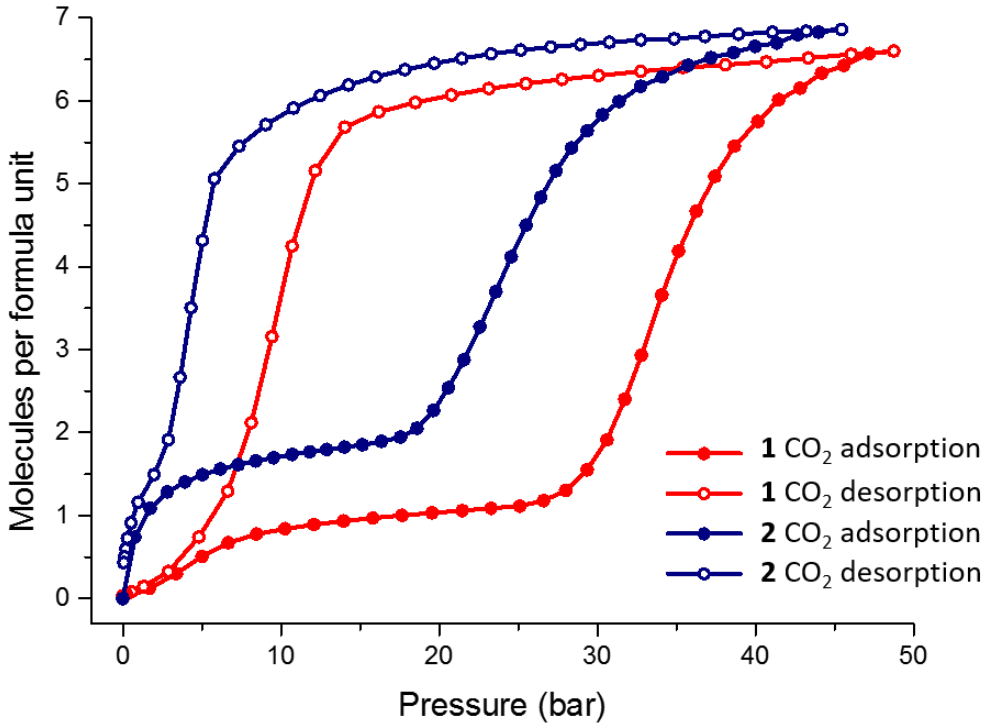

Figure S18 Comparison of the CO_2 sorption isotherms of **1** (red) and **2** (blue) measured at 298 K.

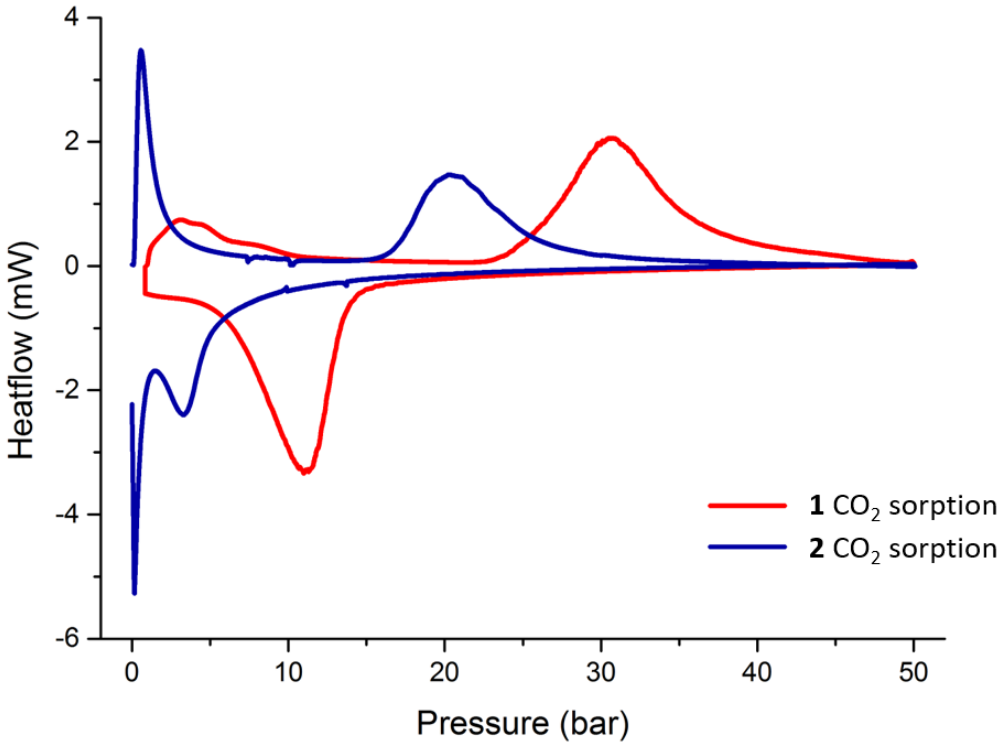

Figure S19 Comparison of the PGDSC traces of **1** (red) and **2** (blue) during the adsorption and desorption of CO_2.

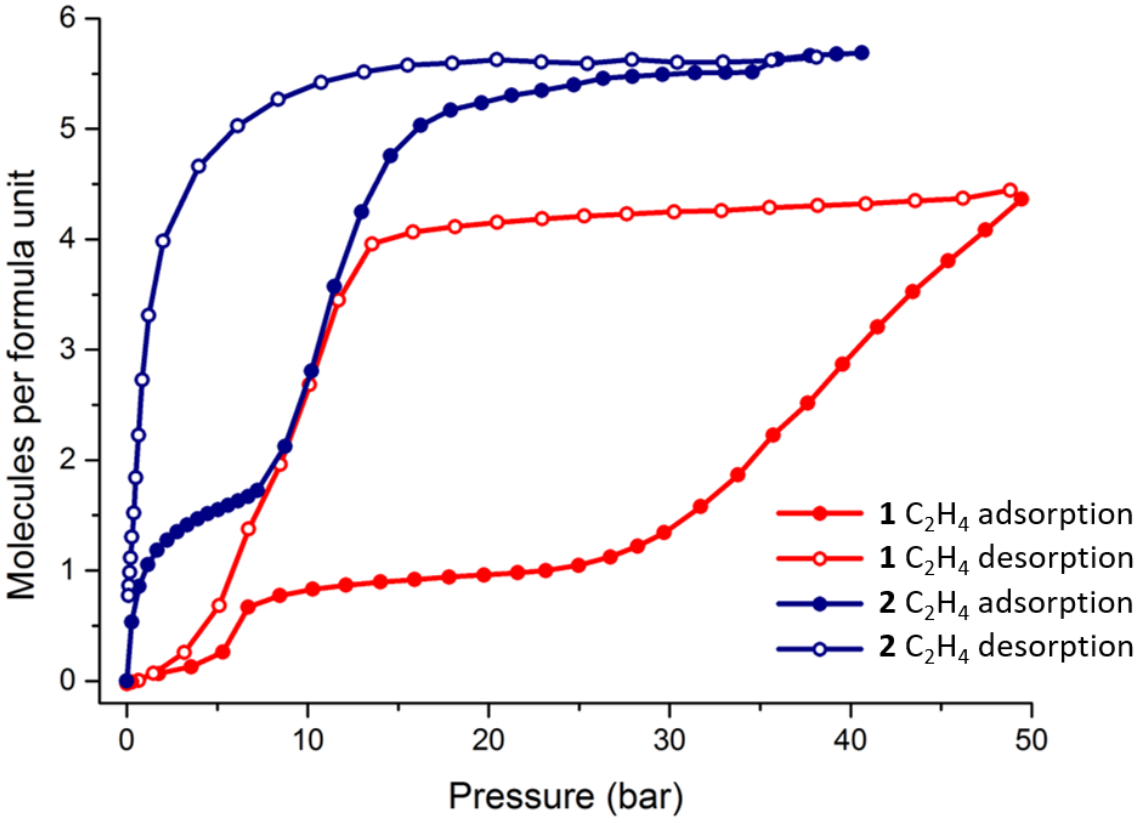

Figure S20 Comparison of the C_2H_4 sorption isotherms of **1** (red) and **2** (blue) measured at 298 K.

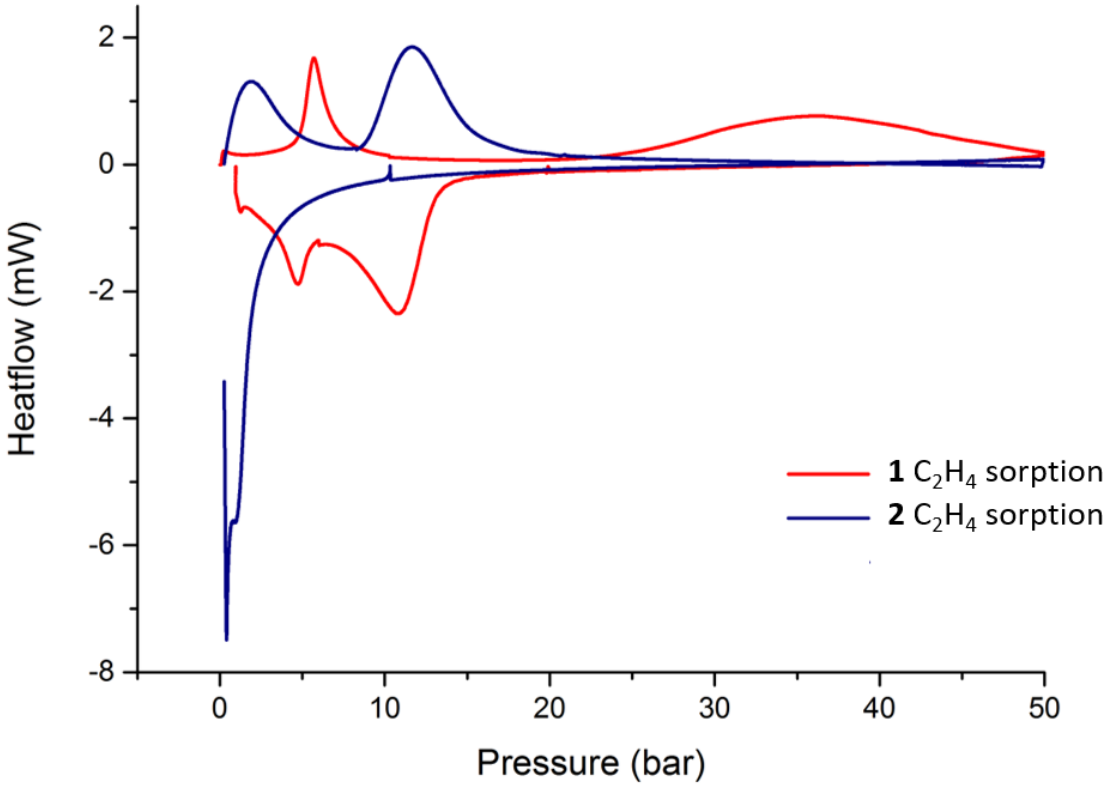

Figure S21 Comparison of the PGDSC traces of **1** (red) and **2** (blue) during the adsorption and desorption of C_2H_4

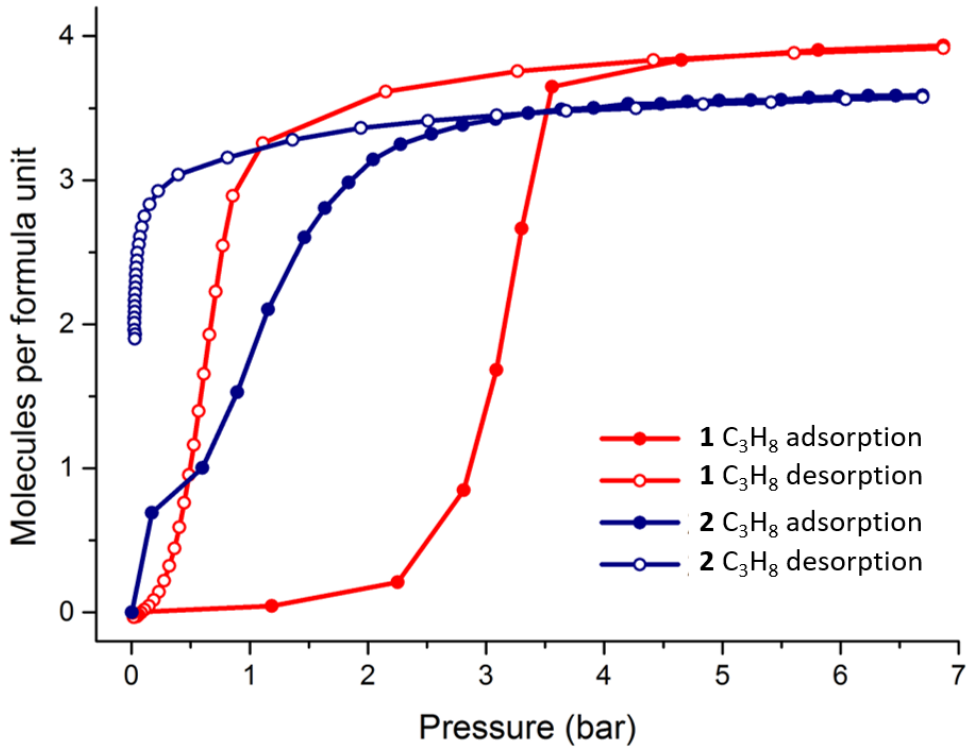

Figure S22 Comparison of the CO_2 sorption isotherms of **1** (red) and **2** (blue) measured at 298 K.

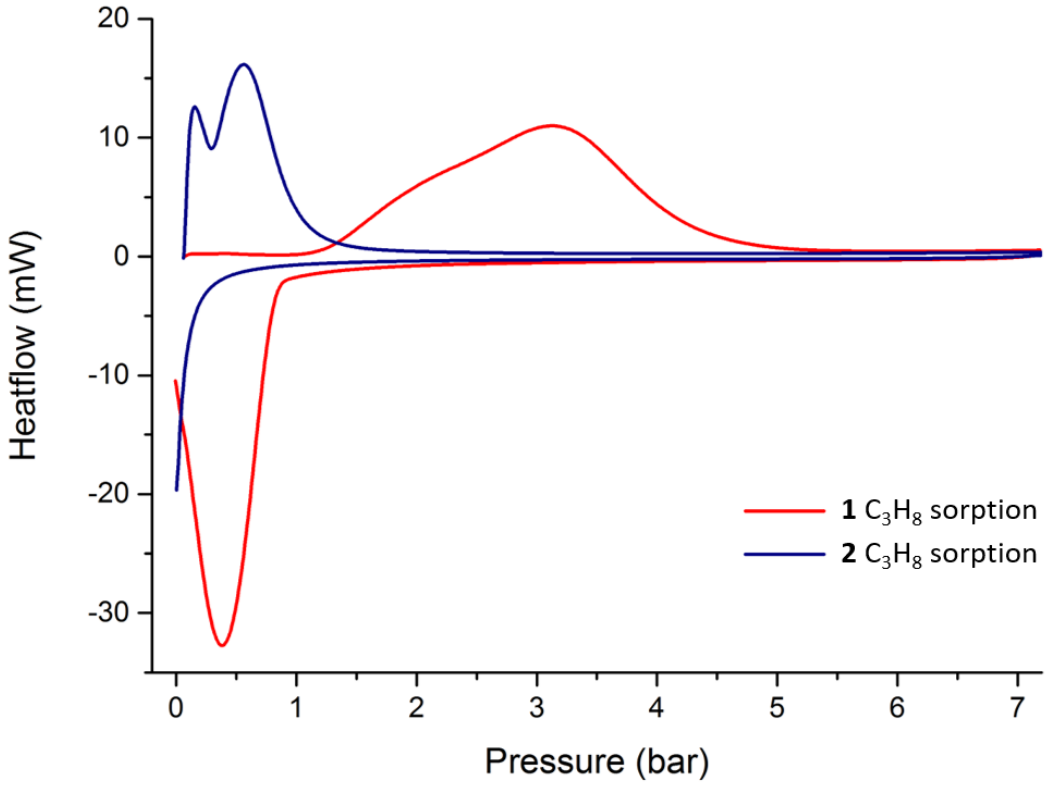

Figure S23 Comparison of the PGDSC traces of **1** (red) and **2** (blue) during the adsorption and desorption of C_3H_8

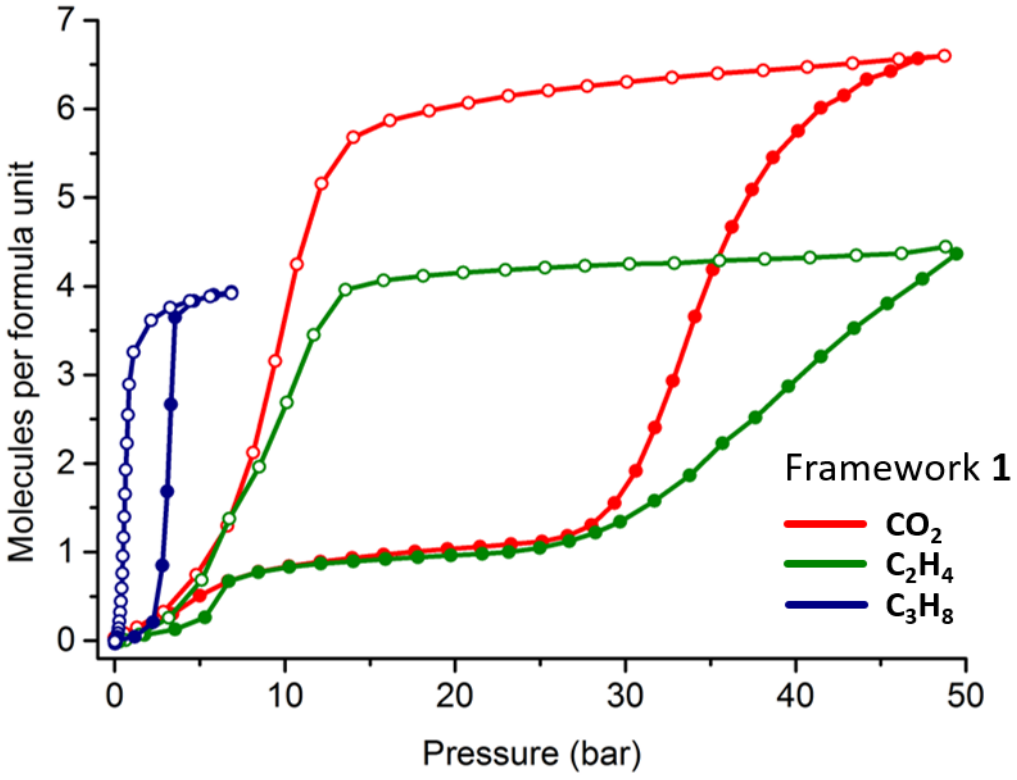

Figure S24 Comparison of the sorption isotherms of **1** measured at 298 K for CO_2 (red), C_2H_4 (green) and C_3H_8 (blue).

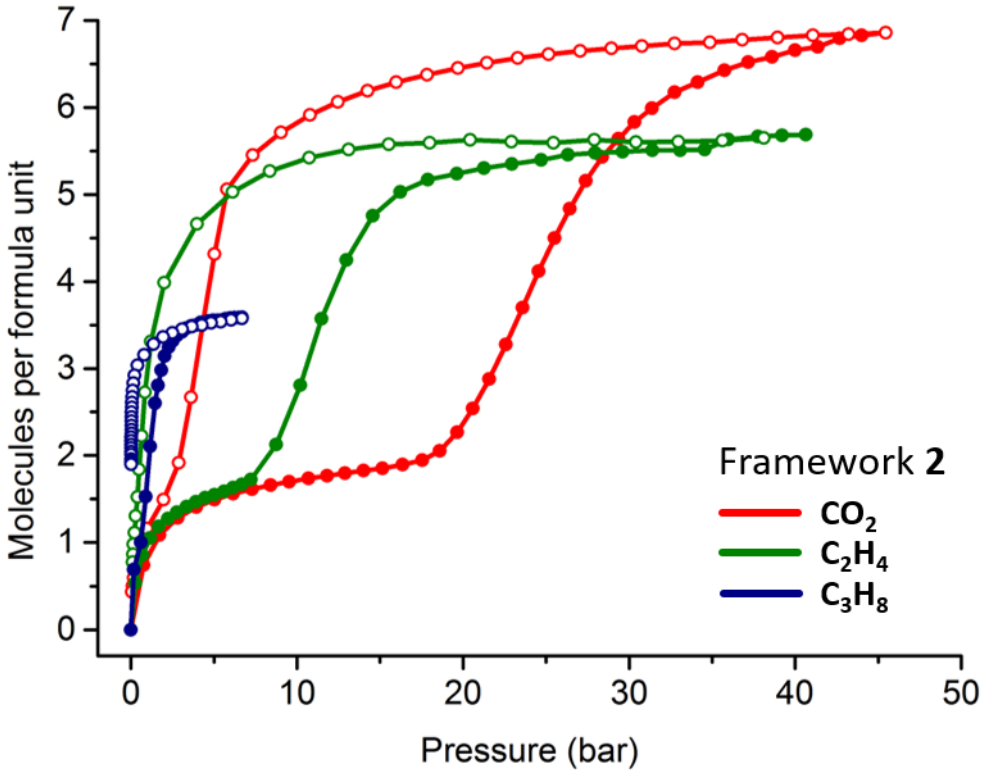

Figure S25 Comparison of the sorption isotherms of **2** measured at 298 K for CO_2 (red), C_2H_4 (green) and C_3H_8 (blue).

In-situ variable pressure powder X-ray diffraction analysis (PXRD)

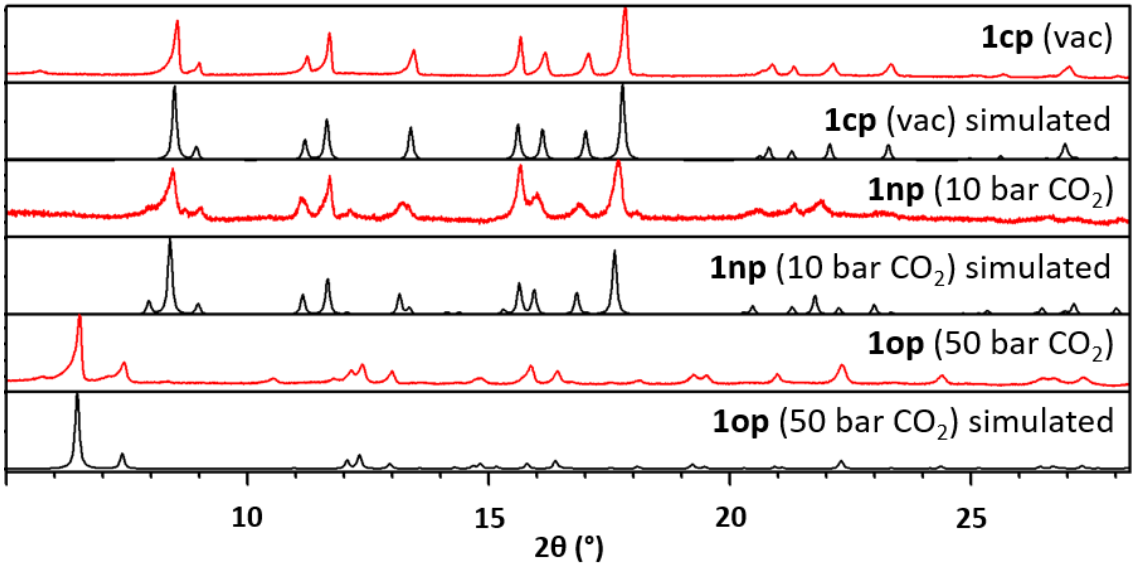

Figure S26 In situ variable pressure-PXRD **1** at different CO_2 adsorption loadings at 298K. To confirm the structural transformations from closed phase (**1cp**)→ narrow pore (**1np**)→ open pore (**1op**), the experimental PXRD patterns were compared with the calculated PXRD from the single crystal structure of each phase.

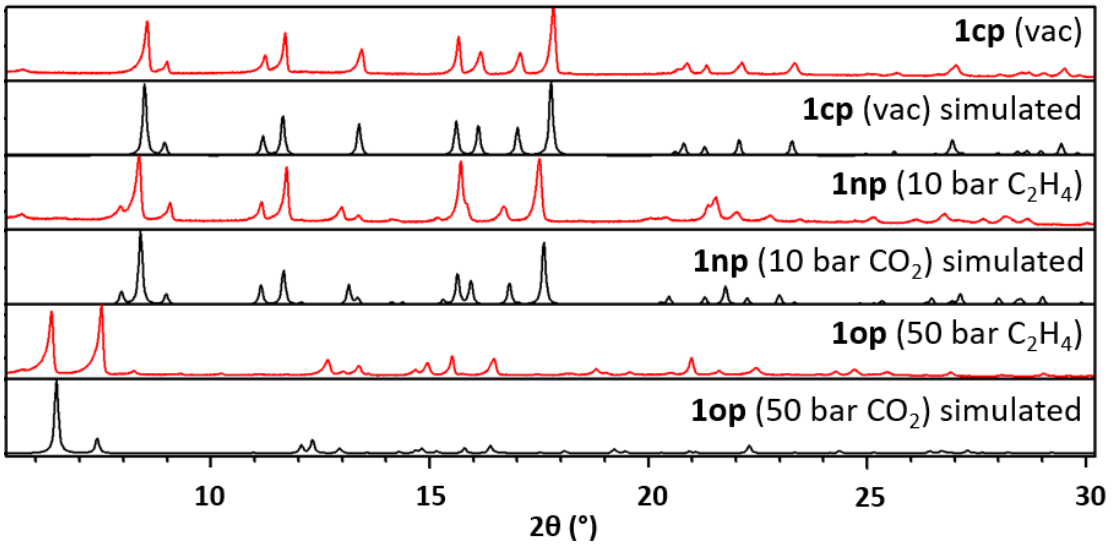

Figure S27 PXRD patterns of **1** at different C_2H_4 adsorption loadings at 298K. The experimental PXRD patterns were compared with the calculated PXRD from the CO_2-loaded single crystal structure of each phase.

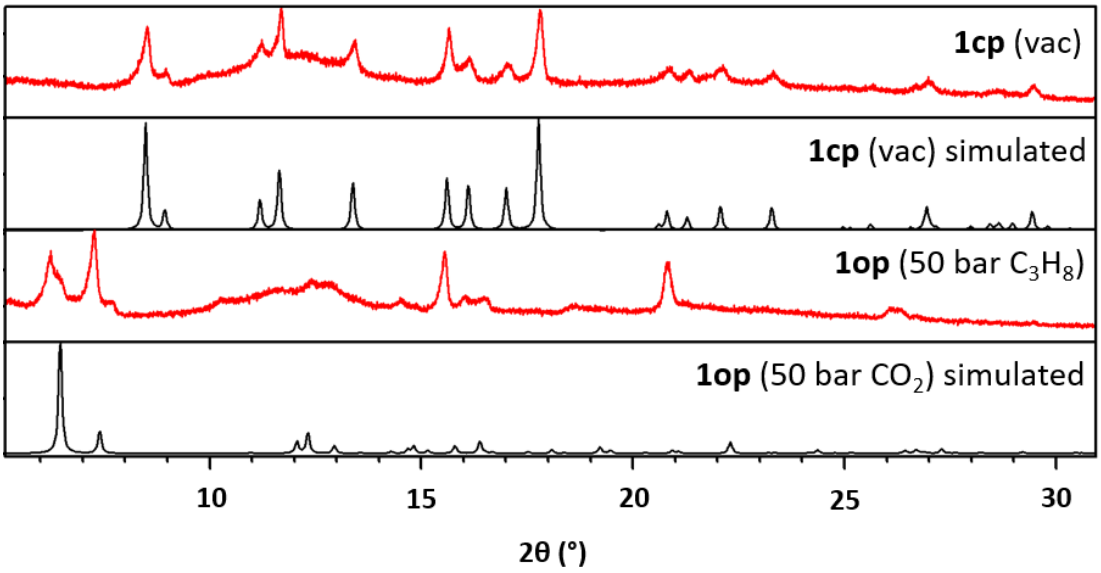

Figure S28 PXRD patterns of **1** at different C_3H_8 adsorption loadings at 298K. The experimental PXRD patterns were compared with the calculated PXRD from the CO_2-sui single crystal structure of each phase.

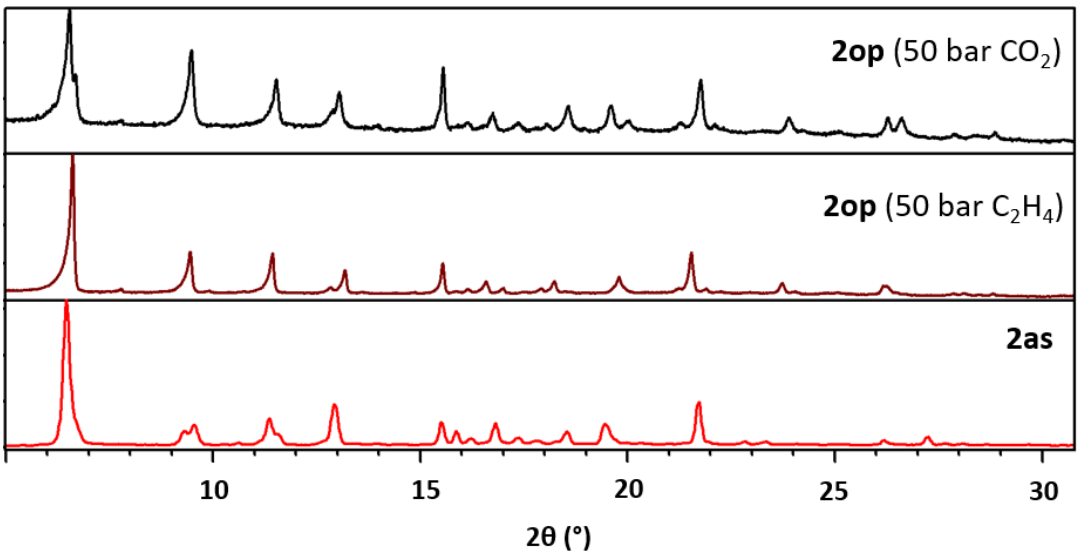

Figure S29 PXRD patterns of **2op** 50 bar CO_2 and 50 bar C_2H_4 298K compared to the experimental PXRD patterns of 2as to confirm the framework has the same structure.

Computational Analysis

Pairs of molecules taken from the crystal structures of **1cp**, **1np** and **1op** obtained through SCXRD measurements at vacuum, 1bar, 10 bar, 20 bar, 26 bar and 50 bar, respectively, were used as models (Figures S30 and S31) for the calculation of the strength of the intermolecular interactions with the software suite Gaussian 09 v. D.01.[20] The hydrogen-atom positions were optimised utilising the density functional theory method PBE0[21] (using the Gaussian keyword PBE1PBE) with the def2TZVP basis set[22] and Grimme's D3 dispersion correction,[23] while keeping the remainder of the atoms fixed in the crystallographically-derived positions. Basis Set Superposition Error corrections were applied through the counterpoise method[24] to yield the interaction energies, $E_{int} = E_{dimer} - 2E_{monomer}$. Other methods and basis sets were tested (PBE-D3/def2-TZVP, PBE-D3/6-311+G(d,p)//PBE-D3/6-31+G(d), PBE-D3/aug-cc-pVTZ//PBE-D3/6-31+G(d) and B3LYP-D3/6-311+G(d,p)//PBE-D3/6-31+G(d)), and all yielded similar results. The values for the Counterpoise-corrected interaction energies is displayed in Table X. Bowing of the fbpeb ligand occurs in the **1np** phase as seen in figure S32. This is due to the inclusion of a molecule of CO_2 above the perfluorinated ring.

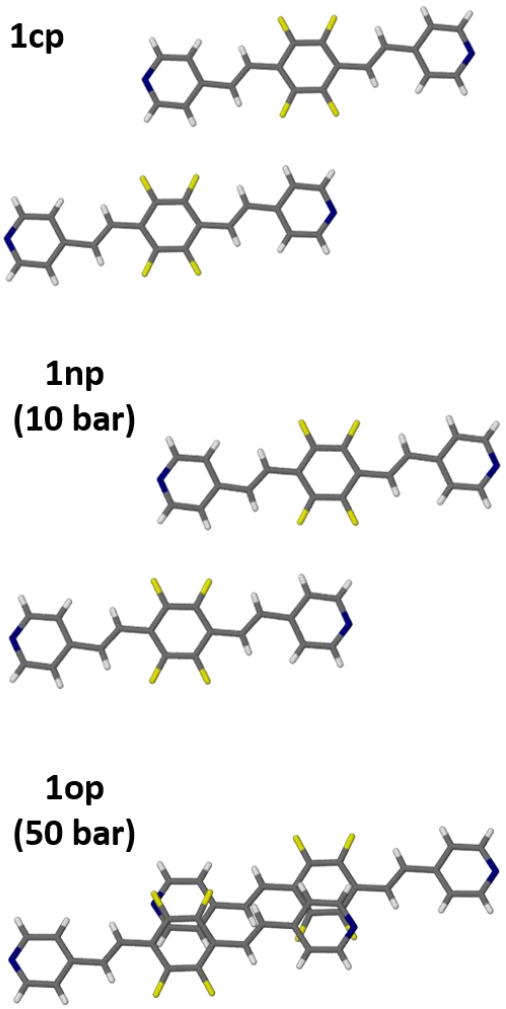

Figure S30 Pairs of fbeb linker molecules taken from the crystal structures of **1cp** (vacuum), **1np** (10 bar) and **1op** (50 bar) used as models for the calculation of the strength of the intermolecular interactions.

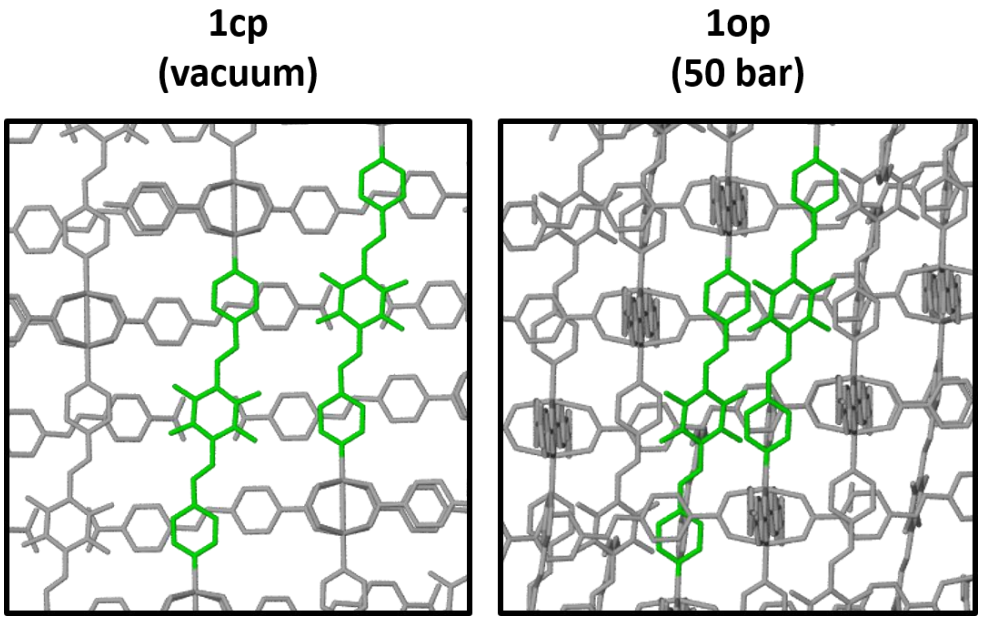

Figure S31 Pairs of fbeb linker molecules (green) positions in nets of the crystal structures of **1cp** (vacuum), **1np** and **1op** (50 bar) used as models for the calculation of the strength of the intermolecular interactions.

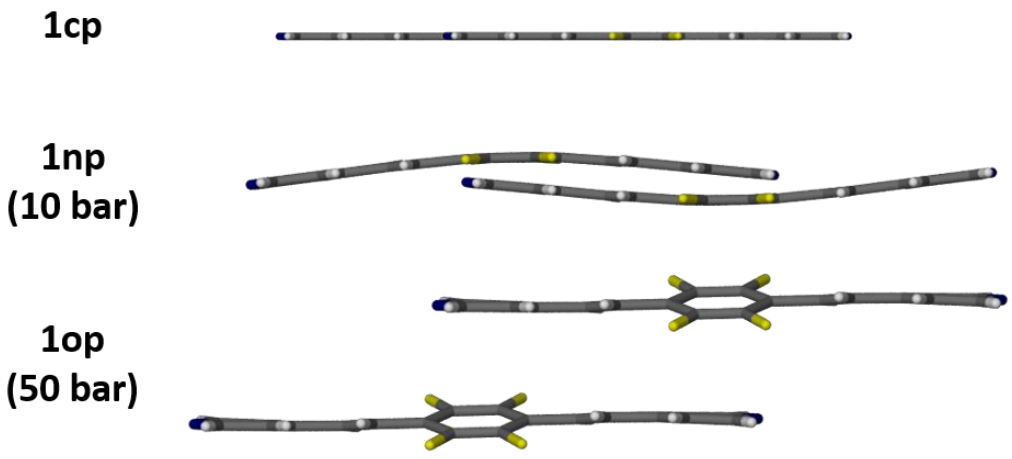

Figure S32 Side view of the pairs of fbeb linker molecules taken from the crystal structures of **1cp** (vacuum), **1np** (10 bar) and **1op** (50 bar) used as models for the calculation of the strength of the intermolecular interactions.

Table S1 Counterpoise-corrected interaction energies at the PBE0-D3/def2-TZVP level of theory in kcal mol^{-1}.

Phase	Pressure (bar)	E_{int} (kcal mol^{-1})
1cp	Vacuum	-3.66
1cp	1	-3.65
1np	10	-3.52
1np	20	-3.45
1op	26	-9.09
1op	50	-8.85

References

1 T. Degen, M. Sadki, E. Bron, U. König, G. Nénert, *Powder Diffr.*, 2014, **29**, S13.
2 C. F. Macrae, I. J. Bruno, J. A. Chisholm, P. R. Edgington, P. McCabe, E. Pidcock, L. Rodriguez-Monge, R. Taylor, J. van de Streek, P. A. Wood*, J. Appl. Crystallogr.*, 2008, **41**, 466.
3 Bruker (2012). SAINT. Bruker AXS Inc., Madison, Wisconsin, USA.
4 Bruker (2001). SADABS. Bruker AXS Inc., Madison, Wisconsin, USA.
5 G. M. Sheldrick, *Acta Crystallogr. Sect. A*, 2008, **64**, 112.
6 G. M. Sheldrick, *Acta Crystallogr. Sect. A*, 2015, **71**, 3.
7 L. J. Barbour, *J. Supramol. Chem.,* 2001, **1**, 189.
8 J. Atwood, L. J. Barbour, *Cryst. Growth Des.,* 2003, **3**, 3.
9 L. A. Malaspina, A. J. Edwards, M. Woińska, D. Jayatilaka, M. J. Turner, J. R. Price, R. Herbst-Irmer, K. Sugimoto, E. Nishibori and S. Grabowsky, *Cryst. Growth Des.*, 2017, **17**, 3812.
10 A. L. Spek, *Acta Crystallogr. Sect. D,* 2009, **65**, 148.
11 A. L. Spek, *Acta Crystallogr. Sect. C,* 2015, **71**, 9.
12 Persistence of Vision Pty. Ltd. (2004). POV-Ray. Persistence of Vision Pty. Ltd., Williamstown, Victoria, Australia.
13 O. V. Dolomanov, L. J. Bourhis, R. J. Gildea, J. A. K. Howard, H. Puschmann, *J. Appl. Crystallogr.,* 2009, **42**, 339.
14 V. A. Blatov, A. P. Shevchenko, D. M. Proserpio, *Cryst. Growth Des.,* 2014, **14**, 3576.
15 Origin(Pro), Version *9.0.0*. OriginLab Corporation, Northampton, MA, USA.
16 W. K. Feldmann, K. White, C. X. Bezuidenhout, V. J. Smith, C. Esterhuysen and L. J. Barbour, *ChemSusChem*, 2019, DOI: 10.1002/cssc.201902990.
17 P. K. Bhowmik, A. K. Nedeltchev, H. Han, *Tetrahedron Lett.,* 2007, **48**, 5383.
18 C. B. Nielsen, M. Johnsen, J. Arnbjerg, M. Pittelkow, S. P. McIlroy, P. R. Ogilby, M. Jørgensen, *J. Org. Chem.,* 2005, **70**, 7065.
19 X. Peng, H. Gao, Y. Xiao, H. Cheng, F. Huang and X. Cheng, *New J. Chem.*, 2017, **41**, 2004.
20 M. J. Frisch, G. W. Trucks, H. B. Schlegel, G. E. Scuseria, M. A. Robb, J. R. Cheeseman, G. Scalmani, V. Barone, G. Mennucci, A. Petersson, H. Nakatsuji, M. Caricato, X. Li, H. P. Hratchian, A. F. Izmaylov, J. Bloino, G. Zheng, J. L. Sonnenberg, M. Hada, M. Ehara, K. Toyota, R. Fukuda, J. Hasegawa, M. Ishida, T. Nakajima, Y. Honda, O. Kitao, H. Nakai, T. Vreven, J. A. M. Jr., J. E. Peralta, F. Ogliaro, M. Bearpark, J. J. Heyd, E. Brothers, K. N. Kudin, V. N. Staroverov, T. Keith, R. Kobayashi, J. Normand, K. Raghavachari, A. Rendell, J. C. Burant, S. S.

Iyengar, J. Tomasi, M. Cossi, N. Rega, J. M. Millam, M. Klene, J. E. Knox, J. B. Cross, V. Bakken, C. Adamo, J. Jaramillo, R. Gomperts, R. E. Stratmann, O. Yazyev, A. J. Austin, R. Cammi, C. Pomelli, J. W. Ochterski, R. L. Martin, K. Morokuma, V. G. Zakrzewski, G. A. Voth, P. Salvador, J. J. Dannenberg, S. Dapprich, A. D. Daniels, O. Farkas, J. B. Foresman, J. V. Ortiz, J. Cioslowski, D. J. Fox, *Gaussian09*, **2013**.

21 C. Adamo, V. Barone, *J. Chem. Phys.*, 1999, **110**, 6158.

22 F. Weigend, R. Ahlrichs, *Phys. Chem. Chem. Phys.*, 2005, **7**, 3297.

23 S. Grimme, J. Antony, S. Ehrlich, H. Krieg, *J. Chem. Phys.*, 2010, **132**, 154104.

24 (a) S. F. Boys, F. Bernardi, *Mol. Phys.*, 1970, **19**, 553; (b) S. Simon, M. Duran, J. J. Dannenberg, *J. Chem. Phys.*, 1996, **105**, 11024.

Chapter 5

Concluding Remarks

MOFs and PCPs are an exceptionally large field of research, growing at an exponential rate. The focus has been on the creation of new MOFs over the past two decades. However, focusing on fine-tuning and controlling the properties of these materials can produce advanced materials with applications in several areas of industry. The field has advanced to a stage where it is important to understand the origin of the properties of MOFs, rather than just extending the database of known MOFs. Flexible stimulus-responsive MOFs are exciting in this regard as this is a developing field, with much left to be explored. Three sets of flexible frameworks are described in this thesis and insight is provided into how small modifications to their structure, due response to a stimulus or change in ligand functionalisation, can have a particularly large impact on properties. This work relates how even subtle changes in structure can significantly influence the behavior of a material.

The first study describes the photoactive framework **CdPCP**, wherein the SBU allows for several possible positions at which cycloaddition can occur between olefinic bonds in the bpeb linker. Either of the two isomers of the bpeb cyclised dimer was selectively synthesised through cycloaddition, by simple exchange of the guest. The nature of the guest included in the channels of the framework directly affected the conformation of the photoactive linker. The choice of guest could control the regioselectivity of the cycloaddition, as this is highly dependent on the alignment of the double bonds.

The initial change in regioselectivity of the cycloaddition reaction was observed on exchange of DMA by DMF. The mere absence of a methyl group in the guest completely changed the conformation of the ligand and produced a distinctly different synthetic product, **Isomer 2**, on irradiation. Interestingly, this isomer has only ever been synthesised within a MOF and not by classical organic methods. This study also went a step further by developing a simple means by which to extract the product from the framework, reinforcing the idea of using the framework as a 'synthetic vessel'. Many studies explore using a MOF as a means to synthesise compounds, but few present the isolated product at the end, which is a crucial prerequisite of the concept of using the framework as a means to synthesise a compound. Cycloaddition in the DMF solvate of **CdPCP** also resulted in linking two-dimensional sheets, forming a three-dimensional framework structure. This reaction can therefore also be seen as a simple means of post-synthetic modification to alter the framework dimensionality. In conclusion, this study highlights the idea of utilising the flexibility of the framework as a synthetic tool.

There are several aspects of this study that could be further explored. Unfortunately we could not identify a link between nature of the included guest and the resulting conformation of the bpeb linker.

A systematic study including a larger range of solvents with different polarities, kinetic diameters and physicochemical properties would provide more data points with which to identify a correlation between the nature of the guest and the conformation of the bpeb linker. It would be ideal to identify the defining characteristic that would allow prediction of the conformation of the bpeb ligand for a given guest. The complexity of the isomers could also be increased by placing substituents on the bpeb linker, although this may also change the structure of the framework such that it no longer complies with Schmidt's topochemical rules.

Green processes have become an important topic in synthetic chemistry, and photochemical reactions are considered to be green. The cycloaddition reaction in the framework takes place quite rapidly and requires only UV light to produce a complex organic compound. Admittedly, synthesis of the initial framework requires the use of DMA and DMSO as solvents at high temperatures. It would therefore be quite interesting to explore the use of mechanochemisty as a means to prepare the framework using liquid-assisted grinding with minimal solvent. This would further elevate the method as a green route to obtaining complex molecules. Mechanochemistry also has the added benefit of potentially simplifying the process of scaling up the synthesis of the framework. Some frameworks have displayed the ability to undergo cycloreversion, where the bonds forming the cycloabutane ring are cleaved using heat.[1] If successful, cycloreversion of **Isomer 1** (synthesised in the DMA solvate of **CdPCP**) would produce [2,2] paracyclophane, which has received increasing attention for its wide application as a ligand in asymmetric synthesis, organic optical materials, molecular junctions and as a rigid backbone in light-emitting diode TADF emitters.[2,3] A simple means to probe the possibility of cycloreversion would be to run a DSC experiment on the cyclised MOF or isolated bpeb dimer ligand. It is highly likely that the cycloreversion process will result in a heat flow response, which will indicate the temperature at which the process may occur.

The second study focused on temperature as the stimulus used to control the regioselectivity of the cycloaddition reaction within the DMA solvate of the same **CdPCP** framework described above. The framework undergoes a rare temperature-induced first order phase transition, which changes the conformation of the bpeb linker within the framework. As before, this change in conformation alters the regioselectivity of the cycloaddition reaction of the framework, therefore selectively forming either of the isomers depending on the temperature at which irradiation occurs. This study highlighted the effect that a subtle structural change can have on the properties of a framework.

Upon cooling, the framework undergoes a structural transition in the form of a conformational change of half the bpeb linkers along a chain in a perfect ABAB fashion. Initially, the only indication of this structural shift was a doubling of one of the unit cell axes. Axis doubling of this nature is often attributed to twinning, and only with repeated observation of the phenomenon in the current framework was this investigated further. Researchers often do not carry out their own intensity data collections and therefore it is highly likely that transitions such as these might go unnoticed. This is also evident in the lack of reported stimulus-responsive frameworks that undergo a structural transition purely as a result of temperature. In the few available studies, many did not focus on full characterisation of the structural

transition using classical methods and rather only reported the presence thereof. This made the current study especially challenging because there is no established convention for dealing with this type of behaviour in MOFs. Comprehensive characterisation of the material was therefore a principal aim of this study, which was achieved. Many interesting properties were discovered during this process. It was revealed that both cycling from one phase to the other, as well as the age of the sample, had an effect on the onset temperature of the transition. Interestingly the phase transition was also coupled to thermosalient behaviour which is also crystal size dependent, as previously demonstrated for several organic materials. Due to the unusual nature of the phase transition, i.e. exactly every alternate bpeb linker changing conformation, it was important to investigate and subsequently eliminate alternate theories. The possibility of inadequate equilibration time, freezing out of pedal motion and "freezing out of disorder" were investigated and it was concluded that the two phases are distinct polymorphs of each other.

The first study showed that irradiation of the DMA solvate at room temperature resulted in the formation of **Isomer 1**. The temperature-induced change in conformation in the bpeb linkers changes the photoactive positions in the framework. As the structural change is reversible, irradiation was carried out at 100 K to ensure the framework is in the low temperature phase. Cycloaddition in the low temperature phase resulted in the formation of **Isomer 2**. It is therefore also possible to selectively synthesise either of the two isomers in the DMA solvate by simply changing the temperature at which irradiation occurs.

In conclusion these studies demonstrated the multistimulus responsive nature of **CdPCP** to light, guest inclusion and temperature. It is one of the few examples of a temperature-induced phase transition in a framework, as well as a rare example of temperature-controlled regioselectivity of cycloaddition in the solid state. Future work should screen other solvates for the same behaviour, as it is quite interesting that only the DMA solvate underwent the low-temperature phase transition. It should also become routine to include low-temperature DSC analysis in the characterisation of flexible frameworks with similar linkers, as polymorphs are probably frequently undetected. Any future work would also require the development of a method or instrument to effectively irradiate large quantities of sample at low temperatures, as this was a great challenge during the course of the project. These two studies on **CdPCP** have highlighted the importance of detailed and careful characterisation of frameworks under a variety of conditions so as not to overlook potential valuable avenues of investigation.

The final study reported in this thesis moves away from cycloaddition and focuses on guest inclusion by means of gas sorption as the property to be modified and tuned. The focus remains on flexible stimulus-responsive frameworks and the impact that functionalisation of the bpeb ligand may have on properties of the framework. The sorption (adsorption and desorption) behaviour of a highly flexible fluorinated pillared-layered Zn(II) MOF that displays both breathing and subnetwork displacement modes of flexibility was investigated. The effect of fluorination of the pillar bpeb linker on the gate-opening pressure and extent of hysteresis was explored by comparing its sorption behaviour

to that of the non-fluorinated isoreticular analogue. The framework is responsive to certain guest molecules, and the stimulus and this response was modified and tuned by functionalisation of the framework. It was found that the fluorination of the framework delayed the onset of the gate-opening pressure substantially, and resulted in greater hysteresis for sorption of CO_2, C_2H_4 and C_3H_8 in comparison to the non-fluorinated analogue. *In situ* SCXRD analysis of the activated and CO_2-included structures of the fluorinated framework was crucial in identifying C-F···H-C interactions. These interactions between the pillar linkers of different nets are responsible for holding the framework closed under elevated pressures. Computational analysis further supported this observation, and revealed the presence of strong π-π interactions between nets within the fully open structure, which are responsible for maintaining the open-pore form for an extended pressure range upon desorption. The study demonstrates ligand fluorination as a tool to tune both gate-opening and hysteresis in pillared-layered frameworks.

Investigation into flexible frameworks remains a challenging venture. A material undergoing a 38% reduction in solvent-accessible space upon activation is difficult to characterise using SCXRD techniques. If successful however, these challenging studies can be extremely rewarding and can lead to many noteworthy findings. This is the first report where fluorination of the pillar linker in a pillar-layered framework is used to tune the gate-opening pressure or extent of hysteresis. Hysteresis is a rarely studied phenomenon and this study reports some of the largest values for the extent of hysteresis to date. Several non-routine methods of analysis including *in situ* variable-pressure X-ray diffraction techniques and PGDSC, were employed to provide valuable insight into the structure-property relationships of the material. PGDSC was a useful tool that provided high-resolution thermograms to measure the response of the framework to gas loading, in terms of onset pressures for gate-opening and closing, and hysteresis. Information is often lost using volumetric sorption analysis, as evidenced by when comparing the sorption isotherms with the PGDSC traces.

The mechanism by which the framework opens and closes in response to gas pressure as a stimulus is likely to be different for various gases. This is evident upon comparison of the isotherms for the different gases (CO_2, C_2H_4 and C_3H_8), which all show uniquely different profiles. The fluorinated framework demonstrates interesting behaviour upon activation as the framework collapses to yield a completely non-porous framework, which is rarely reported. For CO_2 and C_2H_4, the closed pore form converts to the narrow pore form at a low pressure, and gradually increases gas loading over a large pressure range before it converts to the open pore form. However, for C_3H_8, the framework exhibits a 'Type F-IV' isotherm and remains in the closed pore form for an extended pressure range before rapidly converting to the open pore form at a threshold pressure. Flexible materials exhibiting Type F-IV isotherms are particularly rare and highly desirable for pressure-swing adsorption and gas storage due to having larger working capacities. This study shows that fluorination of pillar linkers is a viable pathway to developing frameworks that exhibit Type F-IV sorption profiles in future.

There are several areas where this study could be extended which may result in valuable contributions to the developing field of flexible frameworks. Repeated cycles of gas sorption on flexible

frameworks is currently not commonly reported in the literature and requires further investigation. This study provided some evidence indicating that repeated gas cycling may have a large effect on the gas-sorption behaviour of a framework. A few experts in the field have speculated why this may occur.[4,5] Possible explanations include reduction in particle size over several cycles, or a decrease in the activation energy barrier after the first cycle. Cycling effects were observed for both the fluorinated and non-fluorinated frameworks investigated in the previously mentioned study. The choice of gas influenced the observed effects over successive cycles, suggesting that the nature of the gas plays a role in the extent of change in terms of maximum gas loading and onset pressures for gate openings. A full systematic study should therefore be carried out on both frameworks with gases ranging in size and polarity using both PGDSC and volumetric sorption analysis. Previous cycling studies of flexible frameworks did not have the sensitivity of PGDSC analysis to observe subtleties in sorption behaviour at high resolution, and this would be a unique angle to the proposed study. It would also be interesting to further investigate the mechanism by which the fluorinated framework opens to propane in comparison to CO_2, due to large differences in onset pressures. In this regard, obtaining a single crystal structure of the propane-loaded framework would be invaluable and provide additional mechanistic insights.

Finally this work highlights the importance of subtleties and the influence of seemingly small factors on the properties exhibited by flexible stimulus-responsive materials. The simplest of changes, such as guest exchange or a change of temperature, can selectively control the synthetic product of cycloaddition in a framework due to a simple bond rotation. Fluorination of a linker can double the onset pressure of a gate-opening event and drastically increase the extent of hysteresis of CO_2 in a pillar-layered flexible framework. Overall, these studies provide evidence that highlights the effect that stimuli can have on a flexible material and the relative simplicity of tuning the structure of the material. Fine-tuning of performance under a particular set of conditions should be evident from this work.

This works also highlights the importance of thorough characterisation when investigating flexible stimulus-responsive materials, as the subtle changes described herein are often overlooked. This study provides a deeper understanding of flexible MOFs and PCPs and delivers several potential tools to be used in the development of future framework materials.

5.1 References

1 N.-Y. Li, D. Liu, B. F. Abrahams and J.-P. Lang, *Chem. Commun.*, 2018, **54**, 5831–5834.

2 S. E. Gibson and J. D. Knight, *Org. Biomol. Chem.*, 2003, **1**, 1256–1269.

3 D. M. Knoll, H. Šimek, Z. Hassan and S. Bräse, *Eur. J. Org. Chem.*, 2019, 6198–6202.

4 J. A. Mason, J. Oktawiec, M. K. Taylor, M. R. Hudson, J. Rodriguez, J. E. Bachman, M. I. Gonzalez, A. Cervellino, A. Guagliardi, C. M. Brown, P. L. Llewellyn, N. Masciocchi and J. R. Long, *Nature*, 2015, **527**, 357–361.

5 A.-X. Zhu, Q.-Y. Yang, A. Kumar, C. Crowley, S. Mukherjee, K.-J. Chen, S.-Q. Wang, D. O′Nolan, M. Shivanna and M. J. Zaworotko, *J. Am. Chem. Soc.*, 2018, **140**, 15572–15576.